TECHNISCHE UNIVERSITÄT MÜNCHEN
Fakultät für Elektrotechnik und Informationstechnik
Lehrstuhl für Biologische Bildgebung

Functional Imaging with Multispectral Optoacoustic Tomography: Methods and Applications

Ivan Olefir

Acknowledgements

Looking back at the years of research as a Ph.D. student, it is absolutely clear to me that I would not have reached this point without the help and support of a number of people.

First and foremost, I would like to thank my supervisor Dr. Vasilis Ntziachristos. Many years ago, it was his lectures that enkindled my interest in biomedical imaging and motivated me to do research in this field. In the following years, it was his support that led me to successfully complete the work described in this dissertation. I am thankful for the trust he had in my abilities that motivated me throughout these years and allowed to contribute to some of the most exciting projects I could have ever hoped to work on.

I would like to sincerely thank my mentor and friend Stratis Tzoumas. Most of the things I know about conducting research, from ways to approach a scientific problem to adequately summarizing results in a paper, I learned from him, and I could not wish for a better teacher. I am grateful to him for introducing me to what would become the defining project of my Ph.D., for seeing the potential in me and for his immense patience when repeatedly explaining the simplest concepts. I would like to express my deep gratitude to Dr. Saak V. Ovsepian for mentoring and supporting me throughout the other major project of my Ph.D. His enthusiasm was a perfect counterbalance to my innate skepticism, and without his passion for neuroscience to draw motivation from, the project would not have been nearly as successful. I will miss the short walks we took as a break from work discussing all topics imaginable.

I would like to thank my colleagues and friends Hong, Suhanyaa, Pouyan, Neda and Nikolina for cheering me up and providing free therapy sessions on demand. I hope I could return the favor, at least in part. I am grateful to Kaushik for always being in the haushik, and to Svenja for our discussions that were a great mix of silliness (mostly on my part, of course) and science. I would like to thank my colleagues and friends Ara, Andrei, Andrii, Roman, Dima and especially Murad, who I feel was in a lot of ways responsible for bringing us together, for the scientific insights as well as for some of the funniest stories and jokes I have ever heard. I am grateful to Murad also for all his help and advice that he provided throughout the years. I feel extremely lucky to have been surrounded with such friendly and supportive people. I am also obliged to Gena who had helped me in some of the toughest times for which I am eternally grateful.

I would like to sincerely thank Sarah, Uwe and Pia for not only helping immensely with the lab work but also for making it so much more enjoyable by simply keeping company during the long scan times. I am grateful to Susanne, Lidia and Andi for running things smoothly and lending a helping hand every time I struggled with my worst nightmare - bureaucracy. I would like to especially thank Katharina for helping with all the teaching duties and solving mysteries along the way; and to Chapin for being a guiding light in a stormy sea of paper writing.

Finally, I would like to thank my family. Everything I have achieved is thanks to them, their unconditional love and support and their wise advice that I was at times foolish enough to dismiss. Being scientists themselves, my parents have, perhaps unknowingly to some degree, taught me the critical way of thinking that is instrumental for successfully conducting research. My passion for science and discovery that stems from my childhood and teenage years was noticed and fueled by them, with my questions on school courses often sparking discussions steering far beyond the initial topics in question. I would also like to thank my brother for always being the voice of reason whenever I find myself in a difficult situation.

Abstract

Multispectral Optoacoustic Tomography (MSOT) is an appealing imaging modality for functional imaging in animals and humans benefiting from its spectral imaging capabilities, high spatiotemporal resolution, and imaging depth. Functional imaging with MSOT is achieved by its unique ability to distinguish oxygenated and deoxygenated hemoglobin in tissue based on their corresponding measured optoacoustic (OA) spectra, with the potential for accurate quantification and high-resolution mapping of biologically meaningful blood-related metrics, such as blood oxygen saturation (sO_2). This work advances two aspects of MSOT functional imaging: methodological, by developing and improving the methods for accurate quantification of sO_2; and translational, by utilizing the potential of MSOT for functional brain imaging.

With no established techniques for quantitative label-free imaging of sO_2 at high resolution in deep tissue, MSOT is seen as one of the few imaging modalities capable of achieving this goal that is highly sought after in various biomedical applications. However, sO_2 quantification in MSOT is a challenging problem due the effect of spectral coloring, i.e. the modification of measured OA spectra of hemoglobin with wavelength- and location-dependent optical light fluence which impedes the ability of MSOT to quantify sO_2. Eigenspectra MSOT (eMSOT), a method that makes use of a simple spectral model for light fluence, has been introduced as the only method that was shown to correct for spectral coloring and improve sO_2 quantification accuracy of MSOT in experimental data from small animals. However, the performance of eMSOT is limited by its sensitivity to the noise in the measurements and reliance on a solution of a non-convex inverse problem bound by a number of *ad hoc*, possibly suboptimal constraints.

To address the limitations of eMSOT, the inverse problem is first formulated in the Bayesian framework as a maximum a posteriori (MAP) estimation, where the unknown parameters are treated as random variables. The inversion constraints are modeled as prior distribution and their parameters are optimized. A novel model-based way to estimate noise in the measured OA spectra is introduced and validated on simulated data. The noise estimates are used in the Bayesian algorithm to adaptively weigh the measurements. The Bayesian algorithm is compared to the original eMSOT method in simulations and is found to provide improved sO_2 quantification accuracy in deep-seated highly absorbing targets in the presence of high amounts of spatially non-uniform noise characteristic for MSOT data. To further improve quantification accuracy of eMSOT, the constrained optimization procedure used to solve the inverse problem in both eMSOT and its Bayesian implementation is replaced by a neural network. The proposed architecture is trained on data produced by relatively simple simulations and is shown to be well-suited for solving the inverse problem of eMSOT. An ensemble of 50 models based on the proposed architecture is shown to outperform the original eMSOT in simulations and in most cases of experimental datasets from blood phantoms and small animals (mice) with the available ground truth sO_2 values.

From the application point of view, the sensitivity of MSOT to both oxygenated and deoxygenated hemoglobin combined with high imaging depth at high resolution makes it an ideal instrument for the field of functional brain imaging in small animals. While this potential has been recognized, the majority of studies using macroscopic optoacoustic imaging for neuroscience have so far been limited to the superficial brain tissue with setups providing the limited dorsal view of brain, or not fully utilizing the spectral capabilities of MSOT. We address the mentioned omissions by first examining a hybrid MSOT system capable of acquiring ultrasound images for neuroimaging in small animals and confirming the ability of MSOT to extract meaningful quantitative hemodynamic parameters from deep brain compartments and blood vessels. We further employ MSOT for functional brain imaging of evoked hemodynamic response and visualize the brain activity in deep compartments in the coronal cross-sections. In addition, we demonstrate the superb capabilities of MSOT for structural imaging both *in vivo*, enabling seamless registration of the detected

activity with major anatomical landmarks; and *ex vivo*, enabling morphometric studies in intact mouse brains. Furthermore, we show how molecular imaging with MSOT can enhance the obtained information, making MSOT an extremely versatile instrument for neuroscientific research.

Zusammenfassung

Die multispektrale optoakustische Tomographie (*Multispectral Optoacoustic Tomography*, MSOT) ist aufgrund ihrer Fähigkeit Spektren darzustellen, ihrer hohen raum-zeitlichen Auflösung und ihrer Abbildungstiefe eine geeignete Bildgebungsmethode für die funktionelle Bildgebung bei Kleintieren und Menschen. Die funktionelle Bildgebung mit MSOT wird durch ihre einzigartige Fähigkeit erreicht, sauerstoffreiches von sauerstoffarmem Hämoglobin im Gewebe auf der Grundlage der gemessenen optoakustischen (OA) Spektren zu unterscheiden. Dies birgt das Potenzial für eine genaue Quantifizierung und eine hochauflösende Abbildung biologisch aussagekräftiger blutbezogener Metriken, wie z.B. der Sauerstoffsättigung des Blutes (sO_2). Diese Arbeit bringt die funktionelle MSOT-Bildgebung in zwei Aspekten voran: Einerseits in der Methodik, durch die Entwicklung und Verbesserung der Methoden zur genauen Quantifizierung von sO_2; andererseits in der Translation, durch die Nutzung des Potentials der MSOT für die funktionelle Bildgebung des Gehirns.

Da es keine etablierten Techniken für die quantitative markierungsfreie Bildgebung von sO_2 in hoher Auflösung für tiefes Gewebe gibt, wird die MSOT als eine der wenigen Bildgebungsmodalitäten angesehen, die dieses in verschiedenen biomedizinischen Anwendungen gewünschte Ziel erreichen können. Die Quantifizierung von sO_2 in der MSOT ist jedoch ein schwieriges Problem aufgrund des Effekts der spektralen Färbung (spectral coloring). Spektrale Färbung beschreibt die Veränderung der gemessenen OA-Spektren von Hämoglobin basierend auf der wellenlängen- und ortsabhängigen optischen Lichtfluenz. Dieser Effekt behindert die Fähigkeit der MSOT zur Quantifizierung von sO_2. Eigenspektren MSOT (*Eigenspectra MSOT*, eMSOT), eine Methode, die ein einfaches Spektralmodell für die Lichtfluenz verwendet, wurde als bisher einzige Methode eingeführt, die nachweislich die spektrale Färbung korrigiert und die Genauigkeit der sO_2-Quantifizierung von MSOT in experimentellen Daten von Kleintieren verbessert. Die Leistung von eMSOT ist jedoch durch seine Empfindlichkeit gegenüber dem Rauschen in den Messungen und die Abhängigkeit von der Lösung eines nicht konvexen inversen Problems, das durch eine Reihe von *ad hoc* festgelegten, möglicherweise suboptimalen Einschränkungen gebunden ist, begrenzt.

Um die Einschränkungen von eMSOT zu beheben, wird das inverse Problem zunächst im Bayes'schen Rahmen als eine Maximum-a-posteriori (MAP)-Schätzung formuliert, bei der die unbekannten Parameter als Zufallsvariablen behandelt werden. Die Inversionsbeschränkungen werden als a-priori-Verteilung modelliert und ihre Parameter werden optimiert. Eine neue modellbasierte Methode zur Schätzung des Rauschens in den gemessenen OA-Spektren wird eingeführt und anhand simulierter Daten validiert. Die Rauschschätzungen werden im Bayes'schen Algorithmus verwendet, um die Messungen adaptiv zu gewichten. Der Bayes'sche Algorithmus wird in Simulationen mit der ursprünglichen eMSOT-Methode verglichen und es wird festgestellt, dass er eine verbesserte sO_2-Quantifizierungsgenauigkeit in tiefliegenden, hoch absorbierenden Targets bei hohen Mengen an räumlich ungleichmäßigem Rauschen, das für MSOT-Daten charakteristisch ist, bietet. Um die Quantifizierungsgenauigkeit von eMSOT weiter zu verbessern, wird das eingeschränkte Optimierungsverfahren, das zur Lösung des inversen Problems sowohl in eMSOT als auch in seiner Bayes'schen Implementierung verwendet wird, durch ein neuronales Netz ersetzt. Die vorgeschlagene Architektur wird auf Daten trainiert, die durch relativ einfache Simulationen erzeugt wurden, und es hat sich gezeigt, dass sie für die Lösung des inversen Problems von eMSOT gut geeignet ist. Ein Ensemble von 50 Modellen auf der Grundlage der vorgeschlagenen Architektur übertrifft das ursprüngliche eMSOT in Simulationen und in den meisten Fällen in experimentellen Datensätzen von Blutphantomen und kleinen Tieren (Mäusen) mit verfügbaren Ground Truth sO_2-Werten.

Aus Anwendungssicht macht die Empfindlichkeit der MSOT für sowohl sauerstoffreiches als auch für sauerstoffarmes Hämoglobin in Verbindung mit einer hohen Abbildungstiefe bei hoher Auflösung sie zu einem idealen Instrument für den Bereich der funktionellen Bildgebung des Gehirns bei Kleintieren. Obwohl dieses Potenzial erkannt wurde, war die Mehrzahl der Studien, die

makroskopische optoakustische Bildgebung für die Neurowissenschaften verwenden, bisher auf das oberflächliche Hirngewebe beschränkt, wobei die Aufbauten die eingeschränkte dorsale Ansicht des Gehirns ermöglichten oder die spektralen Fähigkeiten der MSOT nicht voll nutzten. Wir beheben die erwähnten Lücken, indem wir zunächst ein hybrides MSOT-System untersuchen, das Ultraschallbilder für die neurologische Bildgebung bei Kleintieren aufnehmen und die Fähigkeit der MSOT, aus tiefen Hirnkompartimenten und Blutgefäßen aussagekräftige quantitative hämodynamische Parameter zu extrahieren, bestätigen kann. Darüber hinaus setzen wir MSOT für die funktionelle Hirnbildgebung evozierter hämodynamischer Reaktionen ein und visualisieren die Hirnaktivität in tiefen Kompartimenten in koronalen Querschnitten. Des Weiteren demonstrieren wir die hervorragenden Fähigkeiten der MSOT für die strukturelle Bildgebung sowohl *in vivo*, was eine nahtlose Registrierung der detektierten Aktivität mit wichtigen anatomischen Landmarken ermöglicht, als auch *ex vivo*, was morphometrische Studien an intakten Mäusehirnen ermöglicht. Zudem zeigen wir, wie die molekulare Bildgebung mit MSOT die gewonnenen Informationen verbessern kann, was MSOT zu einem äußerst vielseitigen Instrument für die neurowissenschaftliche Forschung macht.

I dedicate this to my parents and my brother.

Publication and Submission Record

This work is a publication based dissertation that is based on four publications that are either published, or accepted for publication in international journals († indicates equal author contribution):

1. **I. Olefir**, S. Tzoumas, H. Yang, and V. Ntziachristos, "A Bayesian approach to eigenspectra optoacoustic tomography," *IEEE Transactions on Medical Imaging*, vol. 37, no. 9, pp. 2070-2079, 2018.

2. **I. Olefir**†, S. Tzoumas†, C. Restivo, P. Mohajerani, L. Xing and V. Ntziachristos, "Deep learning based spectral unmixing for optoacoustic imaging of tissue oxygen saturation", accepted for publication in *IEEE Transactions on Medical Imaging*.

3. **I. Olefir**, E. Merčep, N. C. Burton, S. V. Ovsepian, and V. Ntziachristos, "Hybrid multispectral optoacoustic and ultrasound tomography for morphological and physiological brain imaging," *Journal of Biomedical Optics*, vol. 21, no. 8, p. 086005, 2016.

4. **I. Olefir**, A. Ghazaryan, H. Yang, J. Malekzadeh-Najafabadi, S. Glasl, P. Symvoulidis et al., "Spatial and spectral mapping and decomposition of neural dynamics and organization of the mouse brain with multispectral optoacoustic tomography," *Cell reports*, vol. 26, no. 10, pp. 2833-2846. e3, 2019.

The following publications that I have contributed to during my Ph.D. are relevant to this work but are not included in this dissertation as individual chapters:

5. S. Tzoumas†, A. Nunes†, **I. Olefir**, S. Stangl, P. Symvoulidis, S. Glasl et al., "Eigenspectra optoacoustic tomography achieves quantitative blood oxygenation imaging deep in tissues," *Nature Communications*, vol. 7, p. 12121, 2016

6. S. V. Ovsepian, **I. Olefir**, G. Westmeyer, D. Razansky, and V. Ntziachristos, "Pushing the boundaries of neuroimaging with optoacoustics," *Neuron*, vol. 96, no. 5, pp. 966-988, 2017.

7. H. Yang, **I. Olefir**, S. Tzoumas, and V. Ntziachristos, "Synthetic data framework to estimate the minimum detectable concentration of contrast agents for multispectral optoacoustic imaging of small animals," *Journal of biophotonics*, p. e201900021, 2019.

8. S. Schoeder, **I. Olefir**, M. Kronbichler, V. Ntziachristos, and W. Wall, "Optoacoustic image reconstruction: the full inverse problem with variable bases," *Proceedings of the Royal Society A*, vol. 474, no. 2219, p. 20180369, 2018.

9. S. V. Ovsepian, **I. Olefir**, and V. Ntziachristos, "Advances in optoacoustic neurotomography of animal models," *Trends in biotechnology*, 2019.

List of abbreviations

AED	Absorbed Energy Density
BOLD	Blood Oxygenation Level Dependent
CT	Computed Tomography
DA	Diffusion Approximation
DAQ	Data Acquisition
DOI	Diffuse Optical Imaging
DOT	Diffuse Optical Tomography
eMSOT	Eigenspectra Multi-spectral Optoacoustic Tomography
FEM	Finite Element Method
HbO$_2$	Oxygenated Hemoglobin
HHb	Deoxygenated Hemoglobin
MFP	Mean Free Path
MRI	Magnetic Resonance Imaging
MSOT	Multi-spectral Optoacoustic Tomography
Nd:YAG	Neodymium-doped Yttrium Aluminum Garnet
NIR	Near-infrared
NIRS	Near-infrared Spectroscopy
OA	Optoacoustics
OCT	Optical Coherence Tomography
OPO	Optical Parameter Oscillator
PCA	Principal Component Analysis
PET	Positron Emission Tomography
RNN	Recurrent Neural Network
RTE	Radiative Transfer Equation
SNR	Signal-to-noise Ratio
SPECT	Single Photon Emission Tomography
TMFP	Transport Mean Free Path
US	Ultrasound

Contents

Chapter 1

Functional imaging with multispectral optoacoustic tomography - an overview

1.1 Introduction

1.1.1 Functional imaging in biomedical research and clinical practice

Since the invention of the microscope, biological imaging has become a crucial component in both clinical practice and basic research. A whole spectrum of imaging modalities has evolved expanding the toolkit for interrogation of biological specimens. Microscopy, X-Ray and X-Ray Computed Tomography (CT), Ultrasound (US), Positron Emission Tomography (PET), and Magnetic Resonance Imaging (MRI) are the examples of some of the most popular imaging techniques that are used routinely by doctors and researchers. The benefits of using the mentioned techniques in the clinical setting are obvious: they allow for early diagnosis and effective treatment monitoring [1], and are used for high precision guidance of instruments during medical procedures [2]. With the increasing use of animal models for pre-clinical research, the mentioned techniques have been adapted for small-animal imaging to accommodate the needs of researchers [3, 4]. Importantly, the array of imaging modalities is not limited to the mentioned techniques only. Other, perhaps less widely used imaging methods that have also received a lot of attention for clinical, pre-clinical and basic research include Diffuse Optical Tomography (DOT), Optical Coherence tomography (OCT), Single Photon Emission Tomography (SPECT) and others [5, 6].

Generally, three types of imaging are performed using the aforementioned techniques in both clinical and pre-clinical situations: anatomical (structural), molecular, and functional (physiological). Structural imaging is perhaps the most basic type of biomedical imaging routinely performed in the clinics. It aims at visualizing the anatomy of the specimen and is typically achieved using CT [7], MRI [8] or US [9]. As the name suggests, molecular imaging refers to visualizing spatial distributions of specific molecules, or biomarkers, and allows to delineate certain molecular pathways and monitor cellular function [10, 11]. PET [12] and SPECT [13] are the most widely used molecular imaging modalities. Finally, the aim of functional imaging is to visualize tissue and organ function by means of measuring and visualizing certain physiological and metabolic parameters. Notably, such parameters often relate to blood and include hemodynamics [14, 15], blood perfusion [16], oxygen saturation (sO$_2$) [17], and partial pressure of oxygen (pO$_2$) [18]. This naturally leads to the fact that the most widely used functional imaging techniques are sensitive to certain blood-related parameters such as blood velocity (Doppler US [19]) or fraction of deoxyhemoglobin (Blood Oxygen Level Dependent MRI, or BOLD MRI [20]). PET also achieves functional imaging by visualizing metabolism in the form of glucose uptake [21].

Naturally, the underlying physical principle of operation of every imaging technique determines its characteristics, enabling its application in some situations and limiting in the others. The characteristics of imaging methods that are critical for biomedical imaging include spatial resolution, temporal resolution, sensitivity, and penetration depth. Depending on the area of application, imaging speed, patient safety, cost, and other concerns may be of high importance. Generally,

there is no imaging technique that would excel at every imaging task as there is always a trade-off among these characteristics. Importantly, imaging modalities that allow for *in vivo* imaging are especially valuable. In the context of clinical imaging, they allow to reduce the amount of invasive and potentially dangerous procedures to a minimum, while in the pre-clinical setting they enable the execution of longitudinal studies, where the same object or process can be monitored in its development without external perturbation [22–24].

Most of the radiological imaging methods, such as CT, US or MRI, have been initially developed for structural imaging, with some of them evolving further to allow performing functional imaging as well. CT is a fast and inexpensive imaging method, but uses ionizing radiation, has low soft tissue contrast [25] and is not well-suited for functional imaging in general. US boasts real-time imaging speed, is inexpensive and safe, but prone to numerous imaging artifacts, such as mirroring, shadowing, enhancement, etc. [26, 27] Furthermore, US can provide higher resolution only at shallower depths. MRI has high enough spatial resolution for clinical use but is relatively expensive. Furthermore, higher spatial resolution that is needed for small animal imaging is achieved either by using stronger magnets, leading to increased costs and/or at the cost of the temporal resolution [28]. Despite recent advances in the development of fast imaging sequences, the temporal resolution of MRI still impedes to a certain degree its ability to image fast processes at high resolution. Furthermore, MRI is only sensitive to deoxygenated hemoglobin (HHb) and not to oxygenated hemoglobin (HbO$_2$) limiting its potential for quantitative functional imaging [20]. PET and SPECT excel at imaging molecular targets with high sensitivity but lack the ability to capture anatomical information, have low spatial resolution and are expensive due to the use of radioactive tracers and the consequent need for the corresponding infrastructure [6].

Optical imaging techniques constitute yet another group of imaging modalities. Such modalities rely on light to perform specimen interrogation, which allows to complement and improve upon the weaknesses of the radiological methods. The use of light brings the advantage of having rich optical contrast leading to superb soft tissue contrast. The ability to use a range of fluorescent proteins makes optical imaging techniques suitable for molecular imaging [11, 29] and the optical contrast of HHb and HbO$_2$ enables functional imaging using optical methods. Furthermore, optical imaging techniques do not use ionizing radiation and are generally inexpensive, making them an attractive and accessible alternative to the radiological methods. With all the clear advantages of the optical methods, their major limiting factor lies in high *elastic photon scattering* in tissue, a term referring to the process of absorption and re-emission of photons without the loss of photon energy but with probable change in photon direction. The effects of scattering on a laser beam propagating through a scattering medium is illustrated in Fig. 1.1. The two physical parameters that describe the propagation of photons in scattering media are the photon mean free path (MFP) and the transport mean free path (TMFP). The former characterizes the average distance travelled by a photon in a medium between two subsequent scattering events and the latter refers to the average distance that the photon travels before its direction becomes effectively random. Fig. 1.1A schematically visualizes MFP and TMFP. Black arrows denote the paths of single photons; white circles denote the scatterers. The schematic is overlaid on a picture of a laser beam propagating in a scattering medium. In the visible and near-infrared ranges that are widely used in optical imaging, TMFP is approximately ten times larger than MFP for biological tissues and is of the order of 1 mm [30], which severely limits the imaging depth of the optical techniques. The effect of the increasing scattering coefficient of the medium on the loss of propagation directionality is demonstrated in Fig. 1.1B-E, where a laser beam travels through the media with various scattering coefficients. The media are water with one (Fig. 1.1B), three (Fig 1.1C), ten (Fig. 1.1D) and twenty (Fig. 1.1E) drops of milk added to increase scattering. While in Fig. 1.1B the photons demonstrate ballistic propagation along the whole beam path (large values of MFP and TMFP), in Fig. 1.1C no visible directionality of light is preserved after propagating through approximately one radius of the glass. In Fig. 1.1D, no directionality of the beam is visibly present, signifying low values of both MFP and TMFP parameters. The vital characteristics of various optical imaging techniques are essentially defined by the way the problem of light diffusion is treated.

Optical microscopy is the most mature optical imaging technique, and perhaps the most widely used. Since its invention, the microscope has remained an indispensable tool in the hands of biologists. The maximum imaging depth in conventional microscopy depends on the MFP. In biological tissues this parameter is typically of the order of 0.1 mm (changes with photon wavelength), hence the imaging samples in are sliced to be thinner than 0.1 mm so that no photon scattering takes place leading to optimal image quality. Over more than three centuries of development, several
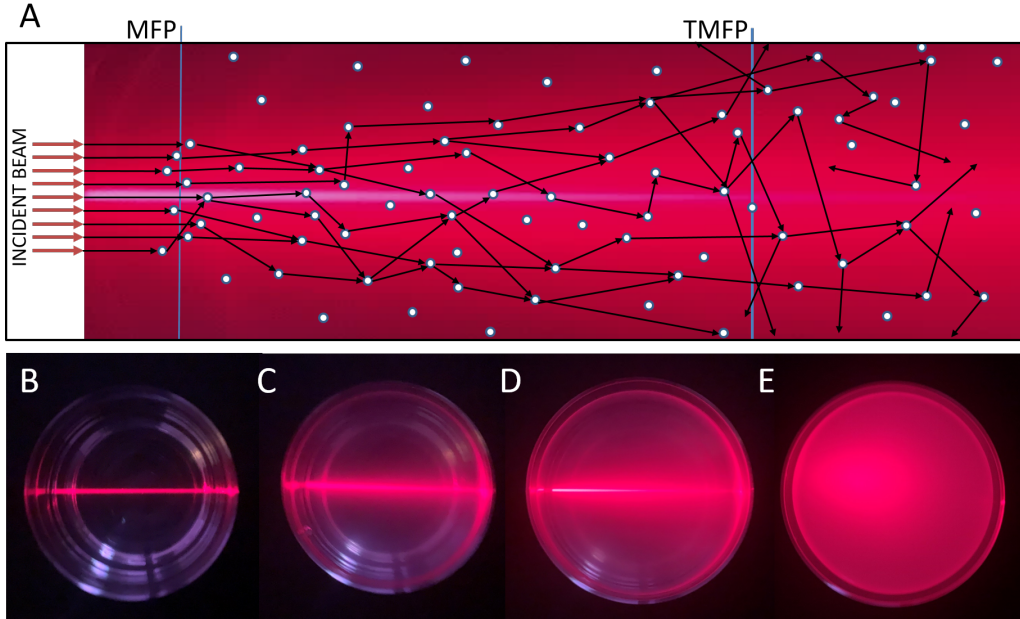
Figure 1.1: Effects of scattering on photon propagation. (A) A schematic representation of photon paths (black arrows) in a scattering medium (scatterers are depicted with white circles). **B-E.** Laser beam propagating in water with one (B), three (C), ten (D) and twenty (E) drops of milk added to increase the scattering in the medium

microscopy methods that have improved penetration depth have been proposed, including confocal [31], two-photon [32] and multiphoton microscopy [32, 33]. Typically, the penetration depth of the advanced microscopic techniques depends on the TMFP. Despite major advancements, the current microscopic techniques generally do not achieve high resolution imaging at depths beyond 1 mm, which is insufficient for various applications, in particular in small-animal imaging [30]. The applicability of microscopy methods for functional imaging of organs is further limited by a small field of view.

Another well-established optical imaging technique that is interferometric in nature, Optical Coherence Tomography, improves upon the depth penetration limit of optical microscopy while retaining high resolution, but still fails to image deeper than 5 mm in highly scattering tissue [34]. Therefore, the most impressive performance of OCT is demonstrated when imaging in transparent tissues. For instance, retina imaging was the first demonstrated clinical application of OCT [35]. Other clinical applications of the imaging modality include such areas as cardiology [36], oncology [37] and dermatology [38].

The development of the theory and techniques for modeling light diffusion has spurred the development of Diffuse Optical Imaging (DOI) techniques that achieve better imaging depth as compared to microscopy methods. Diffuse Optical Tomography (DOT) has been developed and successfully used, among other areas, in mammography [39] and functional brain imaging [40]. In small animal imaging, DOT has been applied to visualize hemoglobin and extrinsic chromophores [41, 42]. However, the spatial resolution of DOI techniques typically remains low [43, 44].

While the fundamental limitations of DOI techniques imposed by tissue scattering have impeded the progress in their development and application, optoacoustic (OA), also termed photoacoustics, has emerged as a biomedical imaging modality that offered a completely new perspective on small animal imaging [45]. An inherently hybrid technique, OA uses light to excite the specimen, and sound as the signal carrier. OA employs the optoacoustic effect – a physical phenomenon of ultrasound generation due to thermoelastic expansion as the result of transient light absorption. Historically, the OA effect has been known since 1880, when Alexander Graham Bell constructed a photophone – a device that could generate sound when exposed to a sunlight beam [46]. However, it was not until the late 1990s that ultrasound detection technology has matured enough for the OA effect to be used as a biological imaging technique. As a hybrid imaging modality, OA has several major advantages compared to DOI techniques. First and foremost, the reliance of OA on the detection of ultrasound almost completely eliminates the dependence of imaging depth on tissue

Table 1.1: An Overview of Modalities in Biomedical Imaging

		Signal Carrier	Resolution (μm)	Imaging Depth	Sensitivity (molar)	Accessibility	Contrast	Imaging Capabilities	Limitations
Optical	CM	light	<1	*	~10^{-12} (pico)	****	*****	• structural • molecular	• low penetration depth
	MPM	light	<1	**	~10^{-12} (pico)	***	*****	• structural • molecular	• low penetration depth
	OCT	light	~10	**	~10^{-9} (nano)	*****	***	• structural • molecular	• low penetration depth
	DOT	light	>1000	*****	~10^{-9} (nano)	*****	***	• functional	• low spatial resolution
Common Radiological	CT	X-rays	~50	*****	~10^{-6} (micro)	****	**	• structural	• low soft tissue contrast • ionizing radiation
	MRI	radio waves	~20	*****	~10^{-9} (nano)	***	*****	• structural • functional • molecular	• low temporal resolution • costly
	PET	γ-rays	~1000	*****	~10^{-15} (femto)	*	*****	• functional • molecular	• costly infrastructure • low spatial resolution • ionizing radiation
	SPECT	γ-rays	~1000	*****	~10^{-15} (femto)	*	****	• functional • molecular	• costly infrastructure • low resolution • use of ionizing radiation
	US	sound	~50	****	~10^{-12} (pico)	*****	*	• structural • functional	• low contrast • numerous image artifacts
Optoacoustic	OAT	sound	~100	***	~10^{-9} (nano)	*****	*****	• structural • functional • molecular	• largely in development, especially for clinical use • multispectral potential not fully realized
	OAM	sound	<1	**	~10^{-12} (pico)	*****	*****	• structural • functional • molecular	• low penetration depth

*Low *****High (relative scale)

CM, confocal microscopy| **MPM** multiphoton (including 2 photon) microscopy| **OCT**, Optical Coherence Tomography| **CT**, Computed Tomography| **MRI**, Magnetic Resonance Imaging| **PET**, Positron Emission Tomography| **SPECT**, Single Photon Emission Tomography| **US**, Ultrasound| **OAT**, Optoacoustic Tomography| **OAM**, Optoacoustic Microscopy

optical scattering since ultrasound scatters several orders of magnitude less than light in biological tissues [45]. At the same time, since light absorption generates the initial pressure rise in tissue, OA still retains rich optical contrast [47]. This leads to OA being able to produce high-resolution images of optical contrast in deep tissue making it an excellent structural imaging technique.

Notably, the feature of OA that makes it well suited for molecular and functional imaging is its spectral imaging capability. Essentially, the wavelength of the excitation laser light can be tuned, which results in the corresponding change in the reconstructed intensity in every voxel, giving rise to a measured OA spectrum at every spatial location in the image. The OA spectrum is correlated to the optical absorption spectrum at a given location. If the molecular constituents at every location are known together with their optical absorption signatures, the recorded OA spectrum can potentially be used to infer the concentrations of the respective chromophores in a process termed spectral unmixing [48]. This capability essentially defines OA as a molecular imaging technique, since it can detect and spatially map distributions of absorbing chromophores based on their absorption spectral signatures. A variety of OA-specific probes has been developed for this purpose, including a selection of absorbing nanoparticles [49–52]. Importantly, a wide range of already existing fluorescent reporters can also be used and resolved with OA [49, 53]. Table 1.1 briefly summarizes the characteristics of the imaging modalities discussed herein and puts OA in the context of other available imaging methods.

From the perspective of functional imaging, it is important to note that the biological contrast in OA stems from hemoglobin since the excitation light is primarily in the visible or near-infrared range (NIR), where hemoglobin is the prominent absorber in tissue [51]. By utilizing its spectral capability, OA is able to measure and differentiate the spectra of oxy- and deoxy-hemoglobin and estimate and spatially map blood and tissue oxygen saturation (sO_2) using an appropriate spectral unmixing technique. A multitude of OA imaging setups have been developed ranging in resolution

and depth penetration, including OA microscopy and mesoscopy, but it is primarily Multispectral Optoacoustic Tomography (MSOT) that is able to visualize hemoglobin gradients at high resolution in tissue depths of more than 1 cm, making it especially well-suited for functional studies in small animals.

The ability of OA to resolve and spatially map a multitude of chromophores at unprecedented depths and resolutions has ensured great interest from a wide range of researchers. OA has been used for imaging various cancer models [54], perfusion [55], liver disease [56], muscle metabolism [57] and even brain activity [58]. Developing and improving methods for improving the functional capabilities of MOST together with pushing the boundaries of its application experimentally is essential for establishing MSOT as a key modality for preclinical research.

1.1.2 Objectives

With commercial OA scanners for small animal imaging available [59] and the problem of tomographic OA image reconstruction solved to an extent that would allow for consistent acquisition of high quality anatomical and spectral data [60], OA imaging has entered a stage where applications would be aimed at utilizing the functional imaging capabilities of MSOT to their full potential. As previously mentioned, the key functional parameter assessed by label-free MSOT is blood oxygen saturation, which plays an important role in studies of cancer, metabolism, inflammation and other fields of biological research.

The promise of (quantitative) label-free hemoglobin imaging has made MSOT an attractive technique for monitoring many biological processes [61]. From the computational perspective, however, the task of sO_2 quantification with MSOT presents a rather complex spectral unmixing problem. This is due to the fact that the spectral signatures of the absorbers get modified with tissue depth due to location- and depth-dependent changes in light fluence. If this effect, termed *spectral corruption* or *spectral coloring*, is not taken into account, sO_2 estimation becomes significantly less accurate, especially as depth increases [62]. This problem has been known since OA began to be used for biological imaging [63], but only recently have the potential effects of spectral coloring on the molecular sensitivity and sO_2 estimation accuracy been studied and described more rigorously [48]. Furthermore, the dependence of optical fluence on the typically unknown optical parameters of imaged tissue renders this physical quantity extremely hard to predict. This for a long time resulted in a lack of robust algorithms for reversing the effect of spectral corruption on experimental data, forcing researchers to perform simple unmixing techniques that ignore spectral corruption and lead to lower sensitivity and less accurate quantification. Eigenspectra MSOT (eMSOT) is the first fluence correction algorithm that has been demonstrated to reliably work in experimental OA data [64]. Despite the advantages it offers, it is still prone to errors as it solves an ill-posed inverse problem bound by *ad hoc*, possibly suboptimal constraints. Furthermore, it is highly sensitive to the quality of the spectral data. With various artifacts and the spatially non-uniform distribution of noise typical for OA images, the performance of the algorithm is still largely user-dependent. Therefore, accurate and robust sO_2 quantification in MSOT data remains a largely unsolved problem.

In terms of applications of the functional imaging capabilities of MSOT, functional brain imaging has received significant attention in recent years. The sensitivity of MSOT to hemoglobin has opened up new perspectives for its use in the neuroimaging field that has been long dominated by MRI, and multiphoton microscopy. In contrast to MRI, MSOT offers high spatiotemporal resolution and sensitivity to both oxy- and deoxyhemoglobin, at a much lower cost. Compared to multiphoton microscopy, MSOT can image much deeper. These advantages of MSOT have naturally spurred its application to problems in neuroimaging. Certain attempts have been made to use OA to unveil functional processes in the brain on multiple scales. A large number of studies in functional brain imaging so far have either used OA microscopy with limited penetration depth or tomographic setups that capture the dorsal view of the brain, thus providing little depth information. Generally, previous work in the field either examined superficial areas of the brain such as the cortex [65–67], or did not make full use of the spectroscopic capabilities of OA [68, 69], instead of focusing on the use of a single illumination wavelength. Correlating the recorded blood signal to specific brain structures has also proved challenging, with most studies visualizing only major superficial blood vessels or anatomical structures.

The objective of this work is twofold: to improve the performance of eMSOT as an sO_2 estimation technique by rendering eMSOT more robust and less user-dependent; and to consolidate the use of MSOT as a neuroimaging technique, by exploring its potential to visualize hemodynamic response in

areas including deep brain tissue, as well as perform structural brain imaging, to enable correlation of functional and structural information.

The first objective lies in the algorithmic domain. As mentioned, spectral corruption limits the quantification abilities of MSOT unless addressed. Although offering a significant improvement over commonly used unmixing algorithms, eMSOT still relies on a number of *ad hoc* parameters that, when chosen suboptimally, render the algorithm prone to errors. Therefore, it is important to optimize the algorithm to ensure the most accurate sO_2 estimation. Furthermore, the quality of the spectral OA data needs to be assessed so that the user can select regions with high-quality measured spectra. One of the aims of this work is, therefore, to develop a method to estimate the noise present in the recorded OA spectra and to detect spectral abnormalities that relate to reconstruction artifacts or the presence of contaminating absorbers. The developed methods should be rigorously evaluated on simulated and experimental data.

The second objective relates to the application of MSOT for functional brain imaging and has been largely exploratory. OA has clearly shown the capability for pushing the horizons of neuroimaging, but multiple omissions need to be addressed, such as underutilization of the spectroscopic capacity and depth penetration of MSOT. Thus it is important to overcome on the mentioned omissions by obtaining functional information on brain circuit activation from deeper compartments and using spectral information to spatially map neural dynamics and correlate them to anatomical MSOT images of the brain.

1.1.3 Outline

This manuscript is organized as a publication based dissertation consisting of six chapters. Chapter 1 summarizes the motivation behind the described work and introduces the key concepts used throughout the rest of the manuscript. Sec. 1.2 more formally introduces MSOT as a modality for functional imaging and neuroimaging and places it among other functional imaging techniques; Sec. 1.3 gives a brief introduction to the physical principles of OA and computational principles of OA image reconstruction and unmixing, introduces the general spectral unmixing problem in optoacoustics as well as gives an overview of the previously proposed solutions; Sec. 1.4 summarizes the methodology used in the described work including the main theoretical and computational aspects of eMSOT spectral unmixing methodology; the performed research related to functional brain imaging; and the hardware components of the MSOT imaging system used in experimental imaging procedures mentioned in this work.

Chapters 2-3 describe the efforts to improve upon the existing spectral unmixing methodologies by rendering eMSOT robust and improving its accuracy in sO_2 quantification. In Chapter 2, a Bayesian framework is used to formulate the eMSOT spectral unmixing problem as a maximum a posteriori estimation. A model for the measured OA spectra that captures their variability due to both light fluence and absorption of hemoglobin is developed for estimating the noise in the recorded OA data. The noise estimation enabled by the model is used in the Bayesian algorithm to negate the influence of noisy measurements on sO_2 quantification accuracy. Using the simulated data, the resulting algorithm is shown to have improved sO_2 quantification accuracy in highly absorbing deep-seated targets (e.g. vessels) under conditions of high spatially non-uniformly distributed noise. In Chapter 3, the core of eMSOT – a constrained optimization procedure – is replaced with a neural network that is trained on simulated data in an attempt to learn the optimal parameters of the algorithm instead of manually setting or optimizing them. It is shown in simulations and experimental data with available gold standard sO_2 values that the resulting deep learning-based algorithm outperforms the original eMSOT in terms of the accuracy of sO_2 estimation.

Chapters 4-5 are dedicated to advancing the use of MSOT for neuroimaging and exploring the capabilities of the imaging technique for functional brain imaging. In Chapter 4, a hybrid US-MSOT system is used for non-invasive label-free anatomical and functional brain imaging under gas challenge. In terms of anatomical imaging, the complementarity of the combined modalities in terms of visualization of various structures is demonstrated. In the functional domain, the response of various brain compartments to the gas challenge has been quantified and compared to that of tissues in the abdominal area. In Chapter 5, MSOT is used for both high-resolution structural and functional imaging in deep brain tissue, demonstrating unprecedented anatomical detail and high-resolution imaging and spectral decomposition of the hemodynamic response to whisker movement.

Chapter 6 summarizes the work and discusses potential directions for future work.

1.2 Functional imaging with MSOT

In this section, functional imaging is discussed in light of Multispectral Optoacoustic Tomography. Subsection 1.2.1. discusses the importance of measuring tissue oxygenation in functional imaging and relates to the first objective of this work. Various methods for measuring tissue oxygenation are reviewed in this subsection. Subsection 1.2.2. reviews brain imaging with MSOT as an application of functional imaging capabilities of optoacoustics and provides context to the second objective of this work.

1.2.1 Imaging tissue oxygenation

The first objective of this work relates to assessing tissue oxygenation by means of MSOT. Tissue oxygenation is a critical functional parameter. Abnormal oxygenation values (typically abnormally low) may be indicative of tissue inflammation [70] or ischemia [71]. In cancerous tumors, hypoxia may indicate adverse treatment trends as hypoxic tumors exhibit resistance to therapy or increased metastatic behavior [72–74]. A change in tissue oxygenation in the brain may indicate brain activation [20]. Due to the importance of this parameter as an indicator of tissue functionality, several methods have been developed over the years to assess tissue oxygenation.

There are various ways of estimating tissue oxygenation. Most rigorously, it can be assessed through quantitative estimation of the partial pressure of oxygen in tissue (pO_2), a parameter that is challenging to measure quantitatively. Quantitative measurements of pO_2 are mostly acquired through using polarography needles that are inserted in tissue in the region of interest to provide temporally resolved measurements [75]. Naturally, this invasive technique does not allow for obtaining spatial maps of pO_2 in tissue. ^{19}F MRI has been used to measure pO_2 in tissue [76], but such measurements are often unreliable since they are often affected by flow artifacts and factors like temperature and dilution. ^{15}O PET has been shown to quantify tissue oxygenation [77] but is limited by the short half-life of ^{15}O. PET using the nitroimidazole based tracers (e.g. [^{18}F]FMISO) has been considered for imaging tumor hypoxia [78] along with immunohistochemistry after the injection of exogenous hypoxia markers, such as [^{3}H]misonidazole [79] or pimonidazole [80]. While hypoxia is the abnormality of interest in many scenarios, the mentioned methods are not quantitative in the strict sense. Moreover, they have further disadvantages, namely the unattainability of immunohistochemistry information *in vivo*, and inherently low spatial resolution of PET-based methods. ^{3}He MRI has been demonstrated to quantify pO_2 directly, but the reliance on the administration of ^{3}He effectively limits the application of this technique to lung-localized examinations [81]. Quantitative spatially resolved measurements of pO_2 have been obtained with Electron Paramagnetic Resonance Imaging (EPRI) [82], but the probe-based nature of the method limits readout reliability in areas with impeded perfusion. Furthermore, the method is characterized by relatively low spatiotemporal resolution, which is inadequate for many small imaging scenarios.

Given the difficulties of measuring pO_2, blood oxygen saturation level is often measured instead, which indirectly indicative of pO_2. sO_2 can be converted to pO_2 using the oxygen dissociation curve of hemoglobin [83]. MRI provides contrast that is dependent on the oxygenation level of tissue through the BOLD mechanism [20]. Quantification of sO_2 using BOLD MRI signal has been a topic of extensive research, but the problem remains challenging and largely unsolved due to the need of meticulous modeling of various physical processes, including, for example, the dependence of BOLD MRI signal on the orientation of the vessels relative to the magnetic field. In addition, BOLD MRI is sensitive only to deoxygenated hemoglobin and not to oxygenated hemoglobin, therefore the measurements are not immediately quantitative. Several quantification methods have been proposed for BOLD MRI that consider a rather complex tissue model [84, 85], but there is still no conclusive solution to the problem. Other approaches based on using magnetic resonance phase, vascular T2 or spin labeling to quantify sO_2 have been considered [86], but such methods are typically limited to venous blood and are applicable to (large) vessels only.

Due to the superb optical contrast of blood, optical methods have been considered for and applied to the problem of oxygenation quantification. The differences in the absorption spectra of oxy- and deoxyhemoglobin render the quantification problem in optical imaging perhaps less challenging than in MRI. One of the most widely used sO_2 quantification devices, a pulse oximeter, is indeed optics-based. The main disadvantage of the device lies in its principle of operation that relies on the pulsation of the arterial blood [87]. The quantitative sO_2 measurements are therefore not spatially resolved and are restricted to the arterial blood only. The same limitation of lacking

the spatial information typically applies to spectroscopic methods such as optical spectroscopy [88] and Near-Infrared Spectroscopy (NIRS) [89]. Optical microscopy methods such as two-photon microscopy [90] and optoacoustic microscopy [91] have been used to visualize spatially resolved maps of sO_2 in vessels. The limited penetration depth of such methods, however, restricts their application to superficial regions. DOT is able to provide a spatial map of sO_2 in deep tissue [42], but has limited spatial resolution ($\sim$1 mm). Especially in the context of small animal imaging, such spatial resolution is often inadequate for resolving anatomical structures of interest. Despite the availability of a wide range of imaging modalities that are able to produce measurements that can be directly or indirectly associated with at least qualitative assessment of tissue sO_2 or pO_2, no single method is able to deliver high-resolution spatial oxygenation maps in deep tissue.

MSOT improves upon many of the limitations of the modalities available for quantification of oxygenation. Due to the optical contrast, MSOT is sensitive to both oxy- and deoxyhemoglobin, with the potential to differentiate them based on their optical absorption spectra. The reliance of MSOT on ultrasound waves as signal carrier means that its penetration depth is much less affected by photon scattering in tissue. The image resolution is defined by the detected ultrasound as well, resulting in resolutions that are more than adequate for small animal imaging. All the mentioned advantages combined in one technique suggest that MSOT has the potential to become an essential tool to gain important insights in various fields of preclinical research.

This potential has for a long time been impeded by the lack of available tools to correct for the effect of *spectral corruption*, i.e. modification of the recorded optoacoustic spectra due to position- and wavelength-dependent changes in optical fluence. This effect can significantly reduce the accuracy of sO_2 quantification by MSOT, especially deeper in the tissue. Currently, the only method that accounts for the spectral coloring and can be used in experimental data is eMSOT [64]. However, it is also prone to errors. The sO_2 quantification problem in MSOT is described in Sec. 1.3.5 and eMSOT algorithm is described in Sec. 1.3.6.

1.2.2 Functional brain imaging

The second objective of this work aims at utilizing the unique advantages of MSOT for functional brain imaging applications. Functional brain imaging has recently received tremendous attention. In an attempt to shed light on one of the hardest problems of functional biology – elucidating brain function - various imaging modalities have been applied in this field of research, including MRI [92], PET [93], CT [94], optical intrinsic signal imaging [95], confocal and multiphoton microscopy [96].

Microscopy techniques are crucial when it comes to studying the smallest functional units of the brain – neurons. On the microscopic scale, optical microscopy methods combined with the use of exogenous contrast agents and genetically encoded reporter proteins have achieved subcellular resolution and penetration depth of more than 1 mm, providing remarkable insights into cellular interactions and neuron signaling in both healthy and diseased brains, with the imaging procedures performed even *in vivo* in behaving mice [97–100]. Specifically, the monitoring of Ca^{2+} signals and voltage dynamics in various neuronal groups was made possible by genetically encoded calcium indicators [101] and voltage sensitive dyes [102, 103]. However, despite significant advances in instrumentation as well as in the development of fluorescent dyes and reporter proteins, the fundamental physical principles effectively limit microscopic imaging techniques to small field of view windows and no more than 1 mm penetration depth [30]. Such constraints also lead to the inevitable invasiveness of imaging procedures, involving skull trepanation to enhance access to brain tissue [104, 105]. OA microscopy has been applied in studies of activity-dependent oxygenation changes as well as vasomotor alterations in response to gas challenge [67, 106], but like other types of optical microscopy, OA microscopy suffers from low penetration depth, making studying the behavior of deep-seated neuron assemblies difficult.

In terms of brain function, it is important to study the dynamics of larger assemblies of neurons acting together and approximating them as one sub-system on a larger, mesoscopic scale [107]. Due to the limitations of the microscopy techniques, their use, in this case, is possible but not always practical [108, 109]. In the mesoscopic regime, brain dynamics can be captured by such techniques as electrocorticography (ECoG) [110], electroencephalography (EEG) [107] or magnetoencephalography (MEG) [111] and calcium imaging [96]. Voltage-sensitive dyes have been used to capture the activity of neural assemblies at mesoscale, and GCaMP imaging has demonstrated the capability for functional mapping the cortical and sub-cortical neuronal assemblies [112]. OA has been used to monitor the hemoglobin dynamics in response to gas challenges and various stimuli, visualizing

intact vasculature of the brain and thus moving away from monitoring the direct neuronal activity [109].

The macroscopic scale aims at the visualization of large neuronal assemblies such as specific cortical areas, allowing study of the connectivity and dependence of such systems on constituting components. One way of locating active areas of the brain is through monitoring metabolism. PET and SPECT have been shown to provide valuable insights into large-scale brain activity using this approach [113]. These modalities, however, are not well-suited for pre-clinical research in small animals due to the inherently low spatial resolution and high associated costs of the required infrastructure.

At the macroscopic scale, neurovascular coupling provides an indirect way to monitor brain activity through changes in blood oxygenation due to active neurons consuming oxygen at an increased rate [114]. Therefore, it is at this scale that the modalities sensitive to blood dynamics are especially useful. Since the discovery of the BOLD mechanism, functional MRI has found extensive use in functional neuroimaging due to its sensitivity and superb penetration depth [115]. The applications of the technique to pre-clinical research have also been demonstrated [116, 117]. However, the limitations of MRI, such as poor spatiotemporal resolution, develop into major disadvantages when applied to small animal imaging. The average human brain has a volume of 1,450 mL, while the average mouse brain has a volume of only 0.5–0.6 mL [118], therefore much smaller voxels are needed to resolve the structures of the mouse brain. With the signal-to-noise ratio (SNR) of MRI being directly proportional to the voxel size, the drop in SNR when imaging mice needs to be compensated by using stronger magnetic field that is associated with a much increased scanner cost [4]. Another strategy for improving the SNR is to prolong scan times, which further impairs the temporal resolution of the modality. Furthermore, since MRI is sensitive only to deoxyhemoglobin, it is hard to differentiate a increase in blood oxygenation from a increased in blood perfusion using this imaging technique.

Due to the ability to visualize hemoglobin gradients coupled with high availability and relatively low cost, optical methods have been considered for functional brain imaging on a macroscopic scale, with the ability of the said methods to capture functional signal from the superficial brain tissue in both humans and animals having been demonstrated [5, 119]. Such changes have also been localized and related to the corresponding stimuli [120–122]. However, the general limitations of optical methods still apply: major loss of resolution at the depths where the photons enter the diffusive regime (i.e. beyond 1 mm) limits visualization and quantification ability of optical techniques.

With its clear advantages over the optical methods, OA tomography has also been used to measure and visualize large scale hemodynamics signals in the brain on a macroscopic scale [118]. The studies mainly concentrated on assessing the dynamics of blood under gas challenges [123] or determining perfusion rates of externally administered contrast agents [124]. Other studies have further established the feasibility of using OA for functional brain imaging by visualizing the neurovascular response to sensory stimuli [125] and creating a connectivity map of a mouse brain cortex [126]. All the aforementioned reports, however, were mostly limited to the superficial brain tissue or used a single illumination wavelength, thus not facilitating the capabilities of the technique to the full potential.

1.3   Background

This section provides an overview of the key physical and mathematical concepts used in optoacoustic imaging. Subsection 1.3.1 discusses the basic physical principles of optoacoustic imaging. Subsections 1.3.2 - 1.3.5 review the forward and inverse problems of optoacoustics in the light of their mathematical formulation and computational methods used for their solution, including the methods used in this work for image reconstruction and simulation of light propagation.

1.3.1   Physics of optoacoustics

OA imaging is based upon the OA effect that can be described as follows. The object of interest is illuminated with a short laser pulse. Absorption of the transient light by the molecules causes a local rise in temperature, which causes local thermoelastic expansion, ultimately leading to an initial pressure rise $p_0(\mathbf{r}, \lambda)$, where $\mathbf{r}$ denotes the spatial coordinates and λ is the illumination wavelength. The laser pulse utilized in OA is typically characterized by the temporal span of several nanoseconds

to ensure thermal and stress confinement. Thermal confinement holds when heat conduction is negligible during the excitation; and stress confinement implies that the absorbing volume expands negligibly during the laser pulse. Under these assumptions, the location- and wavelength-dependent pressure $p_0(\mathbf{r}, \lambda)$ relates to fluence $\Phi(\mathbf{r}, \lambda)$ and tissue absorption coefficient $\mu_a(\mathbf{r}, \lambda)$ as follows [127]:

$$p_0(\mathbf{r}, \lambda) = \Gamma(\mathbf{r})\Phi(\mathbf{r}, \lambda)\mu_a(\mathbf{r}, \lambda), \tag{1.1}$$

where Γ is the Grüneisen parameter. The product

$$H(\mathbf{r}, \lambda) = \Gamma(\mathbf{r})\Phi(\mathbf{r}, \lambda) \tag{1.2}$$

is termed the absorbed energy density (AED). The generated ultrasound propagates towards the acoustic detectors and is being recorded, generating the measured pressure signal $p_d(t, \lambda)$, where t denotes time.

The hybrid nature of optocaoustics leads to the composite forward and inverse problems. The forward problem is split into two sub-problems as follows:

- *The optical forward problem* lies in computing the optical fluence $\Phi(\mathbf{r}, \lambda)$ when the optical properties of the medium and illumination are given.

- *The acoustic forward problem* implies computing the time-dependent pressure signals $p_d(t, \lambda)$ on the detectors around the sample given the initial pressure rise $p_0(\mathbf{r}, \lambda)$.

Similarly, the inverse problem in OA is also twofold:

- *The acoustic inverse problem* consists of reconstructing optoacoustic images $p_0(\mathbf{r}, \lambda)$ given the detector signals $p_d(t, \lambda)$. This is the essential image reconstruction problem in OA.

- *The optical inverse problem* − determine the spatial distribution of the optical properties ($\mu_a(\mathbf{r}, \lambda)$ is typically of primary interest) within the sample given the map of the initial pressure rise $p_0(\mathbf{r}, \lambda)$. This is the main problem of quantitative OA.

The mentioned subproblems are discussed in more detail in the following subsections. For the sake of simplicity, in Subsections 1.3.2 - 1.3.4 we assume illumination by laser pulse at a fixed wavelength λ and omit it in the notation.

1.3.2 Optical forward problem, light propagation

The essential step in determining the optical fluence within the sample with given optical properties is modeling light propagation. In absorbing and scattering media, which is a sound model for biological tissues, light transport is described by the Radiative Transfer Equation (RTE), which is derived from Maxwell's equation using the energy conservation principle [128]. RTE relates the following physical quantities: the light radiance L at position $\mathbf{r}$ that propagates along the direction specified by the unit vector $\hat{s}$; the optical properties of the medium (absorption μ_a and scattering μ_s) and the light source q:

$$(\frac{1}{c_l} + (\hat{\mathbf{s}} \cdot \nabla + \mu_a(\mathbf{r}) + \mu_s(\mathbf{r}))L(\mathbf{r}, \hat{\mathbf{s}}) - \mu_s \int \Theta(\hat{\mathbf{s}}, \hat{\mathbf{s}}')L(\mathbf{r}, \hat{\mathbf{s}}')d\hat{\mathbf{s}}' = q(\mathbf{r}, \hat{\mathbf{s}}, r), \tag{1.3}$$

where c_l is the speed of light in the medium and $\Theta(\hat{\mathbf{s}}, \hat{\mathbf{s}}')$ is the probability of a photon traveling along $\hat{s}$ to scatter in direction $\hat{s}'$. According to the steady-state (time-independent) RTE that is of interest for OA, the relation between the mentioned quantities is as follows:

$$(\hat{\mathbf{s}} \cdot \nabla + \mu_a(\mathbf{r}) + \mu_s(\mathbf{r}))L(\mathbf{r}, \hat{\mathbf{s}}) - \mu_s \int \Theta(\hat{\mathbf{s}}, \hat{\mathbf{s}}')L(\mathbf{r}, \hat{\mathbf{s}}')d\hat{\mathbf{s}}' = q(\mathbf{r}, \hat{\mathbf{s}}). \tag{1.4}$$

The optical fluence is defined as:

$$\Phi(\mathbf{r}) = \int L(\mathbf{r}, \hat{\mathbf{s}}')d\hat{\mathbf{s}}', \tag{1.5}$$

i.e. as the total radiance over all angles.

RTE is challenging to solve computationally, therefore alternative approaches are often used for numerical simulations [127]. One such approach is using the Monte Carlo method, i.e. modeling the

behavior of single photons or groups of photons probabilistically and tracing numerous trajectories in a modeled medium to obtain the spatial distribution of the quantity of interest. The method allows for rigorous modeling of physics but is computationally extremely expensive since an accurate solution requires a large number of tracked trajectories.

An alternative way of modeling light propagation in a numerically tractable manner is to approximate RTE under certain realistic assumptions. Typically, a high-albedo or turbid medium is used as a model for tissue, meaning that scattering events are largely dominant over absorption events. More specifically, $\mu'_s >> \mu_a$, where $\mu'_s = (1 - g)\mu_s$ is the reduced scattering coefficient and g is the scattering anisotropy factor. In such media, radiance is assumed to be nearly isotropic after undergoing sufficient scattering. Under this assumption, radiance can be represented as a series of harmonics and RTE can be reduced to the Diffusion Approximation [127]:

$$\mu_a(\mathbf{r})\Phi(\mathbf{r}) - \nabla \cdot (D(\mathbf{r})\nabla)\Phi(\mathbf{r}) = q_0(\mathbf{r}), \tag{1.6}$$

where q_0 is the first (isotropic) term in the expansion series of q. $D = [3(\mu_a + \mu'_s)]^{-1}$ is the diffusion coefficient. Analytical solutions can be derived for DA under further assumptions. For an infinite homogeneous medium in 1D case, the solution to DA is expressed as:

$$\Phi(z) = \Phi_0 e^{-\mu_{eff} z}, \tag{1.7}$$

where $\mu_{eff} = \sqrt{3\mu_a(\mu_a + \mu'_s)}$ is the effective attenuation coefficient, Φ_0 is the incident fluence and z is medium depth.

In an arbitrary case, DA can be solved for tissues of arbitrary geometry and composition using established numerical methods, e.g. Finite Elements Method (FEM) [129]. The assumption of prominent scattering, i.e. $\mu'_s >> \mu_a$, ensures that the solution to DA is valid at depths higher than $1/\mu'_s$. For biological tissues in the near-unfrared (NIR) range, this distance approximately equals 1 mm [130]. In the present work, FEM solution to Eq. 1.6 is used to simulate light propagation in tissue due to the computational efficiency and ease in handling arbitrary tissue geometries. Furthermore, Eq. 1.7 is used in Chapter 2 to derive a model of OA spectra of tissue.

1.3.3 Acoustic forward problem, acoustic wave propagation

After the generation of the initial pressure rise after the laser pulse excitation, the acoustic waves propagate towards the detectors at locations. This process depends on the mechanical properties of the imaged object and is governed by the acoustic wave equation. The acoustic wave equation can be derived from Navier-Stokes equation assuming propagation in a non-viscous fluid and further linearizing the obtained equations. The acoustic wave equation relates the space and time-dependent pressure p to the speed of sound (SoS) c and material mass density ρ as follows:

$$\frac{\partial^2}{\partial t^2}p(\mathbf{r}, t) - c^2(\mathbf{r})\rho(\mathbf{r})\nabla\left(\frac{1}{\rho(\mathbf{r})}\nabla p(\mathbf{r}, t)\right) = \Gamma(\mathbf{r})\frac{\partial}{\partial t}H(\mathbf{r}, t). \tag{1.8}$$

For certain ideal cases, e.g. simple geometries and constant speed of sound and mass density, analytical solutions to the acoustic wave equation can be derived. Otherwise, numerical methods need to be employed to obtain the solution. The literature on methods for numerically solving the acoustic wave equation is wide, with methods available that solve the corresponding Helmholtz equation in the frequency domain or solve Eq. 1.8 using finite difference time domain methods, time reversal algorithms [131], hybridizable discontinuous Galerkin methods [132] and more.

Under the assumption of uniform SoS and mass density, the acoustic wave equation in OA can be written as:

$$\frac{\partial^2}{\partial t^2}p(\mathbf{r}, t) - c^2\nabla^2 p(\mathbf{r}, t) = \Gamma(\mathbf{r})\frac{\partial}{\partial t}H(\mathbf{r}, t). \tag{1.9}$$

Since the excitation laser pulse is short, the source term on the right hand side of Eq. 1.8 can be rewritten according to $H(\mathbf{r}, t) = H(\mathbf{r})\delta(t)$ using the Dirac function $\delta(t)$. This allows one to derive an analytical Green's function of the form:

$$p(\mathbf{r}_d, t) = \frac{1}{4\pi c}\frac{\partial}{\partial t}\int_{|\mathbf{r}-\mathbf{r}_d|=ct}\frac{p_0(\mathbf{r})}{|\mathbf{r} - \mathbf{r}_d|}dA' \tag{1.10}$$

Eq. 1.10 is called a spherical Radon transform. As evident, according to Eq. 1.10, the pressure at a given coordinate $\mathbf{r}_d$ at a time point t is equal to the initial pressure rise integrated over a sphere. Assuming $\mathbf{r}_d$ to be the coordinates of the detectors, the pressure signals on the detectors can be related to the spatial distribution of the initial pressere rise $p_0(\mathbf{r})$ [133]. It is physically correct to assume wave propagation in 3D. In practice, however, the tomographic setup of MSOT often employs transducers that are focused on a 2D plane, therefore rendering considering 2D variant of Eq. 1.10 viable. Another way of computing pressure on the detectors is linearizing Eq. 1.10 and relating the vectorized measured pressure $\mathbf{p}_d$ signals to the vectorized initial pressure rise $\mathbf{p}_0$ in the matrix form:

$$\mathbf{p}_d = \mathbf{M}\mathbf{p}_0, \tag{1.11}$$

where $\mathbf{M}$ is called the model matrix of the system.

1.3.4 Acoustic inverse problem, optoacoustic image reconstruction

Typically, OA image reconstruction refers to solving the acoustic inverse problem and the spatial map of the initial pressure rise is referred to as an OA image. While the spatial distribution of the absorption coefficient is usually of interest, the acoustic inverse problem is significantly easier to solve than the optical one. A detailed analysis of available image reconstruction methods for OA is presented in [133]. The aim of this section is rather to present and classify the most common approaches. In general, there are three common types of OA image reconstruction techniques: backprojection, time reversal, and model-based.

Backprojection algorithms aim to provide a closed-form solution to Eq. 1.10. Initially developed using mainly heuristic reasoning, the backprojection algorithms are typically used for real-time image reconstruction [134, 135]. The simplest back projection algorithms, however, are not perfectly suitable for subsequent quantitative analysis of the images [133]. For certain ideal detection geometries, the exact backprojection formulas are known [136], but for more complex geometries the explicit solution does not exist.

Time-reversal algorithms aim at propagating the detected pressure backward in time [131]. The analytical time-reversal formula has been shown to be equivalent to the universal backprojection formula presented in [136] under certain assumptions and approximations and is derived for acoustically homogeneous tissue [137]. More advanced time-reversal approaches have concentrated on computational implementations rather than analytical solutions, which enabled extension of the approach to more general cases such as having arbitrary detection surfaces or acoustic heterogeneities in the field of view [138–140].

Finally, model-based algorithms use Eq. 1.11, a discretized form of Eq. 1.10, to solve the inverse problem. An analytical solution to Eq. 1.11 is available in the form of a pseudoinverse: $\mathbf{p}_0 = (\mathbf{M}^T\mathbf{M})^{-1}\mathbf{M}^T\mathbf{p}_d$. However, numerically it is often beneficial to use an iterative minimization algorithm, such as one of the gradient descent-based methods, to find an approximate solution $\mathbf{p}_{rec}$ as [60]:

$$\mathbf{p}_{rec} = \underset{\mathbf{p}_0}{\operatorname{argmin}} \parallel \mathbf{p}_d - \mathbf{M}\mathbf{p}_0 \parallel_2^2 . \tag{1.12}$$

To oppose the ill-posed nature of the problem, the following regularized problem is often solved instead of Eq. 1.12:

$$\mathbf{p}_{rec} = \underset{\mathbf{p}_0}{\operatorname{argmin}} \parallel \mathbf{p}_d - \mathbf{M}\mathbf{p}_0 \parallel_2^2 + R(\mathbf{p}_{rec}), \tag{1.13}$$

where $R(\mathbf{p}_{rec})$ is the regularization term. A typical choice for $R(\mathbf{p}_{rec})$ is the weighted norm of the solution: $R(\mathbf{p}_{rec}) = \alpha \parallel \mathbf{p}_{rec} \parallel_n$, α being the regularization parameter and n indicating the order of the norm. The l2 norm ($n = 2$, Tikhonov regularization [141]) promoting smoothness of the solution or the l1 norm ($n = 1$) enforcing sparsity of the solution are the usual choices [142]. The strategies for solving Eq. 1.13 are essentially the same as the ones described for Eq. 1.12, with a closed-form solution to the problem available as well. The advantage of the model-based approach is the ability to account for more factors with relative ease, such as adding a realistic model of detectors [143]. The main disadvantage of the model-based method, especially as compared to the backprojection algorithm, is a significantly higher computational complexity.

The model-based reconstruction approach has been shown to provide superior image quality for the MSOT scanner used in this work both in terms of visualization of structures and the quality of the provided spectral information. Therefore, throughout this work, model-based reconstruction with Tikhonov regularization is used as described in [60, 144].

In reality, none of the reconstruction methods can provide a perfectly accurate spatial map of the initial pressure rise for multiple reasons. The majority of the reasons relate to the detection of the ultrasound waves. First, for any tomographic method to be exact, an infinite amount of measurements, or projections, along the detection surface should be obtained. In practice, only a finite amount of measurements can be obtained, and for fixed detector geometry, the amount of projections is equal to the number of detectors and is limited by their size. This leads to image distortions commonly known in tomographic imaging as streak artifacts [133]. Angular coverage of the imaged object by the detection surface is of great significance for the subsequent image reconstruction, with limited view resulting in a loss of information and leading to image artifacts in the areas not fully covered with detectors [145]. Transducers themselves act as band-pass filters due to the finite bandwidth of their impulse response. In case of OA imaging using the pulsed laser, the resulting signal is extremely broadband; therefore, imperfect detection itself results in the loss of otherwise useful signal [146]. The frequency-dependent attenuation of ultrasound contributes to the filtering effect [131]. The finite aperture of the transducers creates an inhomogeneous spatial impulse response [147]. Finally, acoustic heterogeneities may lead to a variety of reconstruction artifacts unless accounted for [148]. Notably, the detected pressure is transformed into voltage readouts and those are typically used for reconstruction. For an accurate reconstruction of pressure in respective physical units (Pa), a conversion of the measured signal to Pa should be performed.

Although modern advanced reconstruction methods account for some of the mentioned effects (see, for example, [149]), it seems implausible to correct for every described issue. Furthermore, addressing the mentioned effects is often associated with increased computational effort, often rendering the resulting algorithms impractical to use in some experimental applications.

1.3.5 Optical inverse problem, quantification of absorber concentrations

Solving the optical inverse problem is the main goal of quantitative OA. If the optical absorption $\mu_a(\mathbf{r}, \lambda)$ of the imaged object is known along with its k absorbing constituents and their respective absorption spectra $s_i(\lambda)$, i.e.

$$\mu_a(\mathbf{r}, \lambda) = \sum_{i=1}^{k} c_i(\mathbf{r}) s_i(\lambda), \tag{1.14}$$

where c_i are the respective concentrations of the absorbers, the spectrum at every spatial location may then be represented as follows:

$$p_0(\mathbf{r}, \lambda) = \Gamma(\mathbf{r}) \Phi(\mathbf{r}, \lambda) \sum_i c_i(\mathbf{r}) \epsilon_i(\lambda). \tag{1.15}$$

Theoretically, to recover c_i, measurements at no less than k wavelengths must be available. However, OA does not provide the information on the optical absorption directly. Instead, the absorption signal is coupled to the optical fluence $\Phi(\mathbf{r}, \lambda)$. Since light absorption depends on the excitation wavelength and the amount of light reaching a certain point in tissue essentially depends on the optical properties of the whole illuminated volume, the optical fluence is wavelength-dependent as well. The adverse effect of light fluence on the sensitivity and quantification ability of MSOT has been recognized and studied [48, 150]. Yet, estimation of fluence and decoupling it from the optical absorption thus yielding the pure absorption spectra remains the main challenge in quantitative OA.

Fig. 1.2 illustrates the effect of light fluence on the measured OA spectra of hemoglobin. Fig. 1.2A presents the absorption spectra of oxygenated hemoglobin. Fig. 1.2B demonstrates the simulated measured OA spectra of pure oxygenated hemoglobin. The spectrum that is not altered by light fluence is shown in black and corresponds to the absorption spectrum of oxygenated hemoglobin. Such a spectrum may be measured on the tissue surface, where the optical fluence does not change significantly with wavelengths. The orange spectra correspond to the absorption spectrum of oxygenated hemoglobin modified by the simulated optical fluence spectra that vary depending on tissue depth where the spectrum is measured and surrounding tissue sO$_2$. It can be readily seen that the
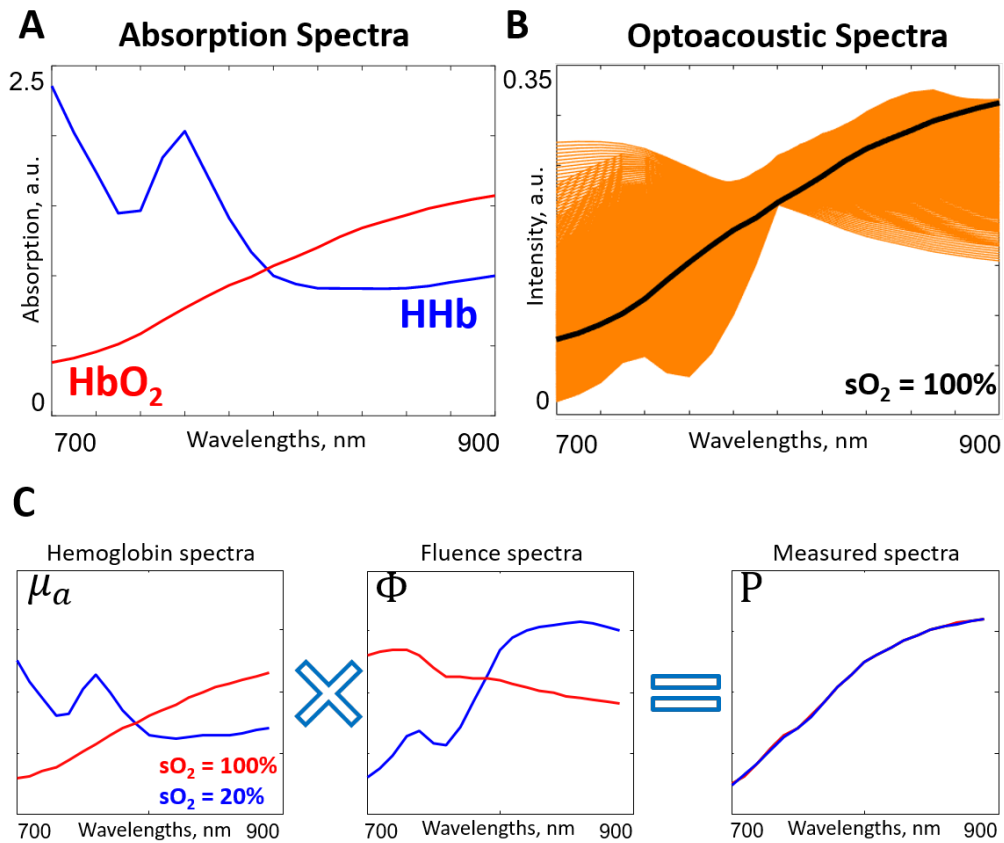
Figure 1.2: Effects of Light Fluence on Optoacoustic Spectra of Hemoglobin. (**A**) Absorption spectra of oxygenated hemoglobin (HbO$_2$, red) and deoxygenated hemoglobin (HHb, blue). (**B**) Simulated spectra of pure oxygenated hemoglobin corresponding to 100% sO$_2$ measured at various tissue depths (up to 1 cm) with various oxygenation levels of surrounding tissue (from 0% to 100% sO$_2$). The spectrum of oxygenated hemoglobin unaltered by optical fluence is shown in black for reference. (**C**) Two absorption spectra of hemoglobin (left panel), corresponding to 100% sO$_2$ (red) and 20% sO$_2$ (blue), when multiplied by two simulated fluence spectra (middle panel) of corresponding colors, result in indiscernible measured optoacoustic spectra (right panel).

initial absorption spectrum can be modified by fluence significantly, losing practically any resemblance to the original spectral signature of the absorber. Fig. 1.2C demonstrates that two distinct absorption spectra of hemoglobin that correspond to significantly different sO$_2$ levels, when altered by optical fluence, may result in an almost identical OA spectrum. In the presence of measurement noise, such spectra would be virtually indistinguishable.

Solving the optical inverse problem in OA is the key to unlocking its full potential for molecular and functional imaging. The importance of this goal has attracted considerable attention from the research community, yielding a spectrum of approaches to solve this problem. Despite this fact, no method but one has been demonstrated to reliably and robustly work in experimental data. In this section, a short review of the proposed methodologies is provided.

Experimental methods. The experimental methods aim at recovering absorption by explicitly measuring and correcting for fluence, i.e. at the time of an imaging experiment. This is typically achieved by introducing an exogenous absorber of known characteristics. An approach based on a local absorber insertion has been demonstrated to work *in vivo* [63], but invasiveness strongly limits its applications, especially in regards to inferring the spatial distribution of fluence. Similarly, some absorbers, e.g. gold nanorods or switchable fluorescent proteins, may be introduced through systemic injections [151, 152]. None of the described non-invasive methods, however, has been demonstrated to work in experimental data obtained *in vivo*, with experimental results limited to phantoms and simulations.

Presumption-based methods. The methods in this category aim at separating fluence form absorption by making certain rather strong assumptions such as assuming a homogeneous and known distribution of the optical properties [153–155]; a small perturbation of absorption over a homogeneous background distribution of the optical properties [156]; fluence remaining unchanged over a small range of wavelengths [49]; or cylindrical absorber in a scattering medium [157]. Such assumptions typically lead to drastic mathematical simplifications that allow for finding approximate or even closed form solutions to optical inverse problems. While the mentioned simplifications may hold in certain scenarios, the applicability of the discussed approaches in complex small animal imaging scenarios is questionable.

Model-based Methods. The methods in this class attempt to solve the most general optical inverse problem of optoacoustics: inferring the spatial distribution of the optical properties given the optoacoustic measurements making as few simplifying assumptions as possible. Such methods typically employ light transport models discussed in Sec. 1.3.2 to simulate light propagation, with some methods using RTE [158–162] and others employing DA [158, 160, 163–166]. In the most general case, both μ_a and μ_s' need to be found. For this task, multispectral OA images need to be used along with the known spectra of the constituent absorbers, since otherwise the absorption and scattering cannot be found simultaneously due to ill-posedness of the problem [130, 167]. Notably, obtaining more measurements with varying illumination patterns as well might mitigate this problem [168, 169]. Generally, the task of recovering spatially resolved maps of μ_a and μ_s' is formulated as a minimization problem, where the unknown optical properties are found that minimize the difference between the experimentally measured absorbed energy density $\mathbf{H}_{exp}$ and its modeled counterpart $\mathbf{H}_{model}$:

$$(\boldsymbol{\mu}_a, \boldsymbol{\mu}_s') = \operatorname{argmin} \parallel \mathbf{H}_{exp} - \mathbf{H}_{model}\left(\boldsymbol{\mu}_a, \boldsymbol{\mu}_s'\right) \parallel_2^2 + R\left(\boldsymbol{\mu}_a, \boldsymbol{\mu}_s'\right), \tag{1.16}$$

where R is the regularizer used to improve the conditioning of the problem and $\boldsymbol{\mu}_a$ and $\boldsymbol{\mu}_s'$ are the discretized spatial maps of μ_a and μ_s', respectively. The solution is recovered in an iterative fashion using an optimization algorithm. The discussed approach has been investigated in terms of using various light transport models, selecting the appropriate optimization algorithms [170], and formulating the inversion problem in a Bayesian framework [163, 164, 171]. The results presented suggest that the recovery of the unknown optical properties is possible in numerical simulations and simple phantoms. However, no results in images of small animals have been shown.

While the general model-based approach is perhaps the most promising of all the methods discussed in this section, it has a number of general limitations that impede its application to the experimental data. First, accurate modeling of physical effects such as light propagation and a large number of unknowns (at least two unknowns per pixel) results in a high computational complexity that drastically limits the throughput of the methods. This alone renders the methods unsuitable for quantification of high-resolution optoacoustic images. Second, the used modeling approach leads to the required accurate knowledge several parameters and physical quantities, such as tissue boundary, incident fluence, and the spatial distribution of the absorbed energy density.

Such knowledge is often not attainable either due to the difficulty of experimentally measuring the required parameters (e.g. incident fluence) or due to the necessity of knowing their absolute values, as it is the case for absorbed energy density. As mentioned in Sec. 1.3.4, the OA reconstruction approaches are prone to introducing various artifacts. Moreover, the reconstructed OA image values are scaled as compared to the theoretical absorbed energy density, with the scaling factor including the spatially dependent Grüneisen parameter, the conversion factor that maps voltage readouts of the detectors to the detected pressure, etc.

The mentioned issues prevent the straightforward application of the described methods to experimental data. Notably, in [172], the full inverse problem was considered, where the proposed algorithm procedure did not rely on minimizing the difference between the modeled and measured absorbed energy density, but rather between the modeled and measured detector readouts. Naturally, the method utilized the computational model for acoustic wave propagation. The algorithm was also designed to recover mechanical properties of the imaged object, namely speed of sound and mass density, with several proposed solutions to mitigate the resulting high computational complexity of the algorithm. The method has been demonstrated to work for an experimentally obtained mouse head measurements. Though the major anatomical landmarks corresponded to those visible in the OA images, the quantitative ability of the methodology for experimental data has not been thoroughly explored.

Other methods. An iterative fixed point method has been proposed in [173] for cases when the assumption of a homogeneous absorption background does not hold. The method reformulates Eq. 1.1 and solves the problem iteratively using fixed-point iterations. However, in the presence of noise and in the areas with low reconstructed intensity values, both of which are characteristics of a typical OA image, the solution is unstable.

Another distinct approach for decoupling fluence takes advantage of different characteristics of spatial distributions of fluence and absorption in an attempt to sparsely represent such distributions in different functional bases [174]. Fourier basis was proposed to represent fluence that varies smoothly throughout the image, and Haar family of wavelets was selected to represent absorption corresponding to the structures within the field of view. The method has been demonstrated to work in experimental images of phantoms. However, similarly to the model-based methods, it is sensitive to the inaccuracies in the image reconstruction. Similarly to the presumption-based methods, its applicability is further limited in cases where its main assumption on the spatial distribution of the absorption does not hold, e.g. when it does vary smoothly.

To this day, linear unmixing likely remains the most widely used method for blood sO_2 estimation in experimental data [175, 176]. It is computationally efficient and straightforward to implement, mostly due to the fact that essentially no fluence correction is performed. The main assumption of linear unmixing is that fluence does not change with wavelength. In other words, the effect of spectral coloring is ignored. Naturally, the results of the linear unmixing algorithms erroneous, especially in deep tissue, where the dependence of light fluence on the excitation wavelengths is prominent. Nonetheless, until recently the method remained widely used to the lack of available alternatives.

1.4 Methodology for functional imaging using MSOT

This section describes the quantification methods and the equipment that are specific to this work as well as more formally defines the problems solved by the efforts described herein. Subsection 1.4.1 introduces the eigenspectra MSOT as a method for quantifying sO_2 using MSOT data, examines the advantages of the algorithm over the other state of the art methods as well as discusses its flaws. Subsection 1.4.2 summarizes the efforts to improve upon the mentioned flaws. Subsection 1.4.3 describes OA instrumentation used for imaging and subsection 1.4.4 briefly summarizes the experimental procedures that involved the use of small animals.

1.4.1 Quantification of sO_2 using eigenspectra MSOT

The model based methods described in Sec. 1.3.1 have probably come the closest to solving the general inverse optical problem of OA, but their application to real data remains challenging. In contrast, a recently developed method termed eigenspectra optoacoustic tomography, solves a much simpler variant of the problem and has been shown to work in experimental images of phantoms and

small animals (mice) [64]. In this section, a review of the method is presented and its advantages and limitations are discussed.

eMSOT is based on the assumption that oxygenated and deoxygenated hemoglobin are the most prominent absorbers in tissue and the contribution of the other absorbers to the OA signal can be neglected. In other words,

$$\mu_a \approx \left(c_{HHb}(\mathbf{r}) s_{HHb}(\lambda) + c_{HbO_2}(\mathbf{r}) s_{HbO_2}(\lambda) \right), \tag{1.17}$$

where $s_{HbO_2}(\lambda)$ and s_{HHb} are the spectra of oxy- and deoxyhemoglobin, respectively, and $c_{HbO_2}(\mathbf{r})$ and $c_{HHb}(\mathbf{r})$ are their respective concentrations. This assumption is typically valid for biological tissue illuminated in the near-infrared region (700 to 900 nm) in absence of exogenous contrast agents. The method assumes the following model of the reconstructed multispectral OA image $p(\mathbf{r}, \lambda)$:

$$p_0(\mathbf{r}, \lambda) = C(\mathbf{r})\Phi(\mathbf{r}, \lambda)\mu_a(\mathbf{r}, \lambda), \tag{1.18}$$

where $C(\mathbf{r})$ accounts for multiple scaling factors including the Grüneisen parameter and various system effects discussed in Sec. 1.3.4. The method considers normalized fluence $\mathbf{\Phi}'(\mathbf{r}) = \mathbf{\Phi}(\mathbf{r})/ \parallel \mathbf{\Phi}(\mathbf{r}) \parallel_2$ as a quantity of interest, where $\mathbf{\Phi}(\mathbf{r})$ is the fluence spectrum at position $\mathbf{r}$ and $\parallel \mathbf{\Phi}(\mathbf{r}) \parallel_2$ is its l2 norm. Similarly, OA spectra $\mathbf{p}_0(r)$ are also normalized as follows: $\mathbf{p}'_0(r) = \mathbf{p}_0(\mathbf{r})/ \parallel \mathbf{p}_0(\mathbf{r}) \parallel_2$. Combining Eqs. 1.17 and 1.18 , Eq. 1.1 is rewritten for the normalized OA spectrum $\mathbf{p}'(\mathbf{r})$ as:

$$p'_0(\mathbf{r}, \lambda) = \Phi'(\mathbf{r}, \lambda) \left(c'_{HHb}(\mathbf{r}) s_{HHb}(\lambda) + c'_{HbO_2}(\mathbf{r}) s_{HbO_2}(\lambda) \right), \tag{1.19}$$

where $c'_{HbO_2}(\mathbf{r}) = c_{HbO_2}(\mathbf{r}) \cdot \frac{C(\mathbf{r})}{\parallel\Phi(\mathbf{r})\parallel_2\parallel\mathbf{p}_0(\mathbf{r})\parallel_2}$ and $c'_{HHb}(\mathbf{r}) = c_{HHb}(\mathbf{r}) \cdot \frac{C(\mathbf{r})}{\parallel\Phi(\mathbf{r})\parallel_2\parallel\mathbf{p}_0(\mathbf{r})\parallel_2}$ are the relative concentrations of oxy- and deoxyhemoglobin, respectively. Notably, the common multiplicative scaling factor of $c'_{HbO_2}(\mathbf{r})$ and $c'_{HHb}(\mathbf{r})$ does not alter the estimation of sO2, since it is a ratiometric quantity:

$$sO_2(\mathbf{r}) = \frac{c_{HbO_2}}{c_{HbO_2} + c_{HHb}} = \frac{c'_{HbO_2}}{c'_{HbO_2} + c'_{HHb}}. \tag{1.20}$$

It is hypothesized that the spectral shape of $\mathbf{\Phi}'$ is not arbitrary, but lies within a certain low-dimensional subspace that can be accurately represented by a few base spectra. To derive the base spectra, a training set is considered that consists of fluence spectra from various tissue depths and background oxygenation levels. The training set is derived using Eq. 1.7 for tissue depths of up to 1 cm and tissue oxygenation levels of 0% to 100%. In this way, a comprehensive dataset is constructed that captures the changes in fluence due to tissue sO2 and depth. All the collected fluence spectra are normalized and PCA is applied to derive the prince components of the training set. It has been shown that only 3 principal components $\Phi_i(\lambda), i = \overline{1,3}$ (or base spectra) along with the mean spectrum $\Phi_M(\lambda)$ of the training dataset are is enough to represent a fluence spectrum in tissue where oxygenated and deoxygenated hemoglobin are the most prominent absorbers:

$$\Phi'(\lambda) = \Phi_M(\lambda) + \sum_{i=1}^{3} m_i \Phi_i(\lambda), \tag{1.21}$$

Eq. 1.21 is termed the eigenspectra model for normalized fluence. In Eq. 1.21, $\Phi_i(\lambda), i = \overline{1,3}$ are termed the eigenspectra, and the scalar coefficients $m_i(\lambda), i = \overline{1,3}$ are termed the eigenparameters. Substituting Eq. 1.21 into Eq. 1.19, the eigenspectra model for the normalized OA spectra is obtained:

$$\hat{p}_0(\mathbf{r}, \lambda, \boldsymbol{\theta}) = \left(\Phi_M(\lambda) + \sum_{i=1}^{3} m_i \Phi_i(\lambda) \right) \left(c'_{HHb}(\mathbf{r}) s_{HHb}(\lambda) + c'_{HbO_2}(\mathbf{r}) s_{HbO_2}(\lambda) \right), \tag{1.22}$$

where $\boldsymbol{\theta} = \left(m_1, m_2, m_3, c'_{HHb}, c'_{HbO_2} \right)$. The eigenspectra model for OA spectra (simply referred to as eigenspectra model throughout the work) is therefore dependent on 5 parameters: eigenparameters m_1, m_2, m_3 and relative concentrations c'_{HHb}, c'_{HbO_2}.

The goal of the method is to estimate normalized fluence at a given point by finding the eigen-parameters for the given OA spectrum measured at this point. This is achieved by finding the parameters of the eigenspectra model that minimize the second norm of the difference between the model $\hat{\mathbf{p}}_0(\mathbf{r}, \boldsymbol{\theta})$ and the corresponding measured spectrum $\mathbf{p}_0'(\mathbf{r})$:

$$\boldsymbol{\theta}_{opt} = \underset{\boldsymbol{\theta}}{\arg\min} \parallel \mathbf{p}_0'(\mathbf{r}) - \hat{\mathbf{p}}_0(\mathbf{r}, \boldsymbol{\theta}) \parallel_2 = \underset{\boldsymbol{\theta}}{\arg\min} f_{\mathbf{r}}(\boldsymbol{\theta}), \tag{1.23}$$

where $f_{\mathbf{r}}(\boldsymbol{\theta}) = \underset{\boldsymbol{\theta}}{\arg\min} \parallel \mathbf{p}_0'(\mathbf{r}) - \hat{\mathbf{p}}_0(\mathbf{r}, \boldsymbol{\theta}) \parallel_2$. To oppose the ill-posed nature of the problem, model inversion is performed for several spatially distributed points with additional constraints added to render the inversion step robust. eMSOT can be summarized in the following steps [64]:

1. **Preprocessing.** Prior estimates $\hat{m}_1(\mathbf{r})$, $\hat{m}_2(\mathbf{r})$ an $\hat{m}_3(\mathbf{r})$ for the eigenfluence parameters $\hat{m}_1(\mathbf{r})$, $\hat{m}_2(\mathbf{r})$ and $\hat{m}_3(\mathbf{r})$ respectively, are computed as described in [64].

2. **Grid placement.** A circular grid $\mathbf{G} = \{r^{(k,l)} | k = 1\overline{1, n_{ln}}, l = \overline{1, n_{pt}}\}$ of n_{ln} lines consisting of n_{pt} pixels each is placed on a region of interest within the MSOT image. The grid must have pixels in the superficial areas of the analyzed sample. The optoacoustic measured spectra at the locations $\mathbf{r}^{(k,l)}$ are normalized to be further used in the model inversion.

3. **Model Inversion.** For the set of model parameters $\boldsymbol{\Theta} = \{\boldsymbol{\theta}_{\mathbf{r}} | \mathbf{r} \in \mathbf{G}\}$, optimal values $\boldsymbol{\Theta}_{opt}$ are found that satisfy:

$$\boldsymbol{\Theta}_{opt} = \underset{\boldsymbol{\theta}}{\arg\min} \sum_{\mathbf{r} \in \mathbf{G}} \parallel \mathbf{p}_0'(\mathbf{r}) - \hat{\mathbf{p}}_0(\mathbf{r}, \boldsymbol{\theta}_{\mathbf{r}}) \parallel_2 + \alpha \parallel \mathbf{W}\mathbf{m}_1 \parallel_2 + \alpha \parallel \mathbf{W}\mathbf{m}_3 \parallel_2, \tag{1.24}$$

subject to:

$$m_2^{k,l} < m_2^{k-1,l-1};$$
$$m_2^{k,l} < m_2^{k,l-1}; \tag{1.25}$$
$$m_2^{k,l} < m_2^{k+1,l-1};$$

$$m_1^{(k,l)} \in \left[min_1^{k,l}\left(\hat{m}_1^{(k,l)}\right); max_1^{k,l}\left(\hat{m}_1^{(k,l)}\right) \right]; \tag{1.26}$$

$$m_3^{(k,l)} \in \left[min_3^{k,l}\left(\hat{m}_3^{(k,l)}\right); max_3^{k,l}\left(\hat{m}_3^{(k,l)}\right) \right]; \tag{1.27}$$

$$c_{HHb}'\left(\mathbf{r}^{(k,l)}\right) \geq 0; c_{HbO_2}'\left(\mathbf{r}^{(k,l)}\right) \geq 0; m_i^{(k,l)} \in [MIN_i, MAX_i]; i = \overline{1,3}; \tag{1.28}$$

where $x^{(k,l)} = x\left(\mathbf{r}^{(k,l)}\right)$ is the value of the parameter x at the location $\mathbf{r}^{(k,l)}$. In Eq. 1.24, $\mathbf{W}$ is a matrix describing the local connectivity of the pixels in the grid; $\mathbf{m}_i = \left[m_i^{(1,1)}, \ldots, m_i^{(n_{ln}, n_{pt})}\right]^T$; α is the regularization parameter, $max_i^{k,l}$ and $min_i^{k,l}$ are the local limits that depend on the position of each point in the grid and the prior values obtained at step 1. Such limits are defined based on simulations [64]. MAX_i and MIN_i are the global limits of the parameters m_i defined irrespective of the grid.

4. **Interpolation.** The values $m_i^{(k,l)}, i = \overline{1,3}, k = \overline{1, n_{ln}}, l = \overline{1, n_{pt}}$ obtained for the sparsely distributed locations $\mathbf{r}^{(k,l)}$ are used to estimate $m_i, i = \overline{1,3}$ for every pixel within the convex hull of the grid points through interpolation.

5. **Fluence correction.** The normalized measured spectra at every spatial location are divided elementwise with the corresponding estimates of the normalized fluence obtained at step 4. The result of the division approximates $\mu_a(\mathbf{r}, \lambda)$. For every location $\mathbf{r}$ within the convex hull of the grid points, the optical absorption spectrum $\boldsymbol{\mu}_a(\mathbf{r})$ is unmixed by means of linear fitting with the spectra of oxy- and deoxyhemoglobin for the relative concentrations of hemoglobin. Tissue sO_2 is then computed according to Eq. 1.20.

Problem statement

eMSOT has been shown to provide improved sO$_2$ estimation accuracy as compared to the commonly used linear unmixing method discussed in Sec. 1.3.5. It has been successfully applied in experimental data obtained from phantoms and small animals [64]. The key advantages of eMSOT that allow for seamless integration into the workflow of OA image analysis is its low computational imprint and the fact that fluence correction can be performed locally in the image. Such beneficial characteristics are derived from the basic assumption that the algorithm is based on, i.e. that the detected OA signal stems only from hemoglobin. Furthermore, as compared to the model-based methods discussed in Sec. 1.3.5, eMSOT considers a spectral inversion problem rather than the spatial one, with spatial information used as supplementary to aid the minimization procedure (Eqs. 1.24 - 1.28) converge to the correct solution. Naturally, this reduces the optical inverse problem to a much simpler model inversion task with a handful of unknowns and allows for local application to the well-reconstructed parts of the OA image.

However, the eMSOT algorithm is still prone to errors. This is due to the inversion constraints Eqs. 1.25-1.28 and regularization. The terms $\alpha \parallel \mathbf{Wm}_i \parallel_2, i = \overline{1,3}$ are used to constrain the variability of the eigenfluence parameters among neighbor grid points. Eq. 1.25 ensures a decrease in $m_2(\mathbf{r})$ with tissue depth. Such behavior was found to be consistent in simulations [64] and therefore assumed to hold in tissue. Eqs. 1.26 and 1.27 reduce the search-space for parameters m_1 and m_3 based on the information obtained at the preprocessing step. The discussed constraints have been shown to be vital for the stability of the model inversion and are generally aimed at preventing the method from converging to the erroneous solution. However, the fact that they are essentially hand-engineered and not optimized leads to the suboptimal performance of the algorithm in some scenarios. Hence, there is a need to optimize the inversion procedure to incorporate constraints that better model the behavior of the eigenparameters.

Furthermore, the performance of the method strongly depends on the quality of the spectral data it operates on. Notably, in OA images, the noise is spatially non-uniformly distributed. This is due to the fact that the noise in the image is the result of the noisy detector signals. Thus, the measured OA spectra stemming from the superficial and highly absorbing areas demonstrate higher SNR than those measured in deep or weakly absorbing tissue. Without the tools to assess data quality, the quantitative results produced by the algorithm remain to a high degree user-dependent. Therefore, one of the goals of this work is to develop methods for spectral quality assessment to reduce the impact of noisy data on the outcome of the sO$_2$ quantification with eMSOT and to guide the user to select areas with higher spectral quality for the analysis.

Improving sO$_2$ eMSOT quantification capabilities

Chapter 2 describes the eMSOT algorithm derived using the Bayesian framework. The model inversion is formulated as a problem of maximum a posteriori estimation problem and the objective function is derived using the probabilistic terms, starting with the basic assumption that the set of the measured normalized OA spectra $\mathbf{P}_{measured}$ can be represented as the corresponding eigenspectra model $\mathbf{P}_{model}$ contaminated with the white noise $\mathbf{N}$:

$$\mathbf{P}_{measured} = \mathbf{P}_{model} + \mathbf{N}. \tag{1.29}$$

Since the initial knowledge of the dependencies of the eigenparameter relies on a connectivity system, the grid $\mathbf{G}$ is modelled as a graph where each pixel represents a node. Gaussian Markov Random Fields are used to model the distribution of the unknown model parameters on a graph [177, 178]. By tuning the parameters of the mentioned distribution, the inversion is optimized to better model the behavior of grid parameters.

When implementing the eMSOT inversion in the Bayesian framework, a problem of estimating the noise present in the measurements arises. Since the level of noise present in spectra is spatially inhomogeneous, noise needs to be estimated per spectrum. To achieve this, a novel tool based on a spectral model of the recorded OA spectra is developed for the estimation of the level of noise in spectral measurements. The model, termed OA spectral model, is based on a similar principle as the one used for deriving eigenspectra model for the normalized optical fluence spectra. It is hypothesized that similarly to spectral patterns of the normalized optical fluence, normalized OA spectra of hemoglobin can also be approximated with high accuracy using a simple low-dimensional linear model. To derive such a model, a training dataset that contains representative optoacoustic

spectra of hemoglobin modified both due to the change of sO_2 and spectral coloring is created and PCA is applied to the spectral dataset to derive the principal components. Further analysis shows that only four such components are sufficient to approximate the measured OA spectra of hemoglobin. The OA spectral model consisting of the four derived base spectra $\mathbf{p}_i, i = \overline{1,4}$ and the mean spectrum of the training dataset $\mathbf{p}_M$ termed OA spectral model, is used to estimate the noise present in the experimentally recoded spectra. Using the estimates of noise, its characteristics such as variance or standard deviation can be computed. The ability of the described method to estimate noise is tested in simulated data. The use for the OA spectral model is twofold. First, the power of noise can be estimated for every measured spectrum in the image and spatially mapped. The so created Spectral Reliability Map highlights the areas of the image with high estimated SNR, guiding the user to analyze the well-reconstructed parts of the image. Second, the variance of the estimated noise is used in the inversion procedure to adaptively lower the impact of the noisy data on the result of the optimization procedure.

The Bayesian algorithm is tested in simulations and compared to the original eMSOT algorithm for its ability to estimate noise in the measurements, reduce the impact of noisy data on fluence estimation, and improve sO_2 estimation in deep-seated, highly absorbing targets, i.e. at locations that demonstrate SNR values that are higher than the surrounding tissue.

Chapter 3 describes the deep learning based eMSOT algorithm, where the model inversion step, formulated as a minimization procedure in the original eMSOT, is replaced by the neural network trained on data derived from relatively simple simulations. In this way, the optimal inversion constraints that model the interplay between the eigenparameters is learned implicitly by the neural network rather than specified a priori. When developing a neural network-based method, the two primary concerns are the design of an appropriate architecture and the availability of a training dataset. In pursuit of an architecture that would be tailored to the specific problem at hand, we developed a model based on a bi-directional Recurrent Neural Network (RNN). Such an architecture was chosen to better account for depth dependence of optical fluence. RNNs are specifically designed to handle sequential data, therefore the input spectra are transformed into a sequence where the spectra at similar tissue depths constitute one point in the input sequence. The RNN-based architecture was compared to other simpler and more generic designs that were produced without the specific problem in mind and was found to outperform such simpler alternatives.

In the specific case of replacing the eMSOT inverse problem with a neural network, only the simulated data can be used for training the model. This is due to the fact that the developed network is predicting the eigenfluence parameters, i.e. it essentially predicts the spectra of normalized fluence that can hardly be obtained experimentally. When training a model on purely simulated data, a natural concern of the ability of the resulting model to generalize to experimental data arises. Notably, the simulations used to create the training dataset for the developed network do not take into account several processes and effects that affect the measured data, such as acoustic wave propagation and detection and the effects of image reconstruction techniques described in Sec 1.3.4. Nonetheless, upon the evaluation of the performance of the method in simulated data and experimental data obtained from blood phantoms and small animals (mice), it is concluded that the network generalizes well to experimentally obtained data and, when compared to the original eMSOT algorithm, outperforms it in terms of sO_2 quantification accuracy in most of the considered cases.

1.4.2   Functional brain imaging using MSOT

The sensitivity of MSOT to hemoglobin and inherent high penetration depth as compared to pure optical imaging methods has paved its way into the neuroimaging research as a powerful tool. On a macroscopic scale, tomographic OA systems have been mainly used to monitor brain hemodynamics during the gas challenge and perfusion rate of administered contrast agents [124, 179]. The gas challenge typically consists of changing the contents of the breathing gas to induce changes in O_2 content of the blood, and tissue oxygenation. With similar experimental protocols, five-dimensional OA data from the brain region has been recorded and analyzed to visualize the dynamics of hemoglobin, sO_2, total hemoglobin, and blood flow in the superficial brain vessels under gas challenge [123]. Earlier, tomographic OA systems have been used to monitor hemodynamic responses of the cerebral cortex to external stimulations [125, 180] and to assess the connectivity of the brain regions in the resting state [126].

Problem statement

As evident, despite the success that OA had in terms of the application in the field of neuroimaging on the microscopic and mesoscopic scales (see Sec. 1.2.2), the research involving tomographic systems for performing functional brain imaging on a macroscopic scale is rather scarce. This is perhaps due to the fact that, among other reasons, the resolution and contrast of tomographic setups may be compromised due to the presence of a skull [66]. The mentioned studies were mostly limited to the superficial brain tissue, i.e. cortex, with used setups providing limited dorsal view of the brain; or did not make full use of the multispectral capabilities of the technique. Furthermore, the reports on the capabilities of OA for imaging brain structure of the brain typically visualize the superficial vasculature.

Brain imaging using MSOT

In order to address the above-mentioned omissions, functional brain imaging of deep brain tissue described in Chapters 4 and 5 was performed using the commercially available MSOT scanners described in Sec. 1.4.3.

In Chapter 4, a hybrid US-MSOT system is examined for its applicability to functional brain imaging and the complementary contrast of both modalities is demonstrated. The functional read-outs are recorded under the gas challenge and analyzed. Using a curve-fitting procedure, the quantitative dynamic characteristics of the obtained time traces of relative sO_2 were extracted. The comparison of the mentioned hemodynamic parameters between the brain and reference abdominal tissue establishes that the reactivity of brain tissue to the gas challenge is higher than that of the abdominal tissue, suggesting a tighter coupling of the brain parenchyma to the breathing state. The results confirm the ability of MSOT to assess meaningful metrics for assessing brain function impairment.

Notably, the skull limits the ability of US and, to a significantly lesser extent, MSOT to reveal structural information about the brain because it strongly reflects ultrasound waves and acts as a band-pass filter of OA signals [181, 182]. Therefore, clearly delineating the skull is the first step towards accordingly correcting the MSOT image by incorporating this information into the MSOT image reconstruction procedure. Thus, US images that clearly reveal the skull outline may be an important asset for making such corrections possible. Furthermore, it is established that the hybrid system in the MSOT imaging regime demonstrates marginally improved spatial resolution as compared to the system with 256 detectors.

After testing the basic applicability of MSOT for visualizing brain structures and quantifying hemodynamic parameters, MSOT was used to perform for the first time high-resolution imaging of the evoked hemodynamic responses to whisker stimulation in deep brain tissue, as described in Chapter 5. To achieve this goal, certain hardware adjustments and developments were made, specifically, a custom breathing mask that ensures adequate ventilation and allows for high amplitude whisker actuation was built along with a custom magnetic actuator of magnetic beads attached to the whiskers. Using correlative analysis of the obtained OA signal time traces with the canonical hemodynamic response function [183] used as a reference, the evoked activity has been detected and spatially mapped, with additional correlative analysis performed to establish the connectivity of the brain regions responsible for processing the sensory inputs. The obtained results are in agreement with the literature on the topic, confirming the results obtained with MSOT against the established imaging modalities. Furthermore, anatomical imaging was performed as well to examine the capabilities of MSOT for visualizing the brain structures. We demonstrate that MSOT provides adequate contrast and excellent spatial resolution that enables performing morphometric studies on intact brain. Furthermore, molecular agent detection algorithms [184] are used in combination with the injections of the contrast agents to investigate whether the molecular imaging capacity of MSOT may further enhance the completeness of information provided by the modality in the task of brain imaging.

The obtained results bring MSOT a step closer to becoming an accepted instrument for neuroscience research and serve as an indication that with further optimization and development, MSOT has the potential to transform neuroimaging in small animal models with its capabilities for non-invasive, label-free functional and anatomical imaging of the brain, with an array of contrast agents providing additional possibilities.
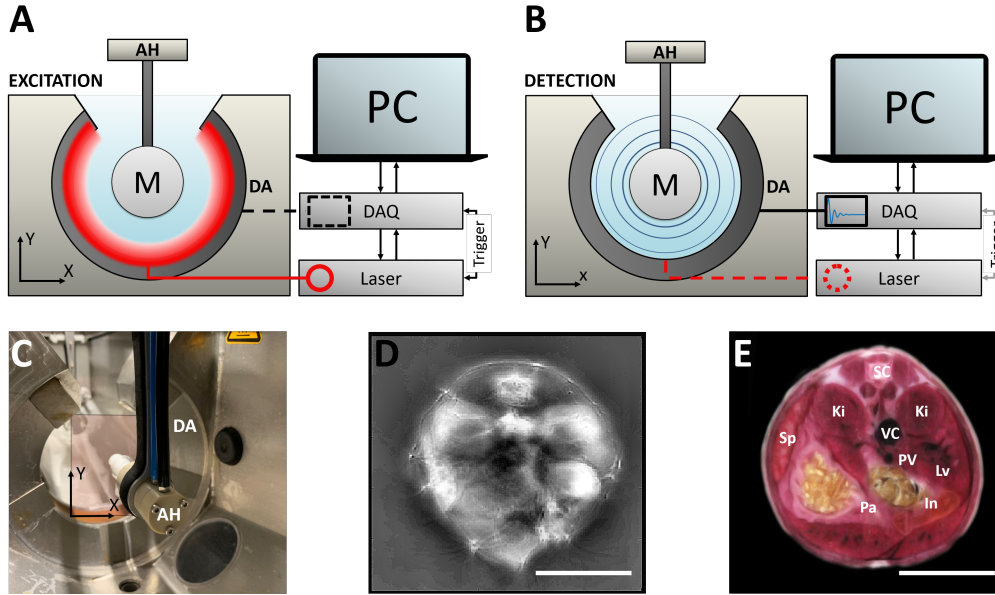
Figure 1.3: MSOT principle of operation. **(A)** During the excitation, a short laser pulse illuminates a mouse (M) positioned in the animal holder (AH) and triggers data acquisition. **(B)** During signal detection, the ultrasound waves generated by the excitation pulse propagate outwards toward the detector array (DA) and the readouts are quantized by the data aqcuisition card (DAQ) and stored on a personal computer. **(C)** A photograph of the imaging chamber of MSOT inVision 256. The imaging plane is shown in red. **(D)** A reconstructed optoacoustic image of an abdominal cross-section of a mouse imaged by inVision 256. **(E)** A cryoslice of approximately the same region as shown in (D) with labeled anatomical references: SC – spinal chord; Ki – kidney; VC – vena cava; PV – portal vein, Sp – spleen; Pa – pancreas; In – intestine. Scale bars: 1 cm.

1.4.3 Instrumentation for MSOT imaging

A number of OA setups for small animal imaging have been developed over the years, including both custom and commercially available systems that typically can be grouped according to the afforded resolution as microscopic, mesoscopic and macroscopic. Of these, tomographic systems operate on a macroscopic scale and are differentiated based on the detection geometry, illumination type and transducer bandwidth.

The bandwidth of the transducer typically determines the resolution and to some extent the imaging depth of the setup. The use of high-frequency transducers results in higher resolution but lower imaging depth due to the frequency-dependent attenuation of ultrasound [185, 186]. Light delivery to the specimen is typically performed using the optical fibers, with macroscopic and meso-scopic systems utilizing diffuse light to ensure even illumination. The choice of the illumination wavelengths range determines the imaging depth as well as the ability to differentiate certain chromophores based on their respective absorption spectra. In terms of the detection geometry, 3D tomographic systems typically use spherical [187] or planar detection [188], thus suffering from the limited view. 2D systems use focused ultrasound transducers and provide images of the transverse plane at the focal plane of the transducers [59, 125]. Such setups are able to reduce the extent of the limited view problem.

All experimental data used in this work has been obtained using one of the commercially available MSOT scanners: MSOT inVision 256 or MSOT inVision 512.

MSOT inVision256

Fig. 1.3 schematically demonstrates the imaging setup used in this work. At the core of the system is the detection module, a 256-element concave semi-full ultrasound detector array (DA) Imasonics SaS, Voray, France with the following characteristics:

- array type: spherical concave array covering 270°, providing ∼90°of access to the animal (M);

- number of channels: 256;

- mechanical focalization: toroidal focusing;

- radius of curvature SR 40 mm;

- radius of the elements (elevation): 37 mm+1 /-2 mm;

- elementary pitch: ~0.735 mm / ~0.37 mm;

- interelement spacing: 0.1 mm;

- width of the elements: 15 mm (chord);

- center frequency (-6 dB): 5 MHz$\pm$10%;

- bandwidth (-6 dB): $\geq$55%.

The system relies on Nd:YAG-pumped optical parametric oscillator (InnoLas Laser GmbH, Krailling, Germany) to produce 9 ns-long laser pulses at a frequency of 10 Hz, per-pulse energy being approximately 120 mJ. The range of wavelengths utilized in this work typically spans from 700 nm to 900 nm.

MSOT inVision512

The main advantage of MSOT inVision 512 as compared to the system described above is its ability to acquire US images in addition to OA data. The system bears most of the same characteristics as the one described above with two notable exceptions: the ultrasound detector array of inVision 512 has 512 detectors and is coupled to an extra DAQ system. In total, the detector array is connected to two DAQ systems, each corresponding to one of the acquisition modes (US and MSOT). Despite a common principle of US and OA signal detection, a second DAQ is employed due to the conventional OA DAQ electronics not supporting the transmission of US pulses and differences in OA and US signal resulting in different amplification and input impedance needed to record US as compared to OA signals. Due to the concave geometry of the detector used, a specific reconstruction algorithms have to be employed to form a US image. To switch between acquisition modes, a multiplex programmable switchboard (MUX) is used.

1.4.4 Animal experiments

All procedures involving animal experimentations were conducted according to the institutional guidelines and the government of Upper Bavaria and complied with German Federal and EU law. Efforts were made to reduce animal usage and suffering. Athymic Nude-FOXN1 Nu/Nu and CD1 mice are the two breeds used in all the experiments. The mice were anesthetized supplying 0.8 L/min isoflurane during the imaging procedures. Throughout the experiments, the animals were breathing one of the following gas mixtures: medical air (20% oxygen) or 100% oxygen, or CO_2. For functional brain imaging, magnetic beads were attached to the mouse whiskers on the left side and stimulated with magnetic force created by a custom built electromagnetic unit. The amount of supplied isoflurane was reduced at the time of imaging to ensure stable breathing. After the imaging procedure, mice were sacrificed by injecting ketamine (180 mg/kg). In rare cases, the mice were sacrificed by inhaling lethal amount of CO_2.

Chapter 2

A Bayesian approach to eigenspectra optoacoustic tomography

2.1 Summary

The paper "A Bayesian Approach to Eigenspectra Optoacoustic Tomography" is authored by Ivan Olefir, Stratis Tzoumas, Hong Yang and Vasilis Ntziachristos. The version herein (Appendix A) is published in the Journal IEEE Transactions on Medical Imaging [189].

While the eigenspectra MSOT algorithm introduced in Sec. 1.4.1 offers unparalleled sO$_2$ quantification accuracy in experimental data, in some cases the algorithm was found to produce erroneous results with absolute estimation errors reaching 15-20%. The general aim of the study is to improve the robustness of the algorithm. The reason for the mentioned errors is twofold: on one hand, the inversion procedure relies on a number of important but not optimized constraints and parameters; and on the other hand, spectra that are severely corrupted by noise prevent the algorithm form converging to the optimal solution. Accordingly, the contribution of the manuscript is twofold as well. First, the problem of model inversion in eMSOT is formulated using Bayesian probabilistic framework as a maximum a posteriori estimation. The inversion constraints are modelled as the prior probability distributions and the parameters of the mentioned distributions are optimized using simulations. Second, a low-dimensional model for the recorded OA spectra is developed that allows for estimation the noise in the measured OA spectra.

The model parameters are modelled as random variables. Due to the spatial sampling of the spectral data and the importance of the spatial dependencies, probabilistic graphical models are used. The model parameters for the spectra at distinct spatial locations are represented by graph nodes and the neighborhood system in the sampled grid is reflected in the connectivity of the nodes. The distribution of the sought parameters is then modelled using Gaussian-Markov Random fields.

For the task of noise estimation that arises when casting the inverse problem of eMSOT in the Bayesain domain, a novel model for the measured OA spectra is derived from a comprehensive set of simulated spectra that captures the variability of the measured spectra due to the absorption of hemoglobin as well as the effects of the optical fluence has been developed. Using the spectral model for OA measurements, it is shown possible to accurately estimate noise in the recorded spectra and spatially map it, producing a so called spectral reliability map of a given MSOT image. Such a map highlights regions of the image where the application of eMSOT would yield optimal results. Furthermore, the obtained noise estimates are used directly in the Bayesian eMSOT to adaptively weigh the contribution of the measured spectra selected for the inversion to the result produced by the algorithm. As the result, the Bayesian algorithm was found to perform better than the original eMSOT for the task of estimating sO$_2$ in a deep seated highly absorbing vessel in the presence of spatially non-uniform noise typical MSOT data. With the power of noise added to the simulated detector signals increasing, we show that the Bayesian algorithm is able to reduce the influence of the noise-corrupted spectra surrounding the vessel on the overall result of the application of the algorithm, while the estimation accuracy of the original eMSOT method decreases. Notably, the estimation accuracy in the regions without inclusions such as vessels with spatially smoothly varying absorption the Bayesian method provides no advantage over eMSOT. Among the disadvantages of the Bayesian algorithm is the significantly increased inversion time (60 sec vs 5 sec of eMSOT).

I conceived the idea of using the Bayesian framework for eMSOT inverse problem together with Stratis Tzoumas. I have derived the mathematical formulation of the Bayesian eMSOT, developed the model for noise estimation and validated it in simulated data. I have developed and implemented simulations for validation of Bayesian eMSOT together with Hong Yang. I have drafted the manuscript that was improved through numerous discussions with all the co-authors. Vasilis Ntziachristos supervised the project.

2.2   Publication

I. Olefir, S. Tzoumas, H. Yang, and V. Ntziachristos, "A Bayesian approach to eigenspectra optoacoustic tomography," *IEEE transactions on medical imaging*, vol. 37, no. 9, pp. 2070-2079, 2018.

Chapter 3

Deep learning based spectral unmixing for optoacoustic imaging of tissue oxygen saturation

3.1 Summary

The paper "Deep learning based spectral unmixing for optoacoustic imaging of tissue oxygen saturation" is authored by Ivan Olefir, Stratis Tzoumas, Courtney Restivo, Pouyan Mohajerani, Lei Xing and Vasilis Ntziachristos. The version herein (Appendix B) is accepted for publication in the Journal IEEE Transactions on Medical Imaging.

    The Bayesian approach to eMSOT described in Chapter 2 has solved the problem of estimating the quality of the spectral data depending on the amount of the present Gaussian noise and suppressing the impact of noisy data on the sO_2 estimation accuracy of the algorithm. Such an improvement is especially evident in sO_2 estimation of deep-seated highly absorbing targets, e.g. vessels. However, the problem of the robust and accurate eigenspectra model inversion persisted. The Bayesian algorithm did not improve sO_2 quantification accuracy in the areas with smoothly changing absorption. In such areas that can serve as a model for muscle tissue away from large blood vessels, accurate sO_2 estimation was still problematic.

    The reason for such errors is inaccurate modeling of the behavior and interdependencies of the sought model parameters. In this work, we have proposed a novel method to solve this problem. The proposed approach solves the inverse problem of eMSOT utilizing a neural network instead of the previously used optimization algorithm. Thus, the dependencies of the model parameters in the inversion step can be learned from the training data instead of manually specifying them in the inversion algorithm.

    The proposed architecture is based on the following idea: due to the strong dependence of the optical fluence on tissue depth, the input spectra are transformed into a sequence where the spectra from the similar depth in tissue constitute one point in the sequence. The resulting sequence is fed to the network that is based on a bi-directional recurrent network since such architecture is well suited to working with sequential data.

    Due to the difficulty obtaining experimental data with the known spatial distribution of fluence, the training data has been derived from simulations. Model validation has been performed on simulated data as well. Since the model was trained on simulated data, it was of the utmost importance to ensure its generalization to real data. Therefore, model testing has been conducted using both simulated and experimental data with the available gold standard values for sO_2. Notably, the simulated data for validation and testing was designed to differ from the training data to prevent overfitting. For additional accuracy, we train an ensemble of 50 networks where the output of the ensemble is the median filtered output of the networks. Based on the results obtained from simulations and experimental data we show that the proposed network architecture is able to learn solving the inverse problem of eMSOT and that such a deep learning based approach has higher sO_2 quantification accuracy than the original algorithm in most considered cases.

    I conceived the idea of the deep learning based algorithm, designed various network architectures and designed and implemented simulations for obtaining the training, validation and test data

together with Stratis Tzoumas. I have implemented and tested the designed architectures together with Courtney Restivo. I have designed and implemented approaches to increase the accuracy of the deep learning based algorithm together with Pouyan Mohajerani. I have drafted the manuscript which was constantly advanced and improved through the discussion with all the co-authors. Vasilis Ntziachristos supervised the project

3.2 Publication

I. Olefir[†], S. Tzoumas[†], C. Restivo, P. Mohajerani, L. Xing and V. Ntziachristos, "Deep learning based spectral unmixing for optoacoustic imaging of tissue oxygen saturation", *submitted to Medical Imaging, IEEE Transactions on*

Chapter 4

Hybrid multispectral optoacoustic and ultrasound tomography for morphological and physiological brain imaging

4.1   Summary

The paper "Hybrid multispectral optoacoustic and ultrasound tomography for morphological and physiological brain imaging" is authored by Ivan Olefir, Elena Merčep, C. Burton, Saak V. Ovsepian and Vasilis Ntziachristos. The version herein (Appendix C) is published in the Journal for Biomedical Optics [190].

Despite the advantages in depth penetration offered by optoacoustic imaging, most studies using macroscopic OA imaging of the brain concentrated on visualization and analysis of data obtained from the superficial brain tissue and demonstrated dorsal anatomical cross-sections. Moreover, the inherent potential of OA setups for performing US imaging due to the utilization of piezo-electronics has not been implemented for brain imaging.

In this work, we examine the applicability of a novel hybrid US-MSOT system to hybrid morphological and physiological brain imaging. Notably, the curved design of the detector array allows for optimal angular coverage of the specimen for OA imaging while simultaneously allows for acquiring US images with the use of special image reconstruction algorithms. We image Athymic nude mice under gas challenge, where the content of the breathing gas changes from medical air to a mixture of medical air with 10% CO_2 followed by pure oxygen. Finally, the breathing gas changes back to the medical air. The imaging of the head was performed followed by a repeated experiment while imaging the abdominal organs.

The resulting data is unmixed for sO_2 and the hemodynamic parameters of the resulting time series are quantified and compared. In particular, the degree of vascular coupling of various tissue was assessed by quantifying the slope of the change in sO_2 value in various regions. Finally, we assess the benefits of the increased number of detectors in the transducer array by comparing the anatomical images obtained with a 256 detector array to the images from the corresponding anatomical cross-section obtained with a transducer array with 512 elements.

From the perspective of anatomical imaging, the obtained results indicate that the OA images obtained with a detector array with 512 elements demonstrate improved resolution as compared to the array with 256 detectors. This is in line with the phantom studies and theoretical predictions. From the perspective of contrast, the two employed modalities (AO and US) reveal complementary features. In the head region, US displays limited penetration depth due to the presence of the skull. In turn, OA boasts improved imaging depth as compared to US. In the abdominal area, however, the disposition is different, with US demonstrating superb penetration but OA still having better resolution. In terms of functional imaging, the results suggest tighter vascular coupling of brain tissue as compared to abdominal tissue. Notably, brain parenchyma exhibited the highest degree of coupling. The results are in line with the previously published research.

28

I have conceptualized the study together with Saak V. Ovsepian and Vasilis Ntziachristos; Neal C. Burton and Elena Merčep performed the animal experiments; Elena Merčep provided technical support for the data acquisition and analysis; I have analyzed the data; I have drafted the manuscript together with Saak V. Ovsepian; the manuscript was continuously advanced through the discussions with all the co-authors; Vasilis Ntziachristos supervised the project.

4.2 Publication

I. Olefir, E. Merčep, N. C. Burton, S. V. Ovsepian, and V. Ntziachristos, "Hybrid multispectral optoacoustic and ultrasound tomography for morphological and physiological brain imaging," *Journal of biomedical optics*, vol. 21, no. 8, p. 086005, 2016.

Chapter 5

Spatial and spectral mapping and decomposition of neural dynamics and organization of the mouse brain with multispectral optoacoustic tomography

5.1 Summary

The paper "Spatial and spectral mapping and decomposition of neural dynamics and organization of the mouse brain with multispectral optoacoustic tomography" is authored by Ivan Olefir, Ara Ghazaryan, Hong Yang, Jaber Malekzadeh-Najafabadi, Sarah Glasl, Panagiotis Symvoulidis, Valerie B. O'Leary, George Sergiadis, Vasilis Ntziachristos. The version herein (Appendix D) is published in the Cell Reports journal [191].

Numerous studies have utilized tomographic OA setups for functional brain imaging. However, most of them either focused on superficial brain areas or relied on a single wavelength excitation, therefore not utilizing the main potential advantages of MSOT for functional neuroimaging. Furthermore, the application of OA to large scale anatomical neuroimaging has also typically been restricted to visualizing major superficial vessels. With the unique capability of a curved array-based tomographic OA system to visualize hemoglobin related contrast in deep brain tissue and the ability to detect quickly unfolding hemoglobin changes established in Chapter 4, MSOT is utilized in this study to correct for the mentioned omissions.

The contribution of this work is threefold. First, we perform functional MSOT of whisker-induced response in the somatosensory barrel cortex. For this, we develop a custom electromagnetic actuator that acts on the magnetic beads glued to the whiskers of an animal. We analyze the obtained data and visualize the detected hemodynamic response in deep layers of the barrel cortex. Moreover, we perform correlative analysis to determine the connectivity of various brain regions when processing whisker inputs. We validate the results by performing the analysis of data from the negative control experiments. Second, we perform label-free structural MSOT of the brain both *in vivo* and *ex vivo* and relate the obtained anatomical images with the histological references. Finally, we examine the possibilities for enhancing structural MSOT brain imaging with exogenous contrast agents by injecting Di-R into the ventricular system of a mouse. Two days after the injection, MSOT of the brain is performed and the data is subsequently unmixed using the molecular agent detection algorithm. The resulting images were verified by performing fluorescence imaging of corresponding brain cross-sections.

In terms of functional imaging, we were able to observe and spatially map the evoked hemodynamic response in the mouse brain. Importantly, such changes were localized, with the cross-sections farther away from the barrel cortex exhibiting little to no response to stimulations, as expected. With the imaging depth provided by MSOT, we visualized the connectivity of brain compartments when processing the whisker inputs, including the deep brain regions. Notably, using the mul-

tispectral capabilities of MSOT, we spectrally decomposed the hemodynamic responses into the contributions of oxygenated and deoxygenated hemoglobin and could analyze them separately. In terms of structural imaging, we obtained brain images that showed rich anatomical contrast, both *in vivo* and *ex vivo*, with a near-ideal match established between the major and fine structures visible in the obtained OA images and the corresponding histological cross-sections. Notably, the images obtained at 700 nm show the richest anatomical content. We performed basic morphometric analysis on the image of the excised whole brain. With the use of exogenous contrast agents, we were able to visualize the ventricular system in the images obtained *in vivo*, further enhancing the capabilities of MSOT for structural imaging. Importantly, while our findings are in line with the previously published studies, all the results were obtained with the data coming from a single MSOT system, further establishing its potential for becoming a vital instrument for neuroscience.

I have conceptualized the study and designed experiments together with Saak V. Ovsepian; Ara Ghazaryan and George Sergiadis have developed the system for whisker stimulation; I have acquired the experimental data together with Ara Ghazaryan, Sarah Glasl, and Saak Ovespian; I have analyzed the data together with Panagiotis Symvoulidis; I have drafted the manuscript together with Saak Ovsepian and Valerie B. O'Leary which was continuously advanced through the discussion with all the co-authors; Saak Ovsepian and Vasilis Ntziachristos supervised the project.

5.2 Publication

I. Olefir, A. Ghazaryan, H. Yang, J. Malekzadeh-Najafabadi, S. Glasl, P. Symvoulidis et al., "Spatial and spectral mapping and decomposition of neural dynamics and organization of the mouse brain with multispectral optoacoustic tomography," *Cell reports*, vol. 26, no. 10, pp. 2833-2846. e3, 2019.

Chapter 6

Conclusions

6.1 Summary and outlook

In the present work, functional (physiological) imaging with MSOT is considered in two aspects. On one hand, the algorithmic problem of quantitative sO_2 imaging is considered, in particular using the eigenspectra MSOT method. On the other hand, MSOT is applied experimentally to functional neuroimaging and its capabilities are used to conduct functional, anatomical and molecular imaging of the mouse brain with a particular focus the imaging of the evoked hemodynamic response of the deep brain to stimuli and correlating them to the corresponding anatomical structures.

In eMSOT, the problem of sO_2 quantification is solved by considering the inverse problem, i.e. the eigenspectra model for the recorded OA spectra is inverted to find the eigenparameters that best fit to the data using constrained minimization. Using the found parameters, the fluence is estimated in the region of interest and the effect of spectral coloring is reverted. From the practical perspective, there is a need for a more robust model inversion method and a tool to assess the quality of the measured OA spectra due to the spatially non-uniform distribution of noise attributed to the OA images.

In an attempt to optimize the eMSOT model inversion, a Bayesian framework is considered and the inverse problem is formulated as a maximum a posteriori estimation. The prior knowledge of the dependencies between various model parameters is formulated as prior distributions instead of minimization constraints and are optimized. To address the need to estimate noise in the measured spectra, a spectral model for the normalized OA spectra is developed that captures the variability of the OA spectra due to the absorption of hemoglobin and effects of fluence. It is shown that using this model, it is possible to estimate the noise in the measured spectra assuming that it comes from the Gaussian distribution. As shown in simulations, using this estimate, it is possible to negate the impact of noisy data on the inversion and improve sO_2 estimation accuracy in deep-seated highly absorbing targets under the presence of high spatially non-uniform noise. Notably, the Bayesian algorithm does not provide increased sO_2 estimation accuracy in the background tissue with smoothly varying absorption. Theoretically, the OA spectral model may be used to detect anomalies in the spectra, i.e. the presence of absorbers other than hemoglobin in concentrations high enough to affect the measured spectra significantly. While the application of the model to this problem has been studied and initial results showcased, a thorough investigation for the anomaly detection with the OA spectral model may constitute a topic for future research.

With the spectra quality assessment tool available, further efforts have been concentrated on designing a robust and accurate method for solving the inverse problem of eMSOT. Attempting to avoid the need to model the behavior and interdependence of the model parameters, a deep learning approach based on a bi-directional recurrent neural network has been considered. The network has been trained on data generated using relatively simple simulations. As shown in simulations and experimental OA images of blood phantoms and small animals (mice) with the available gold standard sO_2 values, the resulting deep learning-based algorithm consistently outperforms the original eMSOT in sO_2 estimation accuracy and is especially well-suited for processing large data volumes. Nonetheless, the deep learning-based approach does not provide perfect sO_2 accuracy, possibly due to the training data not modeling various effects and processes such as acoustic wave propagation and reconstruction. Further research will be aimed at correcting for the mentioned omissions and better modeling the processes unfolding during the OA experiment to result in a more realistic

training dataset. One more direction for the future work may be the optimization of the number of excitation wavelengths used during data acquisition to both optimize the acquisition speed and sO_2 estimation accuracy.

In the domain of neuroimaging, OA has proved itself a strong contender among the more established imaging brain imaging techniques, such as microscopy or MRI, by combining superb sensitivity to hemoglobin, high spatial resolution and penetration depth that is excellent for a small animal imaging technique. Experimentally, it is important to use the mentioned advantages to their full potential.

First, a hybrid US-MSOT system has been studied for applicability to brain imaging in small animals (mice) under the gas challenge. The complementary contrast of US and MSOT has been described and the physiological parameters of hemodynamics in the brain have been compared to those of the abdominal organs as a reference. Notably, while the US has been shown to provide limited anatomical information in the head region due to the skull, this information may potentially be used for improving the reconstruction of the corresponding MSOT images and correcting for the possible SoS heterogeneities due to the presence of the skull. Further research in this direction is of great interest to the neuroimaging applications of OA.

Second, MSOT has been used for functional, anatomical and molecular imaging of the brain, in particular for the high-resolution mapping of macroscopic scale hemodynamic response to somatosensory stimulation. The evoked hemodynamic changes were spectrally decomposed and analyzed in terms of connectivity of regions responsible for processing somatosensory inputs, including the deep brain regions. Although the findings are in agreement with the available research on the topic, further establishing MSOT as a useful tool for neuroscience research, several issues remain to be addressed. For instance, careful optimization of the experimental procedures, such as the selection of the used anesthetic and better control over stimulation amplitude would be beneficial for further comparison of the obtained results with the ones from such techniques as fMRI. This process might involve optimization of instrumentation as well. Experimentally, the use of clearing solutions for the skull should be considered for improving light and sound propagation through the skull. In terms of data analysis, a careful study of used instrumentation and reconstruction methods on the recorded signal is of interest, as this may potentially lead to the enhanced sensitivity by regressing out various signal components that might contaminate the recorded time traces.

Bibliography

[1] R. Weissleder and M. Nahrendorf, "Advancing biomedical imaging," *Proceedings of the National Academy of Sciences*, vol. 112, no. 47, pp. 14424–14428, 2015.

[2] K. Cleary and T. M. Peters, "Image-guided interventions: technology review and clinical applications," *Annual review of biomedical engineering*, vol. 12, pp. 119–142, 2010.

[3] F. Kiessling and B. J. Pichler, *Small animal imaging: basics and practical guide.* Springer Science & Business Media, 2010.

[4] R. S. Balaban and V. A. Hampshire, "Challenges in small animal noninvasive imaging," *ILAR journal*, vol. 42, no. 3, pp. 248–262, 2001.

[5] E. M. Hillman, "Optical brain imaging in vivo: techniques and applications from animal to man," *Journal of biomedical optics*, vol. 12, no. 5, p. 051402, 2007.

[6] A. Rahmim and H. Zaidi, "Pet versus spect: strengths, limitations and challenges," *Nuclear medicine communications*, vol. 29, no. 3, pp. 193–207, 2008.

[7] D. W. Townsend, "Dual-modality imaging: combining anatomy and function," *Journal of Nuclear Medicine*, vol. 49, no. 6, pp. 938–955, 2008.

[8] R. K. Lenroot and J. N. Giedd, "Brain development in children and adolescents: insights from anatomical magnetic resonance imaging," *Neuroscience & biobehavioral reviews*, vol. 30, no. 6, pp. 718–729, 2006.

[9] K. Taylor, D. Carpenter, C. Hill, and V. McCready, "Gray scale ultrasound imaging: the anatomy and pathology of the liver," *Radiology*, vol. 119, no. 2, pp. 415–423, 1976.

[10] R. Weissleder and U. Mahmood, "Molecular imaging," *Radiology*, vol. 219, no. 2, pp. 316–333, 2001.

[11] R. Weissleder and V. Ntziachristos, "Shedding light onto live molecular targets," *Nature medicine*, vol. 9, no. 1, p. 123, 2003.

[12] S. M. Ametamey, M. Honer, and P. A. Schubiger, "Molecular imaging with pet," *Chemical reviews*, vol. 108, no. 5, pp. 1501–1516, 2008.

[13] S. R. Meikle, P. Kench, M. Kassiou, and R. B. Banati, "Small animal spect and its place in the matrix of molecular imaging technologies," *Physics in Medicine & Biology*, vol. 50, no. 22, p. R45, 2005.

[14] D. Jennings, N. Raghunand, and R. J. Gillies, "Imaging hemodynamics," *Cancer and Metastasis Reviews*, vol. 27, no. 4, pp. 589–613, 2008.

[15] N. Westerhof, *Snapshots of hemodynamics.* Springer, 2018.

[16] P. Vaupel, F. Kallinowski, and P. Okunieff, "Blood flow, oxygen and nutrient supply, and metabolic microenvironment of human tumors: a review," *Cancer research*, vol. 49, no. 23, pp. 6449–6465, 1989.

[17] A. R. Padhani, K. A. Krohn, J. S. Lewis, and M. Alber, "Imaging oxygenation of human tumours," *European radiology*, vol. 17, no. 4, pp. 861–872, 2007.

[18] P. Vaupel and A. Mayer, "The clinical importance of assessing tumor hypoxia: relationship of tumor hypoxia to prognosis and therapeutic opportunities," *Antioxidants & redox signaling*, vol. 22, no. 10, pp. 878–880, 2015.

[19] R. Aaslid, T.-M. Markwalder, and H. Nornes, "Noninvasive transcranial doppler ultrasound recording of flow velocity in basal cerebral arteries," *Journal of neurosurgery*, vol. 57, no. 6, pp. 769–774, 1982.

[20] S. Ogawa, T.-M. Lee, A. R. Kay, and D. W. Tank, "Brain magnetic resonance imaging with contrast dependent on blood oxygenation," *proceedings of the National Academy of Sciences*, vol. 87, no. 24, pp. 9868–9872, 1990.

[21] W. A. Weber, M. Schwaiger, and N. Avril, "Quantitative assessment of tumor metabolism using fdg-pet imaging," *Nuclear medicine and biology*, vol. 27, no. 7, pp. 683–687, 2000.

[22] V. Ntziachristos, A. Leroy-Willig, and B. Tavitian, *Textbook of in vivo Imaging in Vertebrates*. John Wiley & Sons, 2007.

[23] M. Baker, "Whole-animal imaging: The whole picture," *Nature*, vol. 463, no. 7283, p. 977, 2010.

[24] M. Rudin, "Noninvasive structural, functional, and molecular imaging in drug development," *Current opinion in chemical biology*, vol. 13, no. 3, pp. 360–371, 2009.

[25] J. Hsieh, "Computed tomography: principles, design, artifacts, and recent advances," SPIE Bellingham, WA.

[26] F. W. Kremkau and K. Taylor, "Artifacts in ultrasound imaging," *Journal of ultrasound in medicine*, vol. 5, no. 4, pp. 227–237, 1986.

[27] M. K. Feldman, S. Katyal, and M. S. Blackwood, "Us artifacts," *Radiographics*, vol. 29, no. 4, pp. 1179–1189, 2009.

[28] S. Kim, W. Richter, and K. Uğurbil, "Limitations of temporal resolution in functional mri," *Magnetic resonance in medicine*, vol. 37, no. 4, pp. 631–636, 1997.

[29] S. Nioka and Y. Chen, "Optical tecnology developments in biomedicine: history, current and future," *Translational Medicine@ UniSa*, vol. 1, p. 51, 2011.

[30] V. Ntziachristos, "Going deeper than microscopy: the optical imaging frontier in biology," *Nature methods*, vol. 7, no. 8, p. 603, 2010.

[31] J. Pawley, *Handbook of biological confocal microscopy*. Springer Science & Business Media, 2010.

[32] F. Helmchen and W. Denk, "Deep tissue two-photon microscopy," *Nature methods*, vol. 2, no. 12, p. 932, 2005.

[33] K. König, "Multiphoton microscopy in life sciences," *Journal of microscopy*, vol. 200, no. 2, pp. 83–104, 2000.

[34] A. M. Zysk, F. T. Nguyen, A. L. Oldenburg, D. L. Marks, and S. A. Boppart, "Optical coherence tomography: a review of clinical development from bench to bedside," *Journal of biomedical optics*, vol. 12, no. 5, p. 051403, 2007.

[35] D. Huang, E. A. Swanson, C. P. Lin, J. S. Schuman, W. G. Stinson, W. Chang, M. R. Hee, T. Flotte, K. Gregory, and C. A. Puliafito, "Optical coherence tomography," *science*, vol. 254, no. 5035, pp. 1178–1181, 1991.

[36] I.-K. Jang, B. E. Bouma, D.-H. Kang, S.-J. Park, S.-W. Park, K.-B. Seung, K.-B. Choi, M. Shishkov, K. Schlendorf, and E. Pomerantsev, "Visualization of coronary atherosclerotic plaques in patients using optical coherence tomography: comparison with intravascular ultrasound," *Journal of the American College of Cardiology*, vol. 39, no. 4, pp. 604–609, 2002.

[37] B. J. Vakoc, D. Fukumura, R. K. Jain, and B. E. Bouma, "Cancer imaging by optical coherence tomography: preclinical progress and clinical potential," *Nature Reviews Cancer*, vol. 12, no. 5, p. 363, 2012.

[38] J. Welzel, "Optical coherence tomography in dermatology: a review," *Skin Research and Technology: Review article*, vol. 7, no. 1, pp. 1–9, 2001.

[39] A. Cerussi, D. Hsiang, N. Shah, R. Mehta, A. Durkin, J. Butler, and B. J. Tromberg, "Predicting response to breast cancer neoadjuvant chemotherapy using diffuse optical spectroscopy," *Proceedings of the National Academy of Sciences*, vol. 104, no. 10, pp. 4014–4019, 2007.

[40] C. Habermehl, S. Holtze, J. Steinbrink, S. P. Koch, H. Obrig, J. Mehnert, and C. H. Schmitz, "Somatosensory activation of two fingers can be discriminated with ultrahigh-density diffuse optical tomography," *Neuroimage*, vol. 59, no. 4, pp. 3201–3211, 2012.

[41] V. Ntziachristos, C.-H. Tung, C. Bremer, and R. Weissleder, "Fluorescence molecular tomography resolves protease activity in vivo," *Nature medicine*, vol. 8, no. 7, p. 757, 2002.

[42] J. P. Culver, T. Durduran, D. Furuya, C. Cheung, J. H. Greenberg, and A. Yodh, "Diffuse optical tomography of cerebral blood flow, oxygenation, and metabolism in rat during focal ischemia," *Journal of cerebral blood flow & metabolism*, vol. 23, no. 8, pp. 911–924, 2003.

[43] A. Gibson and H. Dehghani, "Diffuse optical imaging," *Philosophical Transactions of the Royal Society A: Mathematical, Physical and Engineering Sciences*, vol. 367, no. 1900, pp. 3055–3072, 2009.

[44] Y. Hoshi and Y. Yamada, "Overview of diffuse optical tomography and its clinical applications," *Journal of biomedical optics*, vol. 21, no. 9, p. 091312, 2016.

[45] J. Xia and L. V. Wang, "Small-animal whole-body photoacoustic tomography: a review," *IEEE Transactions on Biomedical Engineering*, vol. 61, no. 5, pp. 1380–1389, 2013.

[46] S. Manohar and D. Razansky, "Photoacoustics: a historical review," *Advances in optics and photonics*, vol. 8, no. 4, pp. 586–617, 2016.

[47] L. V. Wang and S. Hu, "Photoacoustic tomography: in vivo imaging from organelles to organs," *science*, vol. 335, no. 6075, pp. 1458–1462, 2012.

[48] S. Tzoumas, N. C. Deliolanis, S. Morscher, and V. Ntziachristos, "Unmixing molecular agents from absorbing tissue in multispectral optoacoustic tomography," *IEEE transactions on medical imaging*, vol. 33, no. 1, pp. 48–60, 2013.

[49] V. Ntziachristos and D. Razansky, "Molecular imaging by means of multispectral optoacoustic tomography (msot)," *Chemical reviews*, vol. 110, no. 5, pp. 2783–2794, 2010.

[50] A. De La Zerda, C. Zavaleta, S. Keren, S. Vaithilingam, S. Bodapati, Z. Liu, J. Levi, B. R. Smith, T.-J. Ma, and O. Oralkan, "Carbon nanotubes as photoacoustic molecular imaging agents in living mice," *Nature nanotechnology*, vol. 3, no. 9, p. 557, 2008.

[51] J. Weber, P. C. Beard, and S. E. Bohndiek, "Contrast agents for molecular photoacoustic imaging," *Nature methods*, vol. 13, no. 8, p. 639, 2016.

[52] X. Yang, E. W. Stein, S. Ashkenazi, and L. V. Wang, "Nanoparticles for photoacoustic imaging," *Wiley interdisciplinary reviews: nanomedicine and nanobiotechnology*, vol. 1, no. 4, pp. 360–368, 2009.

[53] X. L. Deán-Ben, S. Gottschalk, G. Sela, S. Shoham, and D. Razansky, "Functional optoacoustic neuro-tomography of calcium fluxes in adult zebrafish brain in vivo," *Optics letters*, vol. 42, no. 5, pp. 959–962, 2017.

[54] A. Taruttis, G. M. van Dam, and V. Ntziachristos, "Mesoscopic and macroscopic optoacoustic imaging of cancer," *Cancer research*, vol. 75, no. 8, pp. 1548–1559, 2015.

[55] A. Taruttis, S. Morscher, N. C. Burton, D. Razansky, and V. Ntziachristos, "Fast multispectral optoacoustic tomography (msot) for dynamic imaging of pharmacokinetics and biodistribution in multiple organs," *PloS one*, vol. 7, no. 1, p. e30491, 2012.

[56] C. Tian, Z. Xie, M. L. Fabiilli, and X. Wang, "Imaging and sensing based on dual-pulse nonlinear photoacoustic contrast: a preliminary study on fatty liver," *Optics letters*, vol. 40, no. 10, pp. 2253–2256, 2015.

[57] G. Diot, A. Dima, and V. Ntziachristos, "Multispectral opto-acoustic tomography of exercised muscle oxygenation," *Optics letters*, vol. 40, no. 7, pp. 1496–1499, 2015.

[58] S. Hu, "Listening to the brain with photoacoustics," *IEEE Journal of Selected Topics in Quantum Electronics*, vol. 22, no. 3, pp. 117–126, 2015.

[59] A. Dima, N. C. Burton, and V. Ntziachristos, "Multispectral optoacoustic tomography at 64, 128, and 256 channels," *Journal of biomedical optics*, vol. 19, no. 3, p. 036021, 2014.

[60] A. Rosenthal, D. Razansky, and V. Ntziachristos, "Fast semi-analytical model-based acoustic inversion for quantitative optoacoustic tomography," *IEEE transactions on medical imaging*, vol. 29, no. 6, pp. 1275–1285, 2010.

[61] V. Ntziachristos, M. A. Pleitez, S. Aime, and K. M. Brindle, "Emerging technologies to image tissue metabolism," *Cell metabolism*, 2018.

[62] B. T. Cox, J. G. Laufer, P. C. Beard, and S. R. Arridge, "Quantitative spectroscopic photoacoustic imaging: a review," *Journal of biomedical optics*, vol. 17, no. 6, p. 061202, 2012.

[63] K. Maslov, H. F. Zhang, and L. V. Wang, "Effects of wavelength-dependent fluence attenuation on the noninvasive photoacoustic imaging of hemoglobin oxygen saturation in subcutaneous vasculature in vivo," *Inverse Problems*, vol. 23, no. 6, p. S113, 2007.

[64] S. Tzoumas, A. Nunes, I. Olefir, S. Stangl, P. Symvoulidis, S. Glasl, C. Bayer, G. Multhoff, and V. Ntziachristos, "Eigenspectra optoacoustic tomography achieves quantitative blood oxygenation imaging deep in tissues," *Nature communications*, vol. 7, p. 12121, 2016.

[65] X. Wang, X. Xie, G. Ku, L. V. Wang, and G. Stoica, "Noninvasive imaging of hemoglobin concentration and oxygenation in the rat brain using high-resolution photoacoustic tomography," *Journal of biomedical optics*, vol. 11, no. 2, p. 024015, 2006.

[66] J. Yao and L. V. Wang, "Photoacoustic brain imaging: from microscopic to macroscopic scales," *Neurophotonics*, vol. 1, no. 1, p. 011003, 2014.

[67] J. Yao, L. Wang, J.-M. Yang, K. I. Maslov, T. T. Wong, L. Li, C.-H. Huang, J. Zou, and L. V. Wang, "High-speed label-free functional photoacoustic microscopy of mouse brain in action," *Nature methods*, vol. 12, no. 5, p. 407, 2015.

[68] X. Wang, Y. Pang, G. Ku, G. Stoica, and L. V. Wang, "Three-dimensional laser-induced photoacoustic tomography of mouse brain with the skin and skull intact," *Optics letters*, vol. 28, no. 19, pp. 1739–1741, 2003.

[69] H. Estrada, J. Turner, M. Kneipp, and D. Razansky, "Real-time optoacoustic brain microscopy with hybrid optical and acoustic resolution," *Laser Physics Letters*, vol. 11, no. 4, p. 045601, 2014.

[70] H. K. Eltzschig and P. Carmeliet, "Hypoxia and inflammation," *New England Journal of Medicine*, vol. 364, no. 7, pp. 656–665, 2011.

[71] H. Shi and K. J. Liu, "Cerebral tissue oxygenation and oxidative brain injury during ischemia and reperfusion," *Front Biosci*, vol. 12, no. 1, pp. 1318–1328, 2007.

[72] W. R. Wilson and M. P. Hay, "Targeting hypoxia in cancer therapy," *Nature Reviews Cancer*, vol. 11, no. 6, p. 393, 2011.

[73] A. L. Harris, "Hypoxia—a key regulatory factor in tumour growth," *Nature Reviews Cancer*, vol. 2, no. 1, p. 38, 2002.

[74] J. M. Brown and W. R. Wilson, "Exploiting tumour hypoxia in cancer treatment," *Nature Reviews Cancer*, vol. 4, no. 6, p. 437, 2004.

[75] X. Sun, G. Niu, N. Chan, B. Shen, and X. Chen, "Tumor hypoxia imaging," *Molecular Imaging and Biology*, vol. 13, no. 3, pp. 399–410, 2011.

[76] R. P. Mason, H. Shukla, and P. P. Antich, "In vivo oxygen tension and temperature: simultaneous determination using 19f nmr spectroscopy of perfluorocarbon," *Magnetic resonance in medicine*, vol. 29, no. 3, pp. 296–302, 1993.

[77] R. Frackowiak, G.-L. Lenzi, T. Jones, and J. D. Heather, "Quantitative measurement of regional cerebral blood flow and oxygen metabolism in man using 15o and positron emission tomography: theory, procedure, and normal values," *Journal of computer assisted tomography*, vol. 4, no. 6, pp. 727–736, 1980.

[78] W.-J. Koh, J. S. Rasey, M. L. Evans, J. R. Grierson, T. K. Lewellen, M. M. Graham, K. A. Krohn, and T. W. Griffin, "Imaging of hypoxia in human tumors with [f-18] fluoromisonidazole," *International Journal of Radiation Oncology* Biology* Physics*, vol. 22, no. 1, pp. 199–212, 1992.

[79] R. Urtasun, J. Chapman, J. Raleigh, A. Franko, C. Koch, and thJ, "Binding of 3h-misonidazole to solid human tumors as a measure of tumor hypoxia," *International Journal of Radiation Oncology* Biology* Physics*, vol. 12, no. 7, pp. 1263–1267, 1986.

[80] M. A. Varia, D. P. Calkins-Adams, L. H. Rinker, A. S. Kennedy, D. B. Novotny, W. C. Fowler Jr, and J. A. Raleigh, "Pimonidazole: a novel hypoxia marker for complementary study of tumor hypoxia and cell proliferation in cervical carcinoma," *Gynecologic oncology*, vol. 71, no. 2, pp. 270–277, 1998.

[81] J. M. Wild, S. Fichele, N. Woodhouse, M. N. Paley, L. Kasuboski, and E. J. van Beek, "3d volume-localized po2 measurement in the human lung with 3he mri," *Magnetic Resonance in Medicine: An Official Journal of the International Society for Magnetic Resonance in Medicine*, vol. 53, no. 5, pp. 1055–1064, 2005.

[82] M. C. Krishna, S. Matsumoto, H. Yasui, K. Saito, N. Devasahayam, S. Subramanian, and J. B. Mitchell, "Electron paramagnetic resonance imaging of tumor po2," *Radiation research*, vol. 177, no. 4, pp. 376–386, 2012.

[83] K. Schmidt-Neilsen and J. L. Larimer, "Oxygen dissociation curves of mammalian blood in relation to body size," *American Journal of Physiology-Legacy Content*, vol. 195, no. 2, pp. 424–428, 1958.

[84] T. Christen, P. Bouzat, N. Pannetier, N. Coquery, A. Moisan, B. Lemasson, S. Thomas, E. Grillon, O. Detante, and C. Rémy, "Tissue oxygen saturation mapping with magnetic resonance imaging," *Journal of Cerebral Blood Flow & Metabolism*, vol. 34, no. 9, pp. 1550–1557, 2014.

[85] T. Christen, D. Bolar, and G. Zaharchuk, "Imaging brain oxygenation with mri using blood oxygenation approaches: methods, validation, and clinical applications," *American journal of neuroradiology*, vol. 34, no. 6, pp. 1113–1123, 2013.

[86] L. C. Krishnamurthy, P. Liu, Y. Ge, and H. Lu, "Vessel-specific quantification of blood oxygenation with t2-relaxation-under-phase-contrast mri," *Magnetic resonance in medicine*, vol. 71, no. 3, pp. 978–989, 2014.

[87] K. K. Tremper, "Pulse oximetry," *Chest*, vol. 95, no. 4, pp. 713–715, 1989.

[88] J. Q. Brown, L. G. Wilke, J. Geradts, S. A. Kennedy, G. M. Palmer, and N. Ramanujam, "Quantitative optical spectroscopy: a robust tool for direct measurement of breast cancer vascular oxygenation and total hemoglobin content in vivo," *Cancer research*, vol. 69, no. 7, pp. 2919–2926, 2009.

[89] T. Scheeren, P. Schober, and L. Schwarte, "Monitoring tissue oxygenation by near infrared spectroscopy (nirs): background and current applications," *Journal of clinical monitoring and computing*, vol. 26, no. 4, pp. 279–287, 2012.

[90] A. D. Estrada, A. Ponticorvo, T. N. Ford, and A. K. Dunn, "Microvascular oxygen quantification using two-photon microscopy," *Optics letters*, vol. 33, no. 10, pp. 1038–1040, 2008.

[91] H. F. Zhang, K. Maslov, M. Sivaramakrishnan, G. Stoica, and L. V. Wang, "Imaging of hemoglobin oxygen saturation variations in single vessels in vivo using photoacoustic microscopy," *Applied physics letters*, vol. 90, no. 5, p. 053901, 2007.

[92] N. K. Logothetis, "What we can do and what we cannot do with fmri," *Nature*, vol. 453, no. 7197, p. 869, 2008.

[93] R. Cabeza and L. Nyberg, "Imaging cognition: An empirical review of pet studies with normal subjects," *Journal of cognitive neuroscience*, vol. 9, no. 1, pp. 1–26, 1997.

[94] E. Hoeffner, S. Mukherji, A. Srinivasan, and D. Quint, "Neuroradiology back to the future: brain imaging," *American Journal of Neuroradiology*, vol. 33, no. 1, pp. 5–11, 2012.

[95] G. Gratton, A. M. Chiarelli, and M. Fabiani, "From brain to blood vessels and back: a noninvasive optical imaging approach," *Neurophotonics*, vol. 4, no. 3, p. 031208, 2017.

[96] K. Svoboda and R. Yasuda, "Principles of two-photon excitation microscopy and its applications to neuroscience," *Neuron*, vol. 50, no. 6, pp. 823–839, 2006.

[97] D. G. Ouzounov, T. Wang, M. Wang, D. D. Feng, N. G. Horton, J. C. Cruz-Hernández, Y.-T. Cheng, J. Reimer, A. S. Tolias, and N. Nishimura, "In vivo three-photon imaging of activity of gcamp6-labeled neurons deep in intact mouse brain," *Nature methods*, vol. 14, no. 4, p. 388, 2017.

[98] H. Yu, B. J. Farley, D. Z. Jin, and M. Sur, "The coordinated mapping of visual space and response features in visual cortex," *Neuron*, vol. 47, no. 2, pp. 267–280, 2005.

[99] M. A. Busche, G. Eichhoff, H. Adelsberger, D. Abramowski, K.-H. Wiederhold, C. Haass, M. Staufenbiel, A. Konnerth, and O. Garaschuk, "Clusters of hyperactive neurons near amyloid plaques in a mouse model of alzheimer's disease," *Science*, vol. 321, no. 5896, pp. 1686–1689, 2008.

[100] X. Chen, U. Leischner, N. L. Rochefort, I. Nelken, and A. Konnerth, "Functional mapping of single spines in cortical neurons in vivo," *Nature*, vol. 475, no. 7357, p. 501, 2011.

[101] C. Grienberger and A. Konnerth, "Imaging calcium in neurons," *Neuron*, vol. 73, no. 5, pp. 862–885, 2012.

[102] I. Ferezou, S. Bolea, and C. C. Petersen, "Visualizing the cortical representation of whisker touch: voltage-sensitive dye imaging in freely moving mice," *Neuron*, vol. 50, no. 4, pp. 617–629, 2006.

[103] S. Chemla and F. Chavane, "Voltage-sensitive dye imaging: technique review and models," *Journal of Physiology-Paris*, vol. 104, no. 1-2, pp. 40–50, 2010.

[104] A. Holtmaat, T. Bonhoeffer, D. K. Chow, J. Chuckowree, V. De Paola, S. B. Hofer, M. Hübener, T. Keck, G. Knott, and W.-C. A. Lee, "Long-term, high-resolution imaging in the mouse neocortex through a chronic cranial window," *Nature protocols*, vol. 4, no. 8, p. 1128, 2009.

[105] H.-T. Xu, F. Pan, G. Yang, and W.-B. Gan, "Choice of cranial window type for in vivo imaging affects dendritic spine turnover in the cortex," *Nature neuroscience*, vol. 10, no. 5, p. 549, 2007.

[106] E. W. Stein, K. I. Maslov, and L. V. Wang, "Noninvasive, in vivo imaging of blood-oxygenation dynamics within the mouse brain using photoacoustic microscopy," *Journal of biomedical optics*, vol. 14, no. 2, p. 020502, 2009.

[107] W. J. Freeman, "Mesoscopic neurodynamics: from neuron to brain," *Journal of Physiology-Paris*, vol. 94, no. 5-6, pp. 303–322, 2000.

[108] N. J. Sofroniew, D. Flickinger, J. King, and K. Svoboda, "A large field of view two-photon mesoscope with subcellular resolution for in vivo imaging," *Elife*, vol. 5, p. e14472, 2016.

[109] S. V. Ovsepian, I. Olefir, G. Westmeyer, D. Razansky, and V. Ntziachristos, "Pushing the boundaries of neuroimaging with optoacoustics," *Neuron*, vol. 96, no. 5, pp. 966–988, 2017.

[110] M. Fukushima, Z. C. Chao, and N. Fujii, "Studying brain functions with mesoscopic measurements: Advances in electrocorticography for non-human primates," *Current opinion in neurobiology*, vol. 32, pp. 124–131, 2015.

[111] A. A. Fingelkurts, A. A. Fingelkurts, and S. Kähkönen, "Functional connectivity in the brain—is it an elusive concept?," *Neuroscience & Biobehavioral Reviews*, vol. 28, no. 8, pp. 827–836, 2005.

[112] V. Markounikau, C. Igel, A. Grinvald, and D. Jancke, "A dynamic neural field model of mesoscopic cortical activity captured with voltage-sensitive dye imaging," *PLoS computational biology*, vol. 6, no. 9, p. e1000919, 2010.

[113] M. Bakar, H. S. Kirshner, and R. T. Wertz, "Crossed aphasia: functional brain imaging with pet or spect," *Archives of Neurology*, vol. 53, no. 10, pp. 1026–1032, 1996.

[114] J. A. Filosa and V. M. Blanco, "Neurovascular coupling in the mammalian brain," *Experimental physiology*, vol. 92, no. 4, pp. 641–646, 2007.

[115] M. P. Van Den Heuvel and H. E. H. Pol, "Exploring the brain network: a review on resting-state fmri functional connectivity," *European neuropsychopharmacology*, vol. 20, no. 8, pp. 519–534, 2010.

[116] C. S. Hubbard, S. A. Khan, S. Xu, M. Cha, R. Masri, and D. A. Seminowicz, "Behavioral, metabolic and functional brain changes in a rat model of chronic neuropathic pain: a longitudinal mri study," *Neuroimage*, vol. 107, pp. 333–344, 2015.

[117] E. R. Muir, K. Biju, L. Cong, W. E. Rogers, E. T. Hernandez, T. Q. Duong, and R. A. Clark, "Functional mri of the mouse olfactory system," *Neuroscience Letters*, vol. 704, pp. 57–61, 2019.

[118] S. V. Ovsepian, I. Olefir, and V. Ntziachristos, "Advances in optoacoustic neurotomography of animal models," *Trends in biotechnology*, 2019.

[119] C. Martin, J. Martindale, J. Berwick, and J. Mayhew, "Investigating neural–hemodynamic coupling and the hemodynamic response function in the awake rat," *Neuroimage*, vol. 32, no. 1, pp. 33–48, 2006.

[120] A. Devor, A. K. Dunn, M. L. Andermann, I. Ulbert, D. A. Boas, and A. M. Dale, "Coupling of total hemoglobin concentration, oxygenation, and neural activity in rat somatosensory cortex," *Neuron*, vol. 39, no. 2, pp. 353–359, 2003.

[121] A. K. Dunn, A. Devor, H. Bolay, M. L. Andermann, M. A. Moskowitz, A. M. Dale, and D. A. Boas, "Simultaneous imaging of total cerebral hemoglobin concentration, oxygenation, and blood flow during functional activation," *Optics letters*, vol. 28, no. 1, pp. 28–30, 2003.

[122] E. M. Hillman, "Coupling mechanism and significance of the bold signal: a status report," *Annual review of neuroscience*, vol. 37, pp. 161–181, 2014.

[123] S. Gottschalk, T. Felix Fehm, X. Luís Deán-Ben, and D. Razansky, "Noninvasive real-time visualization of multiple cerebral hemodynamic parameters in whole mouse brains using five-dimensional optoacoustic tomography," *Journal of Cerebral Blood Flow & Metabolism*, vol. 35, no. 4, pp. 531–535, 2015.

[124] N. C. Burton, M. Patel, S. Morscher, W. H. Driessen, J. Claussen, N. Beziere, T. Jetzfellner, A. Taruttis, D. Razansky, and B. Bednar, "Multispectral opto-acoustic tomography (msot) of the brain and glioblastoma characterization," *Neuroimage*, vol. 65, pp. 522–528, 2013.

[125] X. Wang, Y. Pang, G. Ku, X. Xie, G. Stoica, and L. V. Wang, "Noninvasive laser-induced photoacoustic tomography for structural and functional in vivo imaging of the brain," *Nature biotechnology*, vol. 21, no. 7, p. 803, 2003.

[126] M. Nasiriavanaki, J. Xia, H. Wan, A. Q. Bauer, J. P. Culver, and L. V. Wang, "High-resolution photoacoustic tomography of resting-state functional connectivity in the mouse brain," *Proceedings of the National Academy of Sciences*, vol. 111, no. 1, pp. 21–26, 2014.

[127] L. V. Wang and H.-i. Wu, *Biomedical optics: principles and imaging*. John Wiley & Sons, 2012.

[128] J. R. Lorenzo, *Principles of diffuse light propagation: light propagation in tissues with applications in biology and medicine*. World Scientific, 2012.

[129] S. Arridge, M. Schweiger, M. Hiraoka, and D. Delpy, "A finite element approach for modeling photon transport in tissue," *Medical physics*, vol. 20, no. 2, pp. 299–309, 1993.

[130] B. T. Cox, S. R. Arridge, and P. C. Beard, "Estimating chromophore distributions from multiwavelength photoacoustic images," *JOSA A*, vol. 26, no. 2, pp. 443–455, 2009.

[131] B. E. Treeby, E. Z. Zhang, and B. T. Cox, "Photoacoustic tomography in absorbing acoustic media using time reversal," *Inverse Problems*, vol. 26, no. 11, p. 115003, 2010.

[132] S. Schoeder, K. Kormann, W. A. Wall, and M. Kronbichler, "Efficient explicit time stepping of high order discontinuous galerkin schemes for waves," *SIAM Journal on Scientific Computing*, vol. 40, no. 6, pp. C803–C826, 2018.

[133] A. Rosenthal, V. Ntziachristos, and D. Razansky, "Acoustic inversion in optoacoustic tomography: A review," *Current medical imaging reviews*, vol. 9, no. 4, pp. 318–336, 2013.

[134] C. G. Hoelen and F. F. de Mul, "Image reconstruction for photoacoustic scanning of tissue structures," *Applied Optics*, vol. 39, no. 31, pp. 5872–5883, 2000.

[135] C. Hoelen, F. De Mul, R. Pongers, and A. Dekker, "Three-dimensional photoacoustic imaging of blood vessels in tissue," *Optics letters*, vol. 23, no. 8, pp. 648–650, 1998.

[136] M. Xu and L. V. Wang, "Universal back-projection algorithm for photoacoustic computed tomography," *Physical Review E*, vol. 71, no. 1, p. 016706, 2005.

[137] Y. Xu and L. V. Wang, "Time reversal and its application to tomography with diffracting sources," *Physical review letters*, vol. 92, no. 3, p. 033902, 2004.

[138] P. Burgholzer, G. J. Matt, M. Haltmeier, and G. Paltauf, "Exact and approximative imaging methods for photoacoustic tomography using an arbitrary detection surface," *Physical Review E*, vol. 75, no. 4, p. 046706, 2007.

[139] B. T. Cox and B. E. Treeby, "Artifact trapping during time reversal photoacoustic imaging for acoustically heterogeneous media," *IEEE transactions on medical imaging*, vol. 29, no. 2, pp. 387–396, 2009.

[140] Y. Hristova, P. Kuchment, and L. Nguyen, "Reconstruction and time reversal in thermoacoustic tomography in acoustically homogeneous and inhomogeneous media," *Inverse Problems*, vol. 24, no. 5, p. 055006, 2008.

[141] D. Calvetti, S. Morigi, L. Reichel, and F. Sgallari, "Tikhonov regularization and the l-curve for large discrete ill-posed problems," *Journal of computational and applied mathematics*, vol. 123, no. 1-2, pp. 423–446, 2000.

[142] Y. Han, S. Tzoumas, A. Nunes, V. Ntziachristos, and A. Rosenthal, "Sparsity-based acoustic inversion in cross-sectional multiscale optoacoustic imaging," *Medical physics*, vol. 42, no. 9, pp. 5444–5452, 2015.

[143] A. Rosenthal, V. Ntziachristos, and D. Razansky, "Model-based optoacoustic inversion with arbitrary-shape detectors," *Medical physics*, vol. 38, no. 7, pp. 4285–4295, 2011.

[144] X. L. Dean-Ben, V. Ntziachristos, and D. Razansky, "Acceleration of optoacoustic model-based reconstruction using angular image discretization," *IEEE Transactions on medical imaging*, vol. 31, no. 5, pp. 1154–1162, 2012.

[145] A. Buehler, A. Rosenthal, T. Jetzfellner, A. Dima, D. Razansky, and V. Ntziachristos, "Model-based optoacoustic inversions with incomplete projection data," *Medical physics*, vol. 38, no. 3, pp. 1694–1704, 2011.

[146] A. Rosenthal, V. Ntziachristos, and D. Razansky, "Optoacoustic methods for frequency calibration of ultrasonic sensors," *IEEE transactions on ultrasonics, ferroelectrics, and frequency control*, vol. 58, no. 2, pp. 316–326, 2011.

[147] K. Wang, S. A. Ermilov, R. Su, H.-P. Brecht, A. A. Oraevsky, and M. A. Anastasio, "An imaging model incorporating ultrasonic transducer properties for three-dimensional optoacoustic tomography," *IEEE transactions on medical imaging*, vol. 30, no. 2, pp. 203–214, 2010.

[148] X. L. Dean-Ben, R. Ma, D. Razansky, and V. Ntziachristos, "Statistical approach for optoacoustic image reconstruction in the presence of strong acoustic heterogeneities," *IEEE transactions on medical imaging*, vol. 30, no. 2, pp. 401–408, 2010.

[149] K. B. Chowdhury, J. Prakash, A. Karlas, D. Jüstel, and V. Ntziachristos, "A synthetic total impulse response characterization method for correction of hand-held optoacoustic images," *IEEE Transactions on Medical Imaging*, 2020.

[150] H. Yang, I. Olefir, S. Tzoumas, and V. Ntziachristos, "Synthetic data framework to estimate the minimum detectable concentration of contrast agents for multispectral optoacoustic imaging of small animals," *Journal of biophotonics*, p. e201900021, 2019.

[151] B. Cox, J. Laufer, and P. Beard, "Quantitative photoacoustic image reconstruction using fluence dependent chromophores," *Biomedical optics express*, vol. 1, no. 1, pp. 201–208, 2010.

[152] X. L. Deán-Ben, A. C. Stiel, Y. Jiang, V. Ntziachristos, G. G. Westmeyer, and D. Razansky, "Light fluence normalization in turbid tissues via temporally unmixed multispectral optoacoustic tomography," *Optics letters*, vol. 40, no. 20, pp. 4691–4694, 2015.

[153] D. Razansky and V. Ntziachristos, "Hybrid photoacoustic fluorescence molecular tomography using finite-element-based inversion," *Medical physics*, vol. 34, no. 11, pp. 4293–4301, 2007.

[154] D. Razansky, M. Distel, C. Vinegoni, R. Ma, N. Perrimon, R. W. Köster, and V. Ntziachristos, "Multispectral opto-acoustic tomography of deep-seated fluorescent proteins in vivo," *Nature photonics*, vol. 3, no. 7, p. 412, 2009.

[155] R. Ma, A. Taruttis, V. Ntziachristos, and D. Razansky, "Multispectral optoacoustic tomography (msot) scanner for whole-body small animal imaging," *Optics express*, vol. 17, no. 24, pp. 21414–21426, 2009.

[156] J. Ripoll and V. Ntziachristos, "Quantitative point source photoacoustic inversion formulas for scattering and absorbing media," *Physical Review E*, vol. 71, no. 3, p. 031912, 2005.

[157] M. Sivaramakrishnan, K. Maslov, H. F. Zhang, G. Stoica, and L. V. Wang, "Limitations of quantitative photoacoustic measurements of blood oxygenation in small vessels," *Physics in Medicine & Biology*, vol. 52, no. 5, p. 1349, 2007.

[158] T. Tarvainen, B. T. Cox, J. Kaipio, and S. R. Arridge, "Reconstructing absorption and scattering distributions in quantitative photoacoustic tomography," *Inverse Problems*, vol. 28, no. 8, p. 084009, 2012.

[159] L. Yao, Y. Sun, and H. Jiang, "Quantitative photoacoustic tomography based on the radiative transfer equation," *Optics letters*, vol. 34, no. 12, pp. 1765–1767, 2009.

[160] B. Cox, T. Tarvainen, and S. Arridge, "Multiple illumination quantitative photoacoustic tomography using transport and diffusion models," *Tomography and Inverse Transport Theory, G. Bal, D. Finch, P. Kuchment, J. Schotland, P. Stefanov, and G. Uhlmann, eds*, vol. 559, pp. 1–12, 2011.

[161] A. V. Mamonov and K. Ren, "Quantitative photoacoustic imaging in radiative transport regime," *arXiv preprint arXiv:1207.4664*, 2012.

[162] T. Saratoon, T. Tarvainen, B. Cox, and S. Arridge, "A gradient-based method for quantitative photoacoustic tomography using the radiative transfer equation," *Inverse Problems*, vol. 29, no. 7, p. 075006, 2013.

[163] T. Tarvainen, A. Pulkkinen, B. T. Cox, J. P. Kaipio, and S. R. Arridge, "Bayesian image reconstruction in quantitative photoacoustic tomography," *IEEE transactions on medical imaging*, vol. 32, no. 12, pp. 2287–2298, 2013.

[164] A. Pulkkinen, B. T. Cox, S. R. Arridge, J. P. Kaipio, and T. Tarvainen, "A bayesian approach to spectral quantitative photoacoustic tomography," *Inverse Problems*, vol. 30, no. 6, p. 065012, 2014.

[165] A. Pulkkinena, B. T. Coxb, S. R. Arridgec, J. P. Kaipioa, and T. Tarvainena, "Bayesian parameter estimation in spectral quantitative photoacoustic tomography," in *Proc. of SPIE Vol*, vol. 9708, pp. 97081G–1.

[166] B. Banerjee, S. Bagchi, R. M. Vasu, and D. Roy, "Quantitative photoacoustic tomography from boundary pressure measurements: noniterative recovery of optical absorption coefficient from the reconstructed absorbed energy map," *JOSA A*, vol. 25, no. 9, pp. 2347–2356, 2008.

[167] O. Senlik, *Custom Silicon Annular Photodiode Arrays for Spatially Resolved Diffuse Reflectance Spectroscopy*. Thesis, 2016.

[168] G. Bal and G. Uhlmann, "Inverse diffusion theory of photoacoustics," *Inverse Problems*, vol. 26, no. 8, p. 085010, 2010.

[169] G. Bal and K. Ren, "Multi-source quantitative photoacoustic tomography in a diffusive regime," *Inverse Problems*, vol. 27, no. 7, p. 075003, 2011.

[170] H. Gao, H. Zhao, and S. Osher, "Bregman methods in quantitative photoacoustic tomography," *Cam Report*, vol. 10, p. 42, 2010.

[171] A. Pulkkinen, B. T. Cox, S. R. Arridge, J. P. Kaipio, and T. Tarvainen, "Bayesian parameter estimation in spectral quantitative photoacoustic tomography," in *Photons Plus Ultrasound: Imaging and Sensing 2016*, vol. 9708, p. 97081G, International Society for Optics and Photonics.

[172] S. Schoeder, I. Olefir, M. Kronbichler, V. Ntziachristos, and W. Wall, "Optoacoustic image reconstruction: the full inverse problem with variable bases," *Proceedings of the Royal Society A*, vol. 474, no. 2219, p. 20180369, 2018.

[173] B. T. Cox, S. R. Arridge, K. P. Köstli, and P. C. Beard, "Two-dimensional quantitative photoacoustic image reconstruction of absorption distributions in scattering media by use of a simple iterative method," *Applied Optics*, vol. 45, no. 8, pp. 1866–1875, 2006.

[174] A. Rosenthal, D. Razansky, and V. Ntziachristos, "Quantitative optoacoustic signal extraction using sparse signal representation," *IEEE transactions on medical imaging*, vol. 28, no. 12, pp. 1997–2006, 2009.

[175] M.-L. Li, J.-T. Oh, X. Xie, G. Ku, W. Wang, C. Li, G. Lungu, G. Stoica, and L. V. Wang, "Simultaneous molecular and hypoxia imaging of brain tumors in vivo using spectroscopic photoacoustic tomography," *Proceedings of the IEEE*, vol. 96, no. 3, pp. 481–489, 2008.

[176] E. Herzog, A. Taruttis, N. Beziere, A. A. Lutich, D. Razansky, and V. Ntziachristos, "Optical imaging of cancer heterogeneity with multispectral optoacoustic tomography," *Radiology*, vol. 263, no. 2, pp. 461–468, 2012.

[177] H. Rue and L. Held, *Gaussian Markov random fields: theory and applications*. Chapman and Hall/CRC, 2005.

[178] A. Blake, P. Kohli, and C. Rother, *Markov random fields for vision and image processing*. Mit Press, 2011.

[179] C. Li, A. Aguirre, J. K. Gamelin, A. Maurudis, Q. Zhu, and L. V. Wang, "Real-time photoa-coustic tomography of cortical hemodynamics in small animals," *Journal of biomedical optics*, vol. 15, no. 1, p. 010509, 2010.

[180] J. Yao, J. Xia, K. I. Maslov, M. Nasiriavanaki, V. Tsytsarev, A. V. Demchenko, and L. V. Wang, "Noninvasive photoacoustic computed tomography of mouse brain metabolism in vivo," *Neuroimage*, vol. 64, pp. 257–266, 2013.

[181] M. Kneipp, J. Turner, H. Estrada, J. Rebling, S. Shoham, and D. Razansky, "Effects of the murine skull in optoacoustic brain microscopy," *Journal of biophotonics*, vol. 9, no. 1-2, pp. 117–123, 2016.

[182] H. Estrada, J. Rebling, J. Turner, and D. Razansky, "Broadband acoustic properties of a murine skull," *Physics in Medicine & Biology*, vol. 61, no. 5, p. 1932, 2016.

[183] J. C. Rajapakse, F. Kruggel, J. M. Maisog, and D. Yves von Cramon, "Modeling hemodynamic response for analysis of functional mri time-series," *Human brain mapping*, vol. 6, no. 4, pp. 283–300, 1998.

[184] S. Tzoumas, A. Kravtsiv, Y. Gao, A. Buehler, and V. Ntziachristos, "Statistical molecular target detection framework for multispectral optoacoustic tomography," *IEEE transactions on medical imaging*, vol. 35, no. 12, pp. 2534–2545, 2016.

[185] E. Zhang, J. Laufer, R. Pedley, and P. Beard, "In vivo high-resolution 3d photoacoustic imaging of superficial vascular anatomy," *Physics in Medicine & Biology*, vol. 54, no. 4, p. 1035, 2009.

[186] J. Gateau, A. Chekkoury, and V. Ntziachristos, "High-resolution optoacoustic mesoscopy with a 24 mhz multidetector translate-rotate scanner," *Journal of biomedical optics*, vol. 18, no. 10, p. 106005, 2013.

[187] X. L. Deán-Ben and D. Razansky, "Adding fifth dimension to optoacoustic imaging: volumetric time-resolved spectrally enriched tomography," *Light: Science & Applications*, vol. 3, no. 1, p. e137, 2014.

[188] E. Zhang, J. Laufer, and P. Beard, "Backward-mode multiwavelength photoacoustic scan-ner using a planar fabry-perot polymer film ultrasound sensor for high-resolution three-dimensional imaging of biological tissues," *Applied optics*, vol. 47, no. 4, pp. 561–577, 2008.

[189] I. Olefir, S. Tzoumas, H. Yang, and V. Ntziachristos, "A bayesian approach to eigenspectra optoacoustic tomography," *IEEE transactions on medical imaging*, vol. 37, no. 9, pp. 2070–2079, 2018.

[190] I. Olefir, E. Merčep, N. C. Burton, S. V. Ovsepian, and V. Ntziachristos, "Hybrid multispectral optoacoustic and ultrasound tomography for morphological and physiological brain imaging," *Journal of biomedical optics*, vol. 21, no. 8, p. 086005, 2016.

[191] I. Olefir, A. Ghazaryan, H. Yang, J. Malekzadeh-Najafabadi, S. Glasl, P. Symvoulidis, V. B. O'Leary, G. Sergiadis, V. Ntziachristos, and S. V. Ovsepian, "Spatial and spectral mapping and decomposition of neural dynamics and organization of the mouse brain with multispectral optoacoustic tomography," *Cell reports*, vol. 26, no. 10, pp. 2833–2846. e3, 2019.

[192] I. Olefir, S. Tzoumas, C. Restivo, P. Mohajerani, L. Xing, and V. Ntziachristos, "Deep learn-ing based spectral unmixing for optoacoustic imaging of tissue oxygen saturation," *IEEE Transactions on Medical Imaging*, pp. 1–1, 2020.

Appendix A

Publication: A Bayesian approach to eigenspectra optoacoustic tomography

A Bayesian Approach to Eigenspectra Optoacoustic Tomography

Ivan Olefir[ID], Stratis Tzoumas, Hong Yang, and Vasilis Ntziachristos

Abstract—The quantification of hemoglobin oxygen saturation (sO_2) with multispectral optoacoustic (OA) (photoacoustic) tomography (MSOT) is a complex spectral unmixing problem, since the OA spectra of hemoglobin are modified with tissue depth due to depth (location) and wavelength dependencies of optical fluence in tissue. In a recent work, a method termed eigenspectra MSOT (eMSOT) was proposed for addressing the dependence of spectra on fluence and quantifying blood sO_2 in deep tissue. While eMSOT offers enhanced sO_2 quantification accuracy over conventional unmixing methods, its performance may be compromised by noise and image reconstruction artifacts. In this paper, we propose a novel Bayesian method to improve eMSOT performance in noisy environments. We introduce a spectral reliability map, i.e., a method that can estimate the level of noise superimposed onto the recorded OA spectra. Using this noise estimate, we formulate eMSOT as a Bayesian inverse problem where the inversion constraints are based on probabilistic graphical models. Results based on numerical simulations indicate that the proposed method offers improved accuracy and robustness under high noise levels due the adaptive nature of the Bayesian method.

Index Terms—Optoacoustic/photoacoustic imaging, multispectral optoacoustic tomography, photoacoustic tomography, Bayesian methods, oxygen saturation, spectral unmixing.

I. Introduction

TISSUE blood oxygenation is a significant physiological marker of tissue viability, metabolism, hypoxia [1] and even neuronal activation [2]. By unmixing the absorption spectra of oxygenated and deoxygenated hemoglobin, multi-spectral optoacoustic tomography (MSOT) can produce label-free images of blood oxygenation (sO_2) of tissue *in vivo*, at high spatial and temporal resolution [3], [4]. However, accurate quantification of blood sO_2 in deep tissue in MSOT

presents a complex spectral unmixing problem, since the measured optoacoustic (OA) spectrum from a tissue volume element (voxel) depends not only on the local concentration of different photoabsorbers but also on the wavelength-dependent optical fluence reaching that voxel. This effect is known as *spectral coloring* [5]–[7] or *spectral corruption*.

In recent work [8], a novel method termed eigenspectra MSOT (eMSOT) was proposed for accounting for spectral coloring and quantitatively estimating blood sO_2 deep within tissue in the near-infrared (NIR) region. The method is based on the observation that any fluence spectrum recorded in tissue in NIR can be modelled based on four base spectra (eigenspectra), assuming oxygenated and deoxygenated hemoglobin as the two prominent NIR absorbers. The eigenspectra were derived by applying principal component analysis (PCA) to a set of simulated optical fluence spectra, which served as the training dataset. Modelling the light fluence spectrum as a linear combination of the four eigenspectra converts the fluence correction problem from the spatial domain to the spectral domain. Then the sO_2 MSOT estimation problem can be written as a spectral unmixing problem that is dependent on the scalar weights of the linearly combined eigenspectra but independent of the tissue's optical properties. By accounting for the effects of *spectral coloring*, eMSOT has been shown to offer substantially enhanced sO_2 estimation accuracy over the linear unmixing technique in simulations, phantoms and animal measurements [8], especially as tissue depth increases.

In addition to spectral coloring, optoacoustic spectra may also be corrupted due to noise and artifacts present in the images [9], compromising eMSOT convergence and accurate sO_2 estimation. In this work, we aimed to improve the accuracy of sO_2 quantification by eMSOT under noise conditions. To achieve this aim, we formulate the eMSOT sO_2 quantification problem as a Bayesian inverse problem where the noise in the recorded spectra is taken into account. Noise estimation is carried out by considering a new model that describes the recorded optoacoustic spectra and captures their variability due to both light fluence and hemoglobin absorption. Based on this model of recorded optoacoustic spectra we introduce the *spectral reliability map (SRM)* as an estimator of the noise in the measurements. In the SRM-enabled Bayesian eMSOT (BeMSOT), the original inversion constraints are modeled as prior probability distributions and implemented using probabilistic graphical models. We show how the parameters of the prior probability distributions affect the accuracy of sO_2 quantification by BeMSOT and optimize

their values using simulated data. Results based on simulations indicate that the proposed method offers more robust sO$_2$ quantification than eMSOT in the presence of high and non-uniform noise levels, due to the ability of the Bayesian formulation to reduce the impact of unreliable data on algorithm performance.

In the following, we describe the methodology and findings by providing the physical background of optoacoustics and theoretical background of eMSOT (Section II), formulating the eMSOT algorithm as a Bayesian Maximum a Posteriori (MAP) estimation problem (Section III-A), and introducing the novel SRM noise estimator (Section III-B). Simulations are described in Section III-C. In Section IV (Results), we assess the performance of the noise estimation technique and BeMSOT. Finally, Section V (Discussion) places the findings in the perspective of future challenges and developments.

II. BACKGROUND

A. Physics of Optoacoustics. Forward and Inverse Problems

In MSOT, a nanosecond laser pulse illuminates tissue at multiple wavelengths. Due to thermoelastic expansion caused by light absorption, this results in an *initial pressure rise* (IPR) p which relates to the fluence Φ and tissue absorption coefficient μ_a as follows [10]:

$$p(\mathbf{r}, \lambda) = \Gamma(\mathbf{r})\Phi(\mathbf{r}, \lambda)\mu_a(\mathbf{r}, \lambda), \qquad (1)$$

where $\mathbf{r}$ denotes the spatial coordinates, λ is the illumination wavelength, p is the space- and wavelength-dependent initial pressure and Γ is the spatially varying Grüneisen parameter. The generated ultrasound waves subsequently exit the tissue and propagate towards the acoustic detectors.

Due to the hybrid nature of optoacoustics, the forward and inverse problems are two-fold:

- *Optical forward problem* – compute Φ when the optical properties of the medium and illumination are known.
- *Acoustic forward problem* – compute the time-dependent pressure signals $\mathbf{s}_{pr}$ on the detectors around the sample given the initial pressure rise $\mathbf{p}$.
- *Acoustic inverse problem* – reconstruct optoacoustic images $p(\mathbf{r}, \lambda)$ given the detector signals $\mathbf{s}_{pr}$.
- *Optical inverse problem* – determine the spatial distribution of the optical properties within the sample given the map of the initial pressure rise.

Accounting for $\Phi(\mathbf{r}, \lambda)$ and computing $\mu_a(\mathbf{r}, \lambda)$, or solving the *optical inverse problem*, is the key challenge in quantitative optoacoustics.

A multitude of approaches to solving the inverse optical problem have been considered [11], [22]. Typically, the solution is computed by inverting a discretized optical forward model under certain assumptions (e.g. some of the optical parameters being known). The forward model is governed by either the Radiative Transfer Equation [11], [18], [19], [21], [22] or less computationally

expensive Diffusion Approximation [11]–[14], [16], [17], [19]:

$$-\nabla\kappa(\mathbf{r}, \lambda)\nabla\Phi(\mathbf{r}, \lambda) + \mu_a(\mathbf{r}, \lambda)\Phi(\mathbf{r}, \lambda) = 0, \quad r \in \Omega,$$

$$\xi_d\Phi(\mathbf{r}, \lambda) + \frac{1}{2}A\kappa(\mathbf{r}, \lambda)\nabla\Phi(\mathbf{r}, \lambda) \cdot v = s, r \in \partial\Omega, \quad (2)$$

where Ω is the tissue region, $\partial\Omega$ is the tissue boundary, $\kappa(\mathbf{r}, \lambda) = \left(d\left(\mu_a(\mathbf{r}, \lambda) + \mu'_s(\mathbf{r}, \lambda)\right)\right)^{-1}$ is the diffusion coefficient, d is the dimensionality of the domain, μ'_s is the reduced scattering coefficient, ξ_d is a dimensionality-dependent parameter, A describes reflectivity and s is the illumination pattern. The inversion may be performed for one as well as several wavelengths simultaneously.

Such approaches, although theoretically accurate, are however limited by several factors [19]. First, since the optical fluence is modeled accurately in the whole domain, the knowledge of the initial pressure rise in the illuminated volume is required, i.e. accurate image reconstruction is an important prerequisite for the described methods. Such reconstruction is often not achievable, and various artifacts as well as spatially inhomogeneous noise are typically present in the OA images. Second, due to the inverse problem being physics-driven, the absolute values of the absorbed energy density $\Phi(\mathbf{r}, \lambda)\mu_a(\mathbf{r}, \lambda)$ are required, which necessitates calibration for various scaling factors including the Grüneisen parameter as well as knowledge of accurate tissue boundary and illumination. Finally, due to a large number of unknowns, the resulting computational complexity of the problem is very high. The mentioned challenges effectively limit application of such methods in the analysis of experimental data.

In contrast, eMSOT presents a simpler, although less versatile, alternative to the aforementioned approaches. It utilizes a linear spectral model of fluence (the eigenspectra model), converts the inverse problem to lie in the spectral domain and allows local fluence correction while avoiding modelling light transport in the inversion step. Instead of computing the distributions of the optical properties within the sample, eMSOT directly quantifies sO$_2$, making its application to experimental data possible [8].

B. The Eigenspectra Model

The Eigenspectra model is derived based on the assumption that oxygenated and deoxygenated hemoglobin are the main absorbers in tissue in the NIR region (700-900 nm) and that the influence of other absorbers can be neglected. Thus, Eq. 1 can be rewritten as:

$$p(\mathbf{r}, \lambda) = C(\mathbf{r})\Phi'(\mathbf{r}, \lambda)$$
$$\cdot (c_{HHb}(\mathbf{r})\varepsilon_{HHb}(\lambda) + c_{HbO2}(\mathbf{r})\varepsilon_{HbO2}(\lambda))$$
$$= \Phi'(\mathbf{r}, \lambda) \cdot \left(c'_{HHb}(\mathbf{r})\varepsilon_{HHb}(\lambda) + c'_{HbO2}(\mathbf{r})\varepsilon_{HbO2}(\lambda)\right).$$
$$(3)$$

where $\Phi'(\mathbf{r}, \lambda) = \Phi(\mathbf{r}, \lambda)/\|\Phi(\mathbf{r})\|_2$ is the normalized fluence spectrum; $\|\Phi(\mathbf{r})\|_2$ is the l_2-norm of the optical fluence spectrum at position $\mathbf{r}$, $C(\mathbf{r}) = \Gamma(\mathbf{r})\|\Phi(\mathbf{r})\|_2$; c_{HHb} and c_{HbO2} are the concentrations of deoxy- and oxyhemoglobin, respectively; $c'_{HHb} = C \cdot c_{HHb}$ and $c'_{HbO2} = C \cdot c_{HbO2}$ are relative concentrations; and ε_{HHb} and ε_{HbO2} are the corresponding wavelength-dependent absorption coefficients. To exclude

$C(\mathbf{r})$ from consideration, eMSOT operates on normalized initial pressure spectra (or simply *normalized OA spectra*), i.e. $\mathbf{p}'(\mathbf{r}) = \mathbf{p}(\mathbf{r})/\|\mathbf{p}(\mathbf{r})\|_2$. If the relative concentrations can be found, sO2 can be computed as:

$$sO_2 = \frac{c_{\text{HbO2}}}{c_{\text{HbO2}} + c_{\text{HHb}}} = \frac{c'_{\text{HbO2}}}{c'_{\text{HbO2}} + c'_{\text{HHb}}}. \quad (4)$$

In eMSOT, $\Phi'(\mathbf{r}, \lambda)$ is modeled as a linear function of four base spectra derived from PCA of a training dataset of simulated fluence spectra (see [8]):

$$\Phi'(\mathbf{r}, \lambda) = \Phi_{\text{M}}(\lambda) + \sum_{i=1}^{3} m_i(\mathbf{r})\Phi_i(\lambda), \quad (5)$$

where $\Phi_{\text{M}}(\lambda)$ is the mean spectrum in the training data, $\Phi_i(\lambda), i = 1 \ldots 3$ are the principal components, and m_i are scalars referred to as *the eigenfluence parameters*. If $\theta = (m_1, m_2, m_3, c'_{\text{HHb}}, c'_{\text{HbO2}})$, the eigenspectra model $\hat{p}(\mathbf{r}, \lambda, \theta)$ that approximates the normalized OA spectrum $p'(\mathbf{r}, \lambda)$ takes the following form:

$$\hat{p}(\mathbf{r}, \lambda, \theta) = \left(\Phi_{\text{M}}(\lambda) + \sum_{i=1}^{3} m_i(\mathbf{r})\Phi_i(\lambda) \right) \cdot \left(c'_{\text{HHb}}(\mathbf{r})\varepsilon_{\text{HHb}}(\lambda) + c'_{\text{HbO2}}(\mathbf{r})\varepsilon_{\text{HbO2}}(\lambda) \right). \quad (6)$$

C. eMSOT Inversion

eMSOT is formulated as a constrained minimization problem in which the goal is to identify the values of a set of parameters θ_{opt} that minimize the second norm of the difference between the measured normalized spectrum $\mathbf{p}'(\mathbf{r})$ and the modeled $\hat{\mathbf{p}}(\mathbf{r}, \theta)$. The inversion is performed simultaneously for several selected spatially distributed spectra. The locations of the spectra are determined by a circular grid $\mathbf{G} = \{\mathbf{r}^{(k,l)}|k = 1 \ldots n_{\text{ln}}, l = 1 \ldots n_{\text{pt}}\}$ of n_{ln} lines, each consisting of n_{pt} pixels, that is assigned to a region of interest (ROI) in the MSOT image. (Fig. 1 shows an example of such a grid). A detailed overview of eMSOT inversion can be found in Supplementary Materials (available in the supplementary files/multimedia tab) and [8].

III. METHODS

A. Formulation of the BeMSOT Inverse Problem

The eMSOT inversion described in Section II-B has been shown to provide more accurate sO2 quantification in simulations and phantoms than commonly used linear unmixing, and it has been successfully applied in measurements of small animals [8]. However, these validation studies made clear that eMSOT accuracy is sensitive to noise in the data. In order to make eMSOT more robust to noise and thereby improve its overall accuracy, we hypothesized that we could estimate the noise in the MSOT data and, then, use that information in Bayesian-based eMSOT inversion (BeMSOT) to refine the quantification accuracy.

In the following, we will consider the eMSOT inverse problem in a Bayesian framework. The inverse problem will therefore be treated as a problem of statistical inference and the variables will be treated as random variables. It will be

shown that, in contrast to sO2 quantification using eMSOT, which uses no information on the quality of the measured normalized OA spectra, in the resulting problem of MAP estimation the noise in the measurements is taken into account. All inversion constraints in BeMSOT are formulated using probabilistic graphical models.

1) Bayesian Formulation of eMSOT Inversion: We denote as $\mathbf{P}'_{\text{measured}}$ the vector of $n_\lambda n_{\text{ln}} n_{\text{pt}} \times 1$ measured normalized OA spectra on a grid $\mathbf{G}$ of points selected for inversion, where $n_\lambda = 21$ is the number of wavelengths. We denote the set of five unknown variables for every spectrum $(m_1, m_2, m_3, c'_{\text{HHb}}, c'_{\text{HbO2}})$ as Θ with dimensions $n_{\text{ln}} \times n_{\text{pt}} \times 5$. Θ can be written as $\Theta = (\mathbf{M}_1, \mathbf{M}_2, \mathbf{M}_3, \mathbf{C}_{\text{HHb}}, \mathbf{C}_{\text{HbO2}})$, where $\mathbf{M}_i$ denotes the set of all m_i parameters for all grid points, i.e. $\mathbf{M}_i = \{m_i^{(k,l)}|k = 1 \ldots n_{\text{ln}}, l = 1 \ldots n_{\text{pt}}\}$, and $\mathbf{C}_{\text{HHb}}$ and $\mathbf{C}_{\text{HbO2}}$ are defined analogously. Elements of Θ can be referred to based on their linear index (e.g. $\mathbf{M}_1^{(i)}$, $i = 1 \ldots n_{\text{ln}} \times n_{\text{pt}}$) or their node $\mathbf{r}$ in the grid (e.g. $\mathbf{M}_1^{(\mathbf{r})}, \mathbf{r} \in \mathbf{G}$).

Under the assumption of additive noise $\mathbf{N}$, the observation model is written as follows:

$$\mathbf{P}'_{\text{measured}} = \mathbf{P}_{\text{model}}(\Theta) + \mathbf{N}, \quad (7)$$

where $\mathbf{P}_{\text{model}}(\Theta)$ denotes the eigenspectra model that corresponds to the measurements. The solution to the inverse problem is the posterior probability $\pi(\Theta|\mathbf{P}'_{\text{measured}})$, which, according to the Bayes' formula, can be written in terms of conditional probabilities as follows [23]:

$$\pi(\Theta|\mathbf{P}'_{\text{measured}}) = \frac{\pi(\mathbf{P}'_{\text{measured}}|\Theta) \ \pi(\Theta)}{\pi(\mathbf{P}'_{\text{measured}})}, \quad (8)$$

where $\pi(\mathbf{P}'_{\text{measured}}|\Theta)$ is the data likelihood and $\pi(\Theta)$ is the prior probability. $\pi(\mathbf{P}'_{\text{measured}})$ is fixed for a given measurement $\mathbf{P}'_{\text{measured}}$, therefore Eq. 8 can be used in a nonnormalized form:

$$\pi(\Theta|\mathbf{P}'_{\text{measured}}) \propto \pi(\mathbf{P}'_{\text{measured}}|\Theta) \ \pi(\Theta). \quad (9)$$

We will consider a pointwise estimate of Θ, more specifically, a maximum a posteriori estimate Θ_{MAP}:

$$\Theta_{\text{MAP}} = \arg \max_{\Theta} \pi(\Theta|\mathbf{P}'_{\text{measured}}). \quad (10)$$

In the following subsections, we define models for data likelihood and prior distribution for BeMSOT inversion.

2) Data Likelihood in BeMSOT: Under the assumption of noise and Θ being independent, Eq. 7 leads to the likelihood density [23], [24]:

$$\pi(\mathbf{P}'_{\text{measured}}|\Theta) = \pi_N \left(\mathbf{P}'_{\text{measured}} - \mathbf{P}_{\text{model}}(\Theta) \right), \quad (11)$$

where π_N denotes the probability distribution of noise. If $\mathbf{N}$ is Gaussian noise with zero mean and covariance matrix Σ, Eq. 11 becomes:

$$\pi(\mathbf{P}'_{\text{measured}}|\Theta) \propto \exp\left(- \left\| \mathbf{P}'_{\text{measured}} - \mathbf{P}_{\text{model}}(\Theta) \right\|_\Sigma^2 \right), \quad (12)$$

where $\|\mathbf{x}\|_\Sigma^2 = \mathbf{x}^T \Sigma^{-1} \mathbf{x}$. We assume that Σ is a diagonal matrix with dimensions $n_\lambda n_{\text{ln}} n_{\text{pt}} \times n_\lambda n_{\text{ln}} n_{\text{pt}}$ in which each non-zero

entry equals the variance of noise at a specific wavelength in a specific spectrum. $\boldsymbol{\Sigma}$ (or $\boldsymbol{\Sigma}^{-1}$) can be estimated using the method described in Section III-B.

3) Prior Distributions of Unknown Parameters: Defining the prior probability distribution is an essential part of MAP estimation approach [25]. The prior distributions reflect the available knowledge about the expected values of the unknown parameters.

Assuming the sets of unknown variables are independent of one another, $\pi(\boldsymbol{\Theta})$ can be expressed as

$$\pi(\boldsymbol{\Theta}) = \pi(\mathbf{C}_{\text{HHb}})\,\pi(\mathbf{C}_{\text{HbO2}})\prod_{i=1}^{3}\pi(\mathbf{M}_i), \qquad (13)$$

where $\pi(\mathbf{M}_i)$, $\pi(\mathbf{C}_{\text{HHb}})$ and $\pi(\mathbf{C}_{\text{HbO2}})$ are the prior distributions of the respective unknown variables.

In reality, the absolute concentrations of oxy- and deoxyhemoglobin are not independent and depend on the total blood volume at a specific voxel. The blood volume at every voxel can vary and is typically unknown. Since the normalized spectra are used in the inversion and the normalization is performed per-spectrum, the potential quantitative information on the total blood volume is lost and the concentrations found are relative rather than absolute. Therefore, the only constraint imposed on the relative coefficients of oxy- and deoxyhemoglobin is that they cannot be negative, so $\pi(\mathbf{C}_{\text{HHb}})$ can be modeled using the uniform pseudo-distribution

$$\pi(\mathbf{C}_{\text{HHb}}) = \prod_{\mathbf{r}\in\mathbf{G}}\pi\left(c'^{(\mathbf{r})}_{HHb}\right) = \begin{cases} 0, & \exists \mathbf{r}: c'^{(\mathbf{r})}_{HHb} < 0, \\ \delta, & \forall \mathbf{r}: c'^{(\mathbf{r})}_{HHb} \geq 0, \end{cases} \quad (14)$$

and $\pi(\mathbf{C}_{\text{HbO2}})$ can be defined analogously, where δ is a constant. Computationally Eq. 14 is implemented using appropriate inequality constraints.

When modelling the prior distributions of $\mathbf{M}_1$, $\mathbf{M}_2$ and $\mathbf{M}_3$ it is important to take into account the spatial dependencies of parameter values [8]. To achieve this, probabilistic graphical models are used to model the spatial variation of $\mathbf{M}_1$, $\mathbf{M}_2$ and $\mathbf{M}_3$ across neighboring grid points on the graph $(\mathbf{G}_n, \mathbf{G}_e)$, which corresponds to the grid $\mathbf{G}$. $\mathbf{G}_n$ is the set of pixels in the grid (graph nodes) and $\mathbf{G}_e$ is the set of spatial connections between the pixels (graph edges). Fig. 1a shows an example of a radial grid $\mathbf{G}$ of $n_{\text{ln}} = 5$ lines (white radial lines), each consisting of $n_{\text{pt}} = 3$ points, superimposed on a simulated OA image. The pixels used in inversion are marked in red and represent $\mathbf{G}_n$.

For $\mathbf{M}_1$ and $\mathbf{M}_3$, the values of the parameters do not depend directly on the values of neighboring nodes. Instead, due to the nature of light propagation, the spatial smoothness of the solution should be ensured globally [8]. Thus, an undirected graphical model, namely pairwise Markov random field [26], is used, with a Gibbs distribution, which takes the form $\pi(\mathbf{M}_i) = (1/Z)\exp\left(-\sum_{\mathbf{s}\in\mathbf{G}_n}V_i(\mathbf{s})\right), i = 1, 3$ [27]. Here Z is a normalization constant and V_i is the potential function. Fig. 1b presents an undirected graph corresponding to the grid shown in Fig. 1a used to model the prior distributions of $\mathbf{M}_1$ and $\mathbf{M}_3$. The white lines connecting the graph nodes represent the graph edges $\mathbf{G}_e$. The common choice for the prior model is
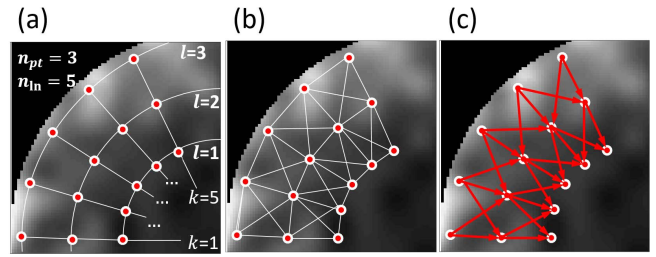
Fig. 1. BeMSOT inversion grid and corresponding graphical models. (a) A radial grid $\mathbf{G}$ (red dots) of $n_{\text{ln}} = 5$ lines (white radial lines), each consisting of $n_{\text{pt}} = 3$ points superimposed on a simulated OA image. (b) An undirected graph corresponding to $\mathbf{G}$ used to model the prior distributions of $\mathbf{M}_1$ and $\mathbf{M}_3$. (c) A directed graph corresponding to $\mathbf{G}$ used to model the prior distributions of $\mathbf{M}_2$ and to ensure that $\mathbf{M}_2$ decreases with depth.

a Gaussian Markov Random Field [27]. For $\mathbf{M}_1$, the potential function V takes the following form:

$$V_1(\mathbf{s}) = GMRF_1(\mathbf{s}),$$
$$GMRF_1(\mathbf{s}) = \sum_{\mathbf{r}\in\partial\mathbf{s}} a_1^{(\mathbf{r},\mathbf{s})}\left|\mathbf{M}_1^{(\mathbf{s})} - \mathbf{M}_1^{(\mathbf{r})}\right|^2, \quad (15)$$

where $\partial\mathbf{s}$ denotes the set of all neighbors of the node $\mathbf{s}$, and $a_1^{(\mathbf{r},\mathbf{s})}$ is a constant coefficient.

It has also been shown previously that for the nodes close to the surface, the correct values of $\mathbf{M}_1$ and $\mathbf{M}_3$ are more likely to lie close to the prior estimates $\hat{\mathbf{M}}_1^{(\mathbf{s})}$ and $\hat{\mathbf{M}}_3^{(\mathbf{s})}$ [8]. With tissue depth, this probability decreases. The constraints based on this observation proved essential for inversion stability. To reflect this behavior in a probability distribution, we augmented the potential functions as follows:

$$V_1(\mathbf{s}) = GMRF_1(\mathbf{s}) + GG_1(\mathbf{s}),$$
$$GG_1(\mathbf{s}) = \left(\frac{\left|\mathbf{M}_1^{(\mathbf{s})} - \mu_{m1}^{(\mathbf{s})}\right|}{2\sigma_{m1}^{(\mathbf{s})}}\right)^q. \quad (16)$$

For $\mathbf{M}_3$ the potential function $V_3(\mathbf{s})$ is defined analogously. $GG_i, i = 1, 3$ correspond to the exponential part of a generalized Gaussian distribution parametrized by the shape parameter q and the scale parameters $\sigma_{m1}^{(\mathbf{s})}$ and $\sigma_{m3}^{(\mathbf{s})}$ [28], [29]. These scale parameters define ranges around the mean values $\mu_{m1}^{(\mathbf{s})}$ and $\mu_{m3}^{(\mathbf{s})}$ within which the values of $\mathbf{M}_1^{(\mathbf{s})}$ and $\mathbf{M}_3^{(\mathbf{s})}$ are more likely to lie. We will refer to these scale parameters as *deviations*. The mean values $\mu_{m1}^{(\mathbf{s})}$ and $\mu_{m3}^{(\mathbf{s})}$ are computed for each eigenfluence parameter $\mathbf{M}_i^{(\mathbf{s})}, i = 1, 3$ based on the prior estimates $\hat{\mathbf{M}}_1^{(\mathbf{s})}$ and $\hat{\mathbf{M}}_3^{(\mathbf{s})}$, as described [8]. It is important to note that the value of q is unknown at this point and remains to be defined.

While $\mathbf{M}_1$ and $\mathbf{M}_3$, do not have a clear relation to a single physical parameter but rather depend on both sO$_2$ and tissue depth, $\mathbf{M}_2$ has been shown to correlate primarily with tissue depth [8]. Therefore the constraints imposed on this parameter in the inversion are different from those imposed on $\mathbf{M}_1$ and $\mathbf{M}_3$. In contrast to the undirected graphical approach, a directed graphical model is used to model the spatial behavior of $\mathbf{M}_2$ and constrain it to decrease with depth. Fig. 1c presents a directed graph corresponding to the grid in Fig. 1a

that is used to model the prior distributions of $\mathbf{M}_2$. The distribution of $\mathbf{M}_2^{(\mathbf{s})}$ at each node $\mathbf{s}$ is conditional on the values $\mathbf{M}_2^{(\mathbf{S})}$ of the parent nodes $\mathbf{S}$ and is modeled as a uniform distribution in the range between $\min \mathbf{M}_2^{(\mathbf{S})}$ and MIN_2, where MIN_2 is a global lower limit of $\mathbf{M}_2$ defined at the eigenspectra model creation step. The distribution of $\mathbf{M}_2^{(\mathbf{s})}$ is implemented through application of appropriate linear constraints.

Substituting Eqs. 9, 12-14 and 16 into Eq. 10 and taking into account the inequalities modeling the distribution of $\mathbf{M}_2$, $\mathbf{C}_{\text{HHb}}$ and $\mathbf{C}_{\text{HbO2}}$ yields

$$
\begin{aligned}
\boldsymbol{\Theta}_{\textbf{MAP}} \\
= \arg\min_{\boldsymbol{\Theta}} & \left\| \mathbf{P}'_{\text{measured}} - \mathbf{P}_{\textbf{model}}\left(\boldsymbol{\Theta}\right) \right\|_{\boldsymbol{\Sigma}_\alpha}^2 \\
+ \beta \sum_{\mathbf{s} \in \mathbf{G_N}} & \left[\left(\sum_{\mathbf{r} \in \partial \mathbf{s}} a_1^{(\mathbf{r},\mathbf{s})} \left| \mathbf{M}_1^{(\mathbf{s})} - \mathbf{M}_1^{(\mathbf{r})} \right|^2 + a_3^{(\mathbf{r},\mathbf{s})} \left| \mathbf{M}_3^{(\mathbf{s})} - \mathbf{M}_3^{(\mathbf{r})} \right|^2 \right) \right. \\
& \left. + \left(\frac{\left| \mathbf{M}_1^{(\mathbf{s})} - \mu_{m1}^{(\mathbf{s})} \right|}{2\sigma_{m1}^{(\mathbf{s})}} \right)^q + \left(\frac{\left| \mathbf{M}_3^{(\mathbf{s})} - \mu_{m3}^{(\mathbf{s})} \right|}{2\sigma_{m3}^{(\mathbf{s})}} \right)^q \right],
\end{aligned}
$$
$$
\begin{aligned}
\text{subject to: } & \mathbf{M}_2^{(k,l)} > \mathbf{M}_2^{(k+1,l)}, \\
& \mathbf{M}_2^{(k,l)} > \mathbf{M}_2^{(k+1,l+1)}, \\
& \mathbf{M}_2^{(k,l)} > \mathbf{M}_2^{(k+1,l-1)} \\
& \mathbf{C}_{\text{HHb}}^{(k,l)} \geq 0, \quad \mathbf{C}_{\text{HbO2}}^{(k,l)} \geq 0.
\end{aligned} \quad (17)
$$

In Eq. 17 β is a constant; $\boldsymbol{\Sigma}_\alpha = \boldsymbol{\Sigma} + \alpha \mathbf{I}$, where $\mathbf{I}$ is the identity matrix; and α is the diagonal loading constant, which dampens large variations in $\boldsymbol{\Sigma}$ that may arise due to large variations in SNR across the measured spectra. Eq. 17 is the main equation of BeMSOT inversion. In order to solve it one needs to define values of the parameters q, $a_1^{(\mathbf{r},\mathbf{s})}$, $a_3^{(\mathbf{r},\mathbf{s})}$, $\sigma_{m1}^{(\mathbf{s})}$ and $\sigma_{m3}^{(\mathbf{s})}$, as well as estimate $\boldsymbol{\Sigma}$. The values for the parameters are set as described in the next subsection. Estimation of $\boldsymbol{\Sigma}$ is described in Sec. III-B. Eq. 17 is solved using the sequential quadratic programming (SQP) algorithm supplied in MATLAB.

4) Choosing Parameters of the Prior Distributions: The prior probabilities $\pi(\mathbf{M_i})$, $i = 1, 3$ incorporate prior knowledge about the deviation of model parameters from the prior estimates $\hat{\mathbf{M}}_1^{(k,l)}$ and $\hat{\mathbf{M}}_3^{(k,l)}$, which are computed as described previously [8]. The deviations $\sigma_{m1}^{(k,l)}$ and $\sigma_{m3}^{(k,l)}$ of the generalized Gaussian distribution, which determine the deviation of the optimized eigenfluence parameters from $\mu_{m1}^{(k,l)}$ and $\mu_{m3}^{(k,l)}$, increase linearly with tissue depth because $\hat{\mathbf{M}}_1^{(k,l)}$ and $\hat{\mathbf{M}}_3^{(k,l)}$ become less accurate with depth [8]. Given the initial deviations $\sigma_{m1}^{(k,0)}$ and $\sigma_{m3}^{(k,0)}$ for the surface grid points, the deviations at an arbitrary grid point are defined as $\sigma_{m1}^{(k,l)} = \gamma_1(d) \cdot \sigma_{m1}^{(k,0)}$, $\sigma_{m3}^{(k,l)} = \gamma_3(d) \cdot \sigma_{m3}^{(k,0)}$, where γ_1 and γ_3 are coefficients that depend on the depth d of the considered point. The values of γ_1 and γ_3 in this study were retained as described [8], and the values of $\sigma_{m1}^{(k,0)}$ and $\sigma_{m1}^{(k,0)}$ were selected based on cross-validation using simulated IPR maps (see Supplementary Materials, available in the supplementary files/multimedia tab).

The coefficients that govern the spatial smoothness of $\mathbf{M}_1$ and $\mathbf{M}_3$ were set to be inversely proportional to the Euclidean

distance $\|\mathbf{r} - \mathbf{s}\|_2$ between the neighboring pixels $\mathbf{r}$ and $\mathbf{s}$: $a_1^{(\mathbf{r},\mathbf{s})} = a_3^{(\mathbf{r},\mathbf{s})} = w \frac{1}{\|\mathbf{r}-\mathbf{s}\|_2}$.

The parameters of the Bayesian inversion method, namely q, w, $\sigma_{m1}^{(\mathbf{s})}$ and $\sigma_{m3}^{(\mathbf{s})}$, were selected using cross-validation of a set of simulations described in the following subsection; the selection process itself is described in Supplementary Materials (available in the supplementary files/multimedia tab).

B. Noise Estimation in BeMSOT Using a Spectral Reliability Map (SRM)

Since the level of noise in OA spectra depends on the voxel location, with shallower voxels typically showing better signal-to-noise ratio (SNR) than deeper ones, noise in eMSOT spectra needs to be estimated on a per-voxel (per-collected spectrum) basis. To estimate the noise present in each individual spectrum, we developed a model for normalized OA spectra, termed an *OA spectral model*. We use the OA spectral model to estimate the underlying ideal noise-free normalized OA spectra of experimental noisy normalized OA spectra, and then estimate the level of random noise in spectra obtained at different locations (voxels), giving rise to a spatial map of estimated noise variance. This map, which we term a *spectral reliability map* (SRM), is used to weight different spectra selected for the BeMSOT inversion according to the amount of estimated noise.

1) OA Spectral Model: The OA spectral model describes noise-free normalized OA spectra recorded at different locations within tissue. Spectrum location $\mathbf{r}$ is not important for model derivation and is therefore omitted to simplify the notation. Building on the eMSOT assumption that the spectrum of light fluence anywhere within tissue can be accurately modeled using a small set of base spectra, the OA spectral model assumes that all possible normalized OA spectra $p'(\lambda)$ (Eq. 1) can also be modelled as a linear combination of a few base spectra $p_i(\lambda)$. These spectra $p_i(\lambda)$ are derived from analysis of a training dataset of noise-free normalized OA spectral patterns. This dataset captures variations in normalized OA spectra due to fluence and absorption of hemoglobin. The training dataset was generated as follows:

1. A set $\hat{\boldsymbol{\Phi}} = \{\Phi_i(\lambda) | i = 1 \ldots 70 \times 21\}$ of 1470 fluence spectra $\Phi_i(\lambda)$ was computed as a 1-D analytical solution for Eq. 2 in an infinite medium in which hemoglobin is the only absorber, as described for eMSOT [8]. The following parameters were assumed: $\mu_a = 0.3$ cm^{-1} at 800 nm, $\mu'_s = 10$ cm^{-1}, depth of up to 1 cm with a step size of 0.0145 cm (70 in total) and for oxygenation levels of 0%-100% with a step size of 5% (21 in total).
2. Absorption spectra of hemoglobin at different oxygenation levels $\hat{\mu}_a = \{\mu_{a,i} | i = 1 \ldots 21\}$ were calculated. While absorption spectra can be calculated as $\mu_a = c'_{\text{HHb}}\varepsilon_{\text{HHb}}(\lambda) + c'_{\text{HbO2}}\varepsilon_{\text{HbO2}}(\lambda)$, we did not use this approach because we are interested only in the shape of the absorption spectrum, not absolute absorption values. Therefore we computed absorption spectra as a function of tissue oxygen saturation c_{O2}: $\mu_a = c_{\text{O2}}\varepsilon_{\text{HHb}}(\lambda) + (1 - c_{\text{O2}})\varepsilon_{\text{HbO2}}(\lambda)$. We varied c_{O2} from 0% to 100%

with a step size of 5%, producing a total of 21 absorption spectra of hemoglobin.

3. Each fluence spectrum in $\hat{\boldsymbol{\Phi}}$ obtained in step 1 was multiplied element-wise by every absorption spectrum in $\hat{\boldsymbol{\mu}}_a$ calculated in step 2. The resulting spectral patterns were normalized to their respective l_2-norms, producing a training dataset $\hat{\mathbf{P}}'$ of 21×1470 normalized OA spectra (30,870).

PCA was applied to this training dataset $\hat{\mathbf{P}}'$ to derive the base spectra $p_i(\lambda)$ as follows:

1. Since PCA requires that input data have a mean value of zero, the mean normalized OA spectrum $p_M(\lambda) = \text{mean}\left(\hat{\mathbf{P}}'\right)$ was computed from the training set $\hat{\mathbf{P}}'$ and subtracted from every spectrum in $\hat{\mathbf{P}}'$, resulting in a zero-mean input set $\hat{\mathbf{P}}'_0$ of 30,870 spectra.

2. PCA was applied to the input set $\hat{\mathbf{P}}'_0$ of spectral patterns obtained in step 1. The resulting principal components were the base spectra $p_i(\lambda)$.

These base spectra (principal components) derived from a distinct precomputed set $\hat{\mathbf{P}}'_0$ can now be combined linearly with the mean spectrum of the training dataset $p_M(\lambda)$ to model an arbitrary normalized OA spectrum $p'(\mathbf{r}, \lambda)$ from a specific location $\mathbf{r}$ in an OA dataset:

$$p'(\mathbf{r}, \lambda) = p_M(\lambda) + \sum_{i=1}^{D} a_i(\mathbf{r}) p_i(\lambda), \qquad (18)$$

where $a_i(\mathbf{r}) = \langle \mathbf{p}' - \mathbf{p}_M, \mathbf{p}_i \rangle_\lambda$, with $\langle ., . \rangle_\lambda$ denoting the scalar product of spectra. The number of components D returned by PCA is equal to the number of wavelengths used (21 in this study). Only a subset of these base spectra is typically needed to approximate the data sufficiently well, i.e.

$$\{\mathbf{p}_M, \mathbf{p}_i | i = 1 \dots D_m\}, \qquad (19)$$

where $D_m < D$. Eq. 19 will be referred to as a D_m-dimensional OA spectral model.

2) Spectral Reliability Map (SRM): Next we applied the D_m-dimensional OA spectral model to noisy OA spectra to estimate what the ideal, noise-free measurements should be. The difference between the noise-free estimation and the experimental values provides an estimate of the noise in the experimental spectra. We modeled a noisy experimental normalized OA spectrum $p'_{exp}(\mathbf{r}, \lambda)$ as $p'_{exp}(\mathbf{r}, \lambda) = p_{nf}(\mathbf{r}, \lambda) + n(\mathbf{r}, \lambda)$, where $p_{nf}(\mathbf{r}, \lambda)$ is a noise-free spectrum of initial pressure and $n(\mathbf{r}, \lambda)$ is noise. Since the main source of OA noise is electronic noise in the imaging system [9], we modeled $n(\mathbf{r}, \lambda)$ as a random Gaussian process with zero mean, assuming that variance of $n(\mathbf{r}, \lambda)$ is constant at all wavelengths, but might vary with $\mathbf{r}$. Since $p_{nf}(\mathbf{r}, \lambda)$ lies almost entirely in a subspace of spectra defined by the D_m base spectra $p_i(\lambda)$ and since $n(\mathbf{r}, \lambda)$ is random and therefore equally distributed across all base spectra, an estimate p_{est} of the noise-free spectrum can be obtained as:

$$\mathbf{p}_{est} = \mathbf{p}_M + \sum_{i=1}^{D_m} \langle \mathbf{p}'_{exp} - \mathbf{p}_M, \mathbf{p}_i \rangle_\lambda \mathbf{p}_i. \qquad (20)$$

Estimation of noise n_{est} can then be calculated as

$$n_{est}(\mathbf{r}, \lambda) = p_{exp}(\mathbf{r}, \lambda) - p_{est}(\mathbf{r}, \lambda). \qquad (21)$$

This is equivalent to projecting $\mathbf{p}'_{exp} - \mathbf{p}_M$ onto the last $D - D_m$ base spectra. Given an MSOT dataset $p(\mathbf{r}, \lambda)$, Eqs. 20 and 21 can be applied to normalized OA spectra $\mathbf{p}'(\mathbf{r})$ at every pixel location $\mathbf{r}$ to estimate the noise $\mathbf{n}_{est}(\mathbf{r})$ superimposed onto the measurements. The corresponding variance in the noise $Var\left(\mathbf{n}_{est}(\mathbf{r})\right)$ can be calculated and spatially mapped, giving what we term a *spectral reliability map (SRM)*:

$$SRM(\mathbf{r}) = Var\left(\mathbf{n}_{est}(\mathbf{r})\right). \qquad (22)$$

The SRM can then be used to weight spectra chosen for eMSOT inversion such that noisier measured normalized OA spectra will influence BeMSOT inversion less.

C. Validation and Performance Assessment

In order to select optimal dimensionality D_m of the OA spectral model and to define values of the parameters of prior distributions, simulations of multispectral IPR maps were used. To assess the performance of BeMSOT, simulations were created with spatially varying amounts of noise. For such simulations with inhomogeneous noise distribution, IPR maps were simulated first, for which the corresponding transducer signals were calculated. Noise was added to the transducer signals and MSOT images were reconstructed from the noisy signals. MSOT images created from multispectral IPR maps were used for BeMSOT inversion.

1) Simulations of IPR Maps: Multispectral IPR maps of a circular tissue sample (radius, 1 cm) with randomly varying optical properties were simulated as described [8] for different excitation wavelengths. Fig. 2 shows the simulated maps, which were generated in the following manner:

1. Spatial maps of optical absorption ($\mu_a(\mathbf{r})$) and reduced scattering ($\mu'_s(\mathbf{r})$) coefficients were created for an illumination wavelength of 800 nm, which is the isosbestic point of hemoglobin. Fig. 2a-b shows an example of random spatial maps of optical properties, while Table 1 provides the means and standard deviations of the normal distributions used. Random maps of tissue sO2 were created by assuming a normal distribution of sO2 values. Fig. 2c shows an example of a simulated sO2 map.

2. Using the maps specified in step 1 as well as the absorption spectra of oxy- and deoxyhemoglobin, the optical absorption $\mu_a(\mathbf{r}, \lambda)$ was constructed for the entire wavelength range used (700-900 nm, step size of 10 nm, 21 maps in total).

3. The *optical forward problem* was solved using a finite-element solution to the diffusion equation (Eq. 2) to simulate light propagation through the sample, generating a light fluence map $\Phi(\mathbf{r}, \lambda)$ for all illumination wavelengths.

4. According to Eq. 1, the multiplication of the absorption map $\mu_a(\mathbf{r}, \lambda)$ specified in step 2 and the light fluence map $\Phi(\mathbf{r}, \lambda)$ obtained in step 3 gives the simulated IPR map $p(\mathbf{r}, \lambda)$. This map assumes that $\Gamma(\mathbf{r}) = 1$, which does not affect sO2 quantification accuracy because all
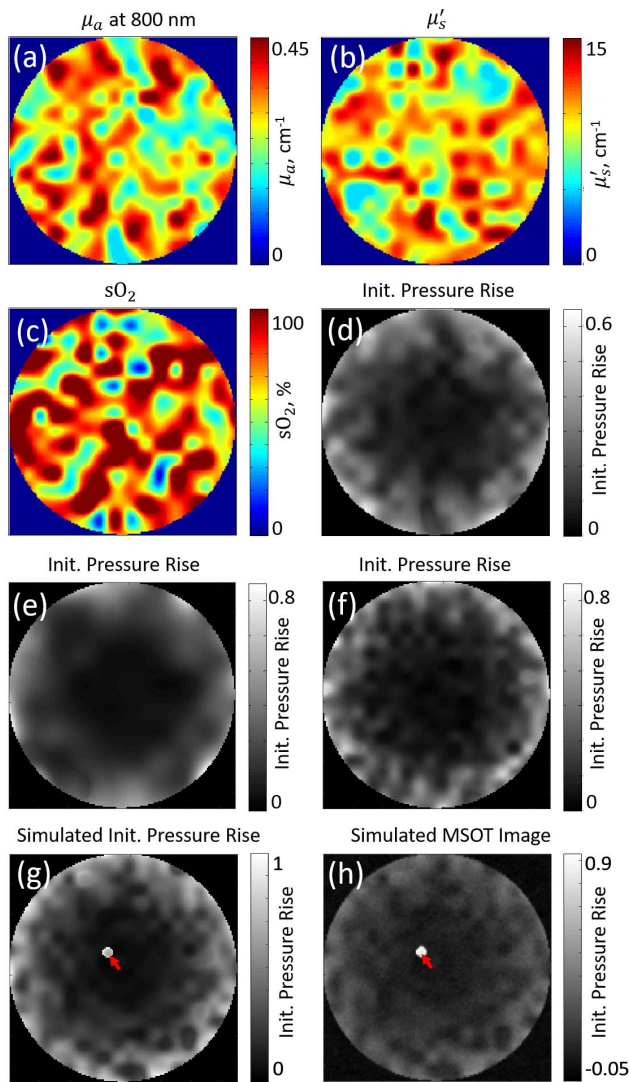
Fig. 2. Simulations of IPR maps and MSOT images. (a-c) Maps generated for an illumination wavelength of 800 nm based on randomly generated values of (a) μ_a, (b) μ'_s and (c) sO_2. (d) IPR image simulated from the maps in panels (a)-(c); (e, f) IPR maps simulated with (e) low and (f) high heterogeneity in the distributions of optical properties. (g) IPR image simulated with an absorbing vessel in deep tissue (red arrow). (h) Simulated MSOT image corresponding to the IPR map shown in panel (e) and showing the simulated blood vessel (red arrow). Negative values in panel (h) are an artifact of reconstruction.

spectra $\mathbf{p}(\mathbf{r})$ are normalized in eMSOT and BeMSOT. Fig. 2d presents a simulated IPR map that corresponds to the optical properties defined in Fig. 2a-c.

IPR maps were generated with different distributions of optical properties in order to simulate a reasonable range of tissue heterogeneity created by the presence of tissue structures. Fig. 2e shows an example of a simulation with low heterogeneity; Fig. 2f, an example with high heterogeneity.

Since the SRM is evaluated on a per-pixel level, the individual spectra extracted from the IPR simulations were augmented with zero-mean Gaussian nose $\mathbf{n}$ of the following powers: 0.8, 1.5, 2.5, 4.5, 6, 8 or 10 percent of spectra power (referred to as percent noise).

2) Simulations of MSOT Images: To create simulations with heterogeneous noise distribution, we started from the

TABLE I
SIMULATION SPECIFICATIONS

Purpose	μ_a mean, cm^{-1}	μ_a std, cm^{-1}	μ'_s mean, cm^{-1}	μ'_s std, cm^{-1}	sO_2 mean, %	sO_2 std, %	Number of simulations
Optimization of the OA spectral model and SRM (Fig. 3)	0.07; 0.1; 0.15; 0.2; 0.25; 0.3	0.1	10	3	5-95, step of 5	20; 30	1710
Application of BeMSOT to simulations of MSOT images (Fig. 5)	0.3	0.1	10	3	5-95, step of 5	20; 30	285
Optimization of BeMSOT (Suppl. Fig. 1)	0.1; 0.2; 0.3	0.1	10	3	5-95, step of 5	20; 30	171

simulated IPR maps and solved the *acoustic forward problem* using a linear model of pressure wave propagation [30], [31], obtaining the corresponding OA pressure signals recorded by the piezoelectric transducers of the imaging system. Then zero-mean Gaussian noise was added to the simulated transducer signals, which were reconstructed into MSOT images. This process involved the following steps:

1. An IPR map $\mathbf{P}_\lambda$ for a specific illumination wavelength λ was simulated and reshaped into a vector $\mathbf{p}_\lambda$.
2. The *forward acoustic problem* was solved. The corresponding OA pressure signals $\mathbf{s}_{pr}$ were simulated as $\mathbf{s}_{pr} = \mathbf{A}_c\mathbf{p}_\lambda$, where $\mathbf{A}_c$ is a model matrix representing the linear model of OA wave propagation. The detection geometry represented in $\mathbf{A}_c$ assumed the geometry of a commercially available, limited-view 2D MSOT imaging system [32], comprising 256 detectors arranged in a ring with a radius of 4 cm, which provides angular coverage of 270 degrees.
3. Zero-mean Gaussian noise was superimposed upon the simulated signals $\mathbf{s}_{pr}$ to obtain noisy signals $\mathbf{s}_{ns}$.
4. The *inverse acoustic problem* was then solved by using the noisy signals $\mathbf{s}_{ns}$ along with $\mathbf{A}_c$ in a model-based reconstruction algorithm [30], [31] to obtain the distorted IPR image $\mathbf{P}_{rec}$. In all cases, speed of sound was assumed to be 1,530 m · s^{-1} during signal simulation and reconstruction. Since noise is superimposed on the signals (step 3) rather than on the spectra, the noise in $\mathbf{P}_{rec}$ is non-uniformly distributed in space, with SNR varying directly with signal intensity.

For example, the simulated IPR map in Fig. 2g was reconstructed into the noisy MSOT image $\mathbf{P}_{rec}$ in Fig. 2h. The reconstructed image contains negative values, which are a reconstruction artifact [33]. The red arrow marks the location of a simulated blood vessel, which should have a much higher SNR than the surrounding area.

For each simulated IPR dataset, the power of noise was varied so that the mean peak SNR (PSNR) of the reconstructed datasets varied from 36 to 32 dB in 1-dB steps. PSNR was defined as $PSNR = 10\log_{10}\frac{(\max \mathbf{P}_{rec})^2}{MSE(\mathbf{P}_{rec},\mathbf{P}_\lambda)}$, with $MSE(\mathbf{P}_{rec}, \mathbf{P}_\lambda)$ denoting the mean squared error of the reconstructed image.

3) Performance Evaluation of the OA Spectral Model, SRM and BeMSOT: For each simulated noise-free normalized OA spectrum $\mathbf{p}'_{nf}$, the fitting residual $res = \left\|\mathbf{p}'_{nf} - \mathbf{p}_{est}\right\|_2$ was
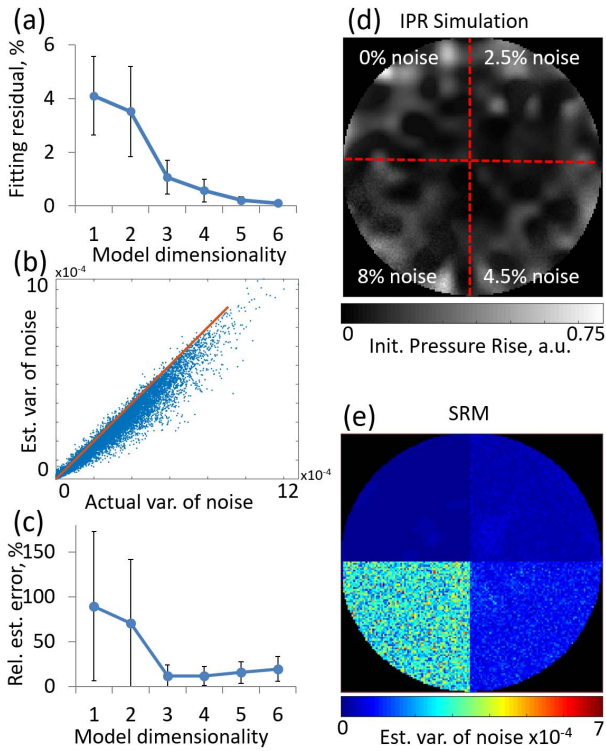
Fig. 3. Optimization and performance of the OA spectral model and SRM. (a) Dependence of fitting residuals *res* on dimensionality D_m of the normalized OA spectral model for approximating noise-free spectra. Mean data (dots) are shown with standard deviations (error bars). (b) Variance of noise estimated with a four-dimensional normalized OA spectral model plotted against the actual standard deviation of noise. The orange line shows ideal 1-to-1 correspondence. (c) Relative errors in the estimation of variance of noise produced by the normalized OA spectral model depending on its dimensionality. Mean data (dots) are shown with standard deviation (error bars). (d) A simulated IPR map (one wavelength presented) with zero-mean Gaussian noise of the specified energy (as noise %) superimposed onto the simulated spectra in four sectors. (e) An SRM computed for the simulated data shown in panel (d).

computed, where $\mathbf{p}_{est}$ was obtained using the normalized OA spectral model according to Eq. 20. The fitting residual was computed for all test spectra for different OA spectral model dimensionalities D_m. For a particular value of D_m, lower residual values mean better approximation by the D_m-dimensional OA spectral model.

For every simulated noisy normalized OA spectrum $\mathbf{p}'_{exp}$, the superimposed noise was estimated using Eqs. 20 and 21. The variance $Var(\mathbf{n}_{est}(\mathbf{r}))$ was compared to the actual variance $Var(\mathbf{n}(\mathbf{r}))$ of superimposed noise. For a particular value of D_m, lower relative estimation errors (i.e. $\frac{|Var(\mathbf{n}_{est}(\mathbf{r})) - Var(\mathbf{n}(\mathbf{r}))|}{Var(\mathbf{n}(\mathbf{r}))} \cdot 100\%$) mean better noise estimation by the D_m-dimensional OA spectral model.

BeMSOT performance was compared to that of eMSOT and linear unmixing based on mean absolute sO_2 estimation error in a deep-seated blood vessel (representative of a target feature in the sample), as well as in non-vessel areas covered by the grid $\mathbf{G}$ used for inversion (representative of sample background). For every pixel, the absolute sO_2 estimation error was computed as $|sO2_{alg} - sO2_{GS}|$, where $sO2_{alg}$ is the sO_2 value obtained by a certain algorithm and $sO2_{GS}$ is the gold standard value.
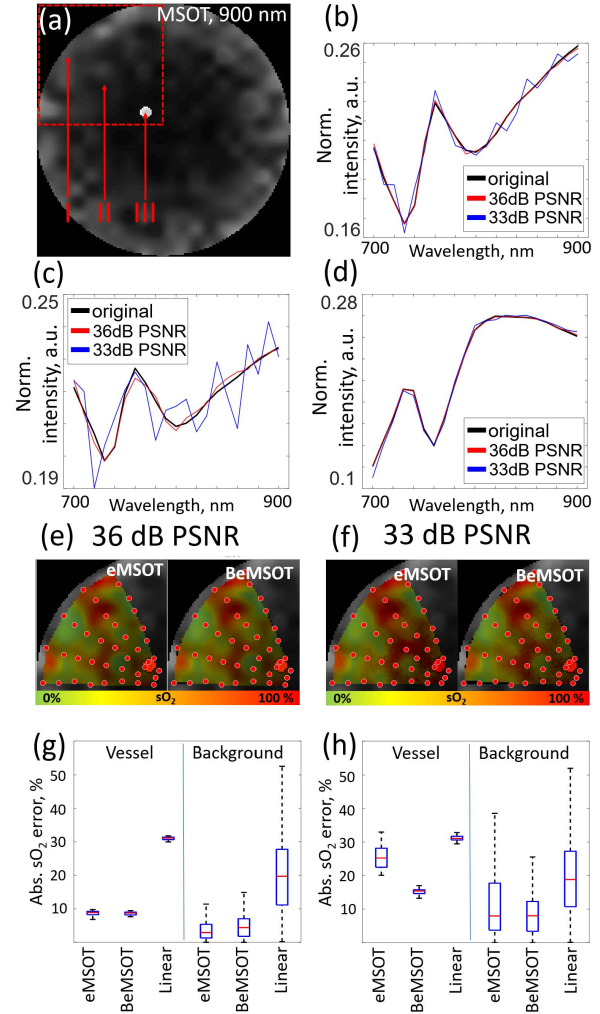
Fig. 4. Comparison of BeMSOT and eMSOT for quantifying sO_2 in simulated MSOT images. (a) A map of simulated IPR (one wavelength presented). The red dashed square marks the ROI shown in panels (e) and (f), while I, II and III denote locations of the spectra shown in panels (b)-(d). (b-d) Respective spectra from locations I-III in panel (a). Black lines correspond to original spectra; red lines, reconstructed data with mean PSNR of 36; and blue lines, reconstructed data with mean PSNR of 33 dB. (e, f) Values for sO_2 obtained from the reconstructions with mean PSNR of (e) 36 dB or (f) 33 dB, overlaid on the IPR image. Inversion grids are shown with red circles (active pixels). (g, h) Errors in sO_2 estimation for the vessel and background obtained with BeMSOT, eMSOT or linear unmixing for the reconstructions with mean PSNR of (g) 36 dB or (h) 33 dB. Blue boxes indicate first and third quartiles; red lines, medians; and whiskers, 2.7 standard deviations from the mean.

In all cases, sO_2 level in the blood vessel was set to be 25% higher than the level in the background, or to 100% if the mean sO_2 level of the background was above 75%. For example, if sO_2 of the background was 35%, sO_2 level of the vessel was set to 60% (35 + 25%); if sO_2 of the background was 80%, sO_2 level of the vessel was set to 100%.

IV. RESULTS

A. Noise Estimation Using the OA Spectral Model and SRM

Fig. 3 demonstrates the optimization of the OA spectral model and the noise estimation capability of the SRM based
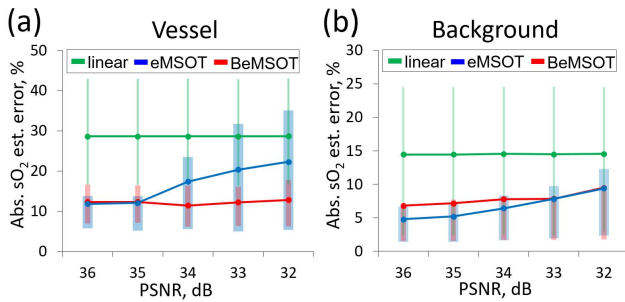
Fig. 5. Statistical evaluation of BeMSOT performance in simulations of MSOT images. Mean error in sO_2 estimation by BeMSOT (red line), eMSOT (blue line) and linear unmixing (green line) in (a) target vessel and (b) background as a function of mean PSNR of the reconstructed images. Results are based on 285 simulations of MSOT images. Error bars indicate first and third quartiles of the plotted data.

on analysis of 384,750 simulated normalized OA spectra sparsely sampled from 1,710 IPR simulations (225 spectra per simulated dataset). Fig. 3a shows how the fitting residual varies with dimensionality D_m; most of the signal is accounted for by the first four principal components. Fig. 3b shows a reasonable fit between the SRM-estimated variance in noise based on a four-dimensional OA spectral model and the ideal prediction of a 1:1 correspondence (orange line). Finally, Fig. 3c shows that D_m values of 3 or 4 minimize relative error in the estimation of the variance of noise. Using more than 4 components leads to model overfitting and increases estimation error due to noise being interpreted as signal. Therefore, subsequent computations were carried out using a four-dimensional OA spectral model.

Fig. 3d presents a simulated IPR dataset (one wavelength shown) in which zero-mean Gaussian noise was added to the spectra at four energies. Fig. 3e shows the corresponding SRM based on Eq. 21 and $D_m = 4$. The spatial analysis of variance identifies areas with different SNR.

B. Comparison of eMSOT and BeMSOT

BeMSOT and conventional eMSOT were compared in their ability to estimate sO_2 from a deep-seated blood vessel and background areas of the image. The results were compared with those obtained by standard linear mixing as a reference. Simulated MSOT images with mean PSNR of 33 and 36 dB in the reconstructed data were used in order to showcase the performance of each algorithm. Fig. 4a presents the simulated MSOT image obtained for illumination at 900 nm, and spectra sampled from three image locations (Fig. 4b-d). SNR varies over the image, with less noise in highly absorbing and shallower areas. Fig. 4e-h show the error of BeMSOT and eMSOT in estimating sO_2 in the deep-seated vessel. As expected, BeMSOT is better able to estimate sO_2 than eMSOT when the target is surrounded by spectra of significantly lower quality, and this is true at both PSNRs tested.

These results were confirmed in statistical analysis of 285 simulations (Fig. 5). Whereas eMSOT performance degrades with increasing noise, BeMSOT can recover sO_2 of the vessel more accurately even at low SNRs. Both methods, in contrast, perform similarly well for the background ROI,

indicating that BeMSOT offers advantages over eMSOT primarily in image areas with strong SNR heterogeneity.

An example comparison of eMSOT and BeMSOT in experimental images of tissue-mimicking phantoms can be found in Supplementary Materials (available in the supplementary files/multimedia tab).

V. DISCUSSION AND CONCLUSION

The mathematical framework of Bayesian inversion has been used extensively for the development of methods that offer robust solutions in inverse problems related to image reconstruction [27], [34], in particular in the field of optoacoustic imaging [12], [14]. In this work, we propose a Bayesian method for the inversion of the eigenspectra model to quantitatively estimate sO_2 level accurately in OA data with spatially heterogeneous noise.

To enable Bayesian formulation of the eMSOT inverse problem, we developed a novel tool called the SRM to estimate noise in the OA spectra. The SRM supports two functions: (1) to estimate the covariance of noise, which allows spectra to be weighted automatically based on their reliability; and (2) to identify well-reconstructed parts of the image for analysis. Even if unreliable areas are included in the BeMSOT inversion, the corresponding SRM can be used as an indication of the trustworthiness of the results. The proposed Bayesian inversion method can flexibly rely more on the less noisy measurements and suppress the impact of noisy data, therefore enhancing the accuracy of sO_2 estimation in data with spatially varying SNR.

Such spatial variation of noise power is characteristic of MSOT. Since MSOT image formation involves light absorption, the images are influenced by heterogeneous noise. Superficial regions as well as highly absorbing structures such as blood vessels show high intensity in images and so provide high SNR, while deeper and less-absorbing areas produce weaker signal easily dominated by noise.

Formulation of the inversion algorithm in Bayesian terms also allows studying how different parameters and constraints, such as constraints of the search space or smoothness of the solution, influence the overall performance of the method and interpretation of the results in probabilistic terms. This comes at the cost of speed: inversion typically takes ∼60 sec for BeMSOT but only ∼5 sec for eMSOT.

Since the presence of prominent absorbers other than oxy- and deoxyhemoglobin violates the assumptions of the eigenspectra model, in future work, the SRM may be adapted to take into account other absorbers, either separately from BeMSOT or in conjunction with an appropriately adapted BeMSOT algorithm. Optical wavelength selection, similarly to linear unmixing [35], may also improve sO_2 estimation accuracy by BeMSOT. Future studies could try to improve inversion accuracy and speed using neural networks, which show promise for applications to the inverse problems in quantitative optoacoustics [36], [37].

We have presented a novel Bayesian method for sO_2 quantification from MSOT images as well as a method to estimate

noise present in the measured OA spectra. It is possible that the extension of this method that takes into account absorbers other than hemoglobin may be useful for quantifying other parameters useful to basic biology and disease, which may substantially extend and improve the quantitative potential of MSOT.

ACKNOWLEDGMENT

REFERENCES

[1] P. Vaupel and L. Harrison, "Tumor hypoxia: Causative factors, compensatory mechanisms, and cellular response," *Oncologist*, vol. 9, no. 5, pp. 4–9, 2004.

[2] N. K. Logothetis and B. A. Wandell, "Interpreting the BOLD signal," *Annu. Rev. Physiol.*, vol. 66, pp. 735–769, Mar. 2004.

[3] V. Ntziachristos, "Going deeper than microscopy: The optical imaging frontier in biology," *Nature Methods*, vol. 7, no. 8, pp. 603–614, 2010.

[4] P. Mohajerani, S. Tzoumas, A. Rosenthal, and V. Ntziachristos, "Optical and optoacoustic model-based tomography: Theory and current challenges for deep tissue imaging of optical contrast," *IEEE Signal Process. Mag.*, vol. 32, no. 1, pp. 88–100, Jan. 2015.

[5] B. T. Cox, J. G. Laufer, P. C. Beard, and S. R. Arridge, "Quantitative spectroscopic photoacoustic imaging: A review," *J. Biomed. Opt.*, vol. 17, no. 6, p. 061202, 2012.

[6] B. T. Cox, J. G. Laufer, and P. C. Beard, "The challenges for quantitative photoacoustic imaging," *Proc. SPIE*, vol. 7177, p. 717713, Feb. 2009.

[7] K. Maslov, H. F. Zhang, and L. V. Wang, "Effects of wavelength-dependent fluence attenuation on the noninvasive photoacoustic imaging of hemoglobin oxygen saturation in subcutaneous vasculature *in vivo*," *Inverse Problems*, vol. 23, no. 6, p. S113, 2007.

[8] S. Tzoumas *et al.*, "Eigenspectra optoacoustic tomography achieves quantitative blood oxygenation imaging deep in tissues," *Nature Commun.*, vol. 7, p. 12121, Jun. 2016.

[9] S. Tzoumas, A. Rosenthal, C. Lutzweiler, D. Razansky, and V. Ntziachristos, "Spatiospectral denoising framework for multispectral optoacoustic imaging based on sparse signal representation," *Med. Phys.*, vol. 41, no. 11, p. 113301, 2014.

[10] L. V. Wang and H.-I. Wu, *Biomedical Optics: Principles and Imaging*. Hoboken, NJ, USA: Wiley, 2012.

[11] T. Tarvainen, B. T. Cox, J. P. Kaipio, and S. R. Arridge, "Reconstructing absorption and scattering distributions in quantitative photoacoustic tomography," *Inverse Problems*, vol. 28, no. 8, p. 084009, 2012.

[12] T. Tarvainen, A. Pulkkinen, B. T. Cox, J. P. Kaipio, and S. R. Arridge, "Bayesian image reconstruction in quantitative photoacoustic tomography," *IEEE Trans. Med. Imag.*, vol. 32, no. 12, pp. 2287–2298, Dec. 2013.

[13] A. Pulkkinen, B. T. Cox, S. R. Arridge, J. P. Kaipio, and T. Tarvainen, "A Bayesian approach to spectral quantitative photoacoustic tomography," *Inverse Problems*, vol. 30, no. 6, p. 065012, 2014.

[14] A. Pulkkinen, B. T. Cox, S. R. Arridge, J. P. Kaipio, and T. Tarvainen, "Bayesian parameter estimation in spectral quantitative photoacoustic tomography," *Proc. SPIE*, vol. 9708, p. 97081G, Mar. 2016.

[15] B. T. Cox, S. R. Arridge, and P. C. Beard, "Estimating chromophore distributions from multiwavelength photoacoustic images," *J. Opt. Soc. Amer. A, Opt. Image Sci.*, vol. 26, no. 2, pp. 443–455, 2009.

[16] B. T. Cox, S. R. Arridge, K. P. Köstli, and P. C. Beard, "Two-dimensional quantitative photoacoustic image reconstruction of absorption distributions in scattering media by use of a simple iterative method," *Appl. Opt.*, vol. 45, no. 8, pp. 1866–1875, 2006.

[17] B. Banerjee, S. Bagchi, R. M. Vasu, and D. Roy, "Quantitative photoacoustic tomography from boundary pressure measurements: Noniterative recovery of optical absorption coefficient from the reconstructed absorbed energy map," *J. Opt. Soc. Amer. A, Opt. Image Sci.*, vol. 25, no. 9, pp. 2347–2356, 2008.

[18] L. Yao, Y. Sun, and H. Jiang, "Quantitative photoacoustic tomography based on the radiative transfer equation," *Opt. Lett.*, vol. 34, no. 12, pp. 1765–1767, 2009.

[19] B. Cox, T. Tarvainen, and S. Arridge, "Multiple illumination quantitative photoacoustic tomography using transport and diffusion models," in *Tomography and Inverse Transport Theory*, vol. 559, G. Bal, D. Finch, P. Kuchment, J. Schotland, P. Stefanov, and G. Uhlmann, Eds. Providence, RI, USA: AMS, 2011, pp. 1–12.

[20] S. Bu *et al.*, "Model-based reconstruction integrated with fluence compensation for photoacoustic tomography," *IEEE Trans. Biomed. Eng.*, vol. 59, no. 5, pp. 1354–1363, May 2012.

[21] A. V. Mamonov and K. Ren. (2012). "Quantitative photoacoustic imaging in radiative transport regime." [Online]. Available: https://arxiv.org/abs/1207.4664

[22] T. Saratoon, T. Tarvainen, B. T. Cox, and S. R. Arridge, "A gradient-based method for quantitative photoacoustic tomography using the radiative transfer equation," *Inverse Problems*, vol. 29, no. 7, p. 075006, 2013.

[23] J. Kaipio and E. Somersalo, *Statistical and Computational Inverse Problems*. vol. 160. New York, NY, USA: Springer, 2006.

[24] D. Calvetti and E. Somersalo, *An Introduction to Bayesian Scientific Computing: Ten Lectures on Subjective Computing*, vol. 2. New York, NY, USA: Springer, 2007.

[25] B. P. Carlin and T. A. Louis, "Bayes and empirical Bayes methods for data analysis," *Statist. Comput.*, vol. 7, no. 2, pp. 153–154, 1997.

[26] S. Z. Li, *Markov Random Field Modeling in Image Analysis*. New York, NY, USA: Springer, 2009.

[27] C. Bouman and K. Sauer, "A generalized Gaussian image model for edge-preserving MAP estimation," *IEEE Trans. Image Process.*, vol. 2, no. 3, pp. 296–310, Jul. 1993.

[28] G. T. Herman, H. Hurwitz, A. Lent, and H.-P. Lung, "On the Bayesian approach to image reconstruction," *Inf. Control*, vol. 42, no. 1, pp. 60–71, 1979.

[29] E. Levitan and G. T. Herman, "A maximum *a posteriori* probability expectation maximization algorithm for image reconstruction in emission tomography," *IEEE Trans. Med. Imag.*, vol. MI-6, no. 3, pp. 185–192, Sep. 1987.

[30] A. Rosenthal, D. Razansky, and V. Ntziachristos, "Fast semi-analytical model-based acoustic inversion for quantitative optoacoustic tomography," *IEEE Trans. Med. Imag.*, vol. 29, no. 6, pp. 1275–1285, Jun. 2010.

[31] X. L. Deán-Ben, V. Ntziachristos, and D. Razansky, "Acceleration of optoacoustic model-based reconstruction using angular image discretization," *IEEE Trans. Med. Imag.*, vol. 31, no. 5, pp. 1154–1162, May 2012.

[32] A. Dima, N. C. Burton, and V. Ntziachristos, "Multispectral optoacoustic tomography at 64, 128, and 256 channels," *J. Biomed. Opt.*, vol. 19, no. 3, p. 036021, 2014.

[33] C. Lutzweiler and D. Razansky, "Optoacoustic imaging and tomography: Reconstruction approaches and outstanding challenges in image performance and quantification," *Sensors*, vol. 13, no. 6, pp. 7345–7384, 2013.

[34] G. Zhang, X. Cao, B. Zhang, F. Liu, J. Luo, and J. Bai, "MAP estimation with structural priors for fluorescence molecular tomography," *Phys. Med. Biol.*, vol. 58, no. 2, p. 351, 2012.

[35] G. P. Luke, S. Y. Nam, and S. Y. Emelianov, "Optical wavelength selection for improved spectroscopic photoacoustic imaging," *Photoacoustics*, vol. 1, no. 2, pp. 36–42, 2013.

[36] T. Kirchner, J. Gröhl, and L. Maier-Hein. (2017). "Local context encoding enables machine learning-based quantitative photoacoustics." [Online]. Available: https://arxiv.org/abs/1706.03595

[37] A. Hauptmann. (2017). "Model based learning for accelerated, limited-view 3D photoacoustic tomography." [Online]. Available: https://arxiv.org/abs/1708.09832

A. eMSOT Inversion

eMSOT is formulated as a constrained minimization problem in which the goal is to identify the values of a set of parameters θ_{opt} that minimize the difference between the measured normalized spectrum $\mathbf{p'(r)}$ and the modeled $\hat{\mathbf{p}}(\mathbf{r},\theta)$:

$$\theta_{opt} = \arg\min_{\theta} f_{\mathbf{r}}(\theta), \qquad (S1)$$

where $f_{\mathbf{r}}(\theta) = \|p'(\mathbf{r}) - \hat{p}(\mathbf{r},\theta)\|_2$. The inversion is performed simultaneously for several selected spatially distributed spectra, as described in the following steps:

1. A circular grid $\mathbf{G} = \{\mathbf{r}^{(k,l)} \mid k = 1...n_{ln}, l = 1...n_{pt}\}$ of n_{ln} lines, each consisting of n_{pt} pixels, is assigned to a region of interest in the MSOT image. MSOT spectra at the locations $\mathbf{r}^{(k,l)}$ specified by the grid points are recorded and normalized.

2. For the model parameters $\Theta = \{\theta_{\mathbf{r}} \mid \mathbf{r} \in \mathbf{G}\}$, a set of values Θ_{opt} is found that satisfies:

$$\Theta_{opt} = \arg\min_{\Theta} \sum_{\mathbf{r} \in \mathbf{G}} f_{\mathbf{r}}(\theta_{\mathbf{r}}) + \eta\|\mathbf{W}\mathbf{m}_1\|_2 + \eta\|\mathbf{W}\mathbf{m}_3\|_2, \quad (S2)$$

subject to :

$$m_2^{(k,l)} > m_2^{(k+1,l)}, m_2^{(k,l)} > m_2^{(k+1,l+1)}, m_2^{(k,l)} > m_2^{(k+1,l-1)}, \quad (S3)$$

$$m_1^{(k,l)} \in \left[\min_1^{k,l}\left(\hat{m}_1^{(k,l)}\right), \max_1^{k,l}\left(\hat{m}_1^{(k,l)}\right)\right], \qquad (S4)$$

$$m_3^{(k,l)} \in \left[\min_3^{k,l}\left(\hat{m}_3^{(k,l)}\right), \max_3^{k,l}\left(\hat{m}_3^{(k,l)}\right)\right], \qquad (S5)$$

$$c_{HHb}^{\prime(k,l)} \geq 0, c_{HbO2}^{\prime(k,l)} \geq 0,$$
$$m_i^{(k,l)} \in [MIN_i, MAX_i], i = 1...3, \qquad (S6)$$

where $x^{(k,l)}$ denotes the value of the parameter x at the location $\mathbf{r}^{(k,l)}$ specified by the point l in the line k of the grid $\mathbf{G}$: $x^{(k,l)} = x(\mathbf{r}^{(k,l)})$. The terms $\hat{m}_1(\mathbf{r})$, $\hat{m}_2(\mathbf{r})$ and $\hat{m}_3(\mathbf{r})$ are prior estimates of the eigenfluence parameters $m_1(\mathbf{r})$, $m_2(\mathbf{r})$ and $m_3(\mathbf{r})$, which are used to constrain the total search space based on a first estimate of tissue oxygenation as described [1]. In Eq. S2, $\mathbf{W}$ is a matrix that describes the connectivity between the pixels in the grid; $m_i = \left[m_i^{(1,1)},...,m_i^{(n_{ln},n_{pt})}\right]^T$ and the terms $\eta\|\mathbf{W}\mathbf{m}_1\|_2, i = 1,3$ are used to constrain the variability of the eigenfluence parameters among neighboring grid points. Eq. 3 constrains $m_2(\mathbf{r})$ to decrease with depth, which is consistent with simulations and has been described [1]. Eqs. S4 and S5 constrain the total search space for parameters m_1 and m_3 based on an initial approximation.

The parameters $\max_i^{k,l}$ and $\min_i^{k,l}$, which are the local limits defined for each point in the grid, depend upon the prior values $\hat{m}_i(\mathbf{r})$ and are defined based on simulations

[1]. MIN_i and MAX_i are the global limits of the parameters m_i defined at the eigenspectra model creation step. Constraints S3 – S6 are analytically described in [1].

3. The values $m_i^{(k,l)} : i = 1...3, k = 1...n_{ln}, l = 1...n_{pt}$ obtained for the sparsely distributed locations $\mathbf{r} \in \mathbf{G}$ on the grid are used to estimate m_i, $i = 1...3$ for every pixel within the convex hull of the selected points by means of interpolation. In this way, normalized fluence within the convex hull of $\mathbf{r} \in \mathbf{G}$ can be estimated using the three model parameters m_1 , m_2 and m_3 .

4. The absorption spectra measured at every spatial location are normalized and divided element-wise by the estimation of the normalized fluence obtained at step 3. This yields the true normalized optical absorption spectrum at each voxel. The optical absorption spectrum is subsequently unmixed using linear fitting to retrieve relative concentrations c'_{HbO2} and c'_{HHb} of oxy- and deoxyhemoglobin, respectively [2]. Tissue sO$_2$ is then computed as:

$$sO_2 = \frac{c'_{HbO2}}{c'_{HbO2} + c'_{HHb}}. \qquad (S7)$$

B. Effects of prior distribution design on the sO$_2$ estimation accuracy

Incorporation of prior knowledge has been shown to be important for the stability of the inversion [1], but the exact limits and shape of the prior distributions have not been thoroughly studied. The parameters that define the effect of the prior distributions are the shape parameter q , the deviations $\sigma_{m1}^{(s)}$ and $\sigma_{m1}^{(s)}$, and the weight w .

The parameter q defines how biased the distribution is towards the mean. In the case of $q = 2$, $GG_i, i = 1,3$ in Eq. 16 of the manuscript are the exponential parts of the normal distributions that favor values close to $\mu_{m1}^{(s)}$ and $\mu_{m3}^{(s)}$. Larger values of q introduce less bias towards $\mu_{m1}^{(s)}$ and $\mu_{m3}^{(s)}$ within $\sigma_{m1}^{(s)}$ and $\sigma_{m3}^{(s)}$, respectively, meaning that all the values within the specified ranges are nearly equally probable.

The deviations $\sigma_{m1}^{(s)}$ and $\sigma_{m3}^{(s)}$ constrain how much the values $m_1^{(s)}$ and $m_3^{(s)}$ may deviate from $\mu_{m1}^{(s)}$ and $\mu_{m3}^{(s)}$. Smaller values of $\sigma_{m1}^{(s)}$ and $\sigma_{m3}^{(s)}$ may result in optimal eigenfluence parameters that lie outside the allowed search space, while large values increase the probability that the algorithm will converge to a local minimum far from the optimal value. In the present study, $\sigma_{m1}^{(k,0)}$ was initially set to $0.01 \cdot (MAX_1 - MIN_1)$, or 1% of the maximum range of m_1 values defined at the model creation step described in Section II-B of the manuscript. Similarly, $\sigma_{m3}^{(k,0)}$ was initially set to $0.002 \cdot (MAX_3 - MIN_3)$. Subsequently, the algorithm was tested using the scaled values $\xi_1\sigma_{m1}^{(k,0)}$ and $\xi_3\sigma_{m3}^{(k,0)}$ as deviations for the surface pixels, where the scaling factors ξ_1 and ξ_3 varied from 1 to 3 in steps of 0.2.

In this way, $\sigma_{m1}^{(s)}$ and $\sigma_{m3}^{(s)}$ were optimized by the appropriate selection of ξ_1 and ξ_3.

The parameter w governs how much the imposed smoothness constraints affect the optimization procedure. Such constraints have been shown to improve inversion accuracy and stability, but excessively large values of w may degrade algorithm performance.

The parameters were optimized using the simulated IPR datasets described in Section III-C of the manuscript with all of the simulated spectra augmented with 2.5% zero mean Gaussian noise. The range of optical properties is summarized in Table 1 in the manuscript. BeMSOT was sequentially applied to 171 datasets for each value of the optimized parameter, while the remaining parameters were kept constant. The grid consisted of 5 lines of 8 pixels each. The sO$_2$ estimated by BeMSOT in each case was compared to the known sO$_2$ values and the estimation error was recorded. We quantified the accuracy of the algorithm in terms of mean absolute sO$_2$ estimation error.
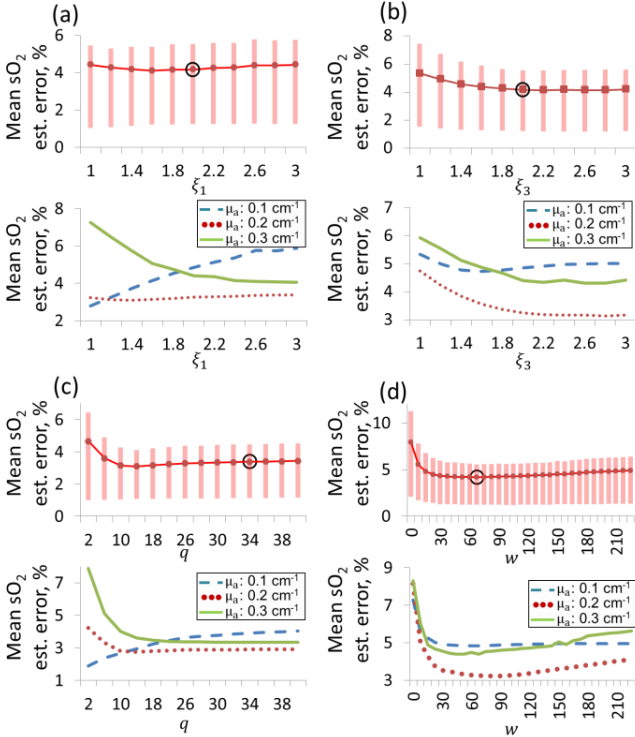
Suppl. Fig. 1: Optimization of the Bayesian eigenspectra algorithm in simulations. (a-d) Mean sO$_2$ estimation error (upper panels) and mean sO$_2$ estimation error grouped by the indicated mean μ_a levels (lower panels) as a function of (a) scaling factor ξ_1, (b) scaling factor ξ_3, (c) shape parameter q, or (d) parameter w. Red dots represent mean values, and red error bars denote the first and third quartiles. Values selected as optimal are marked with black circles.

Suppl. Fig. 1a-d show algorithm performance as a function of the scaling parameters ξ_1 and ξ_3, the shape parameter q and weight w. These results clearly show the importance of appropriately selecting $\sigma_{m1}^{(s)}$ and $\sigma_{m3}^{(s)}$. The algorithm requires a

certain amount of search space to converge to the optimal solution, but increasing $\sigma_{m1}^{(s)}$ and $\sigma_{m3}^{(s)}$ too much may result in convergence to a local minimum and thereby lead to high sO$_2$ estimation error. The lower panels in Suppl. Fig. 1a-b suggest that the mean error strongly depends on the optical properties of the dataset, with higher values of $\sigma_{m1}^{(s)}$ and $\sigma_{m3}^{(s)}$ being better for higher mean absorption (0.2 and 0.3 cm^{-1}).

Suppl. Fig. 1c highlights the improvement in algorithm performance with mean μ_a of 0.2 and 0.3 cm^{-1} for higher values of the shape parameter q, similar to the improvement observed at higher values of ξ_1 and ξ_3.

These simulations indicate that optimal values of the eigenfluence parameters lie far from the estimated values of $\mu_{m1}^{(s)}$ and $\mu_{m3}^{(s)}$ for simulations with higher mean absorption (0.2 and 0.3 cm^{-1}), especially in deep tissue. In these cases, the lower bias towards $\mu_{m1}^{(s)}$ and $\mu_{m3}^{(s)}$ and the higher $\sigma_{m1}^{(s)}$ and $\sigma_{m3}^{(s)}$ values mean that the algorithm can better estimate the eigenfluence parameters. In this study, we set parameters in order to optimize performance across all mean μ_a levels.

Suppl. Fig. 1d shows that smoothness constraints can strongly influence inversion, and that excessively high values of w (excessive smoothing) reduce performance. This was observed across all mean absorption levels in the simulated datasets.

C. Application of eMSOT and BeMSOT to experimental data.

Due to the difficulty in creating experimental datasets with known values of sO$_2$, the experimental datasets are very limited and therefore not appropriate for an extensive evaluation of the methods. We hereby include an example comparison of eMSOT and BeMSOT on two such experimental datasets (blood phantoms; Suppl. Fig. 2). Suppl. Fig. 2 shows quantification of sO$_2$ in two phantoms (panels (a-d) and (e-h), respectively). In both phantoms, a capillary tube filled with blood of known oxygenation (target sO$_2$) was inserted (0% for the phantom in a-d and 100% for the phantom in e-h). BeMSOT offers equivalent accuracy with eMSOT in such datasets. Nevertheless, due to the limited number of such datasets such a comparison can be inconclusive. We also note that due to the homogeneous structure of the phantoms a significant spatial inhomogeneity in SNR of the recorded spectra is difficult to achieve. More information about the tissue-mimicking phantoms can be found in [1].
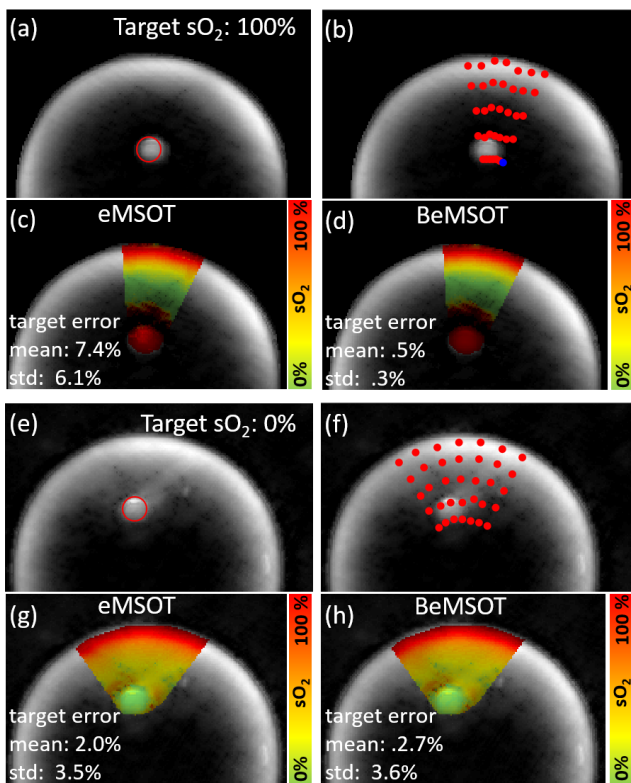
Suppl. Fig. 2: Performance of eMSOT and BeMSOT in experimental data. (a, e) OA images (one wavelengths presented) of tissue mimicking blood phantoms with capillary tubes (targets) filled with blood of known sO_2 (target sO_2). (b, f) Grids (red dots) used for inversion; (c, d, g, h) inversion results overlaid with the grayscale images obtained with eMSOT (c, g) and BeMSOT (d, h) for both phantoms. Statistics for absolute sO_2 estimation errors in the target areas are presented.

REFERENCES:

1. Tzoumas, S., et al., *Eigenspectra optoacoustic tomography achieves quantitative blood oxygenation imaging deep in tissues.* Nature Communications, 2016. **7**: p. 12121.
2. Cox, B., et al., *Quantitative spectroscopic photoacoustic imaging: a review.* J Biomed Opt, 2012. **17**(6): p. 061202.

Appendix B

Publication: Deep learning based spectral unmixing for optoacoustic imaging of tissue oxygen saturation

Deep Learning Based Spectral Unmixing for Optoacoustic Imaging of Tissue Oxygen Saturation

Ivan Olefir, Stratis Tzoumas, Courtney Restivo, Pouyan Mohajerani, Lei Xing and Vasilis Ntziachristos

Abstract— **Label free imaging of oxygenation distribution in tissues is highly desired in numerous biomedical applications, but is still elusive, in particular in sub-epidermal measurements. Eigenspectra multispectral optoacoustic tomography (eMSOT) and its Bayesian-based implementation have been introduced to offer accurate label-free blood oxygen saturation (sO₂) maps in tissues. The method uses the eigenspectra model of light fluence in tissue to account for the spectral changes due to the wavelength dependent attenuation of light with tissue depth. eMSOT relies on the solution of an inverse problem bounded by a number of *ad hoc* hand-engineered constraints. Despite the quantitative advantage offered by eMSOT, both the non-convex nature of the optimization problem and the possible sub-optimality of the constraints may lead to reduced accuracy. We present herein a neural network architecture that is able to learn how to solve the inverse problem of eMSOT by directly regressing from a set of input spectra to the desired fluence values. The architecture is composed of a combination of recurrent and convolutional layers and uses both spectral and spatial features for inference. We train an ensemble of such networks using solely simulated data and demonstrate how this approach can improve the accuracy of sO₂ computation over the original eMSOT, not only in simulations but also in experimental datasets obtained from blood phantoms and small animals (mice) *in vivo*. The use of a deep-learning approach in optoacoustic sO₂ imaging is confirmed herein for the first time on ground truth sO₂ values experimentally obtained *in vivo* and *ex vivo*.**

Index Terms—**Optoacoustic/photoacoustic imaging, multispectral optoacoustic tomography, photoacoustic tomography, deep learning, deep neural networks**

Ivan Olefir, Courtney Restivo, Pouyan Mohagerani and Vasilis Ntziachristos are with the Institute for Biological and Medical Imaging, Helmholtz Zentrum München, Neuherberg, Germany; and Chair of Biological Imaging, Technische Universität München. München, Germany (e-mails: ivan.olefir@tum.de, courtney.restivo@helmholtz-muenchen.de, pouyan.mohajerani@helmholtz-muenchen.de, v.ntziachristos@tum.de); Stratis Tzoumas and and Lei Xing are with the Department of Radiation Oncology, School of Medicine, Stanford University, Stanford, USA (e-mails: stzoumas@stanford.edu, lei@stanford.edu). *Ivan Olefir and Stratis Tzoumas contributed equally to this work*.
Correspondence to Vasilis Ntziachristos (v.ntziachristos@tum.de)

I. INTRODUCTION

Hemoglobin oxygen saturation is an important indicator of tissue function and disease. Quantification and spatial mapping of oxygen saturation (sO₂) in tissue provides valuable information for studies of tumor hypoxia [1], muscle activity [2], brain activation [3], metabolism [4] and other processes [5]. Modern imaging techniques that can provide quantitative spatial maps of sO₂ are limited ether by penetration depth [6], or by resolution [7]. Multispectral Optoacoustic Tomography (MSOT) can uniquely produce high resolution label-free spatial maps of sO₂ in deep tissue by unmixing the recorded optoacoustic (OA) spectra using the reference spectral signatures of oxygenated and deoxygenated hemoglobin [8-10]. The method opens a new way to study tissue oxygenation breaking though the barriers of other imaging techniques. However, the accuracy of sO₂ quantification in MSOT is limited by the fact that optical fluence varies with the location in the sample and wavelength of light, which affects the recorded OA spectra in a non-linear way [11-14]. This phenomenon, known as *spectral coloring* or *spectral corruption*, typically worsens with tissue depth and is challenging to model or predict due to the dependence of light fluence on the typically unknown optical properties in the whole illuminated region. Spectral coloring needs to be accounted for in order to achieve acceptable sO₂ quantification accuracy.

Several methods that reverse the effect of spectral coloring have been proposed [15-25]. One family of methods use a light propagation model that is described by the Radiative Transfer Equation (RTE) [15, 20, 21, 23, 24] or its approximations [15-17, 19, 21, 25] and attempt to invert a model predicting optical fluence. However, the application of these methods to sO₂ quantification in experimental data is challenging due to long computational times, reliance on perfect image reconstruction, and the need for accurate knowledge of various setup specific factors, e.g. illumination. Recently, eigenspectra MSOT (eMSOT) methodology was proposed [26]. The approach makes use of a simple linear spectral model for the wavelength dependence of optical fluence, termed the *eigenspectra model*, that describes fluence spectra based on only three parameters, termed the *eigenfluence parameters*. The spectral unmixing problem in

eMSOT is formulated as the eigenspectra model inversion that relies on optimization to find the eigenfluence parameters that accurately predict the spectrum of the optical fluence. The eigenspectra model is inverted using a set of several sparsely distributed locations in the region-of-interest (ROI) simultaneously, allowing to analyze well-reconstructed parts of the data. However, eMSOT inversion is based on a number of constraints. Such constraints in eMSOT are hand engineered, with the specific values of certain parameters selected in an *ad hoc* manner. These constraints aim to enforce spatial smoothness or depth-dependence of the eigenfluence parameters, and may not be entirely accurate or sufficient, and therefore may lead to inaccuracies with certain samples.

A Bayesian variant of eMSOT was developed that models the constraints as prior distributions and takes into account the noise in the recorded spectra [27]. This algorithm assumes that noise is spatially non-uniform, which can improve sO_2 estimation, especially in deep-seated, highly absorbing structures. Nevertheless, Bayesian eMSOT also suffers from the major restrictions of eMSOT such as the *ad hoc* constraints and the non-convex nature of the optimization problem. Additionally, it requires longer computational times for convergence as compared to the original eMSOT.

Herein we examine deep-learning (DL) for improving eMSOT. DL was selected due to its advantages over other types of machine learning (ML) methods, in particular its performance when learning highly non-linear mappings. ML, and DL in particular, has been previously proposed for optoacoustic sO_2 quantification. Ref. [28, 29] use convolutional neural networks (CNN) that are trained with simulated images. Since training occurs in the spatial domain (whole images), certain spatial features may be learned that do not always capture the appearance of the experimental data, which may affect the performance of the method. A fully connected architecture has been recently proposed to analyze OA spectra [30], independently of spatial dependencies. The method considers an OA spectrum without any knowledge of its location in tissue or neighboring spectra, and maps it to the corresponding sO_2 value. This allows for straightforward training and application since no spatial structure needs to be learned. However, such an approach is limited in accuracy since the problem of decoupling fluence and absorption is generally ill-posed [26], i.e. various combinations of fluence and absorption spectra may result in the same measured OA spectrum. In this respect, spectral information alone is not adequate for inferring blood oxygenation while a combination of spectral and spatial features is required. In [31], a random forest approach has been considered. To account for the spatial context, the method relies on so called Fluence Contribution Maps that are computed for a given system using the Monte Carlo simulations, which may be a potential drawback if the optical properties of the imaged objects significantly deviate from the ones assumed in simulations. Consequently, none of these methods has been demonstrated with experimental data against ground truth sO_2 values.

In this work, we consider the eMSOT framework, which operates on spatially distributed spectra and takes into account spectral and spatial information. We hypothesized that the eMSOT inversion could be replaced by a neural network which learns how to map a set of spatially distributed input spectra to the corresponding eigenfluence parameters. The neural network works without specifying any *ad hoc* inversion parameters or constraints but instead learns such constraints from a large simulated set of training data. Due to the prominent dependence of fluence on tissue depth, we use an architecture for the neural network that is based on a bi-directional recurrent neural network (RNN). The input spectra are split in a sequence depth-wise, where spectra measured at a similar depth constitute one point in the sequence. Using training, validation and test data derived from simulations, we show that the proposed architecture is well-suited to learn how to solve the inverse problem in eMSOT for data that covers a wide range of tissue appearances, physiologically relevant optical parameters and sO_2 levels. We demonstrate that DL-based eMSOT gives more accurate sO_2 estimates than conventional eMSOT on the simulated test data. Using the proposed architecture, we train an ensemble of networks that outperforms conventional eMSOT in the majority of cases for experimental datasets of blood phantoms and small animals, although no experimental data were used in training.

II. METHODS

A. Forward Model

In optoacoustics, illumination of tissue by a short laser pulse leads to the generation of ultrasound waves through thermoelastic expansion of the tissue due to light absorption. The ultrasound waves propagate towards the detectors and pressure signals are recorded. An image reconstruction algorithm is then applied to reconstruct the location- and wavelength-dependent initial pressure rise p_0 that relates to the optical fluence Φ and tissue absorption μ_a as follows [32]:

$$p_0(\mathbf{r}, \lambda) = \Gamma(\mathbf{r})\Phi(\mathbf{r}, \lambda)\mu_a(\mathbf{r}, \lambda), \qquad (1)$$

where $\mathbf{r}$ denotes the spatial coordinates, λ is the illumination wavelength and Γ is the spatially varying Grüneisen parameter.

In eigenspectra MSOT, correcting for the effects of fluence is achieved by using a linear spectral model for the normalized fluence $\Phi'(\mathbf{r}, \lambda) = \Phi(\mathbf{r}, \lambda)/\|\mathbf{\Phi}(\mathbf{r})\|_2$, $\mathbf{\Phi}(\mathbf{r})$ being a vector corresponding to the fluence spectrum at position $\mathbf{r}$; and $\|\mathbf{\Phi}(\mathbf{r})\|_2$ being the l_2-norm of the optical fluence spectrum [26]. It has been hypothesized that the fluence spectra in tissue cannot be arbitrary but instead can be approximated by a low-dimensional spectral model. Such a model is derived by performing principal component analysis (PCA) on a training set of normalized fluence spectra. The spectra in the dataset are simulated to capture the variability of fluence due to tissue depth and varying sO_2. It has been confirmed in simulations and experiments that only 3 principal components

$\Phi_i(\lambda), i = 1...3$ derived by PCA along with the mean spectrum of the training dataset $\Phi_M(\lambda)$ are enough to approximate normalized fluence spectra in tissue as follows [26]:

$$\Phi'(\mathbf{r}, \lambda) = \Phi_M(\lambda) + \sum_{i=1}^{3} m_i(\mathbf{r})\Phi_i(\lambda), \qquad (2)$$

where $\Phi_M(\lambda)$, $\Phi_i(\lambda), i = 1...3$ are termed the eigenspectra, and m_i are scalars referred to as the eigenfluence parameters. For a known spectrum $\Phi'(\mathbf{r}, \lambda)$, the eigenparameters can be computed by projecting $\Phi'(\mathbf{r}, \lambda)$ onto the eigenspectra: $m_i = \langle \mathbf{\Phi}'(\mathbf{r}) - \mathbf{\Phi}_M, \mathbf{\Phi}_i \rangle$, where $\langle \, , \, \rangle$ denotes inner product.

In the near-infrared spectral region, the model for tissue absorption is [33]:

$$\mu_a(\mathbf{r}, \lambda) = c_{HHb}(\mathbf{r})\varepsilon_{HHb}(\lambda) + c_{HbO2}(\mathbf{r})\varepsilon_{HbO2}(\lambda), \qquad (3)$$

where c_{HHb} and c_{HbO2} are the concentrations of deoxy- and oxyhemoglobin, respectively; and ε_{HHb} and ε_{HbO2} are the corresponding absorption spectra. To exclude the spatially varying Grüneisen parameter from consideration, eMSOT considers normalized initial pressure spectra (or simply normalized OA spectra), i.e. $\mathbf{p}'(\mathbf{r}) = \mathbf{p}_0(\mathbf{r})/\|\mathbf{p}_0(\mathbf{r})\|_2$. The eigenspectra model for a normalized OA spectrum therefore is [26]:

$$\hat{p}(\mathbf{r}, \lambda, \boldsymbol{\theta}) = \left(\Phi_M(\lambda) + \sum_{i=1}^{3} m_i(\mathbf{r})\Phi_i(\lambda) \right) \qquad (4)$$
$$\cdot \left(c'_{HHb}(\mathbf{r})\varepsilon_{HHb}(\lambda) + c'_{HbO2}(\mathbf{r})\varepsilon_{HbO2}(\lambda) \right).$$

where c'_{HHb} and c'_{HbO2} are relative concentrations of deoxygenated and oxygenated hemoglobin, respectively, and $\boldsymbol{\theta} = (m_1, m_2, m_3, c'_{HHb}, c'_{HbO2})$ is a vector of model parameters. In this study, a set of illumination wavelength from 700 nm to 900 nm with a step size of 10 nm (21 in total) is utilized.

B. eMSOT Algorithm Overview

Fig. 1 schematically describes the steps of eMSOT algorithm (top row) as well as the steps of the proposed modification based on the use of a neural network (bottom row). eMSOT can be summarized in the following steps:

1. **Grid Setup.** A sparse grid $\mathbf{G} = \{\mathbf{r}^{(k,l)} \mid k = 1...n_{ln}, l = 1...n_{pt}\}$ of points is placed in the ROI by intersecting n_{ln} radial lines and n_{pt} circles with decreasing radii. Fig. 1A shows an example of a grid $\mathbf{G}$ consisting of $n_{ln} = 8$ and $n_{pt} = 8$, i.e. 64 grid points in total (red dots) overlaid with a simulated OA image (grayscale). The spectra $\mathbf{p}(\mathbf{r})$ at spatial locations determined by the grid points $\mathbf{r} \in \mathbf{G}$ are selected for inversion and normalized.

2. **Priors.** Linear unmixing and Finite Element Method (FEM) simulation of light propagation governed by the Diffusion Equation [33] are used to obtain an estimate of optical fluence for the imaged object. This results in prior estimates $\hat{m}_1(\mathbf{r})$, $\hat{m}_2(\mathbf{r})$ and $\hat{m}_3(\mathbf{r})$ of the eigenfluence parameters $m_1(\mathbf{r})$, $m_2(\mathbf{r})$ and $m_3(\mathbf{r})$, respectively. Fig. 1B demonstrates maps of $\hat{m}_1(\mathbf{r})$, $\hat{m}_2(\mathbf{r})$ and $\hat{m}_3(\mathbf{r})$ for the dataset shown in Fig. 1A.

3. **Inversion.** In this key step, model inversion is performed by using a constrained minimization procedure as described in the Supplementary Material Sec. I. In the Bayesian version of the eMSOT algorithm, the inverse problem is derived in a probabilistic framework, with constraints replaced by prior distributions of the sought parameters and the level of noise in the measured signal taken into account [27]. At the core, however, still lies an optimization procedure. Fig. 1C schematically shows this step, with Fig. 1D demonstrating the output of the inversion, which is an estimate of the eigenfluence parameters for each grid point.

4. **Interpolation.** With the values of the eigenfluence parameters $m_i^{(k,l)} : i = 1...3, k = 1...n_{ln}, l = 1...n_{pt}$ for the grid points $\mathbf{r} \in \mathbf{G}$ available, interpolation is used to estimate the values of the eigenfluence parameters for every pixel within the convex hull of $\mathbf{G}$ [27]. Fig. 1E shows the resulting maps of the eigenfluence parameters overlaid in color with the simulated dataset shown in Fig. 1A (shown in grayscale).

5. **sO₂ Estimation.** For every pixel within the convex hull of $\mathbf{G}$, the corresponding values of the eigenfluence parameters are used to reconstruct the estimated fluence. The effect of spectral coloring is then reverted and the resulting spectra, i.e. scaled true absorption spectra, are unmixed linearly for the relative concentrations c'_{HbO2} and c'_{HHb} of oxy- and deoxyhemoglobin, respectively that are used to compute sO₂ [27]. Fig. 1F demonstrates the sO₂ computed by eMSOT in color overlaid with the p_0 map shown in grayscale.

A more detailed description of eMSOT can be found in the Supplementary Material (Sec. I).

C. Deep Learning Based eMSOT

While eMSOT has been shown to provide a much more accurate estimation of sO₂ in tissue as compared to the commonly used linear unmixing method, its accuracy is not absolute. Among other reasons, this is due to the inversion relying on *ad hoc*, hand-engineered constraints (Suppl. Eqs. S2-4) and regularization terms. The Bayesian version of eMSOT implements the mentioned constraints as prior distributions in an attempt to optimize the parameters of the distributions to improve the estimation accuracy while simultaneously weighing the measurements according to the amount of noise present. While certain progress has been made, the method is still prone to errors.

In this study, we aim to replace the optimization procedure in the inversion step with a neural network, resulting in a Deep Learning based eMSOT (DL-eMSOT). A function that maps
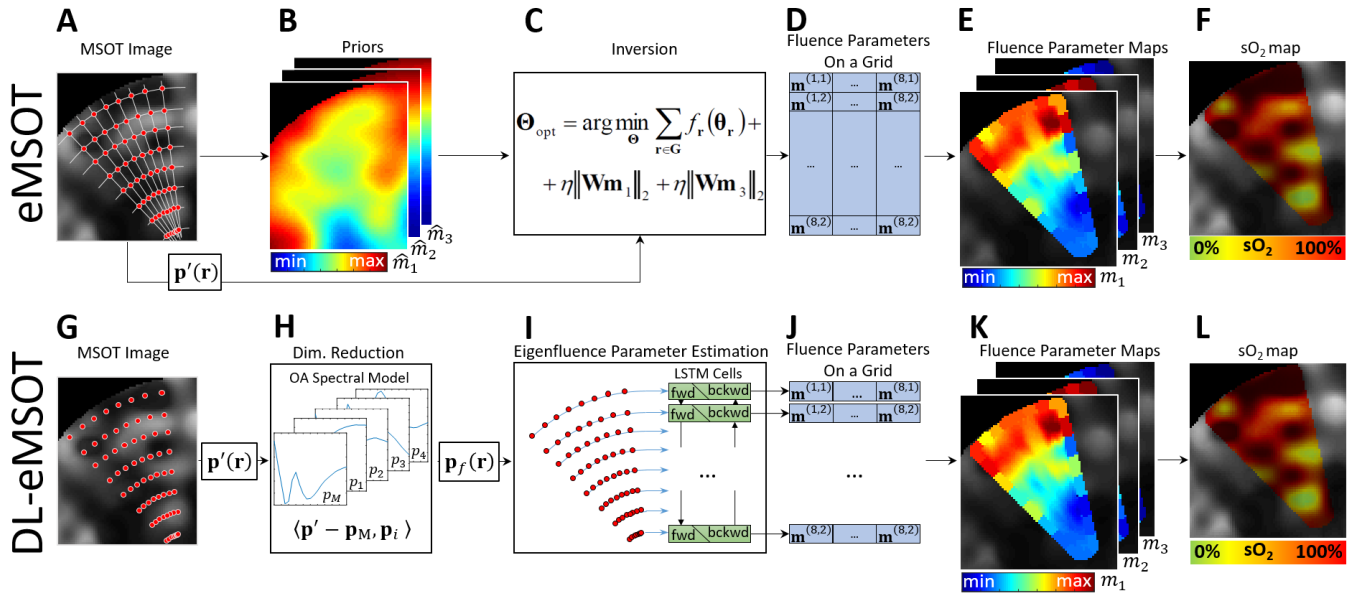
Fig. 1: Original eMSOT and DL-eMSOT. (A-F) Steps of eMSOT. **(A)** A grid of points (red dots) is applied to the dataset in the region of interest. **(B)** A simulation of light propagation is used to produce crude prior estimates of the eigenfluence parameters. **(C)** The priors obtained in (B) are used with the spectra sampled at the locations specified by the grid in (A) in the inversion step (optimization procedure). **(D)** The output of (C) is the eigenfluence parameters for the grid points. The values of the eigenfluence parameters are then interpolated between the grid points **(E)** and are used to estimate and correct for fluence. **(F)** The corrected spectra are linearly unmixed, resulting in an sO2 estimation map. **(G-L)** Steps of DL-eMSOT. **(G)** A grid of points (red dots) is applied to the dataset in the region of interest. **(H)** The spectra sampled at the locations specified by the grid in (G) are projected on a OA spectral model to reduce data dimensionality. **(I)** The resulting data $\mathbf{p}_f$ are fed into a neural network based on a combination of RNN and CNN. **(J)** The output of the neural network is the eigenfluence parameters for the grid points. **(K)** The values of the eigenfluence parameters are interpolated between the grid points and are used to estimate and correct for fluence. **(L)** The corrected spectra are linearly unmixed, resulting in an sO2 estimation map.

the set of original spectra to the set of eigenfluence parameters is learned by means of an appropriately trained neural network. In this way, inversion constraints, such as the spatial dependencies of the eigenfluence parameters, are learned from data rather than being hard-coded, which may improve the accuracy of the method.

C.1. DL-eMSOT Overview

The proposed method is summarized in Fig. 1G-L and consists of the following steps:

1. *Grid Setup*. The first step involves grid placement and spectra extraction and normalization, which are identical to step 1 of eMSOT described above. Here we fix $n_{\mathrm{ln}}=8$ and $n_{\mathrm{pt}}=8$. Fig. 1G shows an example of a grid $\mathbf{G}$ consisting of $n_{\mathrm{ln}}=8$ and $n_{\mathrm{pt}}=8$ grid points (red dots) overlaid with a simulated OA image (grayscale).

2. *Dimensionality Reduction*. Unlike eMSOT, after the normalization of the measured spectra, the resulting set of the normalized spectra $\mathbf{p}'(\mathbf{r}),\mathbf{r}\in\mathbf{G}$ (dimensions $8\times8\times21$) are projected on a 4-dimensional OA spectral model, previously described in [27], to obtain input features $\mathbf{p}_f(\mathbf{r}),\mathbf{r}\in\mathbf{G}$ (dimensions $8\times8\times4$) as follows:

$$\mathbf{p}_f(\mathbf{r}) = \left\{ \left\langle \mathbf{p}'-\mathbf{p}_M,\mathbf{p}_i \right\rangle_\lambda \mid i=1,...,4 \right\} \qquad (5)$$

where $\mathbf{p}_M$ is the mean spectrum of the OA spectral model and $\mathbf{p}_i$ are the four spectral components of the model that

are created by performing PCA on a training set of normalized OA spectra [27]. The OA spectral model describes all possible normalized OA spectra found in tissue under the assumption of hemoglobin being the main absorber. $\mathbf{p}_f(\mathbf{r}),\mathbf{r}\in\mathbf{G}$ are used as input data for the neural network. Fig. 1H illustrates this step which is similar to the traditional dimensionality reduction through PCA frequently used in ML, the difference being that PCA in the case of DL-eMSOT is not computed on the data used for training of the algorithm, but rather on a pre-computed dataset described in [27].

3. *Eigenfluence parameter estimation*. The estimation of the eigenfluence parameters is performed by feeding the input features $\mathbf{p}_f(\mathbf{r}),\mathbf{r}\in\mathbf{G}$ to the neural network that is based on a bi-directional Recurrent Neural Network. Fig. 1I schematically demonstrates the process. RNNs work with sequential data, therefore the input features need to be split into a sequence. Since the depth dependence of fluence is prominent, the input features are split depth-wise, i.e. the input features stemming from the spectra recorded at the same depth constitute one point in the input sequence. The network itself consists of two LSTM cells. One accepts inputs from the superficial layers of pixels first, the other one is starting at the deepest pixels. The output of the cells is then resized using a fully connected layer and reshaped into the $8\times8\times3$ shape followed by two convolutional layers to incorporate

further spatial, non depth-related dependencies. The output (shape 8×8×3) represents the eigenfluence parameters for the spectra in the grid. Fig. 1J shows the output of step 3 as a tensor of the eigenfluence parameters for the spectra in the grid. More details on the architecture of the network are provided in the following subsection.

4. *Interpolation*. This step is identical to step 4 of eMSOT. Fig. 1K shows the resulting maps of the eigenfluence parameters overlaid with the simulated dataset shown in Fig. 1G (grayscale).

5. *sO_2 quantification*. This step is identical to step 5 of eMSOT. Fig. 1L shows the resulting sO_2 map overlaid with the dataset shown in Fig. 1G.

To summarize, the proposed DL-eMSOT algorithm differs from eMSOT in (1) the data preprocessing step and (2) the eigenfluence parameter inference step. In the data preprocessing, DL-eMSOT works with data of reduced dimensionality and uses a OA spectral model previously introduced in [27] to achieve this dimensionality reduction. In the eigenfluence parameter estimation step, DL-eMSOT maps directly the input features to the corresponding eigenfluence parameters by employing a neural network rather than performing inversion using an optimization algorithm. Moreover, DL-eMSOT does not require prior estimates of eigenfluence parameters (step 2 of eMSOT). We train an ensemble of 50 neural networks and their median-filtered output for improved results.

C.2. Architecture

The core of the DL-eMSOT architecture was selected to be a bi-directional RNN. The intuition behind this design selection is the following. The shape of the light fluence spectrum and thus the art of spectral corruption at a specific point depends on the absorption spectra of the surrounding tissue. The spectral corruption manifests itself stronger as the imaging depth increases, while the shallow tissue spectra strongly affect the appearance of the deep tissue spectra. Both of these observations have been hard-coded as spatial constraints in eMSOT (Suppl. Eqs. S2-4) which were crucial for achieving good performance. Since RNNs are ideal in capturing dependencies along sequences, we selected an RNN that operates across the tissue depth to capture the prominent depth dependency of spectral corruption. The grid that samples the spectra for eMSOT can be viewed as containing several layers of points coming from similar depth making it suitable as an input to an RNN. To capture neighbor dependencies between spectra with similar depth we allowed a relatively large number of hidden units in the RNN cells (1024) to allow for more expressive power, as well as applied several convolutional layers to the output of the RNN. Fig. 2 demonstrates the used architecture schematically and a detailed description of the parameters used is provided below.

Input is the tensor of input features. Its size is 8×8×4, 8x8 corresponds to grid dimensions and 4 being the number of features corresponding to each spectrum after dimensionality reduction. The features corresponding to each of the grid layers are concatenated into a single vector thus resulting in a 8×32 tensor, which can be viewed as a sequence of 8 feature vectors that will be used as an input to the bi-directional RNN.

The bi-directional *RNN* is the core element of the architecture and consists of two LSTM cells of identical structure (1×32 input vector, 1×1024 output vector, depth 8). In our experiments we found that using a bi-directional RNN was crucial for achieving optimal performance, while network depth or the number of output neurons per layer were of reduced importance (see Sec. II-D Competing Architectures) The outputs of the two LSTMs are concatenated into an 8×2048 tensor, and reshaped into a 1x16,384 vector to be passed through a dense layer.

Dense layer with 192 output units serves as a means of resizing the output of the bi-directional RNN to the desired output size. The output of the dense layer is reshaped into a 8×8×3 tensor which has the shape of the network output (3 eigenparameters per spectrum on an 8x8 grid).

Two convolutional layers of the *CNN* block (Conv. 1 with 3 2x2 filters and Conv. 2 with 3 1x1 filters) are meant to add expressive power to the network and allow to better account for any local spatial dependencies, specifically within a layer of spectra coming from the same depth.

Tanh are used as activation functions in all layers.

Further notes on the selection of certain hyperparameters (i.e. grid size and ensemble size) are available in the Supplementary Material (Sec. IV).
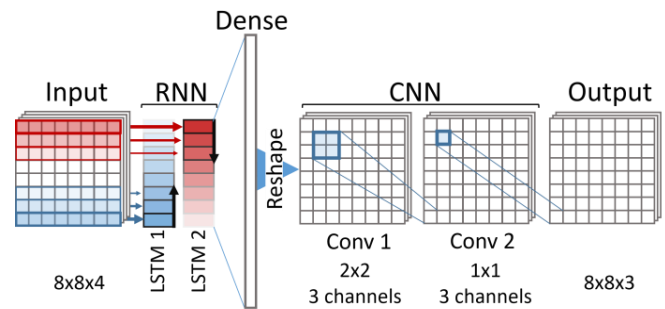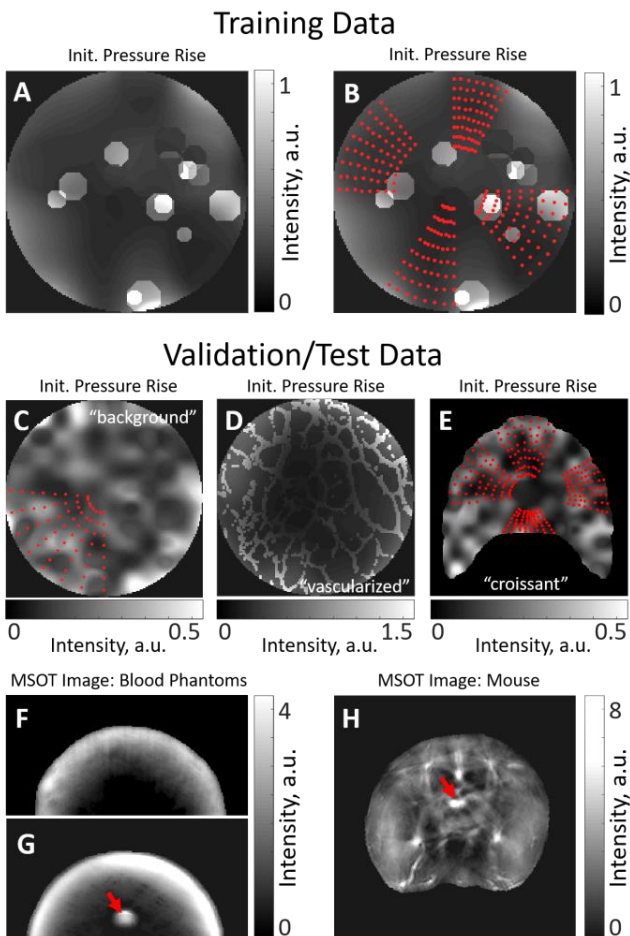

Fig. 2: DL-eMSOT Architecture.

D. Competing Architectures

For reference, we train two more models based on a simple architecture consisting of six fully connected layers and evaluate their performance on simulated data as described above. Similarly to the network proposed in [30], the model termed **DENSE (sO_2)** maps a single input spectrum directly to the corresponding sO_2 value, therefore not taking into account any spatial information. The second model termed **DENSE (fluence)** attempts to solve the inverse problem of eMSOT, but with a less sophisticated architecture than the one proposed for DL-eMSOT. The structure of input and output of this network is therefore identical to that of the proposed RNN based architecture, but the network is based solely on fully connected layers. Details on the reference models are provided in the Supplementary Material (Sec. II).

E. Training

Both all the DL-eMSOT models as well as all the models from the competing architectures were trained with the same parameters *(*batch size: 128; Loss: L2; Optimizer: ADAM; epochs: 200).

Training Data

Init. Pressure Rise

Init. Pressure Rise

Validation/Test Data

Init. Pressure Rise

Init. Pressure Rise

Init. Pressure Rise

MSOT Image: Blood Phantoms

MSOT Image: Mouse

Fig. 3: Training, validation and test data. (A) Simulated OA image (one wavelength presented) used for sampling grids for training. The background is smoothly varying, with numerous randomly placed circular insertions of varying intensity. **(B)** Examples of four grids (red dots) determining the locations of the OA spectra sampled form the dataset presented in **(A)**. The grids have varying width, depth and position. **(C)** Simulated OA image ("background" dataset, one wavelength presented) used for sampling spectra for validation and test of the trained models together with an example of a grid defining the locations of the OA spectra to be sampled. Validation and test datasets have no circular insertions but may have a more inhomogeneous background. Grids used for validation and test may be wider than the grids used for training. **(D)** Simulated OA image ("vascularized" dataset, one wavelength presented) used for sampling test data that shows structures simulating a network of vessels. **(E)** Simulated OA image ("croissant" dataset, one wavelength presented) used for sampling test data from irregularly shaped tissue. The used grids are shown with red dots. **(F)** A uniform blood phantom of known oxygenation and **(G)** a blood phantom with an inserted blood-filled capillary tube (target, red arrow) of known oxygenation. **(H)** An abdominal cross-section of a mouse with an inserted blood-filled capillary tube (target, red arrow) of known oxygenation.

During training, every OA spectrum was augmented with white Gaussian noise $\epsilon \sim N(\mu, \sigma)$ with zero mean μ and standard deviation σ randomly sampled from the uniform distribution $\sigma \sim U(.005 - .015)$ before performing the dimensionality reduction.

The best model was selected by evaluating the absolute error in sO_2 estimation on a validation dataset (see Sec. III-C) every 10 training iterations. If the obtained result was better than that of the previously selected best model, the current model was saved as the new best model. Otherwise, the current model was discarded.

DENSE (fluence) was trained using the same data as the DL-eMSOT. DENSE (sO_2) used the same training dataset, but every spectrum was considered as a separate example unlike DL-eMSOT and DENSE (fluence), where a grid of sampled spectra constituted a training example.

F. Performance Assessment

We quantify the performance of the algorithm in terms of absolute error in sO_2 estimation: $\left| sO2_{alg} - sO2_{GS} \right|$, where $sO2_{alg}$ is the sO_2 value obtained by a certain algorithm and $sO2_{GS}$ is the ground truth value. For simulated data, gold standard values are naturally available for every location in the image. For experimental data, gold standard values are available for certain locations (see Fig. 3). We note that we use this absolute error metric throughout the entire manuscript and it should not be confused with relative sO_2 estimation error. The errors presented herein in per cent are still absolute, since sO_2 is a ratiometric quantity measured in %.

Due to the large size of the evaluation datasets and in order to reduce computational effort, the interpolation step for the simulated data in eMSOT and DL-eMSOT was skipped and the sO_2 error is computed and reported only for the grid pixels. In the Supplementary Material we present the effect of the interpolation in the overall error in a smaller dataset. The interpolation step was retained in the case of experimental data. For the 50 trained DL-eMSOT models, test results on simulated test data are reported per model and as an ensemble, where the outputs of 50 models are median-filtered. Test results on experimental data are reported from an ensemble.

III. DATA

The generation of an appropriate training, validation and test dataset is particularly crucial for obtaining a well-trained neural network that would not only work in specific simulations, but also generalize well to cases not covered by the training dataset. Since the generation of a large and versatile experimental optoacoustic dataset of living tissue with known sO_2 values is impractical, in this work we had to resort to using simulations for the purpose of creating training, validation and test data. Nevertheless, in order for the model to have practical value, it needs to be applicable in experimental data as well. Therefore, we also test the model using a limited set of experimental MSOT images of blood phantoms and mice with available ground truth sO_2 values. We note that no experimental images are used for training the model. In the following subsections, we describe the used data in detail. Fig. 3 shows representative examples of the data used.

A. Simulations of Multispectral p_0 maps

In order to generate training, validation and test data-sets of multispectral optoacoustic images with available ground truth of fluence and sO$_2$ values, simulations of initial pressure rise p_0 were used. A circular slice of tissue with 1 cm radius with varying optical properties was assumed. A detailed description of the algorithm for simulating p_0 maps is provided in [27], below we provide a brief summary of the steps.

1. *Optical properties of the background tissue*: Randomly varying spatial maps of background tissue absorption $\mu_a(\mathbf{r})$ at 800 nm (isosbestic point of hemoglobin), reduced scattering $\mu'_s(\mathbf{r})$ (assumed constant with wavelengths) and sO$_2$ are generated.

2. *(OPTIONAL) Optical Properties of structures*: $\mu_a(\mathbf{r})$, $\mu'_s(\mathbf{r})$ and sO$_2$ maps of the background are augmented to represent structures.

3. *Extension to multispectral range*: Using the output of step 1 or 2 and the absorption spectra of hemoglobin, the optical absorption map $\mu_a(\mathbf{r},\lambda)$ is created for all the illumination wavelengths.

4. *Light propagation*: Light propagation through the sample is simulated by solving the Diffusion Equation using FEM [33] to obtain fluence map $\Phi(\mathbf{r},\lambda)$.

5. *Multispectral p_0 map*: The product of $\mu_a(\mathbf{r},\lambda)$ and $\Phi(\mathbf{r},\lambda)$ results in a simulated map of the initial pressure rise $p_0(\mathbf{r},\lambda)$ assuming $\Gamma(\mathbf{r})=1$. Such an assumption does not affect the performance of the considered algorithms since the eMSOT type of algorithms use normalized OA spectra.

Various randomly generated maps of optical properties were used to simulate a range of biological tissues [34]. Values for both $\mu_a(\mathbf{r})$ and $\mu'_s(\mathbf{r})$ were drawn from normal distributions with means and standard deviations that were different for training, validation and test data to obtain a wide range of biologically plausible scenarios. The mean values of the optical parameters as well as standard deviations for every type of dataset are presented in Supplementary Table 1.

Notably, generation of p_0 maps relies on 2D simulations of light propagation (i.e. assuming infinite sample thickness in z dimension), mainly for computational reasons. Since any fluence pattern simulated in 3D may be obtained by constructing a corresponding 2D simulation with modified optical properties, using 2D simulations in this study is justified by using an extensive set of randomly distributed optical properties.

B. Training Data

For obtaining the training data for the neural network, the following steps were performed:

1. p_0 *Simulations*: Simulated multispectral p_0 maps of tissue were created as described above (1,368 distinct simulations in total). The optical properties were sampled from the normal distributions with the parameters summarized in Supplementary Table 1. The random optical absorption maps were created with low spatial heterogeneity to simulate soft tissue. To include also areas of higher spatial heterogeneity due to vasculature, the simulations were augmented with 0, 4, 8 or 16 randomly located circles of optical absorption that is up to five times (exact number set randomly) higher than the background. The radius of every circle varied also randomly. The sO$_2$ of the circles was randomly set to be 20%-60% higher or lower than the mean sO$_2$ of the background. Fig. 3A shows an example of a generated p_0 map used for training.

2. *Grid Placement*: The grids (8 per dataset) of varying depth, angular width and location were placed on the datasets generated in step 1. Fig 3B demonstrates 4 grids (red dots) placed on the dataset shown in Fig. 3A. The grids always contained 8×8 location points.

3. *Spectra Sampling*: For every grid, the simulated spectra at the locations of the grid points were sampled, normalized and saved, resulting in 10,944 training examples, with one grid of spectra representing one example.

4. *Labels Sampling*: For every recorded spectrum, the corresponding fluence spectrum was sampled from the simulated light fluence map. Each fluence spectrum was normalized and projected on the eigenspectra, yielding a set of three real-valued parameters (m_1,m_2,m_3) corresponding to the labels. The corresponding sO$_2$ values are also sampled, resulting in the sO$_2$ labels dataset.

C. Simulated Validation and Test Data

When producing the validation and test data, the aim was to create data that is sufficiently different in structure to the training data to test the generalization ability of the trained models. Validation and test data consisted of three distinct datasets.

The "background" dataset was created as follows:

1. p_0 *Simulations*: Simulated multispectral p_0 maps of the background were created as described above (Section III-A), resulting in 228 distinct simulations in total. The optical properties were sampled from the distributions with the parameters summarized in Supplementary Table 1. The random absorption maps were created with spatial heterogeneity varying from low to high between datasets. No augmentations of $\mu_a(\mathbf{r})$, $\mu'_s(\mathbf{r})$ and sO$_2$ maps were performed.

2. *Grid Placement*: The grids (8 per dataset) of varying depth, angular width and location were placed on the datasets generated in step 1. The maximum width of the sampled grids exceeded that of the grids in the training data.

3. *Spectra Sampling*: Identical to the training data. The result is 1,824 examples.

4. *Labels Sampling*: Identical to the training data.

Fig. 3C shows an example of a generated p_0 map form "background" dataset with a grid (red dots). Note the width of the grid as compared to the grids shown in Fig. 3B.

The "vascularized" dataset was created as follows:

- p_0 *Simulations*: Simulated multispectral p_0 maps of the background were created as described above (570 distinct simulations in total). The optical properties were sampled from the distributions with the parameters summarized in Supplementary Table 1. The random absorption maps were created with low spatial heterogeneity and augmented with a structure that represents a network of large vessels.
- *Grid Placement*: Identical to "background" dataset.
- *Spectra Sampling*: Identical to the training data. The result is 4,560 examples.
- *Labels Sampling*: Identical to the training data.

Fig. 3D shows an example of a generated p_0 map form "vascularized" dataset.

The "croissant" dataset was created similarly to the "background" dataset, with a notable difference being the irregular shape of the simulated tissue (after which the dataset is named) as compared to other datasets. The purpose of this dataset is to examine the applicability of the considered quantification methods to a dataset with the geometry that is substantially different from that of the training data. The dataset consists of 304 simulations and 4 grids sampled per simulation (1,216 examples in total). Fig. 3E shows a generated p_0 map form "croissant" dataset with the sampled grids denoted by the red dots. We note that the field of view in Fig. 3E is 2.5x2.5 cm^2, while in Fig. 3A-D the field of view is 2x2 cm^2. More details on simulations are available in the Supplementary Material (Sec. III).

For every model, "background" dataset was shuffled and split, with 10% of the set used for model validation and 90% used for test. "Vascularized" and "croissant" datasets were used as test entirely.

D. Experimental Test Data

For the neural network to have practical value, and since it is trained purely on simulated data, it is crucial to generalize well to experimental data in terms of accuracy in sO$_2$ estimation. For this reason, 3 types of experimental data with the available ground truth were used that will be referred to as Uniform Phantoms, Insertion Phantoms and Mouse Data.

Phantoms. The 2-cm-diameter cylindrical tissue mimicking phantoms were created by mixing agarose, intralipid and porcine blood. The details can be found in [26]. Each phantom contained blood of known oxygenation (0% or 100%). Two types of phantoms were used. Uniform Phantoms are homogeneous with the ground truth sO$_2$ values known for the whole phantom. Fig. 3F demonstrates an MSOT image (one wavelength shown) of a uniform phantom. Insertion phantoms contain a capillary tube filled with blood of known oxygenation. Fig. 3G shows an MSOT image (one wavelength shown) of an insertion phantom. The location of the capillary tube is marked with a red arrow.

Mouse Data. All procedures involving animal experiments were approved by the Government of Upper Bavaria. Nude-Foxn1 mice were imaged under anesthesia while breathing medical air, followed by 100% O$_2$. A capillary tube filled with porcine blood of known oxygenation (0% or 100%) was rectally inserted in each imaged animal. More details can be found in [26]. In the final imaging stage, animals were

Table 1. Performance of eMSOT and DL-eMSOT in Simulations

	Mean Error	Median Error	Standard Deviation	[25% , 75%] Percentiles
"background" test data				
eMSOT	4.9%	3.5%	4.8%	[1.5% , 6.8%]
DL-eMSOT	1.4%	0.9%	1.5%	[0.3% , 1.9%]
DL-eMSOT (ensemble)	-	-	-	-
DENSE (sO$_2$)	7.0%	4.1%	8.4%	[1.4% , 9.7%]
DENSE (fluence)	2.8%	2.0%	2.8%	[0.8%, 3.8]
"vascularized" test data				
eMSOT	11.5%	6.87%	14.25%	[2.93% , 13.78%]
DL-eMSOT	3.2%	1.8%	4.5%	[0.6% , 4.0%]
DL-eMSOT (ensemble)	3.0%	1.6%	4.2%	[0.6% , 3.7%]
DENSE (sO$_2$)	9.9%	5.5%	12.7%	[1.9% , 12.9%]
DENSE (fluence)	5.4%	3.4%	6.1%	[1.4%, 7.1%]
"croissant" test data				
eMSOT	4.8%	5.0%	3.4%	[1.4%, 6.5%]
DL-eMSOT	2.3%	2.5%	1.8%	[0.5%. 3.5%]
DL-eMSOT (ensemble	2.0%	2.0%	1.5%	[0.5%, 2.8%]
DENSE (sO$_2$)	7.1%	7.1%	5.1%	[2.2%, 9.6%]
DENSE (fluence)	2.4	2.4	1.7	[0.7%, 3.3%]

sacrificed with an overdose of CO$_2$. Fig. 3H shows an MSOT image of a mouse. The location of the capillary tube is marked with a red arrow.

All experimental data has been obtained with the commercially available inVision256 system [35] and was used for test in its entirety.

IV. RESULTS

A. Simulated Data

First we trained the neural networks (DL-eMSOT, DENSE (fluence)) using 10944 grid examples coming from 1368 simulations of p_0 maps with varying optical properties, spatial structures and sO$_2$ levels. DENSE (sO$_2$) is trained on all the available simulated OA spectra with the corresponding sO$_2$ values used as labels. Then we compared the performance of the resulting algorithms with conventional eMSOT for estimating sO$_2$ in an independent set of ~7500 test grid examples coming from simulated datasets of "background", "vascularized" and "croissant". The test grids included examples having larger angular width than any of the training samples. "background" and "vascularized" simulations also differed from the training simulations in terms of spatial variability of the optical properties ("background") and type of structures present in the image ("vascularized"). The "croissant" dataset differed in simulation geometry. Table 1 provides average test results for the 50 trained DL-eMSOT models as well as for an ensemble and reference networks on

datasets of "background", "vascularized" and "croissant". Since data from the "background" dataset was partly used for validation of the models (see Sec. III-C), it was not used for testing the performance of the ensemble. The results of eMSOT obtained on the same datasets are also shown for reference. As evident, DL-eMSOT achieves the best performance in terms of sO_2 quantification accuracy out of all the considered methods and seems to generalize well to the simulated data that is dissimilar to the training examples. Notably, DENSE (sO_2) which does not consider spatial information demonstrates performance that is worse than that of deep learning methods that take the information from the spatially distributed grid as input. DENSE (fluence) performs consistently better than the original eMSOT, but fails to outperform DL-eMSOT, which is the overall best performing algorithm in our tests.
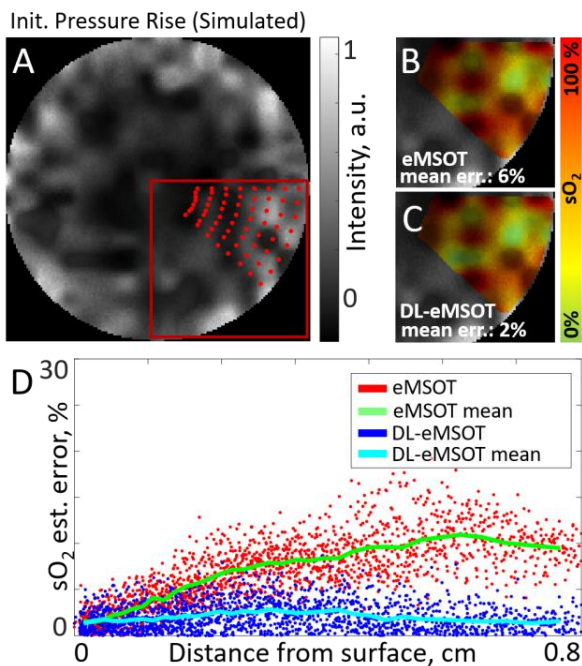
Fig. 4. Performance of eMSOT and DL-eMSOT in Simulated Data. **(A)** Simulated multispectral p_0 map (grayscale, one wavelength presented) with a grid shown with red dots. Red square marks the ROI shown in (B) and(C). **(B, C)** sO_2 for the grid shown in (A) produced by eMSOT (B) and DL-eMSOT (C) shown in color overlaid on the p_0 map. Mean sO_2 estimation error presented for both methods. **(D)** sO_2 estimation errors produced by eMSOT (red, mean shown in green) and DL-eMSOT (blue, mean shown in cyan) presented per tissue depth.

Fig. 4 shows a representative example comparing the performance of eMSOT and DL-eMSOT in a multispectral p_0 simulation coming from the "background" dataset that was not used for validation of any network in the ensemble. Fig. 4A shows a simulated multispectral p_0 map (one wavelength presented) in grayscale together with a grid (red dots) defining the locations of the spectra selected for the application of the quantification methods. The red square defines the ROI shown in Fig. 4B, C. Fig. 4B, C show the sO_2 quantification results produced by eMSOT (Fig. 4B) and DL-eMSOT (Fig. 4C) with mean error of both methods indicated in the corresponding
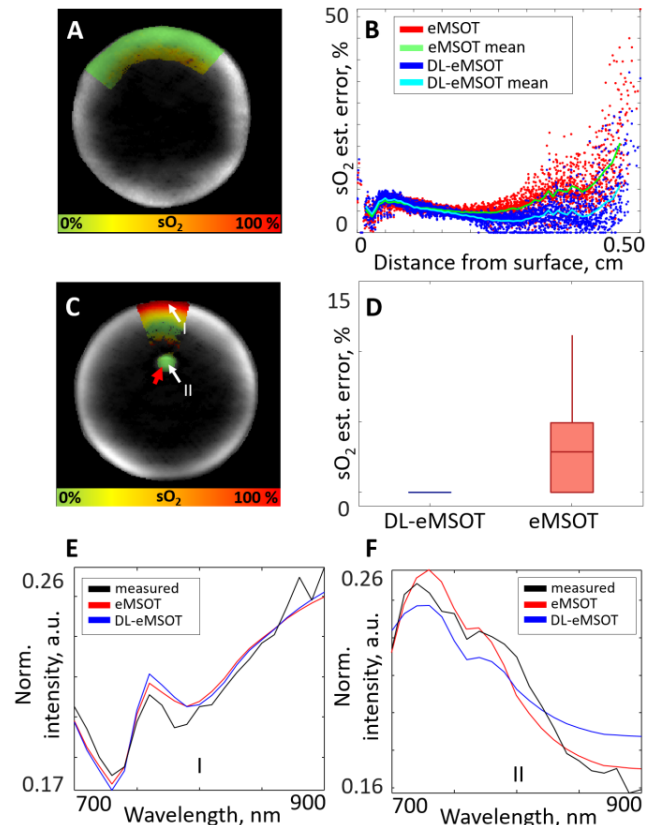
Fig. 5: Comparison of DL-eMSOT and eMSOT for sO_2 estimation in phantom data. **(A)** An MSOT image (one wavelength presented) of a deoxygenated uniform blood phantom with the overlaid color-coded result of DL-eMSOT application. **(B)** Errors in sO_2 estimation for eMSOT (red/green) and DL-eMSOT (blue/cyan) for the phantom shown in (A) on the same grid, presented per pixel depth. **(C)** An MSOT image (one wavelength presented) of a blood phantom with a capillary tube (target) filled with deoxygenated blood (red arrow) with the overlaid color-coded result of DL-eMSOT application. The labels I and II mark the locations of the spectra presented in (E) and (F), respectively. **(D)** Errors in sO_2 estimation for eMSOT and DL-eMSOT at the location of the target shown in (C). **(E, F)** Spectra at locations shown in (C) (black), together with the corresponding fits obtained with eMSOT (red) or DL-eMSOT (blue) algorithms.

panels. Fig. 4D shows the errors produced by both methods as a function of tissue depth. It can be observed that DL-eMSOT manages to better account for spectral coloring as tissue depth increases.
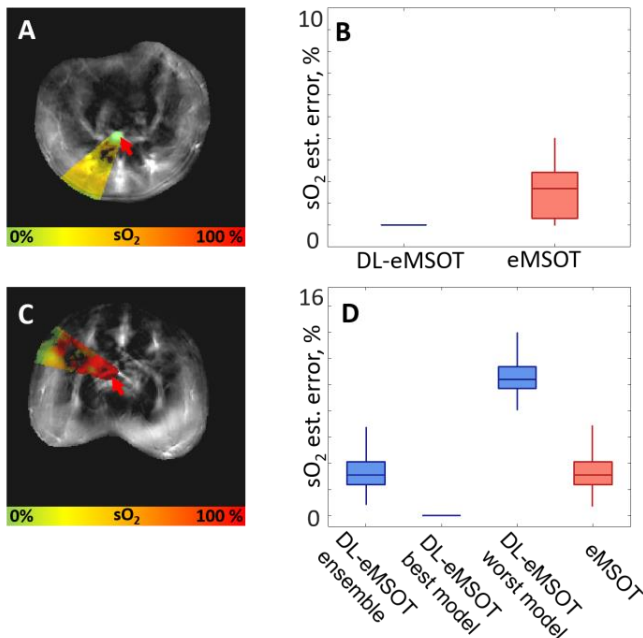
B. Experimental Data

To test the ability of the DL-based eMSOT to generalize to experimental data, we applied an ensemble of 50 neural networks to experimental data.

B.1. Phantoms

Fig. 5 demonstrates the performance of DL-eMSOT ensemble on experimental datasets of the following types: Uniform Phantom (Fig.5A-B), and Insertion Phantom (Fig.5C-F). Fig. 5A shows an MSOT image of a uniform deoxygenated phantom with the color-coded map of sO_2 estimated by DL-eMSOT. Fig. 5B demonstrates the absolute sO_2 estimation

errors obtained by eMSOT (red, green) and DL-eMSOT (blue, cyan) within the same ROI shown in Fig. 5A. The presented errors are sorted per pixel depth. It can be readily seen that DL-eMSOT estimates sO_2 with better accuracy. Fig. 5C shows an MSOT image of an insertion phantom with the color-coded map of sO_2 estimated by DL-eMSOT. The location of the tube filled with deoxygenated blood is marked with a red arrow. The white arrows (I and II) denote the positions at which the spectra analyzed in Fig. 5E, F, respectively, were measured. Fig. 5D shows errors in sO_2 estimation obtained by eMSOT and DL-eMSOT at the location of the inserted tube. Fig 5E, F demonstrate the spectra measured at locations I and II, respectively, shown in Fig. 5C (black) together with the corresponding fits obtained by eMSOT (red) and DL-eMSOT (blue). Notably, the spectra produced using the eigenfluence parameters found by DL-eMSOT are meaningful.

B.2. Mouse Data

Fig. 6: Comparison of DL-eMSOT and eMSOT for sO_2 estimation in experimental animal data. (A, C) MSOT images (one wavelength presented) of abdominal cross-sections of two mice with capillary tubes (targets) filled with blood of known oxygenation (0% (A) and 100% (C), red arrows) with the overlaid color-coded results of DL-eMSOT application. **(B)** sO_2 estimation errors of eMSOT and DL-eMSOT obtained at the location of the target shown in (A). **(D)** sO_2 estimation errors of eMSOT and DL-eMSOT (ensemble, best performing model and worst performing model) obtained at the location of the target shown in (C).

Fig. 6A, C show MSOT images of abdominal cross-sections of two mice with the color-coded maps of sO_2 estimated by DL-eMSOT. The locations of the tubes filled with blood of known oxygenation (0% in Fig. 6A and 100% in Fig. 6C) are marked with red arrows in respective panels. Fig. 6B shows errors in sO_2 estimation obtained by eMSOT and DL-eMSOT at the location of the inserted tube. Fig. 6C shows errors in sO_2

estimation obtained by eMSOT and DL-eMSOT (ensemble, best performing model and worst performing model) at the location of the inserted tube. It can be observed that the dataset presented in Fig. 6C, D constitutes a challenging case for the single RNN-based models as there is high discrepancy between the best and the worst performing models. This case highlights the importance of using an ensemble of models for reducing the upper bound of error.

Fig. 7 summarizes and compares the performance of DL-eMSOT and eMSOT in all available experimental datasets (25 in total) with the corresponding ground truth: uniform phantoms (Fig. 7A), insertion phantoms (Fig. 7B) and mouse data (Fig. 7C). The results are grouped per ground truth sO_2 level: 0% (left panels) and 100% (right panels). Black dashed lines separate results obtained for separate datasets. As evident, DL-eMSOT outperforms eMSOT in 21 cases out of 25 and achieves comparable sO_2 estimation accuracy in 3 of the remaining 4 cases.

The performance of DENSE (fluence) and DENSE (sO_2) on the available experimental data is presented in the Supplementary Material (Sec. V). In summary, DENSE (sO_2) produces very high errors (up to ~90%) in some of the considered cases while DENSE (fluence) is much more robust and is often comparable in its performance to eMSOT and DL-EMSOT, highlighting the importance of the spatial context in the problem of fluence correction.

V. DISCUSSION AND CONCLUSION

An increasingly popular technology, DL has been proposed for solving a variety of problems in imaging [36, 37]. In optoacoustic imaging in particular, DL has been considered for image reconstruction [38], artifact removal [39, 40] and sO_2 quantification [28, 30]. In this study, we design an architecture to solve the inverse problem of eMSOT, i.e. correcting a set of input optoacoustic spectra for light fluence and computing sO_2. We observe that the proposed methodology improves the sO_2 quantification accuracy as compared to eMSOT.

The combination of spectral and spatial information is essential for achieving sO_2 quantification accuracy in MSOT. A straightforward way to incorporate the spatial information into the analysis is to use CNN-based architectures [28, 29]. However, due to the need to use simulated data for training, the resulting networks would be biased by the structure of the training data impeding their generalization. Sparse sampling of the analyzed spectra used in DL-eMSOT alleviates this problem while still providing spatial context, ensuring both adequate performance and generalization to experimental data.

Due to the strong dependence of optical fluence on tissue depth, we split the input spectra into a sequence along the tissue depth, i.e. spectra at the same tissue depth constitute one element of the input sequence. Accordingly, we base the architecture of the neural network on a bi-directional RNN that has been designed to handle sequential data well. We find that the proposed architecture is better suited for learning to solve the inverse problem of eMSOT than a less sophisticated architecture that is designed without the specific problem characteristics in mind. Importantly, in this study we have not
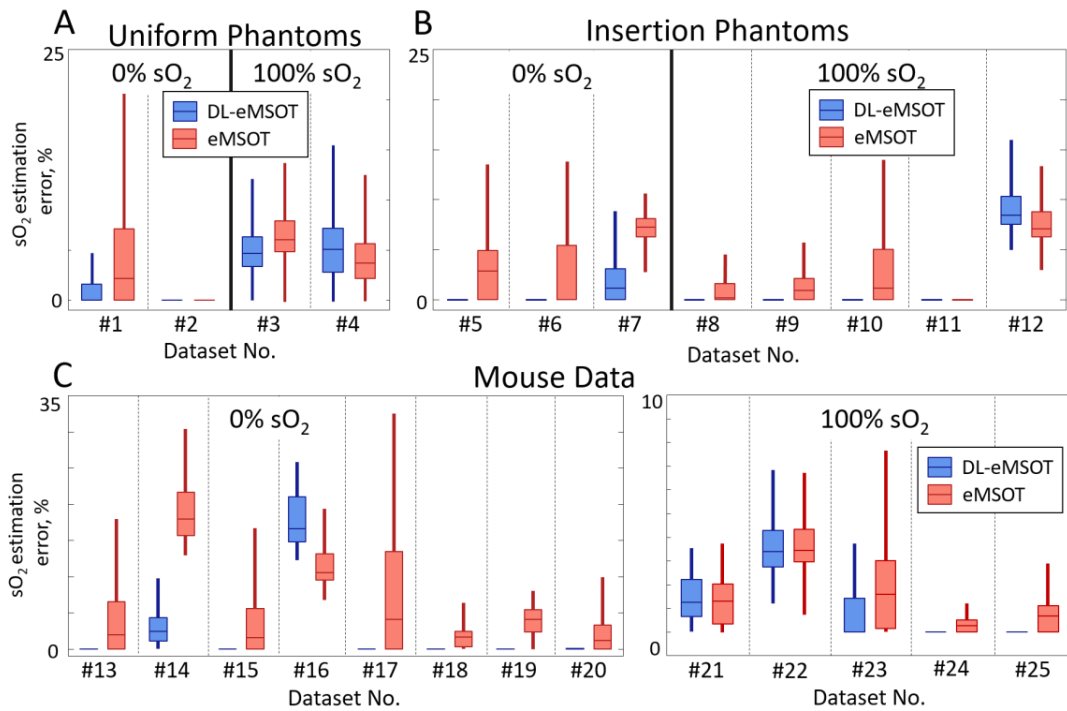
Fig. 7: **Evaluation of DL-eMSOT performance with experimental data. (A-C)** Errors in sO$_2$ estimation for eMSOT (red) and DL-eMSOT (blue) algorithms in (A) uniform phantoms, (B) phantoms with insertions and (C) mouse data. Boxplots represent data mean and 25th and 75th percentiles of data; whiskers cover ~96% of data. Dashed black lines separate results for distinct datasets (25 in total).

performed an exhaustive search for the optimal architecture. Our results rather highlight the importance of tailoring the used architecture to the problem at hand as well as the significance of spatial context in quantitative MSOT imaging.

Because of the lack of OA data with the available ground truth for fluence, we use simulations to obtain data for training the neural network. It is important to note that our simulations do not take into account many physical phenomena that occur in the scanner during imaging. We do not simulate wave propagation, spatial and electric impulse responses of the detectors or effects and artifacts introduced by reconstruction. Despite these simplifications, we find that the ensemble of 50 networks trained on our simulated data performs better than the original eMSOT in both simulated and experimental test data.

In addition to better performance in sO$_2$ estimation accuracy, the proposed method provides potential advantages in terms of processing speed, especially if multiple grids are analyzed simultaneously. Since eMSOT requires ~5 sec per inversion, total inversion time for the test dataset "vascularized" would be approximately 6.3 hours, compared to only 6 minutes for the ensemble of 50 networks. On the other hand, DL-eMSOT still displays errors of ~20% when estimating sO$_2$ from experimental data. Moreover, in certain cases models in the ensemble show considerable discrepancy in the estimated sO$_2$ values. Unfortunately, neural networks do not allow for detailed analysis of suboptimal performance. We assume that including more physical phenomena (acoustic wave propagation, image reconstruction, etc.) in the simulations that produce the training data will improve the

performance of the algorithm, potentially allowing to use a single model instead of an ensemble.

The major limitation in developing accurate sO$_2$ quantification methods for MSOT, including DL-eMSOT, is the lack of experimental data with available ground truth sO$_2$ values. With our experimental setup, we were able to produce only two extreme sO$_2$ values (0% and 100%) in a stable manner and the performance on such a limited dataset is not necessarily indicative of method's true capabilities. Ideally, data with the whole range of possible sO$_2$ values available as ground truth is needed to properly validate the performance of the quantification algorithms.

We have presented a novel sO$_2$ quantification method for MSOT that is based on eMSOT with a neural network employed for model inversion. With more realistic training data available, it should be possible to further improve quantification accuracy of the algorithm, and possibly use the approach for inverting more complex models that take into account various absorbers (e.g. fat, exogenous contrast agents), bringing MSOT closer to disease screening and diagnosis as well as clinical studies.

REFERENCES

[1] P. Vaupel and L. Harrison, "Tumor hypoxia: causative factors, compensatory mechanisms, and cellular response," *The oncologist,* vol. 9, no. 5, pp. 4-9, 2004.

[2] G. Diot, A. Dima, and V. Ntziachristos, "Multispectral opto-acoustic tomography of exercised muscle oxygenation," *Optics letters,* vol. 40, no. 7, pp. 1496-1499, 2015.

[3] N. K. Logothetis and B. A. Wandell, "Interpreting the BOLD signal," *Annu. Rev. Physiol.,* vol. 66, pp. 735-769, 2004.

[4] J. Reber, M. Willershäuser, A. Karlas, K. Paul-Yuan, G. Diot, D. Franz *et al.,* "Non-invasive measurement of brown fat metabolism based on optoacoustic imaging of hemoglobin gradients," *Cell metabolism,* vol. 27, no. 3, pp. 689-701. e4, 2018.

[5] I. Steinberg, D. M. Huland, O. Vermesh, H. E. Frostig, W. S. Tummers, and S. S. Gambhir, "Photoacoustic clinical imaging," *Photoacoustics,* 2019.

[6] H. F. Zhang, K. Maslov, G. Stoica, and L. V. Wang, "Functional photoacoustic microscopy for high-resolution and noninvasive in vivo imaging," *Nature biotechnology,* vol. 24, no. 7, p. 848, 2006.

[7] A. T. Eggebrecht, S. L. Ferradal, A. Robichaux-Viehoever, M. S. Hassanpour, H. Dehghani, A. Z. Snyder *et al.,* "Mapping distributed brain function and networks with diffuse optical tomography," *Nature photonics,* vol. 8, no. 6, p. 448, 2014.

[8] V. Ntziachristos, "Going deeper than microscopy: the optical imaging frontier in biology," *Nat Methods,* vol. 7, no. 8, pp. 603-14, Aug 2010.

[9] P. Mohajerani, S. Tzoumas, A. Rosenthal, and V. Ntziachristos, "Optical and optoacoustic model-based tomography: theory and current challenges for deep tissue imaging of optical contrast," *IEEE Signal Processing Magazine,* vol. 32, no. 1, pp. 88-100, 2015.

[10] M. Li, Y. Tang, and J. Yao, "Photoacoustic tomography of blood oxygenation: a mini review," *Photoacoustics,* vol. 10, pp. 65-73, 2018.

[11] B. Cox, J. G. Laufer, S. R. Arridge, and P. C. Beard, "Quantitative spectroscopic photoacoustic imaging: a review," *J Biomed Opt,* vol. 17, no. 6, p. 061202, Jun 2012.

[12] B. Cox, J. Laufer, and P. Beard, "The challenges for quantitative photoacoustic imaging," in *SPIE BiOS: Biomedical Optics*, 2009, pp. 717713-717713-9.

[13] K. Maslov, H. F. Zhang, and L. V. Wang, "Effects of wavelength-dependent fluence attenuation on the noninvasive photoacoustic imaging of hemoglobin oxygen saturation in subcutaneous vasculature in vivo," *Inverse Problems,* vol. 23, no. 6, p. S113, 2007.

[14] S. Tzoumas and V. Ntziachristos, "Spectral unmixing techniques for optoacoustic imaging of tissue pathophysiology," *Philosophical Transactions of the Royal Society A: Mathematical, Physical and Engineering Sciences,* vol. 375, no. 2107, p. 20170262, 2017.

[15] T. Tarvainen, B. T. Cox, J. Kaipio, and S. R. Arridge, "Reconstructing absorption and scattering distributions in quantitative photoacoustic tomography," *Inverse Problems,* vol. 28, no. 8, p. 084009, 2012.

[16] T. Tarvainen, A. Pulkkinen, B. T. Cox, J. P. Kaipio, and S. R. Arridge, "Bayesian image reconstruction in quantitative photoacoustic tomography," *IEEE transactions on medical imaging,* vol. 32, no. 12, pp. 2287-2298, 2013.

[17] A. Pulkkinen, B. T. Cox, S. R. Arridge, J. P. Kaipio, and T. Tarvainen, "A Bayesian approach to spectral quantitative photoacoustic tomography," *Inverse Problems,* vol. 30, no. 6, p. 065012, 2014.

[18] B. Cox, S. Arridge, and P. Beard, "Estimating chromophore distributions from multiwavelength photoacoustic images," *JOSA A,* vol. 26, no. 2, pp. 443-455, 2009.

[19] B. Banerjee, S. Bagchi, R. M. Vasu, and D. Roy, "Quantitative photoacoustic tomography from boundary pressure measurements: noniterative recovery of optical absorption coefficient from the reconstructed absorbed energy map," *JOSA A,* vol. 25, no. 9, pp. 2347-2356, 2008.

[20] L. Yao, Y. Sun, and H. Jiang, "Quantitative photoacoustic tomography based on the radiative transfer equation," *Optics letters,* vol. 34, no. 12, pp. 1765-1767, 2009.

[21] B. Cox, T. Tarvainen, and S. Arridge, "Multiple illumination quantitative photoacoustic tomography using transport and diffusion models," *Tomography and Inverse Transport Theory, G.*

[22] Bal, D. Finch, P. Kuchment, J. Schotland, P. Stefanov, and G. Uhlmann, eds,* vol. 559, pp. 1-12, 2011.

S. Bu, Z. Liu, T. Shiina, K. Kondo, M. Yamakawa, K. Fukutani *et al.,* "Model-based reconstruction integrated with fluence compensation for photoacoustic tomography," *IEEE Transactions on Biomedical Engineering,* vol. 59, no. 5, pp. 1354-1363, 2012.

[23] A. V. Mamonov and K. Ren, "Quantitative photoacoustic imaging in radiative transport regime," *arXiv preprint arXiv:1207.4664,* 2012.

[24] T. Saratoon, T. Tarvainen, B. Cox, and S. Arridge, "A gradient-based method for quantitative photoacoustic tomography using the radiative transfer equation," *Inverse Problems,* vol. 29, no. 7, p. 075006, 2013.

[25] A. Pulkkinen, B. T. Cox, S. R. Arridge, J. P. Kaipio, and T. Tarvainen, "Bayesian parameter estimation in spectral quantitative photoacoustic tomography," in *Photons Plus Ultrasound: Imaging and Sensing 2016,* 2016, vol. 9708, p. 97081G.

[26] S. Tzoumas, A. Nunes, I. Olefir, S. Stangl, P. Symvoulidis, S. Glasl *et al.,* "Eigenspectra optoacoustic tomography achieves quantitative blood oxygenation imaging deep in tissues," *Nature communications,* vol. 7, p. 12121, 2016.

[27] I. Olefir, S. Tzoumas, H. Yang, and V. Ntziachristos, "A Bayesian Approach to Eigenspectra Optoacoustic Tomography," *IEEE transactions on medical imaging,* vol. 37, no. 9, pp. 2070-2079, 2018.

[28] C. Cai, K. Deng, C. Ma, and J. Luo, "End-to-end deep neural network for optical inversion in quantitative photoacoustic imaging," *Optics letters,* vol. 43, no. 12, pp. 2752-2755, 2018.

[29] J. Gröhl, T. Kirchner, T. Adler, and L. Maier-Hein, "Confidence estimation for machine learning-based quantitative photoacoustics," *Journal of Imaging,* vol. 4, no. 12, p. 147, 2018.

[30] J. Gröhl, T. Kirchner, T. Adler, and L. Maier-Hein, "Estimation of blood oxygenation with learned spectral decoloring for quantitative photoacoustic imaging (LSD-qPAI)," *arXiv preprint arXiv:1902.05839,* 2019.

[31] T. Kirchner, J. Gröhl, and L. Maier-Hein, "Context encoding enables machine learning-based quantitative photoacoustics," *Journal of biomedical optics,* vol. 23, no. 5, p. 056008, 2018.

[32] A. Rosenthal, V. Ntziachristos, and D. Razansky, "Acoustic inversion in optoacoustic tomography: A review," *Current medical imaging reviews,* vol. 9, no. 4, pp. 318-336, 2013.

[33] M. Schweiger, S. Arridge, M. Hiraoka, and D. Delpy, "The finite element method for the propagation of light in scattering media: boundary and source conditions," *Medical physics,* vol. 22, no. 11, pp. 1779-1792, 1995.

[34] S. L. Jacques, "Optical properties of biological tissues: a review," *Physics in medicine and biology,* vol. 58, no. 11, p. R37, 2013.

[35] A. Dima, N. C. Burton, and V. Ntziachristos, "Multispectral optoacoustic tomography at 64, 128, and 256 channels," *Journal of biomedical optics,* vol. 19, no. 3, p. 036021, 2014.

[36] D. Shen, G. Wu, and H.-I. Suk, "Deep learning in medical image analysis," *Annual review of biomedical engineering,* vol. 19, pp. 221-248, 2017.

[37] M. T. McCann, K. H. Jin, and M. Unser, "Convolutional neural networks for inverse problems in imaging: A review," *IEEE Signal Processing Magazine,* vol. 34, no. 6, pp. 85-95, 2017.

[38] J. Schwab, S. Antholzer, and M. Haltmeier, "Learned backprojection for sparse and limited view photoacoustic tomography," in *Photons Plus Ultrasound: Imaging and Sensing 2019,* 2019, vol. 10878, p. 1087837.

[39] S. Antholzer, M. Haltmeier, and J. Schwab, "Deep learning for photoacoustic tomography from sparse data," *Inverse Problems in Science and Engineering,* pp. 1-19, 2018.

[40] D. Allman, A. Reiter, and M. A. L. Bell, "Photoacoustic source detection and reflection artifact removal enabled by deep learning," *IEEE transactions on medical imaging,* vol. 37, no. 6, pp. 1464-1477, 2018.

Supplementary Material

I. eMSOT Algorithm Summary.

In this section, we provide a detailed summary of the original eMSOT algorithm. Fig. 1 in the main text schematically describes the steps summarized below:

1. ***Grid Setup.*** A sparse grid $\mathbf{G} = \left\{ \mathbf{r}^{(k,l)} | k = \overline{1 \dots n_{\ln}}, l = \overline{1 \dots n_{pt}} \right\}$ of points is placed in the ROI. Grid $\mathbf{G}$ is obtained by intersecting $n_{\ln}$ radial lines and n_{pt} circles with decreasing radii and selecting the pixels in the image that lie at the intersections as grid points. The result is a grid having a structure with multiple "layers", i.e. points having similar depth. (see Suppl. Fig. 1 for an example of a grid $\mathbf{G}$). The spectra $\mathbf{p(r)}$ at spatial locations determined by the grid points $\mathbf{r} \in \mathbf{G}$ are selected for inversion and normalized, resulting in a set of normalized OA spectra $\mathbf{p}'^{(\mathbf{r})}, \mathbf{r} \in \mathbf{G}$ (dimensions $n_{\ln} \times n_{pt} \times 21$).

2. ***Priors.*** Linear unmixing and Finite Element Method (FEM) simulation of light propagation are used to obtain an estimate of optical fluence for the imaged object. This results in prior estimates $\hat{m}_1(\mathbf{r})$, $\hat{m}_2(\mathbf{r})$ and $\hat{m}_3(\mathbf{r})$ of the eigenfluence parameters $m_1(\mathbf{r})$, $m_2(\mathbf{r})$, and $m_3(\mathbf{r})$, respectively.

3. ***Inversion.*** In this step, model inversion is performed. Given the model parameters $\mathbf{\Theta} = \{\mathbf{\theta_r} | \mathbf{r} \in \mathbf{G}\}$ for the pixels on a grid, the optimal values $\mathbf{\Theta}_{opt}$ (dimensions $n_{\ln} \times n_{pt} \times 5$) are found as follows [1]:

$$\mathbf{\Theta}_{opt} = \arg\min_{\mathbf{\Theta}} \sum_{\mathbf{r} \in \mathbf{G}} f_\mathbf{r}(\mathbf{\theta_r}) + \eta \|\mathbf{W}\mathbf{m}_1\|_2 \quad\quad\quad \text{(S1)}$$
$$+ \eta \|\mathbf{W}\mathbf{m}_3\|_2,$$
$$subject\ to:$$

$$\begin{array}{c} m_2^{(k,l)} < m_2^{(k-1,l-1)}; \\ m_2^{(k,l)} < m_2^{(k,l-1)}; \\ m_2^{(k,l)} < m_2^{(k+1,l-1)}; \end{array} \quad\quad \text{(S2)}$$

$$\begin{array}{c} m_1^{(k,l)} \in \left[min_1^{k,l}\big(\hat{m}_1^{(k,l)}\big); \ max_1^{k,l}\big(\hat{m}_1^{(k,l)}\big) \right]; \\ m_3^{(k,l)} \in \left[min_3^{k,l}\big(\hat{m}_3^{(k,l)}\big); \ max_3^{k,l}\big(\hat{m}_3^{(k,l)}\big) \right]; \end{array} \quad \text{(S3)}$$

$$\begin{array}{c} c'_{HHb}\big(\mathbf{r}^{(k,l)}\big) \geq 0; \ c'_{HbO2}\big(\mathbf{r}^{(k,l)}\big) \geq 0; \\ m_i^{(k,l)} \in [MIN_i; \ MAX_i]; \ i = 1 \dots 3, \end{array} \quad \text{(S4)}$$

where $f_\mathbf{r}(\mathbf{\theta}) = \|\mathbf{p}'(\mathbf{r}) - \hat{\mathbf{p}}(\mathbf{r},\mathbf{\theta})\|_2$ is the l_2-norm of the difference between the spectrum from the grid point $\mathbf{r}$ and its respective eigenspectra model; $\mathbf{m}_i = \left[m_i^{(1,1)}, \dots, m_i^{(n_{\ln},n_{pt})} \right]^T$; $x^{(k,l)}$ is the value of the parameter x at the grid point $\mathbf{r}^{(k,l)}$; $\mathbf{W}$ describes the neighborhood system in the grid by specifying the nodes in $\mathbf{G}$ that are

immediate neighbors. Suppl. Fig. 1 shows an example of the grid overlaid with a simulated p_0 map where the neighbors are connected with white lines. For the grid nodes $\mathbf{r}$ and $\mathbf{s}$ that are neighbors, $\mathbf{W_{r,s}} = \frac{1}{\|\mathbf{r}-\mathbf{s}\|_2}$, where $\|\mathbf{r} - \mathbf{s}\|_2$ is the Euclidean distance between the nodes. If the nodes $\mathbf{r}$ and $\mathbf{s}$ are not neighbors, $\mathbf{W_{r,s}} = 0$. $min_i^{k,l}$ and $max_i^{k,l}$ are the local limits that depend on priors $\hat{m}_i^{(k,l)}$; and MIN_i, MAX_i are the global limits for the eigenfluence parameter values. Eq. S1 describes minimization of the difference between the measurements and the corresponding eigenspectra model; $\eta \|\mathbf{W}\mathbf{m}_i\|_2$ enforces spatial smoothness of the solution with η governing the desired degree of smoothness; Eq. S2 ensures decrease of values with depth and Eqs. S3-4 constrain the values of the parameters. The problem of fluence correction is ill-posed [1], hence the purpose of Eqs. S2-4 is to constrain the search space of the optimization algorithm and prevent it from converging to a wrong solution. The inversion is performed using the built-in function *fmincon* supplied with MATLAB R2017b. Specifically, the SQP method is used to solve the optimization algorithm with constraints specified accordingly by providing the vectors of appropriate values the parameters are constrained with. At each iteration of SQP, a quadratic problem is solved using an active set strategy. Fig. 1C of the main text schematically depicts the inversion procedure. Fig. 1D shows the output of step 3, where $\mathbf{m}^{(k,l)} = \left[m_1^{(k,l)}, m_2^{(k,l)}, m_3^{(k,l)} \right]^T$. The relative concentrations of oxy- and deoxyhemoglobin found for the normalized spectra on the grid are discarded.
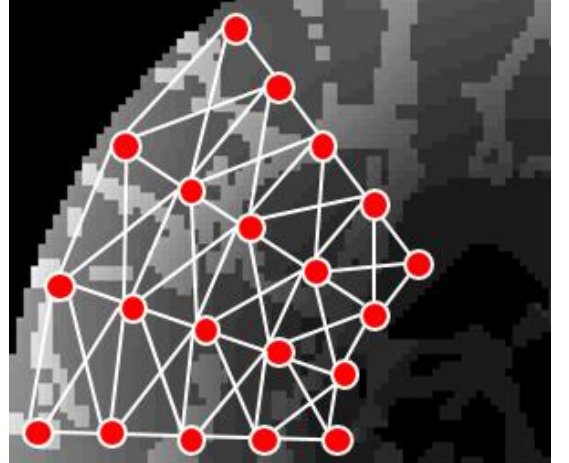
Suppl. Fig. 1. eMSOT grid G. (A) A grid (red) pixels overlaid on a p_0 simulation (1 wavelength presented) shown together with the neighborhood system. Any two nodes of the grid connected with a white line are neighbors. This implies a corresponding entry in the connectivity matrix $\mathbf{W}$.

4. ***Interpolation***. With the values of the eigenfluence parameters $m_i^{(k,l)}$; $i = 1 \ldots 3,; k = 1 \ldots n_{\mathrm{ln}}; l = 1 \ldots n_{\mathrm{pt}}$ for the grid points $\mathbf{r} \in \mathbf{G}$ available, interpolation is used to estimate the values of the eigenfluence parameters for every pixel within the convex hull of $\mathbf{G}$ [1].

5. ***sO₂ Estimation***. For every pixel within the convex hull of $\mathbf{G}$, the corresponding values of the eigenfluence parameters are used to reconstruct the estimated fluence. The effect of spectral coloring is then reverted and the resulting spectra, i.e. scaled true absorption spectra, are unmixed linearly for the relative concentrations c'_{HbO2} and c'_{HHb} of oxy- and deoxyhemoglobin, respectively. sO₂ is then computed as:

$$sO_2 = \frac{c'_{\mathrm{HbO2}}}{c'_{\mathrm{HHb}} + c'_{\mathrm{HbO2}}} \qquad (S5)$$

II. REFERENCE MODELS

In this section, we describe the two reference models trained in this study to compare the performance of DL-eMSOT to, namely DENSE (sO₂) and DENSE (fluence). The models share the same simple architecture consisting of 6 fully connected (dense) hidden layers.

DENSE (sO₂) maps a measured normalized OA spectrum (dimensions 1×21) to the corresponding sO₂ value. DENSE (fluence) solves the inverse problem of eMSOT, i.e. maps the input grid features (dimensions 8×8×4) to the eigenfluence parameters (dimensions 8×8×3). Suppl. Fig. 2 shows the two architectures schematically. Below is a detailed description of the architectures used:

- Number of units/neurons:
  - *Dense 1*: DENSE (sO₂): 92; DENSE (fluence): 512
  - *Dense 2*: DENSE (sO₂): 92; DENSE (fluence): 512
  - *Dense 3*: DENSE (sO₂): 92; DENSE (fluence): 512
  - *Dense 4*: DENSE (sO₂): 92; DENSE (fluence): 512
  - *Dense 5*: DENSE (sO₂): 92; DENSE (fluence): 256
  - *Dense 6*: DENSE (sO₂): 92; DENSE (fluence): 256
  - *Output Layer*: DENSE (sO₂): 1; DENSE (fluence): 192
- Activation: Leaky ReLU (alpha = 0.2)
- Dropout rate: 0.3

DENSE (fluence) was trained using the same data as the DL-eMSOT. DENSE (sO₂) used the same training dataset, but every spectrum was considered as a separate example unlike DL-eMSOT and DENSE (fluence), where a grid of sampled spectra constituted a training example.
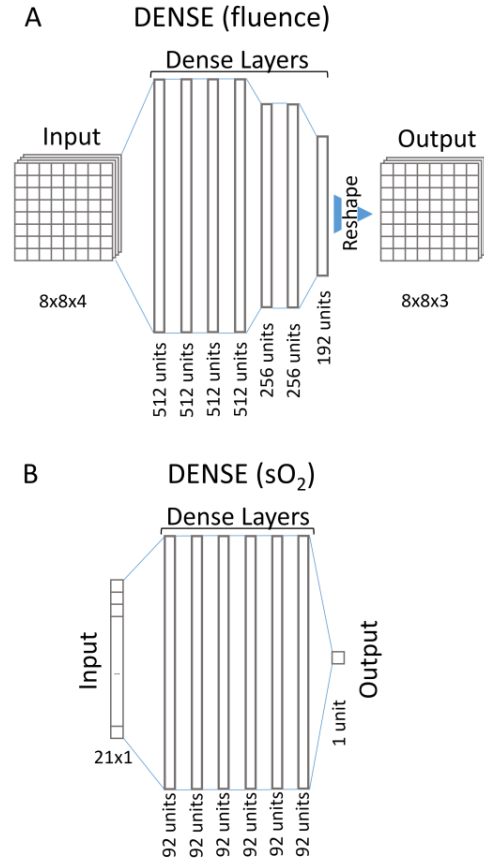
Suppl. Fig. 2: **Architecture of the reference models**. (A) Architecture of DENSE (fluence). (B) Architecture of DENSE (sO₂)

III. SIMULATIONS

Suppl. Fig. 3 illustrates the creation of the simulations described in Sec. III of the main text in more detail. The figure shows examples of the following quantities: randomly varying (augmented) spatial maps of background tissue absorption $\mu_a(\mathbf{r})$ at 800 nm (A, E, I, M – rightmost column), reduced scattering $\mu'_s(\mathbf{r})$ (B, F, J, N– second rightmost column) and sO₂ (C, G, K, O – second leftmost column) corresponding to the output of steps 1 and 2 of the algorithm described in Sec. III. The leftmost column presents the corresponding resulting maps of the initial pressure rise that is the output of step 4 of the algorithm described in Sec. III. The data is shown for four datasets: training data (A-D), 'background' (E-H), 'vascularized' (I-L) and 'croissant' (M-P) datasets.
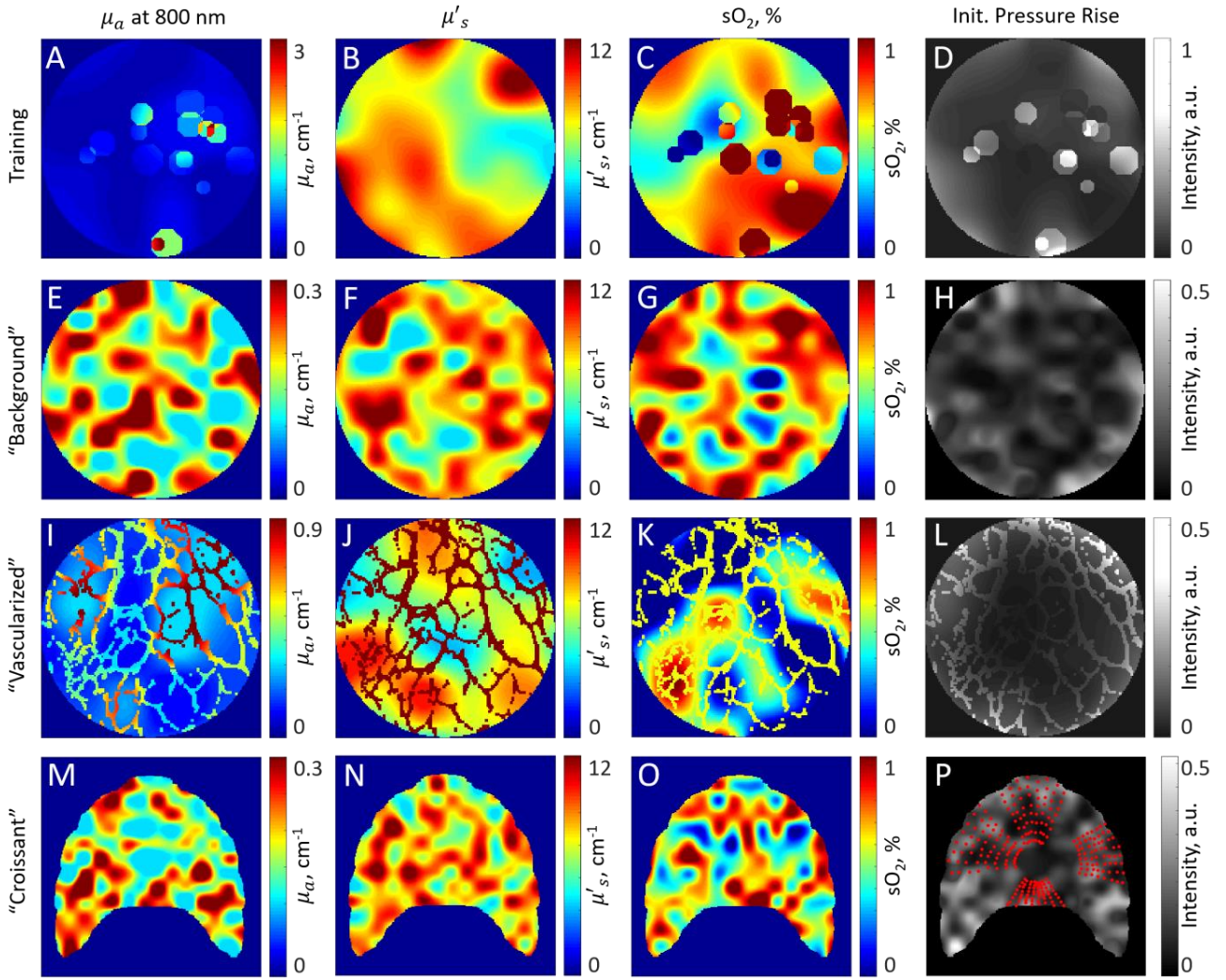
Suppl. Fig. 3: Simulated Data. (A, E, I, M) Randomly varying (augmented) spatial maps of background tissue absorption $\mu_a(\mathbf{r})$ at 800 nm; (B, F, J, N) randomly varying (augmented) spatial maps of reduced scattering $\mu'_s(\mathbf{r})$; (C, J, K, O) randomly varying (augmented) spatial maps of sO_2; (D, H, L ,P) the corresponding resulting maps of the initial pressure rise, with (P) additionally displaying the grids that determined the locations at which the spectra were sampled. The data is presented per four datasets: training data (A-D), 'background' (E-H), 'vascularized' (I-L) and 'croissant' (M-P).

The ranges of the values for the optical parameters used for creating the simulations used throughout the manuscript summarized in Suppl. Table 1.

IV. SUPPLEMENTARY EXPERIMENTS.

Supplementary Table 1. Optical properties for creation of simulated data.

	μ_a, cm^{-1}		μ'_s, cm^{-1}		sO$_2$, %		Spatial Inhomogeneity of Background	Inclusions	# of Simulations
	Mean	Std. Deviation	Mean	Std. Deviation	Mean	Std. Deviation			
Main Datasets									
Training	0.2, 0.25, 0.3	0.1	9, 11	3	5-95, step of 5	20, 30	Low (3 levels)	Circular	1368
Background (Test / Val)	0.2, 0.25, 0.3	0.1	9, 11	3	5-95, step of 5	20, 30	High (2 levels)	None	228
Vascularized (Test)	0.2, 0.25, 0.3	0.1	9, 11	3	5-95, step of 5	20, 30	Low to High (5 levels)	Vessel Network	570
Croissant (Test)	0.2, 0.25, 0.3, 0.35	0.1	9, 11	3	5-95, step of 5	20, 30	High (2 levels)	None	304
Supplementary Datasets									
Suppl. Vascularized (Test)	0.2, 0.25, 0.3	0.1	9, 11	3	5-95, step of 5	20, 30	High (2 levels)	Vessel Network	228
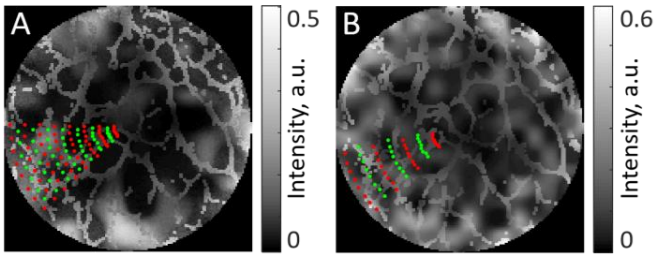
Suppl. Fig. 4. **Data for Supplementary Experiments. (A, B)** Simulated maps of the initial pressure rise (one wavelength presented) from the "supplementary vascularized" dataset. The red dots denote the grid **G** that selects the locations for sampling the spectra. The green dots denote the locations of the spectra where fluence correction is performed by interpolating the eigenparameters found on grid **G**. The grid shown in (B) was used to test DL-eMSOT (sparse) models that operate on grids that are downsampled along tissue depth.

In this section, we provide the results of three additional experiments. First, we tested the performance of the considered quantification methods in the areas where the fluence correction is performed using the interpolated eigenfluence parameters (i.e. points in between the grid points). Secondly, we assess the influence of the grid density on the performance of DL-eMSOT. Finally, we investigate the performance of DL-eMSOT depending on the ensemble size.

A. Performance in the Regions Between the Grid Points.

The performance of the considered quantification methods in the regions where the eigenfluence parameters are interpolated from the grid points was assessed using the "vascularized supplementary" dataset which is a subset of the "vascularized" test set (see Suppl. Table 1 for the details on the optical properties and the number of distinct simulations). Suppl. Fig. 4 demonstrates a p_0 map from "vascularized supplementary" dataset (one wavelength presented). Red dots denote the grid **G** specifying the locations of the spectra to be

Suppl. Table 2. Performance in Supplementary Experiments.

	Mean Error	Median Error	Standard Deviation	[25% , 75%] Percentiles
"Supplementary vascularized" - grid				
eMSOT	11.3%	14.4%	6.5%	[2.7%, 13.3%]
DL-eMSOT	3.6%	4.3%	2.3%	[0.8%, 4.7%]
DL-eMSOT (ensemble)	3.3%	4.0%	2.1%	[0.7%, 4.3%]
DENSE (sO$_2$)	11.2%	13.5%	6.9%	[3.0%, 14.0%]
DENSE (fluence)	5.1%	5.9%	3.2%	[1.3%, 6.8%]
DL-eMSOT sparse	5.5%	3.3%	6.6%	[1.2%, 7.1%]
DL-eMSOT sparse (ensemble)	5.2%	3.1%	6.3%	[1.1%, 6.8%]
"Supplementary vascularized"– interpolated points				
eMSOT	11.0%	13.3%	6.7%	[3.0%, 13.0%]
DL-eMSOT (ensemble)	3.2%	3.8%	2.1%	[0.8%, 4.2%]
DENSE (fluence)	5.0%	5.5%	3.3%	[1.4%, 6.7%]
DL-eMSOT sparse (ensemble)	5.4%	3.3%	6.6%	[1.2%, 7.2%]

used by the methods. The green dots represent the points where sO$_2$ was computed using the eigenfluence parameters that were interpolated from the ones found for the grid. The absolute sO$_2$ estimation errors are presented in Suppl. Table. 2 for both the grid and the interpolated points. Similarly to Table 1 of the main text, we present test results for eMSOT, the average results per DL-eMSOT model (DL-eMSOT), the results of the DL-eMSOT ensemble and the two competing architectures. The results from DENSE (sO$_2$) in the

interpolated regions are not presented since this architecture estimates sO2 on a per pixel level and does not require interpolation. The average results per DL-eMSOT model on interpolated points are not assessed to reduce the computational cost. It can be readily seen that the accuracy on the grid and the interpolated regions are comparable for each tested method, confirming that interpolation of the eigenfluence parameters does not undermine the performance of the eMSOT family of methods in the interpolated regions.

B. Performance on Sparse Grids.

Additionally, to assess the influence of the spatial density of the used grids on the performance of DL-eMSOT, we trained an ensemble of models we termed DL-eMSOT (sparse) that only use 4 out of 8 layers of points from which the spectra are sampled (i.e. every second layer of the grid is ignored). This means that, while the general architecture of DL-eMSOT is retained, the bi-derectional RNN in DL-eMSOT (sparse) has a reduced depth of 4 as compared to DL-eMSOT with the full RNN depth of 8. Suppl. Fig. 4B shows an example of a grid that DL-eMSOT (sparse) operates on (red dots). As compared to the original grid shown in Suppl. Fig. 4A (red dots), the depth dimension in the so applied grid is subsampled.

DL-eMSOT (sparse) models were trained using the training data described in Sec. II of the manuscript, with every second layer of points in every training example being ignored. DL-eMSOT (sparse) has been tested on "vascularized supplementary" dataset, with the results (average per model and ensemble) presented in Suppl. Table 2 for the grid points as well as interpolated regions. The average results per DL-eMSOT (sparse) model on interpolated points are not assessed to reduce the computational cost The results indicate that subsampling the grids along tissue depth leads to a decrease in performance for DL-eMSOT.

C. Performance as a Function of the Ensemble Size.
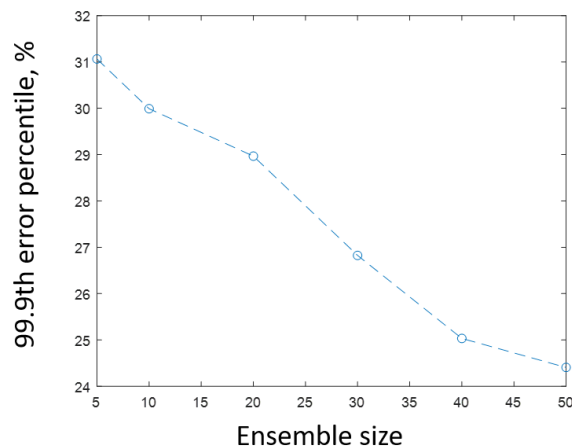
Suppl. Fig. 5. **99.9th percentile of errors of DL-eMSOT ensemble applied to dataset "vascularized" as a function of ensemble size.**

To investigate how ensemble size affects the performance of DL-eMSOT, we have evaluated the performance of DL-eMSOT ensembles of various sizes on "vascularized" test
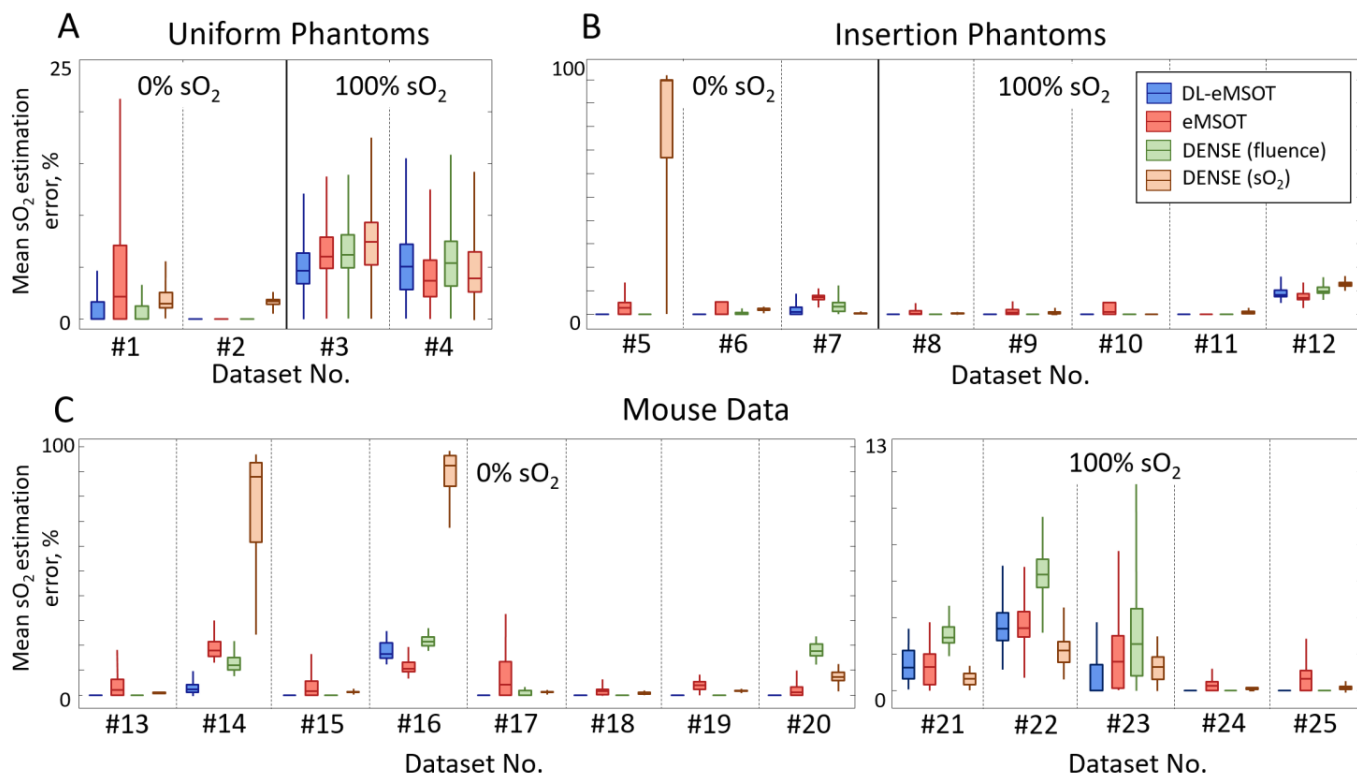
Suppl. Fig. 6: **Evaluation of DL-eMSOT, eMSOT, and the reference models performance with experimental data. (A-C)** Errors in sO2 estimation for eMSOT (red) and DL-eMSOT (blue), DENSE (fluence) (green) and DENSE (sO2) (beige) algorithms in (A) uniform phantoms, (B) phantoms with insertions and (C) mouse data. Boxplots represent data mean and 25th and 75th percentiles of data; whiskers cover ~96% of data. Dashed black lines separate results for distinct datasets (25 in total).

dataset. While the results presented in Table 1 of the main text do not indicate a significant boost in performance when using an ensemble, we have evaluated the 99.9th percentile of errors of every tested ensemble. The 99.9th percentile of errors can be thought of as a maximum sO_2 estimation error except for the most extreme outliers. The results presented in Suppl. Fig. 5 indicate that increased ensemble size is associated with lower values of 99.9th percentile of errors.

V. EXPERIMENTAL RESULTS

Suppl. Fig. 6 summarizes and compares the performance of DL-eMSOT, eMSOT, DENSE (fluence) and DENSE (sO_2) models in all available experimental datasets (25 in total) with the corresponding ground truth: uniform phantoms (Suppl. Fig. 6A), insertion phantoms (Suppl. Fig. 6B) and mouse data (Suppl. Fig. 6C). The results are grouped per ground truth sO_2 level: 0% (left panels) and 100% (right panels). Black dashed lines separate results obtained for separate datasets. It can be seen that in many cases all DL based algorithms perform sufficiently well. However, DENSE (sO_2) demonstrates extremely high errors in multiple datasets. On the other hand, DENSE (fluence) that uses spatial information in the form of the input grid of spectral features demonstrates more stable performance, that is comparable to that of DL-eMSOT, highlighting the importance of spatial context when solving the problem of spectral coloring. However, since the architecture of DENSE (fluence) is not specifically tailored to the solved problem, in numerous cases it underperforms in numerous cases as compared to DL-eMSOT.

SUPPLEMENTARY REFERENCES

[1]   S. Tzoumas, A. Nunes, I. Olefir, S. Stangl, P. Symvoulidis, S. Glasl *et al.*, "Eigenspectra optoacoustic tomography achieves quantitative blood oxygenation imaging deep in tissues," *Nature communications,* vol. 7, p. 12121, 2016.

Appendix C

Publication: Hybrid multispectral optoacoustic and ultrasound tomography for morphological and physiological brain imaging

Hybrid multispectral optoacoustic and ultrasound tomography for morphological and physiological brain imaging

Ivan Olefir
Elena Merčep
Neal C. Burton
Saak V. Ovsepian
Vasilis Ntziachristos

SPIE.

Hybrid multispectral optoacoustic and ultrasound tomography for morphological and physiological brain imaging

Ivan Olefir,[a,b] Elena Merčep,[a,c,d] Neal C. Burton,[d] Saak V. Ovsepian,[a,b] and Vasilis Ntziachristos[a,b,*]
[a]Helmholtz Zentrum München, Institute for Biological and Medical Imaging, Ingolstädter Landstraße 1, Neuherberg 85764, Germany
[b]Technische Universität München, School of Bioengineering, Boltzmannstraße 11, Garching 85748, Germany
[c]Technische Universität München, Faculty of Medicine, Ismaninger Straße 22, Munich 81675, Germany
[d]iThera Medical GmbH, Zielstattstrasse 13, Munich 81379, Germany

Abstract. Expanding usage of small animal models in biomedical research necessitates development of technologies for structural, functional, or molecular imaging that can be readily integrated in the biological laboratory. Herein, we consider dual multispectral optoacoustic (OA) and ultrasound tomography based on curved ultrasound detector arrays and describe the performance achieved for hybrid morphological and physiological brain imaging of mice *in vivo*. We showcase coregistered hemodynamic parameters resolved by OA tomography under baseline conditions and during alterations of blood oxygen saturation. As an internal reference, we provide imaging of abdominal organs. We illustrate the performance advantages of hybrid curved detector ultrasound and OA tomography and discuss immediate and long-term implications of our findings in the context of animal and human studies. © *2016 Society of Photo-Optical Instrumentation Engineers (SPIE)* [DOI: 10.1117/1.JBO.21.8.086005]

1 Introduction

Biomedical imaging has a profound impact on interrogation of the structure and functional dynamics of living organisms, with major implications for diagnostics and healthcare.[1,2] Combined with advances in molecular biology and genetics that spurred the development of small animal models, *in vivo* imaging is increasingly considered for a range of basic and translational research applications. Amid imaging modalities implemented for clinical and basic investigations, ultrasonography (US), magnetic resonance imaging, single-photon emission, positron emission, or x-ray computed tomography (PET and XCT), have been most widely considered for small animal studies.[3–8] In addition, optical methods, such as optical coherence tomography or multiphoton microscopy, have been used *in vivo* at cellular and subcellular resolution,[9,10] but at imaging depths limited to a few millimeters.[11]

Recently, small animal optoacoustic (OA) imaging and, in particular, multispectral optoacoustic tomography (MSOT), has been employed to bridge the gap between the optical microscopy and radiological methods.[11–14] The technique is based on the thermoelastic expansion of the tissue after absorption of transient light energy, with latter giving rise to ultrasonic waves.[15] Image formation is based on detecting generated waves and application of mathematical inversion to determine the optical contrast (absorption) acting as the source of sound. Typically, laser pulses in the 10- to 100-ns range are implemented to induce an ultrasonic response, although continuous-wave intensity-modulated lasers have also been shown to

produce acoustic signals.[12,16,17] The major advantage of MSOT over conventional optical imaging methods is that the image quality is less prone to distortion by photon scattering within the specimen. Therefore high-resolution images of the deep structures can be produced with ultrasound diffraction-limited resolution.[11,18] By illuminating at multiple wavelengths and using spectral unmixing techniques, MSOT can resolve the contributions of different endo- and exogenous photoabsorbing molecules, nanoparticles, or other labels, based on their absorption.[19–21] This spectral capacity of MSOT affords its molecular specificity, capable of distinguishing various endogenous contrasts, including oxy- and deoxy-hemoglobin, melanin, and others, or changes in their functional states. For this reason, MSOT is customarily considered in studies of physiological and pathophysiological processes as well as for molecular imaging.[22–24] A large number of extrinsically administered contrast-enhancing agents is also widely utilized for expanding its applications toward addressing a range of biological questions and unmet clinical need[16,18] at depths and resolutions not feasible with conventional imaging approaches.[25–28]

It has been nevertheless recognized that the combination of OA imaging with other imaging modalities can enhance the MSOT capabilities and applications. This principle was applied in hybrid microscopic studies, where the merger of two-photon and OA microscopy in a single system affords high-resolution imaging of fluorescence, second-harmonic, and optical absorption contrasts within the same specimen, enriching the features resolved.[29] The combination of OA macroscopy with ultrasound imaging has also been considered, taking advantage of a shared signal detector. A commonly used

*Address all correspondence to: Vasilis Ntziachristos, E-mail: v.natziachristos@tum.de

approach implements linear US arrays with integrated fiber-based light delivery systems, where OA and ultrasound data are acquired in a sequential fashion.[30,31] Due to its wide availability and use in the clinical US systems, the linear arrays have been previously adopted for hybrid OA and US imaging, through modification of the existing probes. Such a design therefore inherits flexibility of US modality in terms of access to various measurement sites. However, it has been shown that linear ultrasound detectors do not offer optimal OA image quality.[32,33] Conceivably, the use of concave ultrasound detectors greatly improves the quality and accuracy of images, due to improved angular coverage of the specimen under investigation.[34] This however involves the use of ring-shaped detectors arrays, which limits the flexibility of such hybrid systems and their use to human studies, but with preserved applications for small animal imaging. A hybrid OA–US system with ring detector geometry was proposed by Xia et al.,[35] which used laser illumination of the ring array to generate US pulses. With such approach, the speed of sound within the field of view has been estimated to enhance the quality of OA images. It should be noted, however, that in this study, US played a supporting role in OA image reconstruction and did not yield high-resolution structural images. We have recently introduced a hybrid imaging system consolidating a concave detection array-based ultrasound tomography (UST) with MSOT, using the same array detector, capable of concurrently obtaining OA and ultrasound readouts.[36] The system was shown to generate hybrid images of the bladder, using US and near-infrared dye perfused in the bladder *in vivo*. Nevertheless, the ability of such a system to generate coregistered physiological (hemodynamic) and structural data has not been fully explored.

In this study, we implemented hybrid MSOT–UST imaging for correlative morphological and functional measurements of the mouse brain. We evaluate anatomical UST data with physiological information of MSOT and compare the performance of MSOT with 256 and 512 detector elements. As a reference, we investigate the performance of the hybrid system for imaging of abdominal organs. Finally, we project onto future applications and potential challenges related with use of dual MSOT–UST imaging for basic and translational physiology and neuroscience research and discuss avenues for further improvements.

2 Materials and Methods

2.1 Hybrid Ultrasound and Optoacoustic Tomography

Figure 1 presents a schematic of the hybrid imaging platform with main components. The principal module shared between both systems is a 512-element concave ultrasound detector array (DA) [Imasonics SaS, Voray, France; array type: spherical concave array covering 270 deg; number of channels: 512; mechanical focalization: toroidal focusing; radius of curvature SR 40 mm$\pm$1 mm; radius of the elements (elevation): 37 mm + 1/ − 2 mm; elementary pitch (*p*): ∼0.735 mm/ ∼ 0.37 mm; interelement spacing (*e*): 0.1 mm; width of the elements (*h*): 15 mm (chord); center frequency (−6 dB): 5 MHz $\pm$ 10%; bandwidth (−6 dB): ≥55% in transmit/receive mode] coupled to laser beam and controlling multiplexer (MUX). The concave multielement detector is connected to two data acquisition (DAQ) systems, each corresponding to one of the acquisition modes. Despite a common mechanism of US and OA signal detection, a second DAQ has to be employed due to (1) conventional OA DAQ electronics not supporting the transmission of US pulses and (2) differences in amplification and input impedance needed to acquire readouts from the two modalities. The data are stored and processed on a personal computer (PC). In the multispectral tomography mode [MSOT, Fig. 1(a)], short laser pulses pass through a diffuser, to ensure even illumination of the specimen. The ultrasound waves produced due to the thermoelastic expansion of the specimen are detected and processed to form images with proprietary software (iThera Medical GmbH,
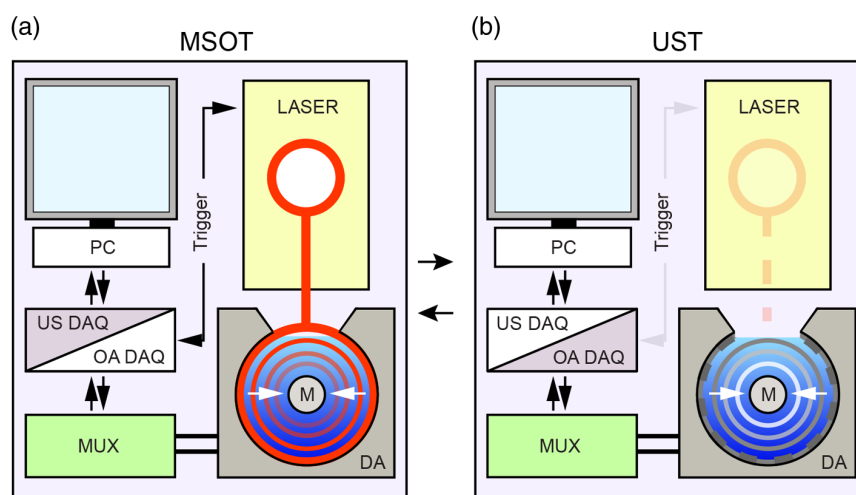
Fig. 1 Hybrid MSOT–UST imaging system: a schematic. (a) MSOT: a laser pulse triggers the DAQ system and illuminates the mouse (M) generating the ultrasonic waves due to light absorption, which are sampled by transducers on a detector ring and reconstructed into an image by PC. (b) UST: the mouse is interrogated by US waves that are generated by the transducers on the DA; the US waves reflected from within the sample due to the acoustic impedance mismatch of the different tissues are subsequently detected and processed into an image. MUX is been used for switching between various acquisitions modes.

Munich, Germany). In the UST acquisition mode [Fig. 1(b)], the specimen is interrogated by US pulses through an array and reflected signals are sampled with acoustic sensors as specified elsewhere.[36]

A holder consisting of a semiflexible light- and sound-permeable polyethylene membrane is used to horizontally mount the animal into the center of the concave DA. For optimal sound coupling, the detector and the animal holder are immersed in water. The plastic membrane separates the animal from being in contact with the water, while offering ∼360 deg of water coupling and ∼90 deg of open access to the animal from the top. In both MSOT and US acquisition modes, one two-dimensional (2-D) cross-sectional plane (∼1-mm thick) is scanned at a time. Plane sectioning is performed by horizontal translation of the animal holder with respect to the detection ring with a minimum step of 0.1 mm. Due to the unconventional geometry of the detector used, specific reconstruction algorithms have to be employed to form a US image.[37] To switch from one acquisition mode into another, a custom made multiplex programmable switchboard was used.[36] For MSOT, 9-ns laser pulses of different wavelengths have been used ($\lambda = 715, 730, 775, 800, 850,$ and 900 nm), which were produced with an Nd:YAG-pumped optico-parametric modulator (InnoLas Laser GmbH, Krailling, Germany) at 10 Hz and per-pulse energy of 120 mJ, with the intensity kept constant throughout the imaging sessions (laser pulse fluence on the surface of the imaged objects under 20 mJ/cm^2 for similar illumination[38]). Affirmatory imaging of used specimen at specified above wavelengths was also performed using a commercial MSOT scanner (MSOT256-TF, iThera Medical GmbH, Munich, Germany), with OA signals collected with a 256-element detector ring.[34] MSOT images have been acquired at 10 Hz and averaged 10 frames per wavelength, to reduce the variability due to the breathing motion and improve the signal-to-noise ratio.

2.2 Animals and Experimental Procedures

Young adult mice (Hsd:Athymic Nude-Foxn1nu/nu) were used for these experiments, which were housed in the animal housing facility (21°C ± 2°C, humidity 36% ± 2% at 12/12-h light/dark cycle) at the Institute of Biomedical Imaging, Helmholtz Zentrum München, with food and water provided *ad libitum*. All procedures involving animal experimentations were conducted according to the institutional guidelines and the government of Upper Bavaria and complied with German Federal and EU law. Efforts were made to reduce the animal usage and suffering.

MSOT and UST of the head and abdominal organs were conducted and related to anatomical references.[39] Experiments were carried out under general anesthesia (1.8% isoflurane in 100% O$_2$ at 0.81 ml/min). Baseline measurements at normal breathing were followed by a gas challenge. In total, four breathing states were cycled with supplied gas composition altered as follows: (1) medical air, (2) a mixture of medical air and 10% CO$_2$, (3) 100% oxygen, and (4) medical air. Every breathing condition lasted for ∼2 min resultant in a total of ∼8 min per imaging session.

2.3 Data Analysis and Presentation

Raw data have been analyzed off-line in MATLAB®. Signals were filtered with a bandpass filter (400 kHz to 8 MHz) with multispectral images reconstructed using a model-based algorithm[40] resulting in 2-D images of the measured planes. MSOT images of the head region taken at 900 nm with MSOT512 and MSOT256 were automatically coregistered in MATLAB®. For resolution comparison, the intensity of selected high-contrast regions of interest (ROIs) have been profiled; data were extracted from corresponding locations of coregistered images using MATLAB® and plotted in arbitrary units (a.u.). Intensity profile graphs were fitted using Gaussian function with full width at half maximum (FWHM) taken as an indication of the resolving power and compared between two (MSOT256 and MSOT512) systems. For correlation of MSOT and UST readouts, semiautomatic data registration was performed in MATLAB® by matching three pairs of control points selected manually at the corresponding anatomical landmarks defined on both MSOT and US images. Anatomical MSOT images were corrected for light fluence computed with a finite element solution to diffusion approximation assuming homogeneous absorption of 0.3 cm^{-1} and reduced scattering of 10 cm^{-1}. For studies of blood oxygenation dynamics, measurements were made with MSOT while inhaled gas content was altered as specified above. Prior to data unmixing, the MSOT readouts were calibrated to account for the absorption by a 4-cm-thick layer of water. The ROIs of functional recordings, which included blood vessels and parenchymal tissue distal from major blood supply routes, were defined for tracking the oxygenation saturation (sO$_2$) changes overtime. Calibrated multispectral data were subsequently unmixed based on absorption spectra of oxy- and deoxy-hemoglobin using a linear curve-fitting algorithm (MATLAB®). No optical fluence correction was used prior to unmixing. The values for sO$_2$ were averaged over respective ROIs, with oxygenation levels computed relative to the baseline (denoted as "relative sO$_2$" in tables and figures) defined as the average oxygenation level in the kidney area prior to the breathing challenge. The resulting temporal profiles from the ROIs in the abdominal area were processed with median filter of order 7 to mitigate the noise. To characterize the dynamic response of tissue to gas challenge, data corresponding to the timeframes of 220 to 290 s for brain ROIs and 220 to 355 s for abdominal ROIs were extracted from the selected profiles, with values normalized to the range from 0 to 1 for individual profiles. Sigmoid functions of $1/(1 + e^{\tau(x-b)})$ were fitted to the extracted data, where x denotes time, b characterizes the center of the curve, and τ governs steepness of ascent (higher values mean faster rise). Obtained values of τ are summarized in Table 1. Graphs and color maps have been generated in MATLAB® or in EXCEL; the final figures were prepared using IgorPro (6.1) and Adobe Illustrator (CS6).

3 Results

To validate the performance of the hybrid system and its utility for correlative UST and MSOT *in vivo*, we imaged the brain and abdominal organs of living mice under normal conditions and during alterations of sO$_2$ induced by gas challenge.

3.1 Hybrid Imaging of the Brain

Figure 2 shows a cryosection of the mouse head *ex vivo* annotated for major anatomical references of the brain (a), with corresponding UST and MSOT cross sections obtained *in vivo* (b and c, respectively). The MSOT image is labeled to highlight the regions chosen for the analysis of hemodynamics. As evident, high-contrast structures with distinct contours can be

Table 1 Summary of sO_2 dynamics and corresponding values. Anatomical references are numerated in accordance to the MSOT images in Figs. 2 and 4.

	Organ	Anatomical references	Baseline sO_2 (Rel. %)	Peak sO_2 (Rel. %)	sO_2 rise (tau)
Vessels	Head	Sagittal sinus (1)	118	178	0.607
		Maxillary artery (2)	128	194	0.329
		Medial cerebral artery (5)	131	176	0.519
		Maxillary artery (6)	123	185	0.293
		Mean	125	183	0.437
		Std	6	8	0.151
	Abdominal	Sup. vessel (3)	125	155	0.090
		Sup. vessel (2)	135	167	0.061
		Sup. vessel (6)	121	152	0.068
		Spinal br. of Lumb. art (4)	134	173	0.231
		Mean	129	161	0.112
		Std	7	10	0.081
Parenchyma	Head	Brain (3)	116	150	1.302
		Brain (4)	102	144	1.264
		Mean	109	147	1.283
		Std	10	4	0.027
	Abdominal	Kidney (1)	100	113	0.065
		Kidney (5)	110	131	0.099
		Mean	105	122	0.082
		Std	7	13	0.024

distinguished in both UST and MSOT images, although with notable differences. In MSOT cross sections, the heterogeneous optical absorption at various depths unveils discrete outlines of major vascular elements such as the dorsal sagittal sinus, medial cerebral, maxillary and internal carotid arteries along with the contours of the parietal cortex, hippocampal formation, and optic chiasm.[39] On corresponding UST images, strong contrasts due to ultrasound impedance mismatch highlight the skin to skull interface, with most of the signal provided by thick cranial bones causing strong reflection of the US waves while the brain itself appears obscured. As evident from the overlaid UST and MSOT tomograms [Fig. 2(d)], the combination of two modalities results in coregistered image acquired with the shared ultrasonic DA.

Due to its spectral dimension,[18] MSOT can obtain readouts of the brain hemodynamics and sO_2 in conjunction with anatomical data *in vivo*. Figures 2(e) and 2(f) show images of the dorsal compartments of mouse brain overlaid with color-coded oxygenation maps corresponding to different breathing conditions (air and 100% O_2, respectively) with supply of 100% O_2 increasing tissue oxygenation levels. The overall dynamics of the sO_2 in defined ROIs [Figs. 2(e), 2(f); enboxed 1 and 4] of the dorsal cerebrum with their changes related to the breathing conditions are summarized in Figs. 2(g) and 2(h), respectively (blue circles and error bars represent correspondingly mean relative oxygenation and standard deviation within respective ROIs). After a stable baseline recording, supply of 10% CO_2 causes deoxygenation of the brain tissue and sagittal sinus while supply of 100% O_2 leads to a steep increase in sO_2 in both areas.

To evaluate the kinetics of the hemoglobin gradient changes, we analyzed the rates of the relative sO_2 changes upon O_2 challenge. Figure 3 presents the graphs of the kinetics of sO_2 in brain tissue (a) and sagittal sinus (b). Black circles denote normalized data points pulled from regions marked by arrows 3 (a) and 1 (b) in Fig. 2(c), while red lines correspond to the fitted sigmoid functions. Faster sO_2 rates within the brain tissue are evident as compared to that of sinus, consistent with measurements of the sO_2 dynamics and comparison between several brain areas and major blood vessels (Table 1). These findings suggest a tighter coupling of the oxygenation of the neural tissue with the breathing state. It is important to note that changes in sO_2 induced by the gas challenge were reversible, confirming that the effects of experimental interventions were transient and remain within physiological limits, and were not associated with irreversible impairments of the brain hemodynamics.
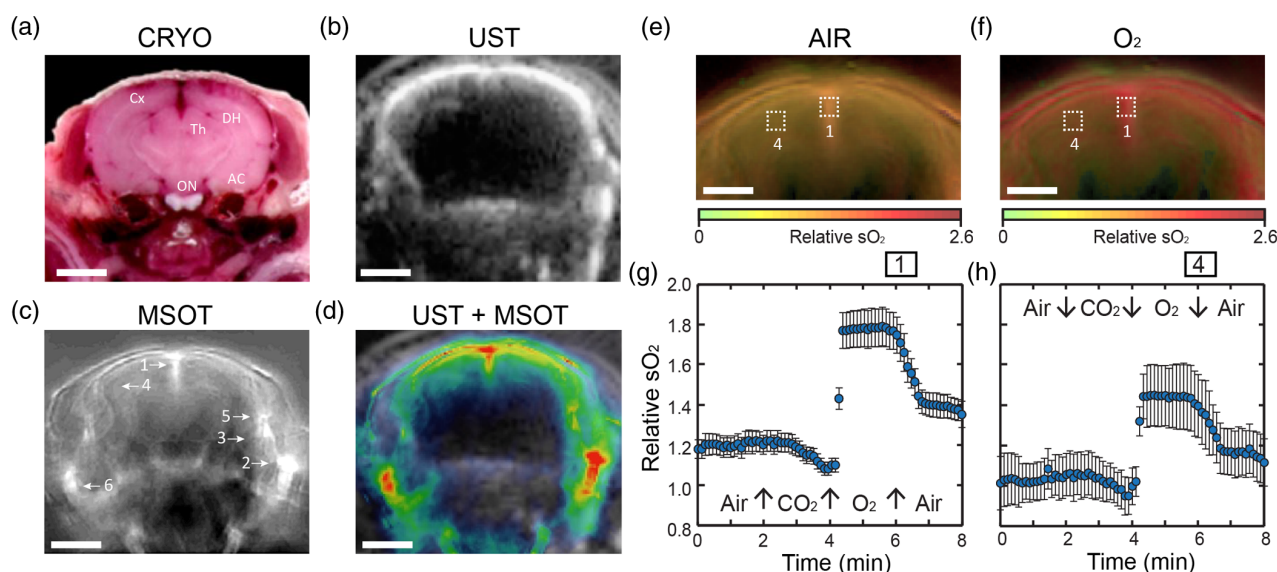
Fig. 2 Hybrid UST and MSOT imaging of the brain. (a) Annotated cross section of a mouse head (brain, coronal plane) with corresponding UST, MSOT, and overlaid images (b, c, and d, respectively). Scale bars: 2 mm. Annotations: Cx, cortex; DH, dorsal hippocampus; Th, thalamus; AC, amygdalar complex; and ON, optic nerve. The regions of interest (c, 1 to 6) for analysis of the sO_2 dynamics are highlighted on MSOT image with arrows (with measurements summarized in Table 1). 1, sagittal sinus; 2 and 6, maxillary arteries; 3 and 4, parenchymal tissue; and 5, medial cerebral artery. (e and f) Color-coded relative sO_2 maps obtained at indicated breathing phases overlaid with anatomical MSOT images. (g and h) Time courses of changes from respective regions of interests (enboxed, 1 and 4) corresponding to sagittal sinus (g) and parietal cortex (h). Blue circles and error bars denote mean relative sO_2 and standard deviations of measurements within respective ROIs, correspondingly. Experimental conditions are indicated within individual graphs. Scale bars: 1.8 mm.

3.2 Comparison of 256 Versus 512 Multispectral Optoacoustic Tomography

To investigate if an increase in the number of ultrasonic detectors in hybrid MSOT–UST platform affects the image quality and resolution of the system, we compared the intensity profiles of defined ROIs on head cross-sectional images acquired with hybrid MSOT512 with those obtained by stand-alone MSOT256.

Figures 4(a) and 4(b) present an annotated histological cross section of a mouse head *ex vivo* (coronal section) taken at the plane that corresponds to −5.3-mm Bregma of the mouse brain atlas.[41] Figures 4(c)–4(f) show tomographic cross sections of
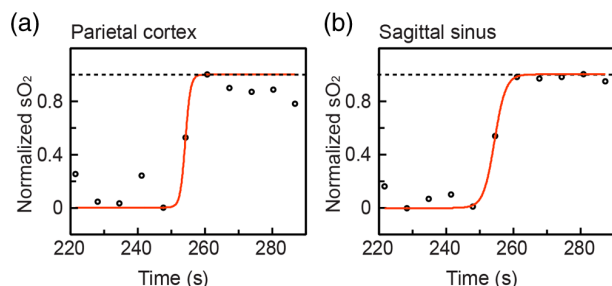
the same anatomical plane obtained with the MSOT512 (c and d) and MSOT256 (e and f) systems at 715-nm (c and e) and 900-nm (d and f) wavelengths. As optical absorption of brain tissue is wavelength dependent, the 715- and 900-nm images reveal spectral differences corresponding to different molecular constituents.[16] While hemoglobin provides the major contrast at 715 nm, at 900 nm, water and adipose tissue are expected to contribute more to contrast generation.

Comparison of the intensity profiles obtained from three defined anatomical references revealed subtle but interesting differences. Figure 4(g) (I to III) present the intensity profiles extracted from locations denoted in Figs. 4(d) and 4(f) (I, II, and III), respectively. The normalized graphs (g, left column) correspond to MSOT512 (black) and MSOT256 (blue, dashed). For comparison of the resolving power of MSOT512 versus MSOT256, we fitted Gaussian curves to the normalized intensity profiles (I to III) and computed their relative FWHM. Figure 4(g) (middle and right columns) shows Gaussian fits for the MSOT256 and MSOT512 measurements, respectively. The computed FWHM values are summarized in Table 2 and advocate improved imaging resolution with MSOT512.

3.3 Hybrid Imaging of Abdominal Organs

Figure 5 presents a cryosection of the mouse abdomen *ex vivo* annotated for major anatomical references (a), with corresponding UST and MSOT cross sections obtained *in vivo* (b and c, respectively) and their coregistered overlay (d). High absorbance of major blood supply routes, such as spinal branch of lumbar arteries and vertebral column with adjacent caudal vena cava along with large parenchymal organs such as left
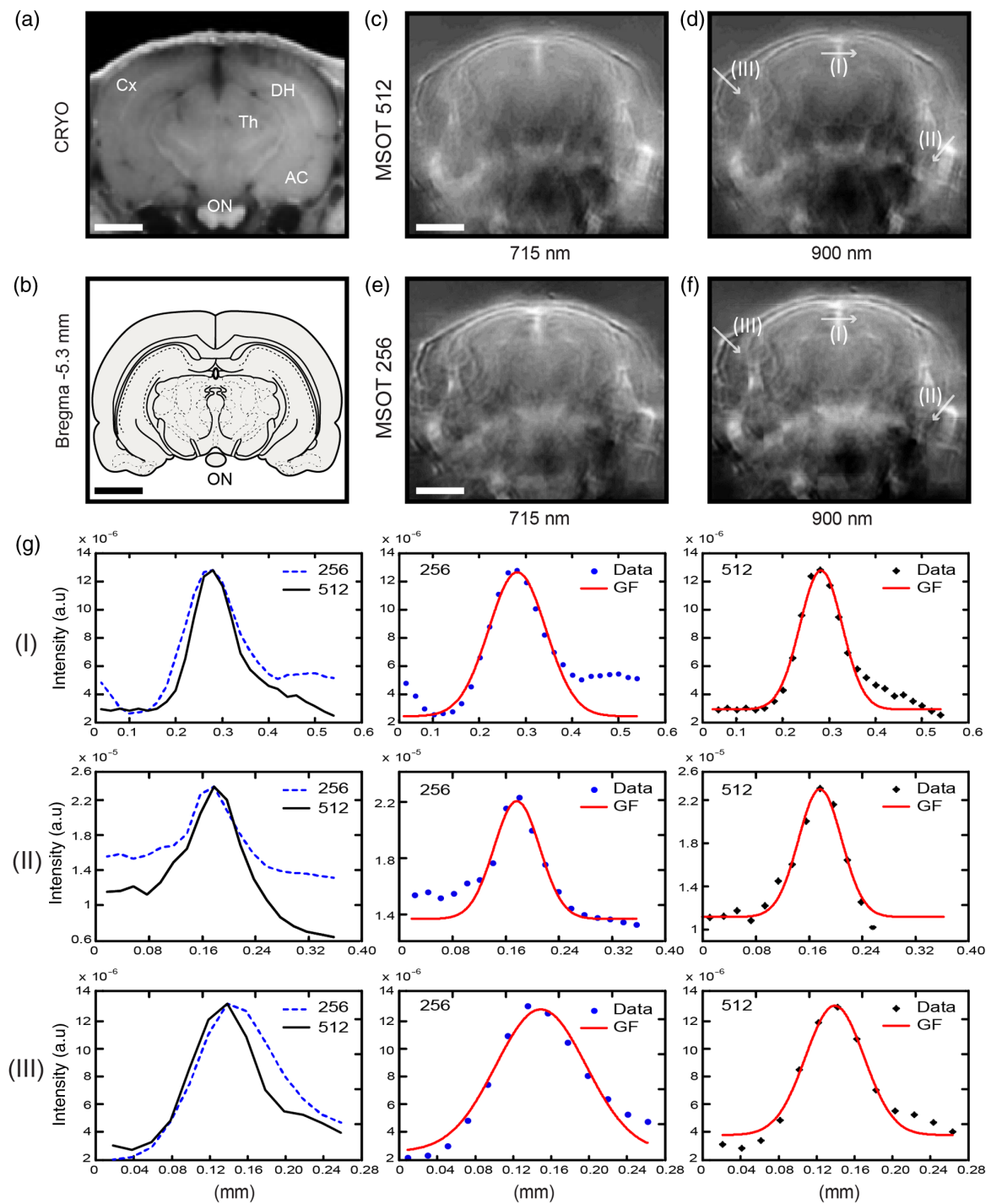

Fig. 3 Graphical representation of the kinetics of the sO_2 within large blood vessels and parenchyma of the brain measured with MSOT. (a and b) Representative sO_2 dynamics overtime pulled from ROIs [corresponding to arrows: 3 and 1, in Fig. 2(c), respectively]. Individual data points overtime are fitted with sigmoid functions with values (tau) defining the slope summarized in Table 1.

Fig. 4 Intravital imaging of a mouse brain with MSOT256 and MSOT512: a comparative analysis. (a) Annotated histological cross section (HIST) of a mouse brain with (b) schematic representation of the corresponding anatomical cross section of the brain: Cx, cortex; DH, dorsal hippocampus; Th, thalamus; AC, amygdalar complex; and ON, optic nerve. Scale bars: 2 mm. (c–f) Tomographic images of the mouse brain obtained with MSOT512 (c and d) and MSOT256 (e and f) at 715 nm (c and e) and 900 nm (d and f). Arrows (I–III) mark approximate locations of intensity profiles extractions. Scale bars: 2.5 mm. (g) Summary of intensity profiles extracted from the coregistered images (d and f). Intensity profiles from MSOT256 (blue, dashed) and MSOT512 (black, solid) are matched at their maxima (left column), fitted with the Gaussian functions (middle and right columns). The FWHM values are presented in Table 2.

Table 2 Comparative FWHM fits of the intensity profiles of sagittal sinus, maxillary artery, and subcutaneous artery using MSOT256 and MSOT512 (units in mm).

Scanners	Sagittal sinus (I)	Maxillary artery (II)	Subcutaneous artery (III)
MSOT256	0.146	0.106	0.083
MSOT512	0.104	0.078	0.074
Difference (%)	28.661	32.425	10.592

and right kidneys, spleen, the head of the pancreas, and epigastria vessels, is visible on MSOT images. UST images, on the other hand, offer better contrast and visualization of organs at greater depths, revealing kidneys, liver, pancreas, vertebral column with the spinal cord and other structures. Importantly, blood reach formations, such as medium and small vascular elements, and parts of liver hardly distinguishable on UST images are revealed better by MSOT, while collagen and connective tissue rich structures and bones reveal higher contrast at UST. Thus, UST of the abdominal organs unveils rich anatomical data on deeper structures, while MSOT provides complementary features based on optical contrast. The latter is especially important for functional imaging, as it affords intravital assessment of local sO_2 and hemoglobin concentration. Figures 5(e) and 5(f) present abdominal cross sections merged with color-coded oxygenation maps computed from MSOT data corresponding to two different breathing phases [air (e) and 100% O_2 (f)]. Similar to brain measurements, assessment of
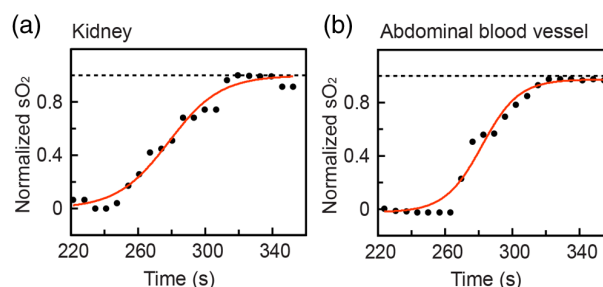
Fig. 6 Graphical representation of the kinetics of the sO_2 within large blood vessels and parenchyma of abdominal organs measured with MSOT. (a and b) Representative sO_2 dynamics overtime pulled from ROIs [corresponding to arrows: 1 and 3, in Fig. 5(c), respectively]. Individual data points overtime are fitted with sigmoid functions with values (tau) defining the slope summarized in Table 1.

the sO_2 kinetics of abdominal organs under different breathing conditions in two ROIs (enboxed 1 and 4) revealed clear correspondence of the hemodynamics with the composition of supplied gas, with dynamics of the sO_2 changes related to the gas challenges readily visible [Figs. 5(g) and 5(h)]. After baseline recording while breathing air, supply of CO_2 causes gradual deoxygenation of the abdominal structures while supply of pure O_2 results in rapid increase in tissue and blood oxygenation. Similar to the brain, these processes remain within physiological limits and reversed upon supply of normal breathing air.

To evaluate the kinetics of the hemoglobin gradient changes in abdominal organs, we analyzed the rates of the relative sO_2 changes upon O_2 challenge. Figure 6 presents the analysis of
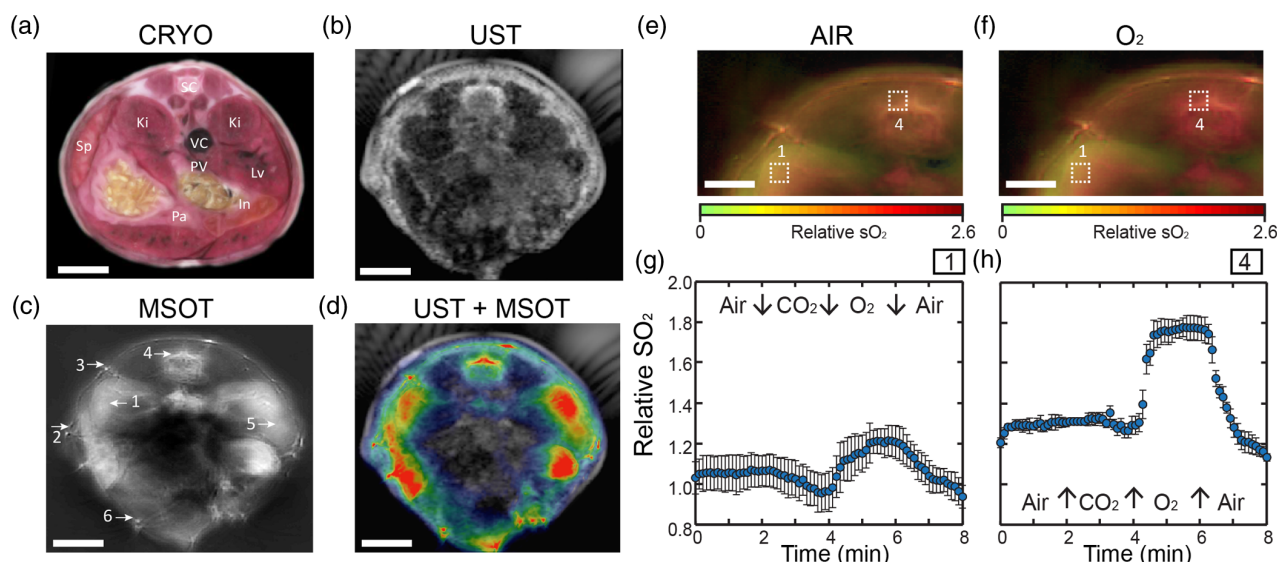
Fig. 5 Hybrid UST and MSOT imaging of abdominal organs. (a) Annotated cross section of a mouse abdomen with UST, MSOT, and overlaid images (b, c, and d, respectively). Annotations: SC, spinal cord; Ki, kidney; Sp, spleen; VC, vena cava; PV, portal vein; Pa, pancreas; Lv, liver; and In, intestine. Scale bars: 3 mm. The regions of interest (1 to 6) for analysis of the sO_2 dynamics are highlighted on (c) MSOT image with arrows (summarized in Table 1). 1 and 5, kidneys; 2, 3, and 6, superficial vessels; and 4, spinal branch of lumbar artery. (e and f) Color-coded relative sO_2 maps obtained at indicated breathing phases overlaid with anatomical images. (g and h) Time courses of changes from respective regions of interests (enboxed, 1 and 4). Blue circles and error bars denote mean relative sO_2 and standard deviations of measurements within respective ROIs, correspondingly. Experimental conditions are indicated within individual graphs. Scale bars: 2 mm.

the sO_2 kinetics of kidney tissue (a) and an abdominal blood vessel (b), with data obtained from regions marked by arrows 1 and 3 in Fig. 5(c), respectively. Black circles correspond to the normalized data points with red lines showing the fitted sigmoid functions. Parenchymal organs showed slower sO_2 rates compared to those of the brain (Table 1), supporting tighter coupling of the brain sO_2 with breathing state and overall greater oxygen consumption of neural tissue and its lower tolerance to hypoxia.[42,43]

4 Discussion

Hybrid imaging systems offer a highly promising future to correlative biomedical and clinical studies. At present, dual PET–CT implementations are widely applied for combining the intravital molecular imaging with high-resolution structural information.[44,45] Likewise, hybrid XCT and fluorescence molecular tomography have proven more instructive compared to stand-alone counterparts.[46,47] In this study, we applied a MSOT–UST system for structural and functional spectral OA and ultrasound imaging and validated its performance on the head and abdominal organs in adult mice *in vivo*.

The combination of ultrasound and multispectral OA imaging for interrogation of biological specimens has been considered in the past with the use of linear DAs.[32,48] However, the latter has proven to be unable to produce volumetric OA readouts, with imaging capabilities limited to 2-D visualization of superficial layers of the specimen. Recently, curved-array MSOT–UST system has been developed and used for imaging the entire mouse in tomographic mode.[36] This system was not, however, considered for imaging functional processes unfolding within the brain or abdominal organs. The capability of the curved DA to visualize the entire animal at ultrasound diffraction-limited resolution combined with high frame rate measurements of functional dynamics are especially attractive for reconstructing physiological processes in near real-time with their correlation with structural data. In this study, we used curved-array MSOT–UST system for dual structural and functional imaging *in vivo* to characterize the performance of both modalities and highlight advantages and limitations of using such a hybrid system for experimental and preclinical research. As expected, hybrid images exhibited complementary features. Indeed, on the head scans, UST clearly revealed the boundaries between various tissue types, with skull reflecting most of the ultrasound waves and, thus, appearing as a high contrast; the brain in these images was hardly visible. Thus, the structural US images of the brain have limited diagnostic and exploratory value, as expected. Nevertheless, US modality provides numerous benefits in brain imaging applications. Indeed, MSOT reconstruction suffers from acoustic inhomogeneity of skull that can be corrected to some extent by incorporating structural information provided by US into OA image reconstruction process. It could also help delineating brain region in MSOT images. MSOT images, in turn, revealed hemoglobin gradients with strongest signals corresponding to the compartments with high blood content such as large vessels, inner parenchymal organs, and the brain. The latter, however, comes with considerable deterioration of the image quality with increase of the imaging depth. Due to high optical absorption of the hemoglobin, MSOT readouts contain important functional information on hemodynamics, which is of direct relevance to the level of tissue oxygenation and metabolism rate. This capability of MSOT is particularly attractive in light of growing interest in direct

measurements of the oxygen consumption and hemoglobin gradients *in vivo*. With further improvements and corrections for aberrations and signal loss within highly scattering tissues, MSOT could provide powerful means for simultaneous structural and multispectral functional imaging with better correlation of the UST data. The latter should facilitate also accurate representation of molecular data in the context of anatomical readout, including the biodistribution of reporters and contrast agents as well as changes in the hemodynamics and metabolic activity in various tissues and organs. It is worth noting that unlike the brain, US imaging of the abdomen reveals more clearly structural features and contours of inner organs and is capable of visualizing tissue interfaces at greater depths. In turn, MSOT exhibits worse performance in terms of structural imaging due to attenuation of light with depth and provides complimentary optical contrasts based on the hemoglobin concentrations and blood oxygenation with the ability to track the sO_2 dynamics. Such correlative arrangement greatly enriches the content of obtained anatomical and functional data and should facilitate better characterization and understanding of a wide range of biological processes and functions. Importantly, MSOT measurements of the hemodynamics relate meaningfully with applied gas challenges, with physiological values matching closely those reported previously.[49] The onset rates of sO_2 changes defined here are also within the expected kinetic ranges.[50] Combined with exogenous labels and reporters,[18] further advancements of hybrid MSOT–UST imaging should facilitate the interrogation processes with direct relevance to pharmacokinetics, biodiagnostics, and pathophysiological studies.[28,51–54] With regard to MSOT imaging quality, it should be noted that the implemented ultrasound array with 512 transducers moderately improves MSOT resolution as compared to its predecessor with 256 element detectors. Better resolution of the selected profiles shown here agrees with the experimental phantom results[34,36] as well as theoretical predictions[55] reported previously.

At this stage, major technical challenges remain ahead that need to be addressed. One area that requires attention is motion artifacts related with the breathing of experimental mice, which due to small animal size, cause incongruity between corresponding MSOT and UST images. A semiautomatic approach for relating MSOT and UST data can be taken to partially overcome this problem, with registration performed based on carefully selected reference points. The main difficulty with this approach stems from the fact that differences in contrasts and penetration between two modalities make the choice of structural references nontrivial. Further research is currently on the way to address these challenges and optimize the signal propagation with more effective data collection. Notwithstanding, described here hybrid system holds great potential for gaining new insights into numerous questions, which necessitate concurrent acquisition with correlation of structural, functional, and molecular data.

To conclude, as a modality with numerous applications in the biological imaging, MSOT is increasingly used for neuroimaging.[56] The multispectral capability that affords its molecular specificity and ability to differentiate numerous endogenous and exogenous absorbers make it a valuable tool for brain imaging with potential applications ranging from high-resolution structural mesoscopy to imaging of functional processes involving changes of hemoglobin and neural dynamics, vascular dynamics, metabolism (i.e., oxygen consumption rate), and biodistribution of contrasts and drugs. Along with

pertinence for basic animal research, MSOT has also growing implications for preclinical studies in animal models and potentially in humans. Indeed, reports from animal model of Parkinson's disease, Alzheimer's disease, epilepsy, and stroke have shown the feasibility and usefulness of OA imaging, yielding new insights into the disease mechanisms. With further optimizations, OA tools are likely to be used in the near future also in human studies.

Acknowledgments

References

1. R. Salzer, *Biomedical Imaging: Principles and Applications*, John Wiley & Sons, Incorporated, Hoboken, New Jersey (2008).
2. F. Kiessling, J. Pichler, and P. Hauff, *Small Animal Imaging*, Springer, Heidelberg (2011).
3. E. Mark et al., "In vivo validation of the bold mechanism: a review of signal changes in gradient echo functional MRI in the presence of flow," *Int. J. Imaging Syst. Technol.* **6**(2–3), 153–163 (1995).
4. E. R. Sowell et al., "Development of cortical and subcortical brain structures in childhood and adolescence: a structural MRI study," *Dev. Med. Child Neurol.* **44**(1), 4–16 (2002).
5. T. L. Szabo, *Diagnostic Ultrasound Imaging: Inside Out*, Academic Press, Amsterdam, Boston (2004).
6. K. Kubota, "From tumor biology to clinical PET: a review of positron emission tomography (PET) in oncology," *Ann. Nucl. Med.* **15**(6), 471–486 (2001).
7. H. T. Benamer et al., "Accurate differentiation of Parkinsonism and essential tremor using visual assessment of [123I]-FP-CIT SPECT imaging: The [123I]-FP-CIT study group," *Mov. Disorders* **15**(3), 503–510 (2000).
8. W. A. Kalender, "X-ray computed tomography," *Phys. Med. Biol.* **51**(13), R29 (2006).
9. V. Andresen et al., "Infrared multiphoton microscopy: subcellular-resolved deep tissue imaging," *Curr. Opin. Biotechnol.* **20**(1), 54–62 (2009).
10. J. A. Izatt et al., "Micrometer-scale resolution imaging of the anterior eye in vivo with optical coherence tomography," *Arch. Ophthalmol.* **112**(12), 1584–1589 (1994).
11. V. Ntziachristos, "Going deeper than microscopy: the optical imaging frontier in biology," *Nat. Methods* **7**(8), 603–614 (2010).
12. P. Beard, "Biomedical photoacoustic imaging," *Interface Focus* **1**(4), 602–631 (2011).
13. V. Ntziachristos et al., "Looking and listening to light: the evolution of whole-body photonic imaging," *Nat. Biotechnol.* **23**(3), 313–320 (2005).
14. L. V. Wang and S. Hu, "Photoacoustic tomography: in vivo imaging from organelles to organs," *Science* **335**(6075), 1458–1462 (2012).
15. A. G. Bell, "On the production and reproduction of sound by light," *Am. J. Sci.* **20**, 305–324 (1880).
16. V. Ntziachristos and D. Razansky, "Molecular imaging by means of multispectral optoacoustic tomography (MSOT)," *Chem. Rev.* **110**(5), 2783–2794 (2010).
17. A. Petschke and P. J. La Riviere, "Comparison of intensity-modulated continuous-wave lasers with a chirped modulation frequency to pulsed lasers for photoacoustic imaging applications," *Biomed. Opt. Express* **1**(4), 1188–1195 (2010).
18. A. Taruttis and V. Ntziachristos, "Advances in real-time multispectral optoacoustic imaging and its applications," *Nat. Photonics* **9**, 219–227 (2015).
19. S. Tzoumas et al., "Unmixing molecular agents from absorbing tissue in multispectral optoacoustic tomography," *IEEE Trans. Med. Imaging* **33**(1), 48–60 (2014).
20. A. A. Oraevsky, "Contrast agents for optoacoustic imaging: design and biomedical applications," *Photoacoustics* **3**(1), 1–2 (2015).
21. A. Liopo, R. Su, and A. A. Oraevsky, "Melanin nanoparticles as a novel contrast agent for optoacoustic tomography," *Photoacoustics* **3**(1), 35–43 (2015).
22. D. Razansky et al., "Multispectral opto-acoustic tomography of deep-seated fluorescent proteins in vivo," *Nat. Photonics* **3**(7), 412–417 (2009).
23. J. A. Copland et al., "Bioconjugated gold nanoparticles as a molecular based contrast agent: implications for imaging of deep tumors using optoacoustic tomography," *Mol. Imaging Biol.* **6**(5), 341–349 (2004).
24. A. Taruttis, G. M. van Dam, and V. Ntziachristos, "Mesoscopic and macroscopic optoacoustic imaging of cancer," *Cancer Res.* **75**(8), 1548–1559 (2015).
25. X. Wang et al., "Noninvasive laser-induced photoacoustic tomography for structural and functional in vivo imaging of the brain," *Nat. Biotechnol.* **21**(7), 803–806 (2003).
26. S. Hu and L. V. Wang, "Neurovascular photoacoustic tomography," *Front Neuroenerg.* **2**, 10 (2010).
27. A. Buehler et al., "High resolution tumor targeting in living mice by means of multispectral optoacoustic tomography," *EJNMMI Res.* **2**, 14 (2012).
28. A. Taruttis et al., "Real-time imaging of cardiovascular dynamics and circulating gold nanorods with multispectral optoacoustic tomography," *Opt. Express* **18**(19), 19592–19602 (2010).
29. G. J. Tserevelakis et al., "Hybrid multiphoton and optoacoustic microscope," *Opt. Lett.* **39**(7), 1819–1822 (2014).
30. J. J. Niederhauser et al., "Combined ultrasound and optoacoustic system for real-time high-contrast vascular imaging in vivo," *IEEE Trans. Med. Imaging* **24**(4), 436–440 (2005).
31. M. Lakshman and A. Needles, "Screening and quantification of the tumor microenvironment with micro-ultrasound and photoacoustic imaging," *Nat. Methods* **12**(4), iii–v (2015).
32. S. A. Ermilov et al., "Development of laser optoacoustic and ultrasonic imaging system for breast cancer utilizing handheld array probes," *Proc. SPIE* **7177**, 717703 (2009).
33. C. Kim et al., "Deeply penetrating in vivo photoacoustic imaging using a clinical ultrasound array system," *Biomed. Opt. Express* **1**(1), 278–284 (2010).
34. A. Dima, N. C. Burton, and V. Ntziachristos, "Multispectral optoacoustic tomography at 64, 128, and 256 channels," *J. Biomed. Opt.* **19**(3), 036021 (2014).
35. J. Xia et al., "Enhancement of photoacoustic tomography by ultrasonic computed tomography based on optical excitation of elements of a full-ring transducer array," *Opt. Lett.* **38**(16), 3140–3143 (2013).
36. E. Mercep et al., "Whole-body live mouse imaging by hybrid reflection-mode ultrasound and optoacoustic tomography," *Opt. Lett.* **40**(20), 4643–4646 (2015).
37. E. Mercep et al., "Hybrid optoacoustic tomography and pulse-echo ultrasonography using concave arrays," *IEEE Trans. Ultrason. Ferroelectr. Freq. Control* **62**(9), 1651–1661 (2015).
38. A. Buehler et al., "Video rate optoacoustic tomography of mouse kidney perfusion," *Opt. Lett.* **35**(14), 2475–2477 (2010).
39. T. Iwaki, *A Color Atlas of Sectional Anatomy of the Mouse*, Braintree Scientific Inc., Tokyo, Japan (2001).
40. D. Lu et al., "Efficient non-negative constrained model-based inversion in optoacoustic tomography," *Phys. Med. Biol.* **60**(17), 6733–6750 (2015).
41. G. Paxinos and C. Watson, *The Rat Brain in Stereotaxic Coordinates*, 6th ed., Academic Press/Elsevier, Amsterdam, Boston (2007).
42. V. Jain, M. C. Langham, and F. W. Wehrli, "MRI estimation of global brain oxygen consumption rate," *J. Cereb. Blood Flow Metab.* **30**(9), 1598–1607 (2010).
43. F. Xu, Y. Ge, and H. Lu, "Noninvasive quantification of whole-brain cerebral metabolic rate of oxygen (CMRO2) by MRI," *Magn. Reson. Med.* **62**(1), 141–148 (2009).
44. P. E. Kinahan et al., "Attenuation correction for a combined 3D PET/CT scanner," *Med. Phys.* **25**(10), 2046–2053 (1998).
45. T. Beyer et al., "A combined PET/CT scanner for clinical oncology," *J. Nucl. Med.* **41**(8), 1369–1379 (2000).
46. A. Ale et al., "FMT-XCT: in vivo animal studies with hybrid fluorescence molecular tomography-x-ray computed tomography," *Nat. Methods* **9**(6), 615–620 (2012).
47. A. Ale et al., "Fluorescence background subtraction technique for hybrid fluorescence molecular tomography/x-ray computed tomography imaging of a mouse model of early stage lung cancer," *J. Biomed. Opt.* **18**(5), 056006 (2013).

48. K. Daoudi et al., "Handheld probe integrating laser diode and ultrasound transducer array for ultrasound/photoacoustic dual modality imaging," *Opt. Express* **22**(21), 26365–26374 (2014).
49. N. C. Burton et al., "Multispectral opto-acoustic tomography (MSOT) of the brain and glioblastoma characterization," *NeuroImage* **65**, 522–528 (2013).
50. S. Gottschalk et al., "Noninvasive real-time visualization of multiple cerebral hemodynamic parameters in whole mouse brains using five-dimensional optoacoustic tomography," *J. Cereb. Blood Flow Metab.* **35**(4), 531–535 (2015).
51. M. L. Li et al., "Simultaneous molecular and hypoxia imaging of brain tumors in vivo using spectroscopic photoacoustic tomography," *Proc. IEEE* **96**(3), 481–489 (2008).
52. L. D. Liao et al., "Transcranial imaging of functional cerebral hemodynamic changes in single blood vessels using in vivo photoacoustic microscopy," *J. Cereb. Blood Flow Metab.* **32**(6), 938–951 (2012).
53. A. Taruttis et al., "Multispectral optoacoustic tomography of myocardial infarction," *Photoacoustics* **1**(1), 3–8 (2013).
54. A. Taruttis et al., "Fast multispectral optoacoustic tomography (MSOT) for dynamic imaging of pharmacokinetics and biodistribution in multiple organs," *PLoS One* **7**(1), e30491 (2012).
55. M. Xu and L. V. Wang, "Analytic explanation of spatial resolution related to bandwidth and detector aperture size in thermoacoustic or photoacoustic reconstruction," *Phys. Rev. E* **67**(5), 056605 (2003).
56. J. Yao and L. V. Wang, "Photoacoustic brain imaging: from microscopic to macroscopic scales," *Neurophotonics* **1**(1), 011003 (2014).

Biographies for the authors are not available.
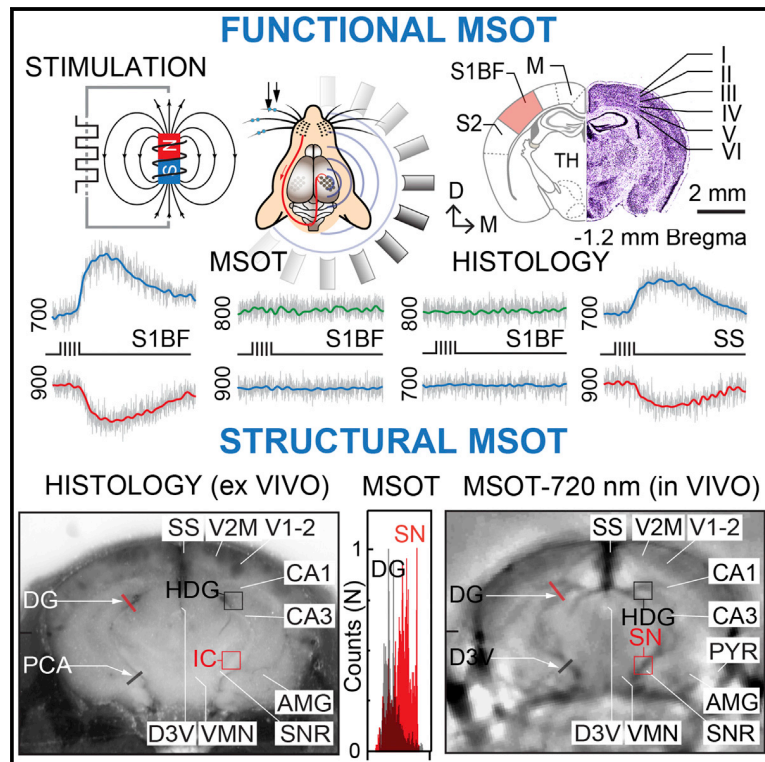
Appendix D

Publication: Spatial and spectral mapping and decomposition of neural dynamics and organization of the mouse brain with multispectral optoacoustic tomography

Cell Reports

Spatial and Spectral Mapping and Decomposition of Neural Dynamics and Organization of the Mouse Brain with Multispectral Optoacoustic Tomography

Graphical Abstract

Authors

Ivan Olefir, Ara Ghazaryan, Hong Yang, ...,
George Sergiadis, Vasilis Ntziachristos,
Saak V. Ovsepian

Correspondence

v.ntziachristos@helmholtz-muenchen.de
(V.N.),
saak.ovsepian@gmail.com (S.V.O.)

In Brief

Olefir et al. apply multispectral
optoacoustic (photoacoustic)
tomography (MSOT) for noninvasive
spatial and spectral mapping and
decomposition of neural dynamics and
organization of the intact mouse brain
in vivo. The results extend the boundaries
of noninvasive high-resolution
observations beyond the reach of
intravital optical neuroimaging in small-
animal studies.

Highlights

- Noninvasive functional and structural neuroimaging in mice using MSOT

- Resting and activity-dependent response mapped on entire brain cross-sections

- Connectivity between various structures revealed with coherence analysis

- High-resolution structural tomography achieved based on endogenous contrasts

CellPress

Spatial and Spectral Mapping and Decomposition of Neural Dynamics and Organization of the Mouse Brain with Multispectral Optoacoustic Tomography

Ivan Olefir,[1,2] Ara Ghazaryan,[1] Hong Yang,[1] Jaber Malekzadeh-Najafabadi,[1] Sarah Glasl,[1] Panagiotis Symvoulidis,[1,2] Valerie B. O'Leary,[3] George Sergiadis,[4] Vasilis Ntziachristos,[1,2,7,8,*] and Saak V. Ovsepian[1,2,5,6,7,*]

[1]Institute of Biological and Medical Imaging (IBMI), Helmholtz Zentrum Munich, Ingolstadter Landstrasse 1, 85764 Neuherberg, Germany
[2]Chair of Biological Imaging, Technical University Munich, 81675 Munich, Germany
[3]Department of Medical Genetics, Third Faculty of Medicine of Charles University, 11636 Prague, Czech Republic
[4]Department of Electrical and Computer Engineering, Aristotle University, 54124 Thessaloniki, Greece
[5]Department of Experimental Neurobiology, National Institute of Mental Health, Topolová 748, 25067 Klecany, Czech Republic
[6]Department of Psychiatry and Medical Psychology, Third Faculty of Medicine of Charles University, 11636 Prague, Czech Republic
[7]These authors contributed equally
[8]Lead Contact
*Correspondence: v.ntziachristos@helmholtz-muenchen.de (V.N.), saak.ovsepian@gmail.com (S.V.O.)
https://doi.org/10.1016/j.celrep.2019.02.020

SUMMARY

In traditional optical imaging, limited light penetration constrains high-resolution interrogation to tissue surfaces. Optoacoustic imaging combines the superb contrast of optical imaging with deep penetration of ultrasound, enabling a range of new applications. We used multispectral optoacoustic tomography (MSOT) for functional and structural neuroimaging in mice at resolution, depth, and specificity unattainable by other neuroimaging modalities. Based on multispectral readouts, we computed hemoglobin gradient and oxygen saturation changes related to processing of somatosensory signals in different structures along the entire subcortical-cortical axis. Using temporal correlation analysis and seed-based maps, we reveal the connectivity between cortical, thalamic, and sub-thalamic formations. With the same modality, high-resolution structural tomography of intact mouse brain was achieved based on endogenous contrasts, demonstrating near-perfect matches with anatomical features revealed by histology. These results extend the limits of noninvasive observations beyond the reach of standard high-resolution neuroimaging, verifying the suitability of MSOT for small-animal studies.

INTRODUCTION

Unveiling a structure-functional relationship in the nervous system is one of the key priorities of neuroimaging. In this pursuit, optical imaging has been the main workhorse, enabling over many decades the high-resolution structural brain imaging (Wilt et al., 2009). With superb contrast, resolution, and multiplexing capabilities, optical interrogation has also recently become an integral part of functional neuroimaging, empowering sensing of voltage and calcium dynamics of individual neurons and synaptic connections (Chen et al., 2011; Grienberger et al., 2014; Perron et al., 2009; Peterka et al., 2011; Stettler et al., 2006). Notwithstanding these advances, investigation of the brain using light has several fundamental limitations, due to diffraction and scattering, which constrain observations to the surface (Hillman, 2007; Hong et al., 2014; Ntziachristos, 2010). For microscopy, penetration of several hundred microns into brain has been achieved using two-photon excitation via cranial opening, which could be extended further by surgical removal of superficial tissue mass, with downsides of invasiveness and loss of circuit integrity (Dombeck et al., 2010; Helmchen and Denk, 2005; Kerr and Denk, 2008; Willem et al., 2015). Using three-photon GCaMP6 excitation, the activity of neurons in the dorsal hippocampus was recently recoded *in vivo*, albeit with major depth-dependent loss of spatial resolution (Ouzounov et al., 2017). For macroscopic brain imaging usage, the limits set by light scattering have been partly surmounted by the utilization of diffusive imaging methods such as diffuse optical tomography (DOT) and near-infrared spectroscopy (NIRS), which enabled measurements in thick samples, but with poor spatial resolution (Boas et al., 2004; Culver et al., 2003; Eggebrecht et al., 2014; Siegel et al., 1999).

Unlike optical imaging, high-resolution radiological methods such as fMRI and ultrasonography (US) enable excellent penetration with 3D isotropic visualization of intact biological samples. However, the principal downfall of fMRI is its low sensitivity, which limits spatial and especially temporal resolution (Denic et al., 2011; Hoyer et al., 2014; Jonckers et al., 2015; Logothetis, 2008), above all detrimental in small-animal studies, where miniature brain size and tiny structures downgrade the data quality (Farahani et al., 1990; Hoyer et al., 2014; Yang et al., 2006). Unlike fMRI, functional US (fUS) affords first-rate resolution in time and space, empowering exquisite connectivity analysis and hemodynamic readouts in murine and human applications (Errico et al., 2015; Gesnik et al., 2017; Macé et al., 2011; Osmanski et al., 2014). While suitable for mapping brain activation by sensory

inputs, high-resolution fUS in adult murine models requires skull thinning or cranial opening (Macé et al., 2011; Osmanski et al., 2014). Using optimized US sequence with specialized probes, a recent report showed the feasibility of noninvasive transcranial fUS in young mice (< 1 month old [m.o.]), validating its utility for neuroimaging in behavioral studies (Tiran et al., 2017).

Optoacoustic (photoacoustic) imaging combines the superb contrast mechanisms of optical imaging with the high resolution and penetration depth of US (Beard, 2011; Ntziachristos et al., 2005; Taruttis and Ntziachristos, 2015). Despite unique capacities for multiscale and multispectral interrogation of thick biological samples, optoacoustic functional neuroimaging so far has remained largely confined to the cerebral cortex (Liao et al., 2012; Nasiriavanaki et al., 2014; Tang et al., 2015; Wang et al., 2003, 2013; Yao et al., 2015). The majority of functional neuroimaging reports have also neglected the multispectral assets of the methodology, using only a single illumination wavelength (Liao et al., 2012; Nasiriavanaki et al., 2014; Ovsepian et al., 2017; Wang et al., 2003; Yao and Wang, 2014). A few attempts at mapping functional dynamics of brain circuits and hemoglobin gradient changes in deeper brain compartments have been limited to studies of drug-induced seizure or solid tumor xenografts, with dubious physiological relevance (Burton et al., 2013; Gottschalk et al., 2017). Finally, reports using optoacoustic imaging for structural brain studies *in vivo* have succumbed to visualization of large superficial vessels and major anatomical references (Laufer et al., 2009; Lin et al., 2015; Razansky et al., 2011; Stein et al., 2009).

Thus, to date, the most valuable assets of optoacoustic interrogation neither have been properly validated nor utilized for brain imaging (Ovsepian et al., 2017). In this study, we set out to address some of the omission by testing the efficacy of multispectral optoacoustic tomography (MSOT) for high-resolution label-free functional and structural imaging with reconstruction of the entire mouse brain. We visualize, map, and decompose the spatial and spectral characteristics of a neurovascular response induced by whisker inputs on the entire forebrain cross-sections within intact mice. Based on the temporal coherence of hemodynamic signals and oxygen saturation gradients, we reconstruct the connectivity involved in processing and integration of somatosensory signals along the entire subcortical-cortical axis, which replicates closely the circuitry revealed by neurophysiological studies and tract tracing. Finally, we make original use of MSOT for label-free and contrast-based imaging of mouse brain anatomy and tract tracing *ex vivo* and *in vivo*, to relate volumetric data with results of light-microscopic observations.

RESULTS

Despite outstanding capabilities for high-resolution interrogation and volumetric imaging of deep tissue, the vast majoroty of functional optoacoustic brain studies in small-animal models have so far been confined to the cortex. To date, activity-related changes in hemodynamic gradients within deep compartments of the brain have been unexplored. Taking advantage of the strong central representation and well-defined connections of somatosensory whisker projections of mice, we imaged the neurovascular responses related to activity and processing of whisker

inputs on the entire forebrain cross-sections using MSOT (Figures S1–S3). We applied whisker stimulation (mechanical deflections) and monitored changes in deoxyhemoglobin (Hb) and oxyhemoglobin (HbO$_2$) gradients in the brain, with computed tissue oxygenation ($_S$O$_2$) level.

Figures 1A–1C show the experimental layout of functional MSOT studies and illustrates a mouse brain cross-section containing the somatosensory barrel cortex along with several major anatomical structures, together with traces of Hb, HbO$_2$, and isosbestic point (700, 900, and 800 nm) signal changes as well as traces from negative control experiments collected from mice without whiskers stimulation. While in all experimental trials initial changes in Hb gradients and $_S$O$_2$ signals related to the activation of whisker inputs were most prominent in the somatosensory barrel field of the contralateral side, over a short period of time, the evoked responses spread over the adjacent somatosensory cortex hindlimb and primary motor areas, as well as ipsilateral somatosensory barrel and motor fields. Interestingly, under our experimental settings, the total blood volume (i.e., signal detected at 800 nm) in activated cortical regions remained largely unchanged, possibly due to weak intensity of whisker inputs. Figures 1D–1G illustrate a representative series of MSOT images overlaid with thresholded Hb, HbO$_2$, and $_S$O$_2$ maps at consecutive time points from two experiments. Analysis of signal density changes across different layers of the somatosensory barrel field revealed a distinctly lamellar pattern of the hemodynamic response with significant differences evident in the signal onset and distribution across different cortical layers (Figure 1H). Unlike HbO$_2$ changes concomitantly across multiple layers of the barrel cortex and reaching the highest intensity in the superficial compartments, the Hb response first appeared in L4–L5 and spread toward both the superficial and deeper cortical layers. Importantly, all alterations in hemodynamic signals related to the somatosensory whisker inputs were stimulus specific, as similar trails with non-magnetized whiskers showed no HbO$_2$ or Hb changes (Figure 1C). Likewise, in similar experiments with two consecutive series of whisker stimulation, a strong activity-dependent depression in the response to the second stimulation series was observed, in line with history-dependent plasticity of the hemodynamic response (Figure S4).

As somatosensory inputs to the barrel cortex are conveyed through the lemniscal route, via ventral and posterior thalamic relay nuclei, and through extrathalamic modulatory tracts, via basal forebrain projections (Brecht et al., 2004; Zaborszky et al., 2015), we set out to investigate whether neurovascular response changes related to whisker inputs can be detected in these and other functionally associated deep-brain structures. Figures 2A–2C show three consecutive MSOT cross-sections of a mouse brain with a series of Hb and HbO$_2$ recordings related to the activation of whisker inputs. As can be readily seen, the amplitude of hemodynamic response strongly depends on the anatomical plane, with the strongest changes in Hb gradients confined to the cross-section containing the somatosensory barrel field and associated thalamic nuclei of the contralateral side. Extending the analysis of stimulation-evoked responses with $_S$O$_2$ measurements over extensive brain areas revealed activation of wider fields, involving ventral and reticular thalamic nuclei, basal forebrain, and amygdala, with however
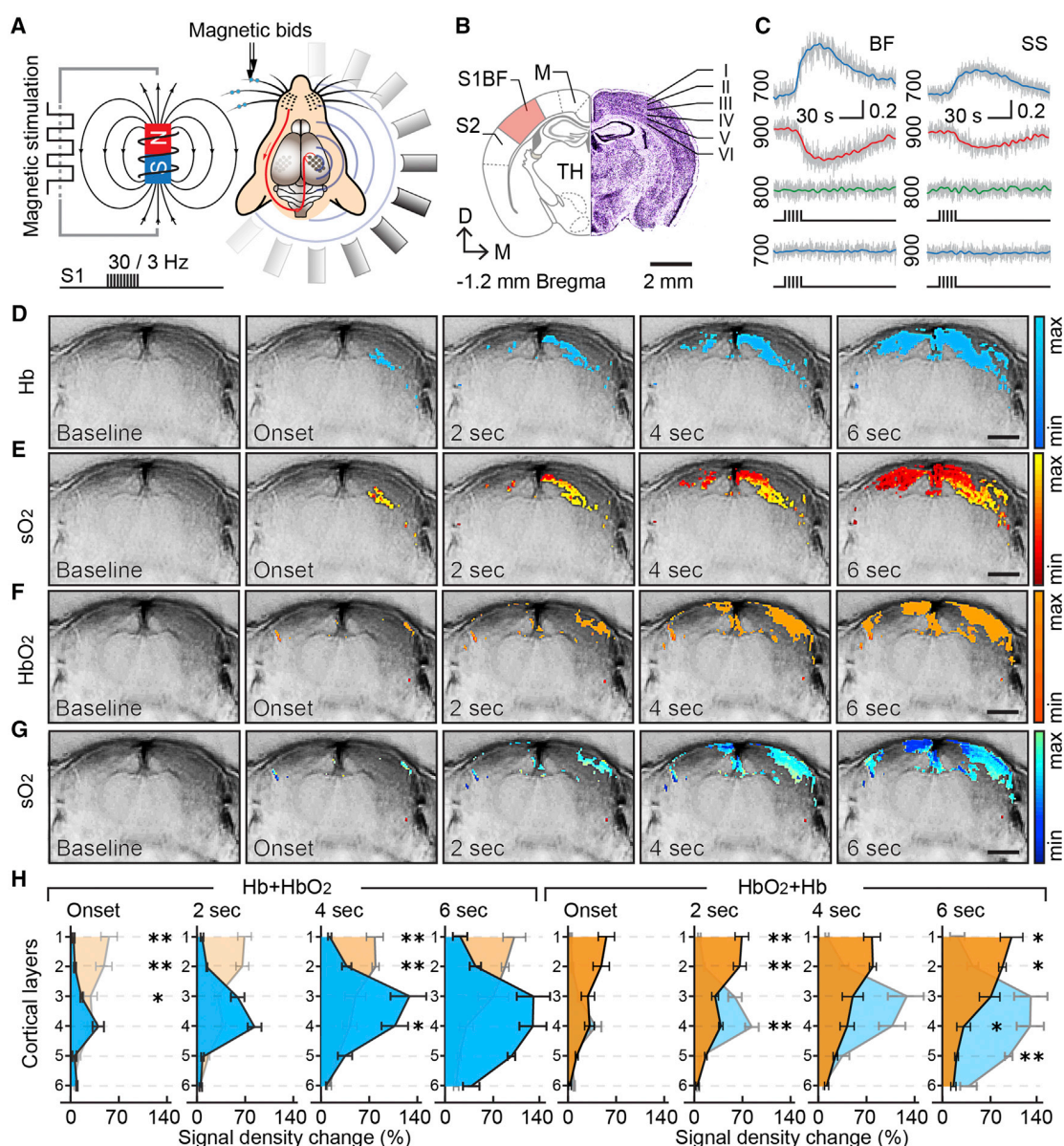
Figure 1. Functional MSOT of Whisker-Induced Response in the Somatosensory Barrel Cortex

(A) Schematic of the experimental design of whisker stimulation with pull-push magnet and brain imaging with MSOT.

(B) Representation of mouse brain cross-section containing anatomical references such as somatosensory barrel cortex (S1BF), S2 somatosensory field (S2), and motor cortex (M) (left), with Nissl-stained brain slice of corresponding plane showing cortical layers of the S1BF (right).

(C) Typical traces of HbO_2 (900 nm), Hb (700 nm), and isosbestic (800 nm) signal from experimental group (top), and HbO_2 and Hb signals from negative control group verifying that changes in Hb and HbO_2 signals are specific to activation of whisker inputs.

(D–G) Consecutive time series of anatomical brain images overlaid with Hb (D), HbO_2 (F), and $_sO_2$ (E and G) maps before (baseline) and after (2-s increments) whisker stimulation. Activation maps presented in different colors show pixel-wise changes in the intensity of MSOT signal related to the stimulation of whisker inputs, with signal intensity changes presented in arbitrary units.

(H) Distribution and dynamics of the whisker evoked Hb, HbO_2, and $_sO_2$ signal density across different layers of S1BF of the somatosensory cortex. Graphs present means and SEM of signal density changes in different cortical layers from six independent trials with their comparison (*p < 0.05; **p < 0.005; unpaired t test).

no consistent response detectable in areas corresponding to lateral ventricles (Figures 2D–2G).

Next, the extent of the temporal coherence in the neurovascular response between multiple brain regions was analyzed, with results summarized in cross-correlation matrices of Hb, HbO_2, and $_sO_2$ signals collected across entire brain cross-sections containing the somatosensory barrel field and related structures (Figures 3A–3D). Analogous measurements from negative
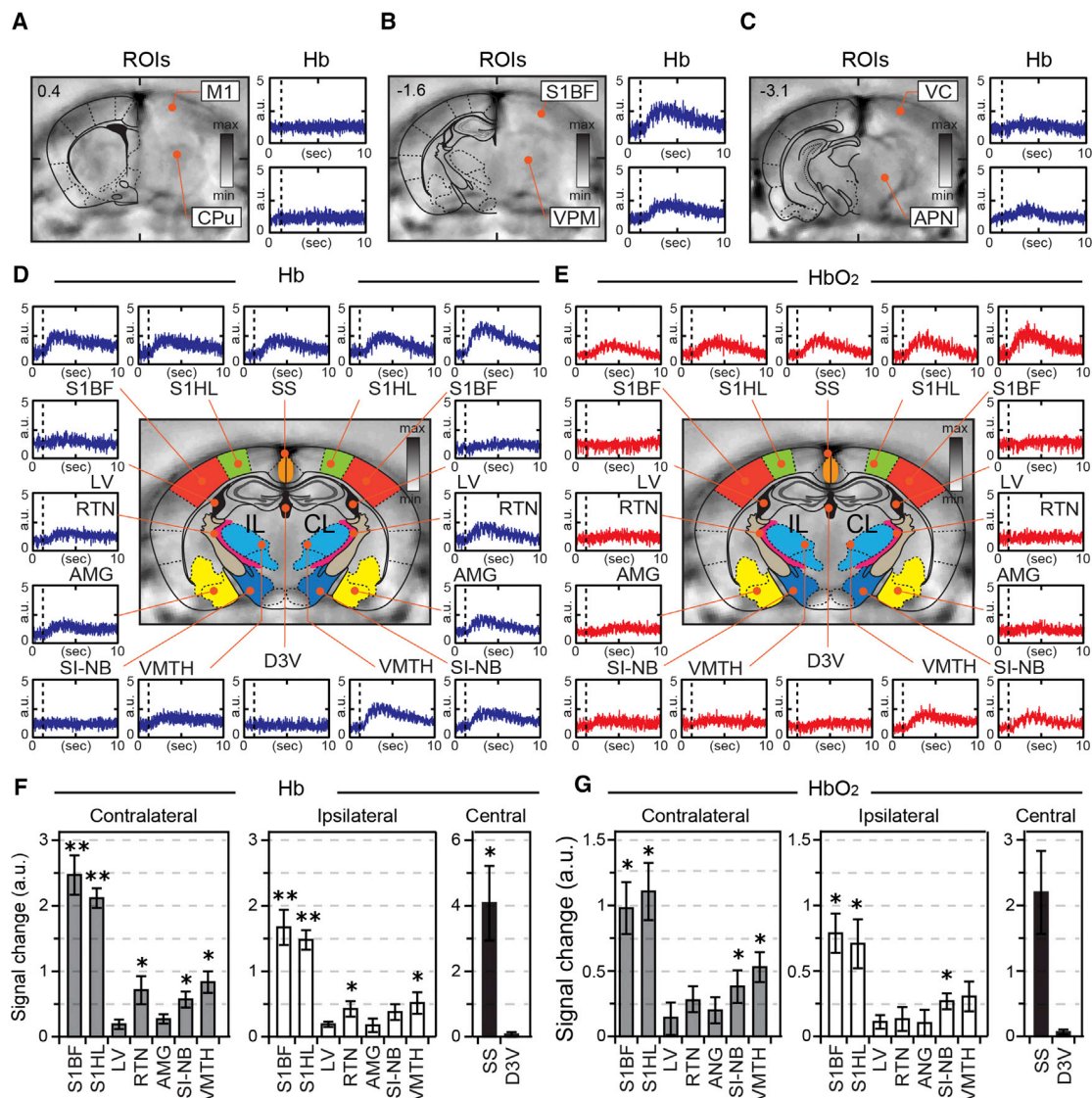
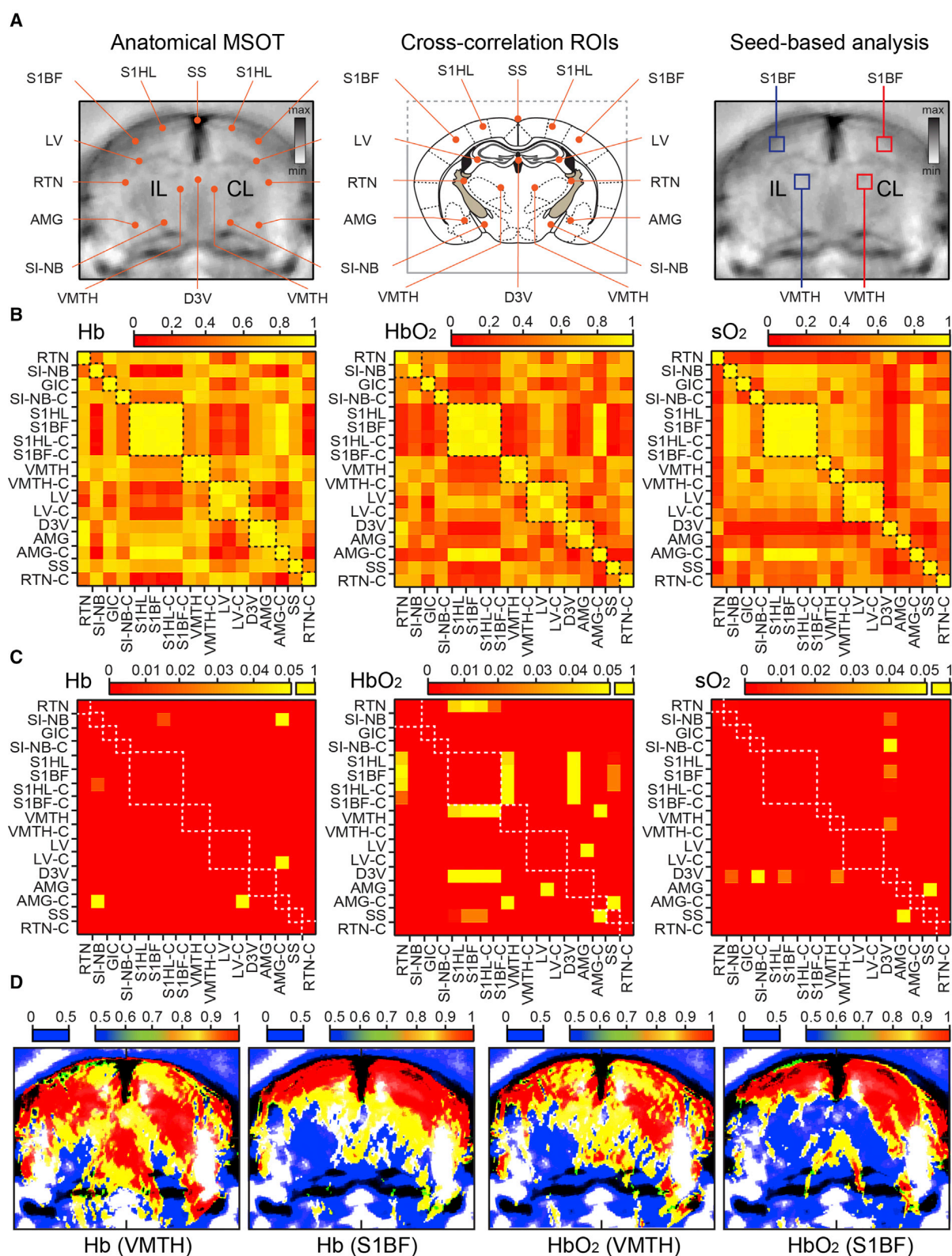**Figure 2. Location Specificity of Hemodynamic Changes across Mouse Brains Induced by Whisker Inputs**

(A–C) Consecutive anatomical MSOT images of mouse brain overlaid with schematic maps of corresponding planes (A, B, and C; left part) with representative recordings of Hb signal from marked regions of interest (ROIs) (A, B, and C; right). Anatomical references: M1, motor cortex; CPu, caudate putamen; S1BF, somatosensory cortex barrel field; VPM, ventral posterior nucleus; VC, visual cortex; APN, anterior pretectal nucleus. Note that Hb changes are specific to the anatomical plane containing S1BF.

(D and E) Typical recordings of Hb (D) and HbO_2 (E) signal from selected ROIs of the mouse brain. IL and CL, ipsilateral and contralateral to the stimulation side. RTN, reticular thalamic nucleus; SI-NB, substantia innominate nucleus basalis; S1HL, primary somatosensory, hindlimb; S1BF, primary somatosensory, barrel field; VMTH, ventromedial thalamic nucleus; LV, lateral ventricle; D3V, third dorsal ventricle; AMG, amygdala; SS, sagittal sinus; AMG, amygdala. For illustration purposes, all functional readouts have been inverted to represent more clearly the relative change.

(F and G) Summary graphs illustrating the mean values with SEM of Hb (F) and HbO_2 (G) signal changes (i.e., peak amplitude) in different brain compartments pulled from six independent trials with their comparison (*$p < 0.05$; **$p < 0.005$; unpaired t test).

control experiments, without activation of whisker inputs, are shown in Figures S5A and S5B. As can be readily appreciated, repetitive whisker stimulation activates rapid and temporally coherent hemodynamic response in the somatosensory barrel fields as well as in adjacent somatosensory hindlimb areas of both sides. In addition, coherent activation of a hemodynamic response was detectable in related reticular and ventral thalamic

nuclei, as well as throughout the basal forebrain area, which correlated with the response of the barrel field in a statistically significant fashion (Figure 3C). Of note, the extent of functional coupling of evoked activity and correlation indexes were consistently higher in Hb and $_SO_2$ graphs compared to HbO_2. Alterations in the hemodynamic signal induced by the activation of the somatosensory inputs were also readily detectable on the

A

Anatomical MSOT · Cross-correlation ROIs · Seed-based analysis

B · Hb · HbO₂ · sO₂

C · Hb · HbO₂ · sO₂

D

Hb (VMTH) · Hb (S1BF) · HbO₂ (VMTH) · HbO₂ (S1BF)

(legend on next page)

correlation seed maps of the entire brain cross-sections, when the contralateral ventromedial thalamic nucleus or the somatosensory barrel field were taken as the seed for such analysis (Figure 3D). Consistent with the results of cross-correlation maps, stimulation-related hemodynamic changes synchronized with the seed areas were detectable in reticular and ventral thalamic nuclei, as well as in the basal forebrain area.

Having verified the *in vivo* functional neuroimaging capacities of MSOT across the entire cross-section of the mouse brain, we set to explore and characterize its capabilities as a high-resolution anatomical imaging tool, to verify the accurate assignment of functional readouts to various brain structures. Serial cross-sectional anatomical images of the mouse brain were acquired along the rostro-caudal axis at 0.1 mm steps *in vivo* followed by *ex vivo* imaging without perfusion or after perfusion. Figures 4A–4E present consecutive coronal and horizontal anatomical scans of an *ex vivo* mouse brain at 740-nm wavelength and relate them with anatomical references from the mouse brain atlas. As is clearly visible, at the specified wavelength as well as throughout almost the entire range of the NIR window (700–900 nm), the endogenous absorbers of perfused (bloodless) brains strongly contribute to the formation of anatomical MSOT images (Figures 4C–4E and S6). Indeed, the distinctly stratified and compartmental appearance of brains in coronal cross-sections with a lamellar outlook of olfactory bulbs, along with numerous structural details within the inner forebrain, midbrain, and hindbrain, including cerebellum and brainstem, recapitulate with high fidelity the schematized features of the corresponding anatomical planes from the brain atlas (Figures 4A–4E; Videos S4 and S5). To verify more rigorously the relationship of the structural features as revealed by *ex vivo* MSOT with major anatomical formations of the mouse brain, we compared coronal MSOT scans with structural details on matching stereotactic matching cross-sections enhanced with Nissl staining, captured at low magnification light microscopy (Figures 5A and 5B). As can be readily seen, there is a near-perfect correspondence between the coarse and fine features of the two series of images, with structures revealed by histology also clearly visible and quantifiable on MSOT cross-sections. Importantly, spectral decomposition of images revealed highly localized and specific traits across various brain regions, with melanin-rich midbrain dopaminergic nuclei as well as myelinated bundles of the midbrain, hypothalamus, and medulla readily discernable. In the ventral midbrain and dorsal medulla, for instance, neuro-melanin-rich substantia nigra pars compacta (SNc) and adrenergic pontine-reticular nuclei can be readily delineated on the MSOT scans (Figures 5C–5F).

Because hemoglobin is the principal endogenous chromophore and the main source of optoacoustic signal *in vivo*, its fairly uniform presence throughout the brain degrades structural features formed by other endogenous absorbers. To more rigorously define the anatomical brain imaging capabilities of MSOT *in vivo*, we compared the major structural features exposed by MSOT in the living animal with those captured with camera on the cryosliced frozen mouse head. As illustrated on a series of images (Figure 6A; Video S6), numerous major anatomical features visible on coronal cryosections were also readily discernable on MSOT cross-sections acquired at 720 nm, showing a near-perfect cross-correspondence. Similar to the *ex vivo* MSOT brain images, the structures revealed by anatomical MSOT *in vivo* could be quantified using morphometric tools and methods (Figures 6B and 6C), although the contrast and prominence of superficial and deep structural details are more distinguishable in *ex vivo* images. To find out whether the deep neuroimaging imaging capabilities of MSOT *in vivo* can be further enhanced using exogenous contrast agents, we applied Di-R for visualizing the ventricular system of the mouse brain and for tracing nigrostriatal dopaminergic projections. The high extinction coefficient of Di-R in aqueous medium makes it ideal for imaging the ventricular system as well as tracing water-rich axonal bundles. Two days after tracer injection in the dorsal chamber of the lateral ventricle, or in the caudate nucleus, *in vivo* MSOT scans of the entire brain were acquired, followed by perfusion of mice and histological verification of injection sites and visualization of the labeling of neuronal tracts, using light microscopy (Figures 7A–7J). In mice injected with Di-R in the dorsal cistern of the lateral ventricle, 3D reconstruction and spectral unmixing showed strong labeling of the ventricular system of the injected side, with dorsal, lateral, and ventral chambers readily visible (Figures 7A–7C). These anatomical features revealed with MSOT were further verified by low-power fluorescence imaging of corresponding brain cross-sections (Figures 7D and 7E). Similarly, in mice receiving Di-R injection in the dorsal striatum, the site of tracer infusion could be visualized on *in vivo* MSOT cross-sections, as also confirmed by *ex vivo* cryo-slicing and histology (Figures 7F–7H). We could not, however, visualize the nigro-striatal dopaminergic projections or SNc nucleus on whole-brain MSOT scans, even though the presence of Di-R dopaminergic axons and neurons were detectable with immunostaining and light microscopy (Figures 7I and 7J).

DISCUSSION

High-resolution imaging of large-scale neural dynamics and the organization of the brain in intact animal models are of major relevance to basic and translational neuroscience, relating specific functional processes to various structures without disruption of tissue homeostasis and integrity. Despite the major

---

Figure 3. Temporal Coherence of Hemodynamic Changes Induced by Stimulation of Whisker Inputs in Mouse Brain

(A) Structural MSOT images (left and right panels) with marked ROIs used in cross-correlation analysis (left) and in seed-based correlation mapping the functional connectome (right), along with schematized map of corresponding brain plane with anatomical references (middle). For abbreviations, see Figure 2 legend.

(B and C) Correlation matrix of Hb, HbO$_2$, and $_s$O$_2$ illustrating the degree of temporal coherence of hemodynamic response induced by whisker inputs (B) and corresponding graph of the distribution of p values of same ROIs (C).

(D) Seed-based correlation maps of the same brain illustrating areas with temporally coherent changes in Hb and HbO$_2$ signals (i.e., co-activation) in response to whisker inputs. Whisker input driven changes of the hemodynamic signals in the contralateral somatosensory cortex barrel field (S1BF) and contralateral ventromedial thalamic nucleus (VMTH) have been used as seeds for current coherence maps, with the degree of correlation presented in the color bars.
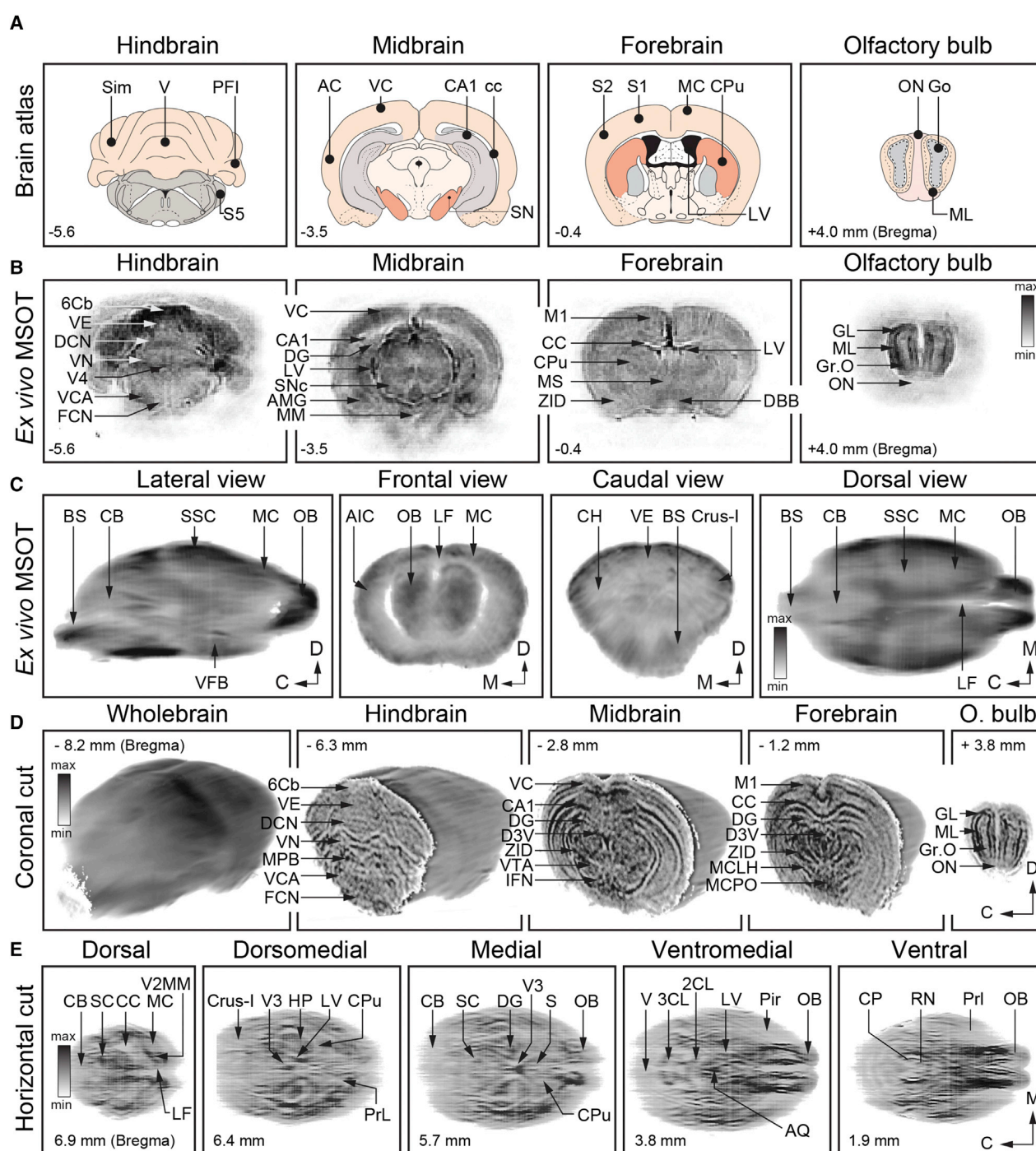
Figure 4. Structural Brain Imaging with MSOT Ex Vivo

(A and B) Schematized anatomy of a mouse brain at four different coronal planes (Bregma coordinates underneath) (A) with corresponding MSOT cross-sections of non-perfused ex vivo brain (B). Note exquisite structural details revealed at all planes and depths throughout entire brain cross-sections. ON, olfactory nerve; Go, granule cells of olfactory bulb; ML, mitral cell layer; S1 and S2, somatosensory cortex 1 and 2; MC, motor cortex; CPu, caudate putamen; LV, lateral ventricle; AC and VC, auditory and visual cortices; CA1, hippocampal CA1 area; cc, corpus callosum; SN, substantia nigra; Sim, simple lobule; V, vermis; PFI, para-floccules; S5, trigeminal nucleus; Gr.O, granule cells of olfactory bulb; GL, granule cell layer; MS, medal septum; DBB, diagonal band Broca; DG, dentate gyrus; LV, lateral ventricle; SNc, substantia nigra pars compacta; AMG amygdala; MM, medial mammillary nucleus; 6Cb, cerebellar lobule 6; VE, vermis; DCN, deep cerebellar nucleus; VN, vestibular nucleus; V4, fourth ventricle; VCN, ventral cochlear nucleus; FNC, facial nucleus.

(legend continued on next page)

advances in neuroimaging, there is pressing need for technologies and methods enabling noninvasive scalable observations of static and dynamic processes in the brain. This is particularly pertinent to small-animal neuroimaging applications, where miniature scales and weak signals impose major challenges. As a highly promising interrogation method, optoacoustic imaging has shown great potential for a range of applications in murine neuroimaging. However, up until now, all of the major assets of optoacoustic imaging have been underrated or overlooked (Ovsepian et al., 2017). Much emphasis has been placed on resolving the vasculature on the brain surface and analysis of the neurovascular response in the cortex using an open-skull approach (Liao et al., 2012; Nasiriavanaki et al., 2014; Tang et al., 2015; Wang et al., 2003, 2013; Yao et al., 2015), with little progress made on systematic studies of processes and functions unfolding in the deeper compartments within the intact brain. Recently, an attempt has been made to visualize the functional connectome across an entire brain cross-section in craniotomized rats; however, images were acquired showing grossly distorted vascularization, possibly due to data overprocessing (Li et al., 2017).

In this study, we applied MSOT for high-resolution mapping of large-scale neurovascular dynamics in cross-sections of the mouse brain in response to somatosensory whisker inputs. We visualized and spectrally decomposed hemodynamic changes related to processing and allocation of whisker signals along the entire subcortical-cortical axis of the forebrain, to map Hb and HbO_2 gradients and tissue oxygenation level changes in multiple anatomical planes and brain compartments. Using the same modality, we also obtained scans of mouse brains with significant structural detail, based on intrinsic chromophores and exogenous contrast agents. These unveiled a close-to-perfect match between key anatomical features as revealed by MSOT with those discovered using customary histology and microscopy. The strong central representation along with the well-defined connectivity and discreet response to whisker inputs (Brecht and Sakmann, 2002; Feldmeyer et al., 2013; Petersen, 2007) render the whisker somatosensory system an ideal experimental model, enabling access to fundamental neurobiological processes using neuroimaging and electrophysiological methods (Berger et al., 2007; Grinvald et al., 1986; Petersen et al., 2001; Yang et al., 1996). In agreement with results of optical imaging and neurophysiological reports, our MSOT scans showed strong activation of the barrel cortex by repetitive whisker inputs. The stimulation and type of anesthesia used in this study were based on careful consideration of numerous reports that investigated functional dynamics within this sensory system (Berger et al., 2007; Jonckers et al., 2015; Petersen et al., 2003; Yang et al., 1997). Unlike focusing on cellular-resolution microscopic readouts of functional changes in small neuronal groups within the superficial cortical layers, or low-resolution surrogate blood-oxygen-level-dependent (BOLD) signal of fMRI, we mapped and spectrally decomposed the activation and processing of somatosensory inputs by the brain at high spatial and temporal resolution. Although our observations are in general agreement with results of earlier reports showing whisker-induced hemodynamic changes in the contralateral barrel field (Feldmeyer et al., 1999; Petersen, 2007; Schubert et al., 2003), we were also able to detect expanded HbO_2 and Hb alterations involving the ipsilateral barrel cortex as well as throughout thalamic nuclei, caudal basal forebrain nuclei, and other subcortical structures. These findings are in line with neuroanatomical data on ascending lemniscal projections, which relay whisker somatosensory inputs via ventral and posterior thalamic nuclei and through extra-thalamic circuits, activating a range of subcortical structures (Brecht et al., 2004; Zaborszky et al., 2015). In this context, it is important to note that the intensity and pattern of brain responses to somatosensory inputs from whiskers can be affected by multiple factors, including the type of anesthesia, stimulus intensity, and number of activated whiskers, with prolonged strong inputs capable of activating BOLD signal over wider brain areas, including the ipsilateral to the stimulation side cortical and subcortical structures, via long-range associative connections (Alonso et al., 2008; Logothetis, 2008; Mirabella et al., 2001).

Closer analysis of the initiation and spread of the hemodynamic signals showed that Hb changes in the cortex can faithfully replicate the order of processing and integration of whisker inputs given that thalamo-cortical projections target and synchronously activate the L4 neurons, with spread of the activity from therein across entire cortical columns (Bruno and Sakmann, 2006; Petersen, 2007; Yu et al., 2014). Indeed, such activation patterns caused a faster response onset and more robust Hb signal in deep cortical layers. In contrast, HbO_2 signal changes appeared more diffuse, with higher signal intensity predominantly in the superficial layers. Although we do not have a ready explanation for such dissociation between Hb and HbO_2 signals, the compensatory nature of HbO_2 response, which in the cerebral cortex is enabled largely by activation of the superficial vascular bed via penetrating arterioles feeding deeper

(C) Lateral, frontal, caudal, and dorsal views of reconstructed mouse brain, from left to right. Maximum intensity projections. C, caudal; D, dorsal; M, medial; BS, brainstem; CB, cerebellum; SSC, somatosensory cortex; MC, motor cortex; OB, olfactory bulb; AIC, agranular insular cortex; LF, longitudinal fissure; CH, cerebellar hemisphere; VE, vermis; Crus-1, cerebellar crus 1.

(D) MSOT of the whole brain and series of cross-sections at four different planes. 6Cb, sixth cerebellar lobule; VE, vermis; DCN, deep cerebellar nucleus; VN, vestibular nuclear complex; MPB, medial parabrachial nucleus; VCA, ventral cochlear nucleus; FCN, facial nucleus; VC, visual cortex; CA1, CA1 area; DG, dentate gyrus; D3V, dorsal 3 ventricle; ZID, zona incerta dorsalis; VTA, ventral tegmental area; IFN, interfascicular nucleus; M1, motor cortex; CC, corpus callosum; MCLH, magnocellular lateral hypothalamus; MCPO, magnocellular preoptic nucleus; GL, glomerular layer; ML, mitral cell layer; Gr.O, granule cell layer; ON, olfactory nerve.

(E) Horizontal MSOT sections of the mouse brain at five (D, dorsal; DM, dorso-medial; M, medial; MV, medio-ventral; and V, ventral) planes with reference to interaural plane (distance in millimeters). CB, cerebellum; SC, superior colliculus; CC, corpus callosum; MC, motor cortex; V2MM, secondary visual cortex; LF, longitudinal fissure; V3, ventricle 3; HP, hippocampus; LV, lateral ventricle; CPu, caudate putamen; PrL, pre-limbic cortex; DG, dentate gyrus; S, septum; OB, olfactory bulb; V, vermis; 3CL, 3 cerebellar lobule; 2CL, 2 cerebellar lobule; AQ, aqueduct cerebral; Pir, piriform cortex; CP, cerebellar peduncle; RN, reticular nucleus; Prl, prelimbic cortex.
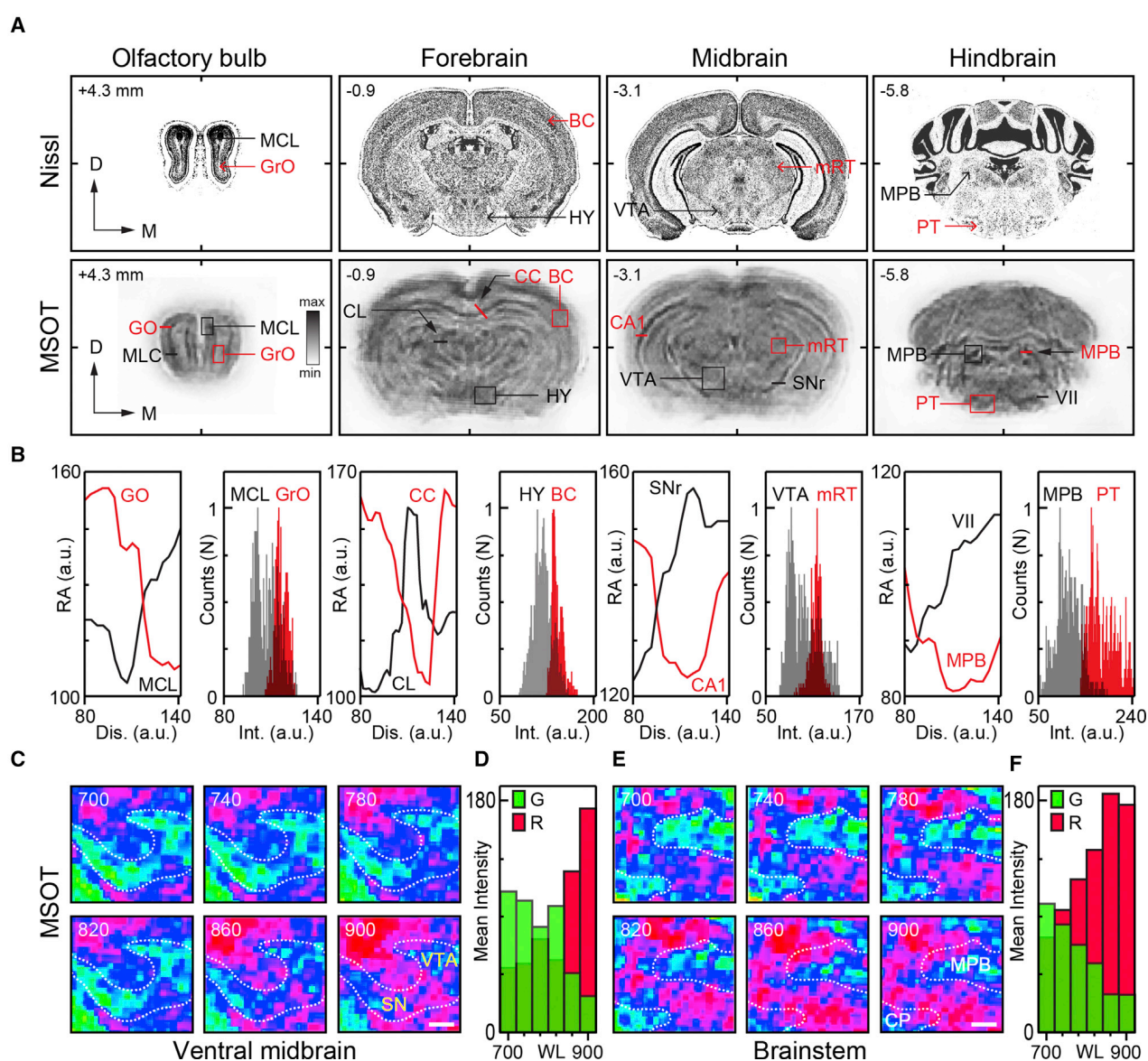
Figure 5. Morphometry and Correlation of Anatomical Features Revealed by MSOT with Those of Histochemistry

(A) Typical Nissl-stained mouse brain sections at consecutive planes (top) with corresponding MSOT images (bottom) (millimeters from bregma) (modified with permission from http://atlas.brain-map.org/atlas). Note close resemblance between major features of two sets of images. MCL, mitral cell layer; GrO, granule cell layer; BC, barrel cortex; HY, hypothalamus; VTA, ventral tegmental area; mRT, mesencephalic reticular thalamic nucleus; MPB, medial parabrachial nucleus; PT, pyramidal tract; CL, central thalamic nucleus; CC, corpus callosum; SN, substantia nigra; CA1, hippocampal CA1 region; VII, facial nucleus.

(B) Intensity profile graphs and absorption density distribution histograms of selected structures marked in (A) verifying the feasibility of semiquantitative morphometry using MSOT scans of *ex vivo* mouse brain.

(C and D) MSOT images of the VTA and SNc area of the midbrain taken at different wavelengths (C) with representation of spectral changes attributable to melanin-rich structures (blue) in the region (D). (C) Scale bar: 100 μm.

(E and F) Spectral map of the MPB and cerebellar peduncle (CP) region of medulla (E) with representation of spectral changes (F) presumably due to presence of melanin in the region (between 700 and 900 nm). Scale bar: 100 μm. Note wavelength-dependent changes in the spectral content of MSOT images over the analyzed range (ratio of red and green pixels in C and E plotted in D and F).
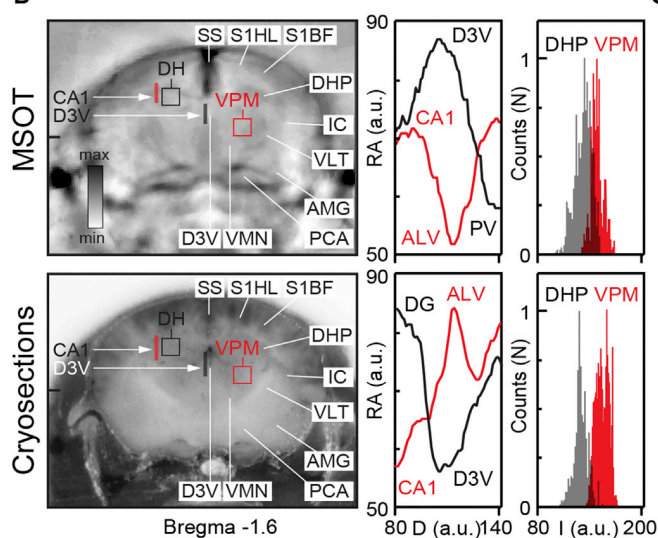
tissue, could account for the stronger HbO$_2$ signal in the superficial layers (Nishimura et al., 2007; Schaffer et al., 2006; Yu et al., 2014). We would like to stress, however, that at present the coincidence and extent of coupling between the neuronal activity and BOLD responses remain open for debate and require

further in-depth studies. Nevertheless, the specificity of activation of whisker inputs as demonstrated herein was verified by the absence of Hb and HbO$_2$ signals in anatomical planes lacking representations of somatosensory whisker inputs (Figures 2A–2C).
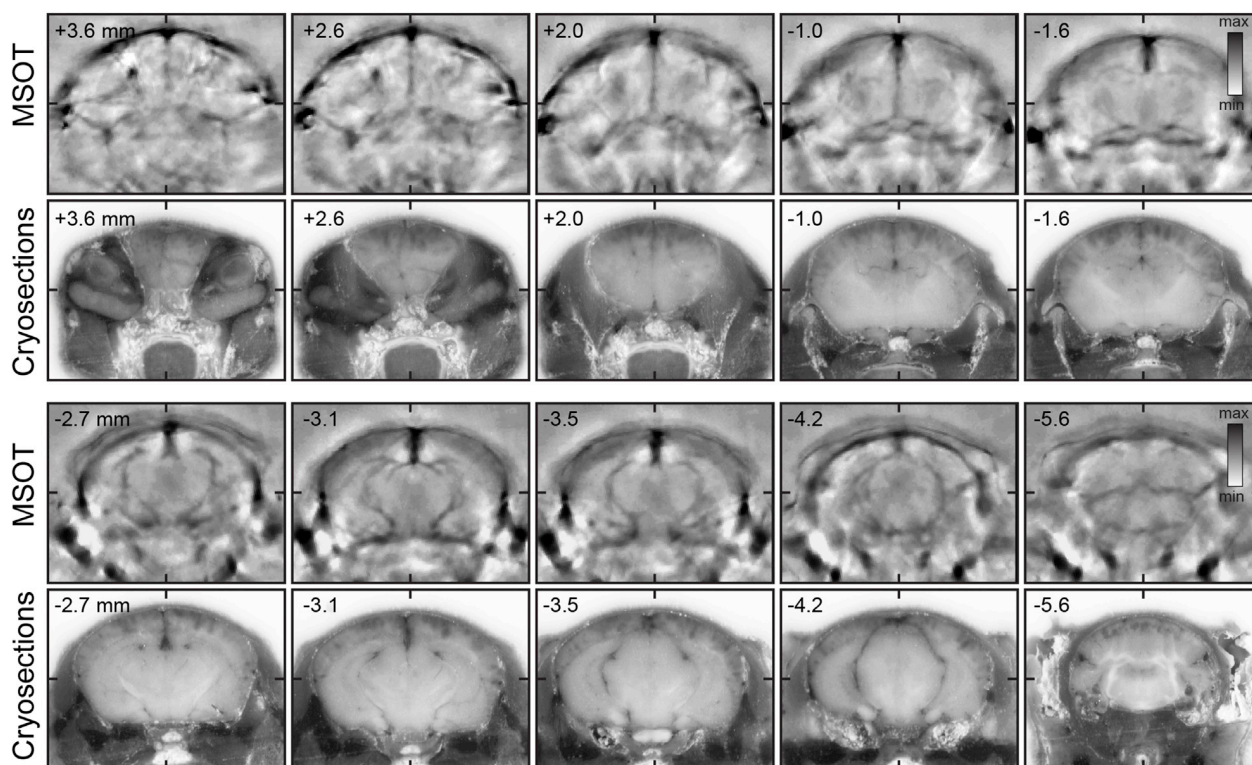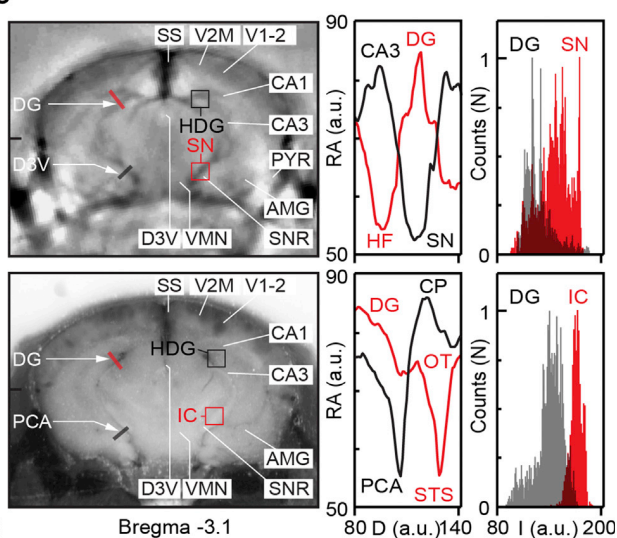
Figure 6. Label-Free Anatomical MSOT of Intact Mouse Brain *In Vivo*

(A) Series of consecutive MSOT cross-sections acquired *in vivo* (MSOT, average of 10 frames) and corresponding low-power images of the same frozen mouse brain captured on the cryo-slicer (cryosections). Note numerous exquisite structural details revealed by MSOT at all anatomical planes and depths throughout the entire brain cross-sections, with their nearly perfect correspondence with those captured using a high-resolution digital camera.

(B and C) Anatomical images and intensity profile graphs with absorption density distribution analysis of selected anatomical structures (bregma −1.6 mm, B, and bregma −3.1 mm, C) (red and black lines and boxed areas) demonstrating the utility of label-free MSOT for semiquantitative morphometry and neuroanatomical measurements *in vivo* in intact mice. SS, sagittal sinus; S1HL, somatosensory cortex hindlimb area; S1BF, somatosensory cortex barrel field; DHP, dorsal hippocampus; CA1, hippocampal CA1 area; VPM, ventral posterior-medial thalamic nucleus; IC, internal capsule; VLT, ventrolateral thalamic nucleus; VMN, ventromedial thalamic nucleus; AMG, amygdala; D3V, third ventricle; PCA, posterior central artery; PV, periventricular nucleus; ALV, stratum alveus; SN, substantia nigra; CP, cerebral peduncle; OT, optical tract; HF, hippocampal fissure; STS, sagittal transverse sinus; DG, dentate gyrus. Scale bar: 100 μm.
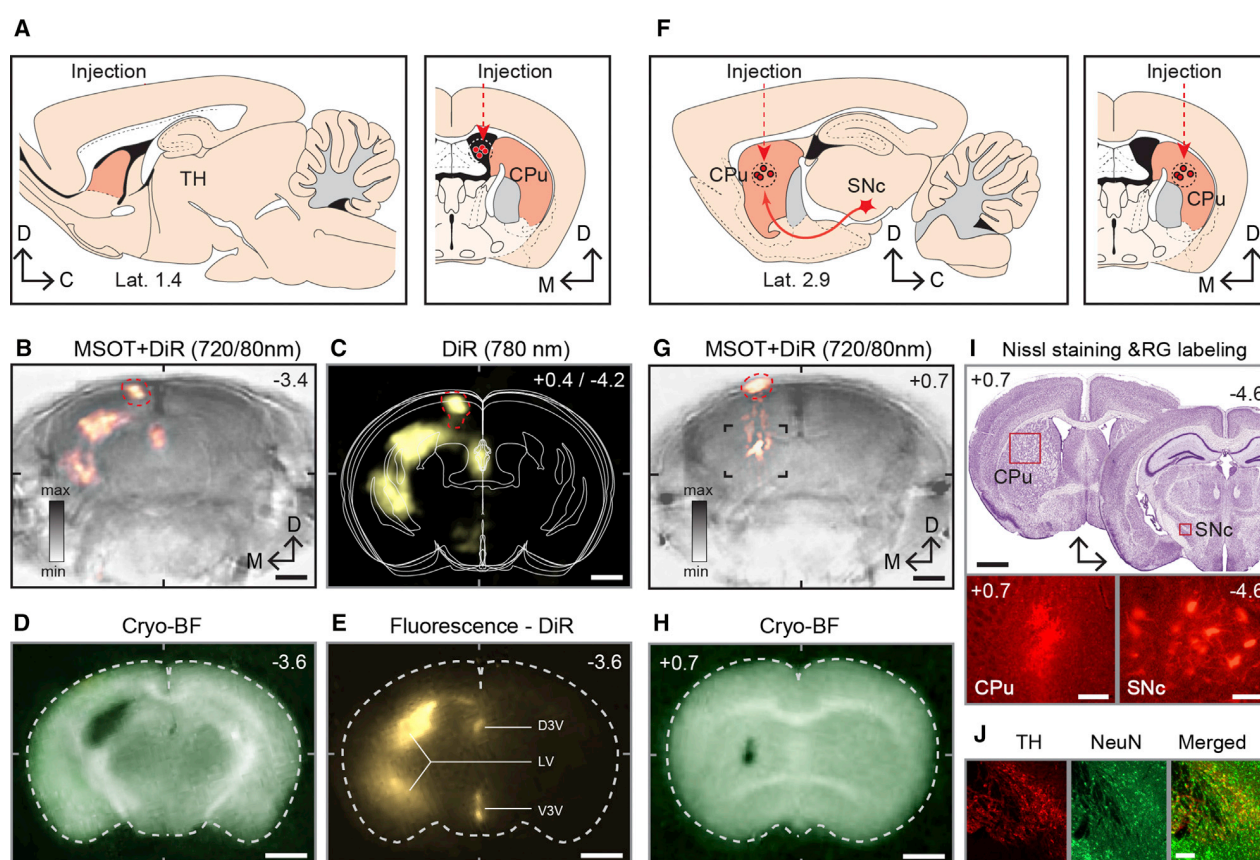
Figure 7. Enhancing Structural Brain Imaging with MSOT Using Exogenous Contrasts

(A–E) Visualizing mouse ventricular system with MSOT using NIR Di-R tracer.

(A) A schematic of the sagittal and coronal brain sections showing the site of intraventricular injection of a tracer. Anatomical references: CPu, caudate putamen; TH, thalamus.

(B and C) MSOT cross-section of the mouse brain overlaid with unmixed and reconstructed images of the cerebral ventricles (B) with corresponding simplified schematics of brain cross-sections between −2.6 and −4.0 mm of bregma (C).

(D and E) Histological verification of the Di-R injection site (D) and ventricular labeling using cryo-slicing and fluorescence light microscopy (E). Anatomical references: D3V, dorsal 3 ventricle; LV, lateral ventricle; V3V ventral 3 ventricle.

(F) A schematic of the sagittal and coronal brain sections with the site of NIR Di-R infusion revealed in dorsal striatum for retrograde labeling of SN dopaminergic projection neurons.

(G and H) Anatomical MSOT cross-section of the mouse brain overlaid with unmixed and reconstructed images of tracer injection plane (G) with histological verification (H).

(I) Validation of the injection sites and the location of SN shown in Nissl-stained brain sections and in fluorescence microscopic images of the injections site in CPu and retrogradely labeled neurons in the SNc.

(J) Immunofluorescence verification of dopaminergic neurons using anti-tyrosinase antibody and neuron-specific marker NeuN.

With respect to anatomical MSOT imaging, it is critical to note that, within the NIR range (700–900 nm), in addition to Hb, other endogenous absorbers can contribute constructively toward the formation of structural images, revealing exquisite anatomical details across entire brain cross-sections. In intact animals, as we have shown, these features are strongly masked by an overwhelming hemoglobin signal but can be partly recovered using special imaging conditions and data processing. While the contribution of individual absorbers in the formation of anatomical images remains to be characterized, water, cytochromes, lipid, and melanin are expected to play a major role (Jacques, 2013; Ovsepian et al., 2017; Weber et al., 2016; Yao and Wang, 2014). As shown, structures such as the cerebral cortex,

hippocampus, corpus callosum, basal ganglia, thalamic nuclei, ventricular system, olfactory bulb, cerebellum, together with a range of brainstem formations could be readily distinguished and quantified on MSOT scans by simple semi-quantitative analytical tools and spectral decomposition methods. It is reasonable to assume that, with its relatively uniform distribution in the brain, water absorption, like that of hemoglobin, also contributes toward the background signal, while the different density of proteins and lipids are expected to play key roles toward formation of structural features in the neuron-rich cerebral cortex and hippocampus, as well as in deep nuclei. Likewise, fat is expected to contribute and shape myelinated bundles and white-matter-rich hubs (Ovsepian et al., 2017). Clearcut appearance

of neuro-melanin-rich midbrain dopaminergic and adrenergic nuclei (Barden and Levine, 1983; Saper and Petito, 1982) as revealed with MSOT are also of considerable interest as this could potentially serve as a biomarker for studies of neurodegenerative disease affecting these major supra-spinal hubs. As shown here, anatomical MSOT neuroimaging can be further enhanced using exogenous contrast agents. However, at this point, mapping the connectome and major neural projections with tracers seems to be over-ambitious due to the inherent low sensitivity of MSOT, urging further research and optimization of hardware and experimental procedures.

In summary, our results show the powerful capabilities of MSOT for functional and structural neuroimaging, and highlight some limitations and areas for future optimization. Given additional research and refinement, MSOT is expected to advance noninvasive neuroimaging of small-animal models onto a new level, offering an impressive means for addressing a wide range of outstanding questions, with implications for basic neurobiology and translational neuroscience.

STAR★METHODS

Detailed methods are provided in the online version of this paper and include the following:

- KEY RESOURCES TABLE
- CONTACT FOR REAGENT AND RESOURCE SHARING
- EXPERIMENTAL MODEL AND SUBJECT DETAILS
- METHOD DETAILS
  - Multispectral optoacoustic tomography (MSOT)
  - Brain imaging with MSOT
  - Di-R injection into the brain and immunohistochemistry
- QUANTIFICATION AND STATISTICAL ANALYSIS

SUPPLEMENTAL INFORMATION

Supplemental Information includes six figures, one table, and six videos and can be found with this article online at https://doi.org/10.1016/j.celrep.2019.02.020.

AUTHOR CONTRIBUTIONS

S.V.O. and I.O. designed the study. I.O., A.G., H.Y., J.M.-N., and S.V.O. performed the experiments. A.G. and G.S. developed the stimulation system. S.G. provided technical support. I.O., H.Y., J.M.-N., P.S., and S.V.O. conducted data analysis and interpretation. S.V.O., I.O., V.B.O., and V.N.

wrote the manuscript. All authors read and approved the final version of the manuscript.

REFERENCES

Alonso, B.d.C., Lowe, A.S., Dear, J.P., Lee, K.C., Williams, S.C., and Finnerty, G.T. (2008). Sensory inputs from whisking movements modify cortical whisker maps visualized with functional magnetic resonance imaging. Cereb. Cortex *18*, 1314–1325.

Barden, H., and Levine, S. (1983). Histochemical observations on rodent brain melanin. Brain Res. Bull. *10*, 847–851.

Beard, P. (2011). Biomedical photoacoustic imaging. Interface Focus *1*, 602–631.

Berger, T., Borgdorff, A., Crochet, S., Neubauer, F.B., Lefort, S., Fauvet, B., Ferezou, I., Carleton, A., Lüscher, H.R., and Petersen, C.C. (2007). Combined voltage and calcium epifluorescence imaging in vitro and in vivo reveals subthreshold and suprathreshold dynamics of mouse barrel cortex. J. Neurophysiol. *97*, 3751–3762.

Boas, D.A., Dale, A.M., and Franceschini, M.A. (2004). Diffuse optical imaging of brain activation: approaches to optimizing image sensitivity, resolution, and accuracy. Neuroimage *23* (Suppl 1), S275–S288.

Brecht, M., and Sakmann, B. (2002). Whisker maps of neuronal subclasses of the rat ventral posterior medial thalamus, identified by whole-cell voltage recording and morphological reconstruction. J. Physiol. *538*, 495–515.

Brecht, M., Krauss, A., Muhammad, S., Sinai-Esfahani, L., Bellanca, S., and Margrie, T.W. (2004). Organization of rat vibrissa motor cortex and adjacent areas according to cytoarchitectonics, microstimulation, and intracellular stimulation of identified cells. J. Comp. Neurol. *479*, 360–373.

Bruno, R.M., and Sakmann, B. (2006). Cortex is driven by weak but synchronously active thalamocortical synapses. Science *312*, 1622–1627.

Burton, N.C., Patel, M., Morscher, S., Driessen, W.H., Claussen, J., Beziere, N., Jetzfellner, T., Taruttis, A., Razansky, D., Bednar, B., and Ntziachristos, V. (2013). Multispectral opto-acoustic tomography (MSOT) of the brain and glioblastoma characterization. Neuroimage *65*, 522–528.

Chen, X., Leischner, U., Rochefort, N.L., Nelken, I., and Konnerth, A. (2011). Functional mapping of single spines in cortical neurons in vivo. Nature *475*, 501–505.

Culver, J.P., Durduran, T., Furuya, D., Cheung, C., Greenberg, J.H., and Yodh, A.G. (2003). Diffuse optical tomography of cerebral blood flow, oxygenation, and metabolism in rat during focal ischemia. J. Cereb. Blood Flow Metab. *23*, 911–924.

Dean-Ben, X.L., Ntziachristos, V., and Razansky, D. (2012). Acceleration of optoacoustic model-based reconstruction using angular image discretization. IEEE Trans. Med. Imaging *31*, 1154–1162.

Denic, A., Macura, S.I., Mishra, P., Gamez, J.D., Rodriguez, M., and Pirko, I. (2011). MRI in rodent models of brain disorders. Neurotherapeutics *8*, 3–18.

Dombeck, D.A., Harvey, C.D., Tian, L., Looger, L.L., and Tank, D.W. (2010). Functional imaging of hippocampal place cells at cellular resolution during virtual navigation. Nat. Neurosci. *13*, 1433–1440.

Eggebrecht, A.T., Ferradal, S.L., Robichaux-Viehoever, A., Hassanpour, M.S., Dehghani, H., Snyder, A.Z., Hershey, T., and Culver, J.P. (2014). Mapping distributed brain function and networks with diffuse optical tomography. Nat. Photonics *8*, 448–454.

Errico, C., Pierre, J., Pezet, S., Desailly, Y., Lenkei, Z., Couture, O., and Tanter, M. (2015). Ultrafast ultrasound localization microscopy for deep super-resolution vascular imaging. Nature *527*, 499–502.

Farahani, K., Sinha, U., Sinha, S., Chiu, L.C., and Lufkin, R.B. (1990). Effect of field strength on susceptibility artifacts in magnetic resonance imaging. Comput. Med. Imaging Graph. *14*, 409–413.

Feldmeyer, D., Egger, V., Lubke, J., and Sakmann, B. (1999). Reliable synaptic connections between pairs of excitatory layer 4 neurones within a single "barrel" of developing rat somatosensory cortex. J. Physiol. *521*, 169–190.

Feldmeyer, D., Brecht, M., Helmchen, F., Petersen, C.C., Poulet, J.F., Staiger, J.F., Luhmann, H.J., and Schwarz, C. (2013). Barrel cortex function. Prog. Neurobiol. *103*, 3–27.

Franklin, K.B.J., and Paxinos, G. (2008). The Mouse Brain in Stereotaxic Coordinates (Elsevier).

Gesnik, M., Blaize, K., Deffieux, T., Gennisson, J.L., Sahel, J.A., Fink, M., Picaud, S., and Tanter, M. (2017). 3D functional ultrasound imaging of the cerebral visual system in rodents. Neuroimage *149*, 267–274.

Gottschalk, S., Fehm, T.F., Deán-Ben, X.L., Tsytsarev, V., and Razansky, D. (2017). Correlation between volumetric oxygenation responses and electrophysiology identifies deep thalamocortical activity during epileptic seizures. Neurophotonics *4*, 011007.

Grienberger, C., Chen, X., and Konnerth, A. (2014). NMDA receptor-dependent multidendrite Ca^{2+} spikes required for hippocampal burst firing in vivo. Neuron *81*, 1274–1281.

Grinvald, A., Lieke, E., Frostig, R.D., Gilbert, C.D., and Wiesel, T.N. (1986). Functional architecture of cortex revealed by optical imaging of intrinsic signals. Nature *324*, 361–364.

Helmchen, F., and Denk, W. (2005). Deep tissue two-photon microscopy. Nat. Methods *2*, 932–940.

Hillman, E.M. (2007). Optical brain imaging in vivo: techniques and applications from animal to man. J. Biomed. Opt. *12*, 051402.

Hong, G., Diao, S., Chang, J., Antaris, A.L., Chen, C., Zhang, B., Zhao, S., Atochin, D.N., Huang, P.L., Andreasson, K.I., et al. (2014). Through-skull fluorescence imaging of the brain in a new near-infrared window. Nat. Photonics *8*, 723–730.

Hoyer, C., Gass, N., Weber-Fahr, W., and Sartorius, A. (2014). Advantages and challenges of small animal magnetic resonance imaging as a translational tool. Neuropsychobiology *69*, 187–201.

Jacques, S.L. (2013). Optical properties of biological tissues: a review. Phys. Med. Biol. *58*, R37–R61.

Jonckers, E., Shah, D., Hamaide, J., Verhoye, M., and Van der Linden, A. (2015). The power of using functional fMRI on small rodents to study brain pharmacology and disease. Front. Pharmacol. *6*, 231.

Kerr, J.N., and Denk, W. (2008). Imaging in vivo: watching the brain in action. Nat. Rev. Neurosci. *9*, 195–205.

Laufer, J., Zhang, E., Raivich, G., and Beard, P. (2009). Three-dimensional noninvasive imaging of the vasculature in the mouse brain using a high resolution photoacoustic scanner. Appl. Opt. *48*, D299–D306.

Li, L., Zhu, L., Ma, C., Lin, L., Yao, J., Wang, L., Maslov, K., Zhang, R., Chen, W., Shi, J., and Wang, L.V. (2017). Single-impulse panoramic photoacoustic computed tomography of small-animal whole-body dynamics at high spatiotemporal resolution. Nat. Biomed. Eng. *1*, 0071.

Liao, L.D., Lin, C.T., Shih, Y.Y., Duong, T.Q., Lai, H.Y., Wang, P.H., Wu, R., Tsang, S., Chang, J.Y., Li, M.L., and Chen, Y.Y. (2012). Transcranial imaging of functional cerebral hemodynamic changes in single blood vessels using in vivo photoacoustic microscopy. J. Cereb. Blood Flow Metab. *32*, 938–951.

Lin, L., Xia, J., Wong, T.T., Li, L., and Wang, L.V. (2015). In vivo deep brain imaging of rats using oral-cavity illuminated photoacoustic computed tomography. J. Biomed. Opt. *20*, 016019.

Logothetis, N.K. (2008). What we can do and what we cannot do with fMRI. Nature *453*, 869–878.

Macé, E., Montaldo, G., Cohen, I., Baulac, M., Fink, M., and Tanter, M. (2011). Functional ultrasound imaging of the brain. Nat. Methods *8*, 662–664.

Mirabella, G., Battiston, S., and Diamond, M.E. (2001). Integration of multiple-whisker inputs in rat somatosensory cortex. Cereb. Cortex *11*, 164–170.

Nasiriavanaki, M., Xia, J., Wan, H., Bauer, A.Q., Culver, J.P., and Wang, L.V. (2014). High-resolution photoacoustic tomography of resting-state functional connectivity in the mouse brain. Proc. Natl. Acad. Sci. USA *111*, 21–26.

Nishimura, N., Schaffer, C.B., Friedman, B., Lyden, P.D., and Kleinfeld, D. (2007). Penetrating arterioles are a bottleneck in the perfusion of neocortex. Proc. Natl. Acad. Sci. USA *104*, 365–370.

Ntziachristos, V. (2010). Going deeper than microscopy: the optical imaging frontier in biology. Nat. Methods *7*, 603–614.

Ntziachristos, V., Ripoll, J., Wang, L.V., and Weissleder, R. (2005). Looking and listening to light: the evolution of whole-body photonic imaging. Nat. Biotechnol. *23*, 313–320.

Olefir, I., Mercep, E., Burton, N.C., Ovsepian, S.V., and Ntziachristos, V. (2016). Hybrid multispectral optoacoustic and ultrasound tomography for morphological and physiological brain imaging. J. Biomed. Opt. *21*, 86005.

Osmanski, B.F., Pezet, S., Ricobaraza, A., Lenkei, Z., and Tanter, M. (2014). Functional ultrasound imaging of intrinsic connectivity in the living rat brain with high spatiotemporal resolution. Nat. Commun. *5*, 5023.

Ouzounov, D.G., Wang, T., Wang, M., Feng, D.D., Horton, N.G., Cruz-Hernández, J.C., Cheng, Y.T., Reimer, J., Tolias, A.S., Nishimura, N., and Xu, C. (2017). In vivo three-photon imaging of activity of GCaMP6-labeled neurons deep in intact mouse brain. Nat. Methods *14*, 388–390.

Ovsepian, S.V., Olefir, I., Westmeyer, G., Razansky, D., and Ntziachristos, V. (2017). Pushing the boundaries of neuroimaging with optoacoustics. Neuron *96*, 966–988.

Perron, A., Mutoh, H., Launey, T., and Knöpfel, T. (2009). Red-shifted voltage-sensitive fluorescent proteins. Chem. Biol. *16*, 1268–1277.

Peterka, D.S., Takahashi, H., and Yuste, R. (2011). Imaging voltage in neurons. Neuron *69*, 9–21.

Petersen, C.C. (2007). The functional organization of the barrel cortex. Neuron *56*, 339–355.

Petersen, R.S., Panzeri, S., and Diamond, M.E. (2001). Population coding of stimulus location in rat somatosensory cortex. Neuron *32*, 503–514.

Petersen, C.C., Grinvald, A., and Sakmann, B. (2003). Spatiotemporal dynamics of sensory responses in layer 2/3 of rat barrel cortex measured in vivo by voltage-sensitive dye imaging combined with whole-cell voltage recordings and neuron reconstructions. J. Neurosci. *23*, 1298–1309.

Razansky, D., Buehler, A., and Ntziachristos, V. (2011). Volumetric real-time multispectral optoacoustic tomography of biomarkers. Nat. Protoc. *6*, 1121–1129.

Saper, C.B., and Petito, C.K. (1982). Correspondence of melanin-pigmented neurons in human brain with A1-A14 catecholamine cell groups. Brain *105*, 87–101.

Schaffer, C.B., Friedman, B., Nishimura, N., Schroeder, L.F., Tsai, P.S., Ebner, F.F., Lyden, P.D., and Kleinfeld, D. (2006). Two-photon imaging of cortical surface microvessels reveals a robust redistribution in blood flow after vascular occlusion. PLoS Biol. *4*, e22.

Schubert, D., Kötter, R., Zilles, K., Luhmann, H.J., and Staiger, J.F. (2003). Cell type-specific circuits of cortical layer IV spiny neurons. J. Neurosci. *23*, 2961–2970.

Siegel, A., Marota, J.J., and Boas, D. (1999). Design and evaluation of a continuous-wave diffuse optical tomography system. Opt. Express *4*, 287–298.

Stein, E.W., Maslov, K., and Wang, L.V. (2009). Noninvasive, in vivo imaging of blood-oxygenation dynamics within the mouse brain using photoacoustic microscopy. J. Biomed. Opt. *14*, 020502.

Stettler, D.D., Yamahachi, H., Li, W., Denk, W., and Gilbert, C.D. (2006). Axons and synaptic boutons are highly dynamic in adult visual cortex. Neuron *49*, 877–887.

Tang, J., Xi, L., Zhou, J., Huang, H., Zhang, T., Carney, P.R., and Jiang, H. (2015). Noninvasive high-speed photoacoustic tomography of cerebral hemodynamics in awake-moving rats. J. Cereb. Blood Flow Metab. *35*, 1224–1232.

Taruttis, A., and Ntziachristos, V. (2015). Advances in real-time multispectral optoacoustic imaging and its applications. Nat. Photonics *9*, 219–227.

Tiran, E., Ferrier, J., Deffieux, T., Gennisson, J.L., Pezet, S., Lenkei, Z., and Tanter, M. (2017). Transcranial functional ultrasound imaging in freely moving awake mice and anesthetized young rats without contrast agent. Ultrasound Med. Biol. *43*, 1679–1689.

Tzoumas, S., Kravtsiv, A., Gao, Y., Buehler, A., and Ntziachristos, V. (2016). Statistical molecular target detection framework for multispectral optoacoustic tomography. IEEE Trans. Med. Imaging *35*, 2534–2545.

Wang, X., Pang, Y., Ku, G., Xie, X., Stoica, G., and Wang, L.V. (2003). Noninvasive laser-induced photoacoustic tomography for structural and functional in vivo imaging of the brain. Nat. Biotechnol. *21*, 803–806.

Wang, L., Maslov, K., and Wang, L.V. (2013). Single-cell label-free photoacoustic flowoxigraphy in vivo. Proc. Natl. Acad. Sci. USA *110*, 5759–5764.

Weber, J., Beard, P.C., and Bohndiek, S.E. (2016). Contrast agents for molecular photoacoustic imaging. Nat. Methods *13*, 639–650.

Willem, M., Tahirovic, S., Busche, M.A., Ovsepian, S.V., Chafai, M., Kootar, S., Hornburg, D., Evans, L.D., Moore, S., Daria, A., et al. (2015). η-Secretase processing of APP inhibits neuronal activity in the hippocampus. Nature *526*, 443–447.

Wilt, B.A., Burns, L.D., Wei Ho, E.T., Ghosh, K.K., Mukamel, E.A., and Schnitzer, M.J. (2009). Advances in light microscopy for neuroscience. Annu. Rev. Neurosci. *32*, 435–506.

Yang, Q.X., Smith, M.B., and Wang, J. (2006). Magnetic Susceptibility Effects in High Field MRI*Vol. 26* (Springer).

Yang, X., Hyder, F., and Shulman, R.G. (1996). Activation of single whisker barrel in rat brain localized by functional magnetic resonance imaging. Proc. Natl. Acad. Sci. USA *93*, 475–478.

Yang, X., Hyder, F., and Shulman, R.G. (1997). Functional MRI BOLD signal coincides with electrical activity in the rat whisker barrels. Magn. Reson. Med. *38*, 874–877.

Yao, J., and Wang, L.V. (2014). Photoacoustic brain imaging: from microscopic to macroscopic scales. Neurophotonics *1*, 011003.

Yao, J., Wang, L., Yang, J.M., Maslov, K.I., Wong, T.T., Li, L., Huang, C.H., Zou, J., and Wang, L.V. (2015). High-speed label-free functional photoacoustic microscopy of mouse brain in action. Nat. Methods *12*, 407–410.

Yu, X., Qian, C., Chen, D.Y., Dodd, S.J., and Koretsky, A.P. (2014). Deciphering laminar-specific neural inputs with line-scanning fMRI. Nat. Methods *11*, 55–58.

Zaborszky, L., Csordas, A., Mosca, K., Kim, J., Gielow, M.R., Vadasz, C., and Nadasdy, Z. (2015). Neurons in the basal forebrain project to the cortex in a complex topographic organization that reflects corticocortical connectivity patterns: an experimental study based on retrograde tracing and 3D reconstruction. Cereb. Cortex *25*, 118–137.

STAR★METHODS

KEY RESOURCES TABLE

REAGENT or RESOURCE	SOURCE	IDENTIFIER
Antibodies		
Chicken, polyclonal anti-TH	Abcam	CN76422
Rabbit, polyclonal anti-NeuN	Abcam	CN104225
AlexaFluor594, goat anti-chicken TH	Abcam	N150176
AlexaFluor488 goat anti-rabbit NeuN	Life Technologies	A-11008
Experimental Models: Organisms/Strains		
Nude-FOXN1 Nu/Nu mice	Jackson Laboratories	000819-B6.Cg-Foxn1 < nu > J
CD1 mice	Charles River	Crl:CD1(ICR)-022
Software and Algorithms		
IgorPro	Wavemetr, Oregon	Version 6.1
A model-based reconstruction algorithm	IBMI GmbH	Dean-Ben al., 2012
Other		
NIR Di-R	Thermo-Fisher, DE	D12731
MSOT256-TF	iThera Med. GmbH	256-TF
Nd-YAG laser pumped OPO	InnoLas Las. GmbH	Model SL450

CONTACT FOR REAGENT AND RESOURCE SHARING

Further information and requests for resources and reagents should be directed to and will be provided by the Lead Contact, Vasilis Ntziachristos (v.ntziachristos@helmholtz-muenchen.de).

EXPERIMENTAL MODEL AND SUBJECT DETAILS

Young adult Hsd:Athymic Nude-FOXN1 Nu/Nu and CD1 mice used in all experiments described in the study (Table S1) were housed in a special housing facility at 21°C and 36% ± 2% humidity. The light-dark cycles were maintained at 12 h, with food and water provided *ad libitum*. All experiments involving living animals were conducted in accordance with the institutional guidelines and procedures approved by the government of Upper Bavaria, in compliance with German Federal and European Union law. Necessary steps have been taken to reduce animal use and suffering.

METHOD DETAILS

Multispectral optoacoustic tomography (MSOT)

The MSOT (MSOT256-TF, iThera Medical GmbH, Munich, Germany) used for all imaging experiments has a cylindrically curved detector array (R = 40 mm), providing 270° angular coverage of the imaging specimen (Olefir et al., 2016). Figure S1A shows a schematic representation of MSOT. The detector containing 256 elements manufactured from a piezo-composite material covers up to 7.5 MHz, with 5 MHz ± 10% (−6 dB) center frequency. All channels are digitized in parallel at 10 Hz repetition and sampling rate of 40 MHz, using a custom designed data acquisition (DAQ) card. Illumination within the near infra-red (NIR, 680-940 nm) is provided by a tunable Nd-YAG laser pumped optical parametric oscillator (OPO, InnoLas Laser GmBH, Krailling, Germany) with 9 ns pulse duration, 90 mJ peak pulse energy at 750 nm wavelength with a repetition rate of 10 Hz. The laser beam multiplexed to five fiber bundles is arranged over the detector array to provide circular illumination of the imaging plane, which is fixed or moved stepwise in a rostrocaudal direction with 0.1 mm increment.

Brain imaging with MSOT

Male mice (4-8 weeks old) were used for all experiments, which were conducted under general isoflurane anesthesia. To avoid direct contact with the US coupling water medium in the imaging chamber, animals were wrapped in optically and acoustically transparent foil prior to their placement in the holder in a supine position relative to the MSOT detector array. After *in vivo* imaging sessions, mice were injected with a lethal dose of ketamine (180 mg/kg) and processed for *ex vivo* brain imaging experiments, cryo-slicing and

immunohistochemistry. For *ex vivo* MSOT, brains were excised without or after perfusion (4% PFA in 0.1 M PBS) followed by 24 h post-fixation in 4% PFA. Wavelength selection was based on experimental requirements as well as consideration of light fluence maps, and absorption spectra of endogenous chromophores of the brain (Figures S1B–S1D).

For all functional brain imaging studies, mice were anesthetized, with customized magnetic beads attached to 6-10 large whiskers of rows B, C and D of the left side, which was used as the actuator of whisker stimulation. Anesthetized mice (1.2 - 1.8% vaporized isoflurane in air at 0.8 L/min) were placed in the MSOT, with the level of isoflurane subsequently reduced (0.7 - 1.0%) to achieve stable and shallow breathing, predictive of a highly responsive brain state. A custom-made rostral mask was utilized to ensure sufficient space for free whisker movement upon application of the magnetic force, while seamless contact was maintained between the mouse head and the coupling water medium (Figure S2A; Videos S1–S3). An 'in-house' designed electromagnetic unit containing an induction coil with a metallic rod in the middle was placed in the imaging chamber in close proximity to the mouse rostrum, to generate sufficient magnetic force for whisker deflections. The latter was controlled by a customized AC amplifier and an impulse generator unit (Figure S2B) to deliver rectangular current pulses (100 ms) at 3-5 Hz frequency.

The selection of imaging planes was based on the coordinates described in the mouse brain atlas (Franklin and Paxinos, 2008), as well as on anatomical references visualized by the MSOT *in vivo*, to ensure that selected cross-sections contain the somatosensory cortex barrel field and connected thalamic nuclei. As an additional reference, we used *in vivo* MSOT brain images co-registered with *ex vivo* scans, with the latter highlighting exquisite structural details. A series of functional images from adjacent planes (1.5 mm rostral or caudal from the central plane) were also acquired to ensure brain structures displaying the most pronounced signals had been captured in MSOT studies. To safeguard fast acquisition of multispectral data, measurements of stimulation induced activities were conducted at three wavelengths: 700 nm, 800 nm, 900 nm, which correspond to the absorption optima of deoxy- and oxy- Hb (Hb = 700 nm and HbO_2 = 900 nm) and isosbestic point, a measure of the total blood volume (805 nm) (Figures S1D, S3A, and S3B). For both, structural and functional imaging studies, raw data were collected without averaging at $\sim$3.3 Hz per each wavelength. Based on selected wavelengths, changes in Hb gradients and blood volume could be tracked over time and projected on anatomical MSOT cross-sections. After 60 s baseline imaging, whisker were stimulated over 10-30 s without interruption of the data collection, which was followed by 60 s post-stimulation recordings. For control experiments, the same protocols were followed with whiskers being not decorated with magnetic beads.

For *ex vivo* structural MSOT studies, non-perfused or perfused brains fixed with PFA were attached to a custom-made transparent rod placed in the center of the MSOT detector array, and imaged within 680-940 nm range, with 100 nm increment and 200 μm step-wise movements of the sample in the rostrocaudal direction. For *in vivo* structural MSOT, experimental procedures were similar to that of functional imaging studies except measurements were acquired along the entire rostro-caudal axis of the brain at 200 μm steps. Throughout these experiments, mice were supplied with air or transiently (30-45 s) challenged with 10% CO_2, to achieve a better contrast and visibility of deep structures. All structural imaging experiments were followed by euthanizing the mice with ketamine overdose (180 mg/kg), deep freezing and slicing (100 μm) of mice brains for correlative imaging using a Leica Cryostat CM1950.

Di-R injection into the brain and immunohistochemistry

Under deep anesthesia (ketamine 80 mg/kg and xylazine 10 mg/kg) the head of the mouse was fixed in a stereotactic frame with the skull surgically opened under local anesthesia (bupivacaine, 0.5%). Using a dental drill, small holes were bored over the dorsal cistern of the lateral ventricle (−0.34 mm bregma, 1.4 mm lateral, 1.5 mm deep) or over the caudate nucleus (+0.5 mm bregma, 1.5 mm lateral, 2.7 mm deep) (Franklin and Paxinos, 2008). NIR Di-R (Thermo-Fisher, Germany) was slowly pressure-injected (1.0 μL over 5-6 min) into the lateral ventricle or the dorsal striatum with a Hamilton syringe (22-gauge needle) followed by careful removal of the injector and wound stitching. In control experiments, similar procedures were followed except mice were injected with an equivalent volume of DMSO only. After surgery, animals were placed back into their home cage. Following 4 days recovery period, animals were used for *in vivo* and *ex vivo* MSOT brain imaging at peak Di-R absorption wavelength (Figure S1D) followed by histology and immunostaining. For the latter, coronal PFA fixed sections containing the substantia nigra were dried on a heating plate and treated with 4% PFA for 7 min, followed by rinsing with TBST (0.1 mM). The slices were blocked with 10% goat serum in TBS and Triton (0.1 mM and 0. 3%, respectively) for 1 hour at room temperature. After washes of blocking solution, tissue was incubated with primary antibodies (chicken, polyclonal anti-tyrosine hydroxylase, 1:50 and rabbit, polyclonal anti-NeuN, 1:50) (Abcam, CN76422, and CN104225, respectively) diluted in TBS- Triton 0.3% in a moisture chamber at 4°C overnight. On the following day the secondary antibodies (AlexaFluor594, goat anti-chicken 1:200 for tyrosine hydroxylase and AlexaFluor488 goat anti-rabbit 1:200 for NeuN) (Abcam N150176 and Life Technologies A-11008) were added for 1 h in a moisture chamber at room temperature before and after rinsing with TBS-Triton 0.3% for 3 times over 10 min. Tissue sections were subsequently mounted with Prolong Gold anti-fade mounting media containing DAPI and viewed in a Zeiss Axio-Imager M2 Microscope. For negative control sections, all procedures were kept the same except that goat serum in TBS was used instead of primary antibodies. For *ex vivo* validation of the injection site and structural MSOT results, we performed immunohistochemistry on 10 μm thick frozen sections cut by the Leica Cryostat CM1950.

QUANTIFICATION AND STATISTICAL ANALYSIS

MSOT images were generated using a model-based reconstruction algorithm (Dean-Ben et al., 2012) with Tikhonov regularization. All acquired frames were co-registered to suppress the motion artifacts with rigid registration of the algorithm based on mutual

information, which was supplied in MATLAB. Every frame was filtered using a Gaussian filter, with standard deviation (SD) of 2 pixels (200 μm). Similar to functional MRI data (Jonckers et al., 2015), in the resulting time-series, every pixel in the frame has an associated time trace representing the change of image intensity at the corresponding location. As functional imaging studies were performed at 3 wavelengths, all acquired data consisted of 3 time series. For every pixel, the corresponding intensity and time profile were filtered in the Fourier domain, with a low-pass filter in the range of up to 0.1 Hz, to remove high-frequency noise and any irrelevant signal fluctuations. A time trace of a hemodynamic response was generated based on the canonical Hemodynamic Response Function (HRF) $hrf(t)$ convolved with a ramp function $r(t)$ representing the stimulation pattern ($r(t) = 1$ if the stimulation is on at time t and 0 otherwise), resulting in the expected response function, $f(t)$: $f(t) = hrf(t) * r(t)$.

For temporal coherence analysis and determining the extent of the correlation of the activity between various brain subfields, intensity traces were correlated with $f(t)$. The absolute correlation values obtained for each pixel were plotted to generate a spatial correlation map. The correlation map threshold was tuned to discard pixels that do not correlate with the expected response strongly (correlation value below 0.5) or significantly ($p \leq \frac{0.05}{N}$, where N is the total number of traces considered for a specific wavelength). For every pixel p_i, the corresponding baseline intensity variability range was computed as $\mu_i \pm 2\sigma_i$, where μ_i and σ_i are the mean and standard deviation of the pixel intensity during the baseline measurement. For illustration purposes of brain activation, thresholded pixels altered by activation were overlaid in color over the anatomical images. A pixel p_i shown as active at time t has a corresponding correlation value higher than 0.5 and the corresponding intensity value at time t exceeding the baseline variability range. Pixel color is coded to represent the deviation of its value from μ_i. Pixels with the corresponding time traces having negative values were discarded as such values have no physical meaning. This, however, did not mean that the corresponding time trace did not bear information on activation. For every obtained multispectral frame, sO$_2$ was computed using a linear unmixing algorithm. To achieve better accuracy of sO$_2$ estimation, all frames were calibrated for 4 cm water absorption prior to spectral decomposition. For illustration purposes of thresholded pixels, the corresponding computed sO$_2$ values were overlaid in color on anatomical images, with pixels labeled as activated at either 700 nm or 900 nm illumination wavelengths.

For brain circuit analysis, 17 regions of interest (ROIs) were identified in MSOT brain cross-sections. Time traces corresponding to pixels in a particular region were averaged to improve the SNR. The resulting time series p_i, $i = 1 \ldots 17$ were compared pairwise. Correlation values as well as the corresponding P values were computed and presented. Furthermore, for each of the investigated time series, the activation amplitude A was computed as $A = \max|p_i - \mu_i|$, where μ_i is the mean value of p_i during the baseline measurement. For seed-based correlation analysis, several seed regions have been identified. For every region, the corresponding traces have been averaged and the resulting time series was correlated to every trace outside of the seed region. The resulting correlation maps were thresholded as described above.

Anatomical MSOT images were generated through averaging 10 frames of the same anatomical planes acquired at a single specified excitation wavelength. For assessment and presentation of the Di-R data, reconstructed MSOT images were analyzed with a QL-shrinkage detection algorithm (Tzoumas et al., 2016) that estimates the spatial distribution of a contrast agent in the recorded multispectral dataset based on absorption spectrum.

In whole brain imaging studies with tracer injection, the resulting images and spatial distribution of Di-R were rendered in 3D and overlaid with anatomical images using Amira (ThermoFisher). All color maps are generated with MATLAB, while IgorPro was used for plotting graphs. Final figures were prepared using IgorPro (6.1, Wavemetrics, Oregon) and Adobe Illustrator (CS6 package). Where applicable, the mean values and standard error of the means (SEM) have been presented in graphs, to illustrate the distribution of the parameters of interest. Unpaired and paired Students t tests and one-way analysis of variance (ANOVA) have been used for variance analysis and comparison, with p values less than 0.05 defining differences as statistically significant.
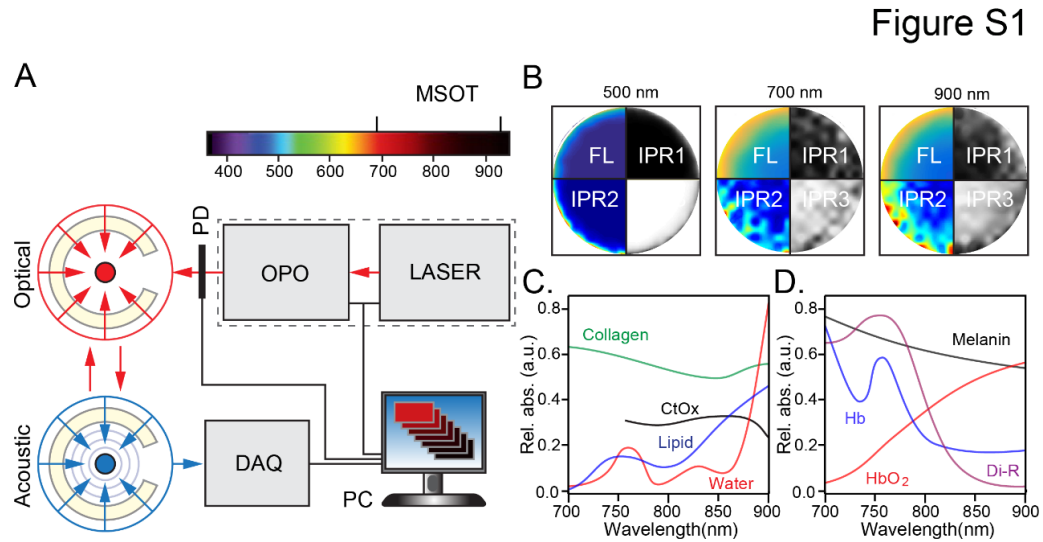
Supplemental Information

Spatial and Spectral Mapping and Decomposition

of Neural Dynamics and Organization of the Mouse

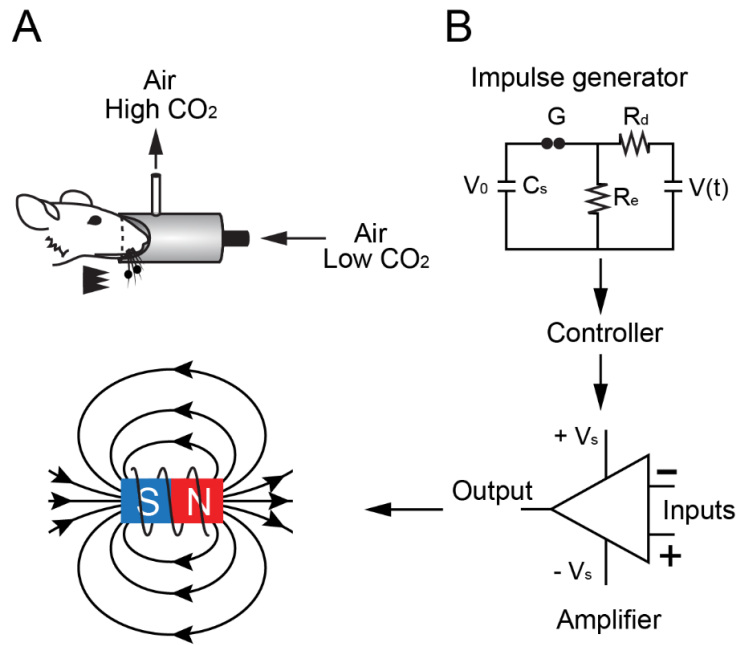**Brain with Multispectral Optoacoustic Tomography**

Ivan Olefir, Ara Ghazaryan, Hong Yang, Jaber Malekzadeh-Najafabadi, Sarah Glasl, Panagiotis Symvoulidis, Valerie B. O'Leary, George Sergiadis, Vasilis Ntziachristos, and Saak V. Ovsepian

Figure S1: Experimental setup and optimization of imaging parameters for brain imaging with MSOT. Related to Figure 1. (A) Schematic representation of the MSOT: illumination (optical, red) and detection (acoustic, blue) modules; OPO – optical parametric oscillator; PD – photodiode; DAQ – data acquisition system; PC – personal computer. (B) Series of simulation highlighting the effective illumination of circular biological sample at different wavelengths, with a radius of 1 cm. Only oxy- and deoxyhemoglobin absorption values are implemented. FL – optical fluence and spatial maps of the initial pressure rise in three different color maps (IPR1 that is used traditionally, IPR2 that highlights the contrast between different simulated structures and IPR3 that is used throughout the manuscript to demonstrate images). Note much stronger attenuation of the illumination in deeper compartments at 500 nm as compared to 700 nm or 900 nm. (C) NIR absorption spectra of the main endogenous chromophores of the brain. CtOx – cytochrome oxidase; Hb and HbO_2 – deoxy- and oxyhemoglobin.

Figure S2

A

Air
High CO_2

Air
Low CO_2

S N

B

Impulse generator

G R_d

V_0 C_s R_e $V(t)$

Controller

$+ V_s$

Output

$-$

Inputs

$+$

$- V_s$

Amplifier

Figure S2: Custom designed breathing mask and device for mechanical whisker stimulation using a push-pull magnet. Related to Figure 1 and Figure 2. (A) Schematic illustration of the custom designed face mask enabling ample air supply with maintained ample space for free deflection of the whiskers decorated with magnetic beads (top) and a coil magnet providing force for movement of the whiskers within the MSOT imaging chamber. (B) A custom designed impulse generator and controller for induction and delivery of stimulation patterns for activation of whisker input in mice.
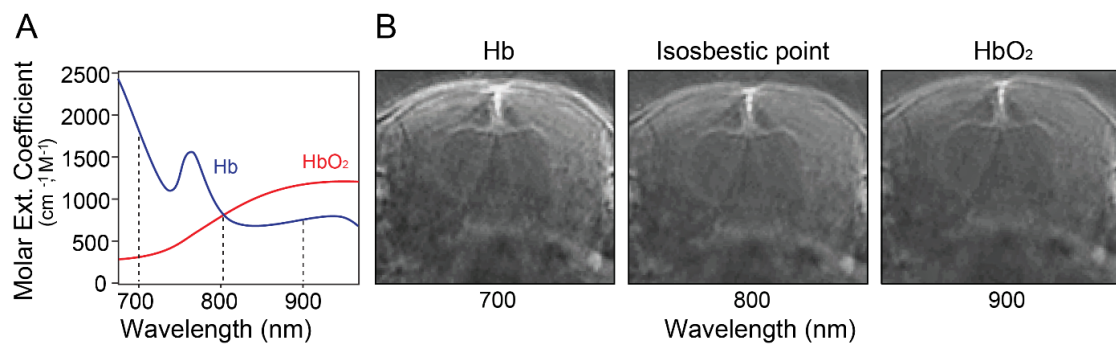
Figure S3: Selection of illumination wavelengths for anatomical imaging and mapping of stimulation induced hemodynamic response and changes of hemoglobin gradients with MSOT in the mouse brain *in vivo*. Related to Figure 1 and Figure 2. (A) Graph of NIR absorption spectra of Hb and HbO$_2$ with selection of 700 nm and 900 nm wavelengths for deoxy- and oxyhemoglobin readouts, while 805 nm wavelength, corresponding to the isosbestic point of hemoglobin was used as a readout of total blood volume changes. (B) Raw images of mouse brain cross-sections at -1.2 mm Bregma acquired at three different wavelengths.
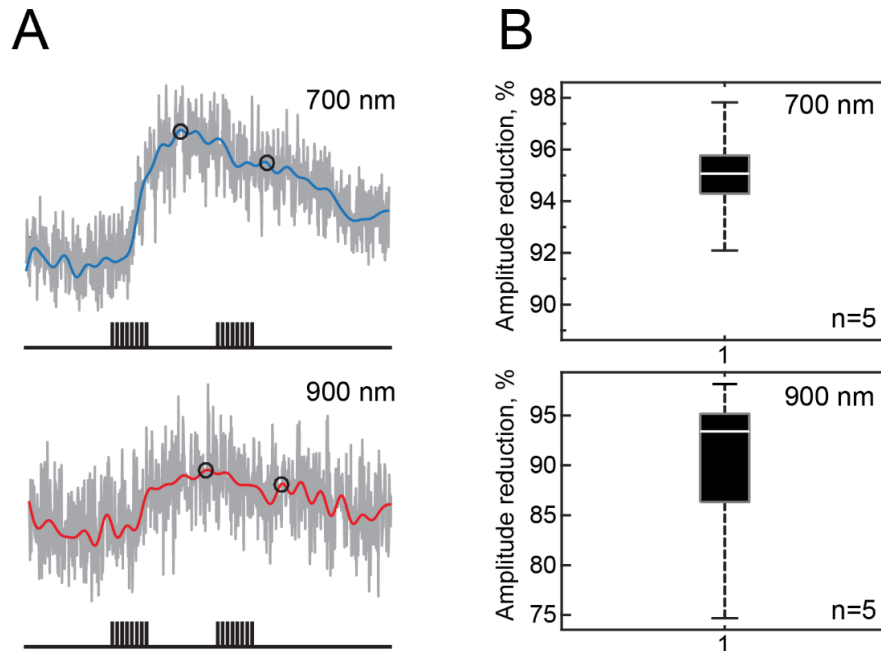
Figure S4: Activity-dependent inhibition of the hemodynamic changes in the somatosensory barrel field induced by two series of repetitive stimulation trains. Related to Figure 1. (A) Representative traces of Hb and HbO_2 signals activated in the somatosensory cortex barrel field induced by two barrages of whisker stimulation ($8 \times 4Hz$) separated by 10 sec interval. Filtered traces have been used for this analysis, with peak amplitude defined manually at the first and second response driven by whisker inputs. (B) Summary graphs illustrating reduction of both Hb and HbO_2 signal in response to two series of stimulation.
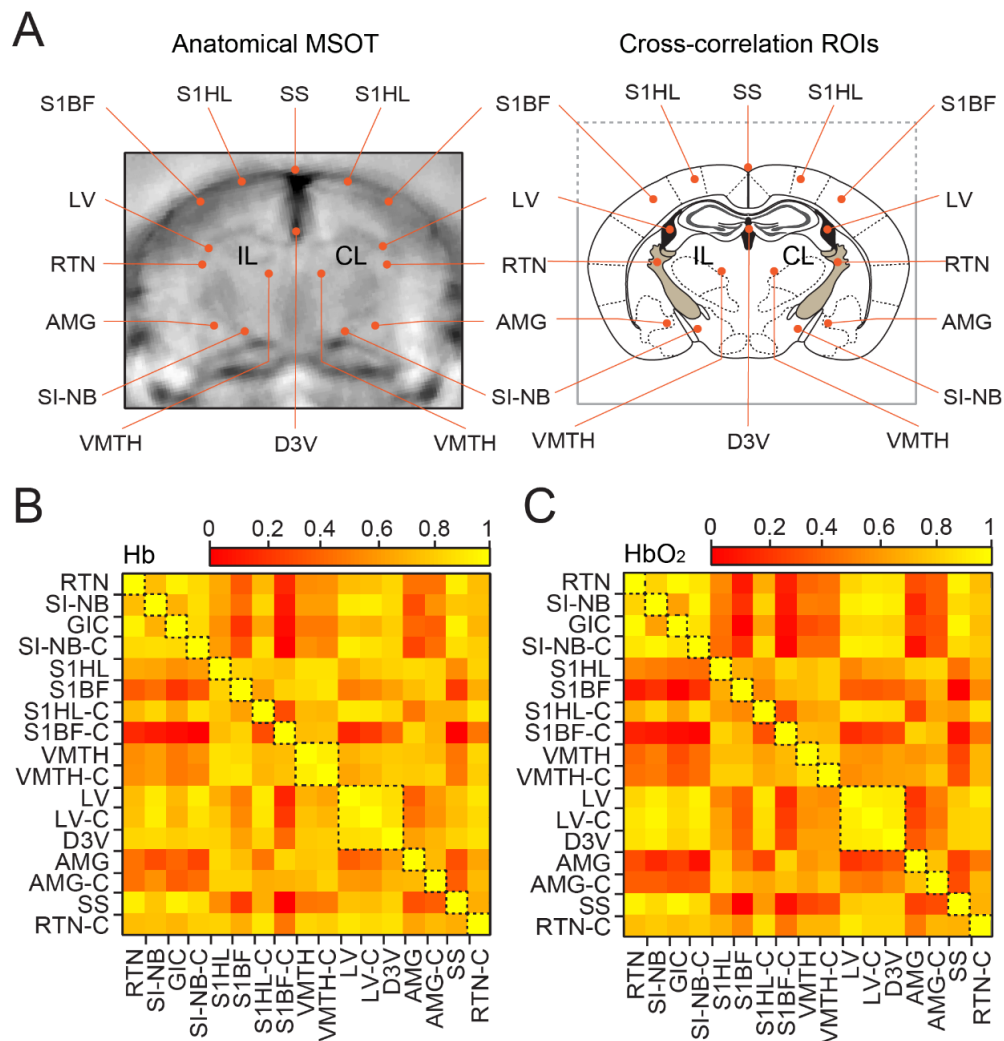
Figure S5: Mapping hemodynamic response in the resting brain of anaesthetized mice with MSOT. Related to Figure 3. (A) Anatomical MSOT cross-section of the brain containing the somatosensory barrel cortex, with regions of interest selected for Hb and HbO$_2$ analysis. Abbreviations: RTN – reticular thalamic nucleus; SI-NB – substantia innominate nucleus basalis; GIC – granular insular cortex; SI-NB-C – substantia innominate nucleus basalis contralateral; S1HL – primary somatosensory, hind limb; S1BF – primary somatosensory, barrel field; S1HL-C – primary somatosensory, hind limb contralateral; S1BF-C – primary somatosensory, barrel field

contralateral; VMTH – ventromedial thalamic nucleus; VMTH-C – ventromedial thalamic nucleus, contralateral; LV – lateral ventricle; LV-C – lateral ventricle, contralateral; D3V – third dorsal ventricle; AMG – amygdala; AMG-C – amygdala contralateral; SS – sagittal sinus; RTN-C – reticular thalamic nucleus, contralateral. (B, C) Cross-correlation matrices of Hb (700 nm), HbO_2 (900 nm) from seventeen regions of interest.
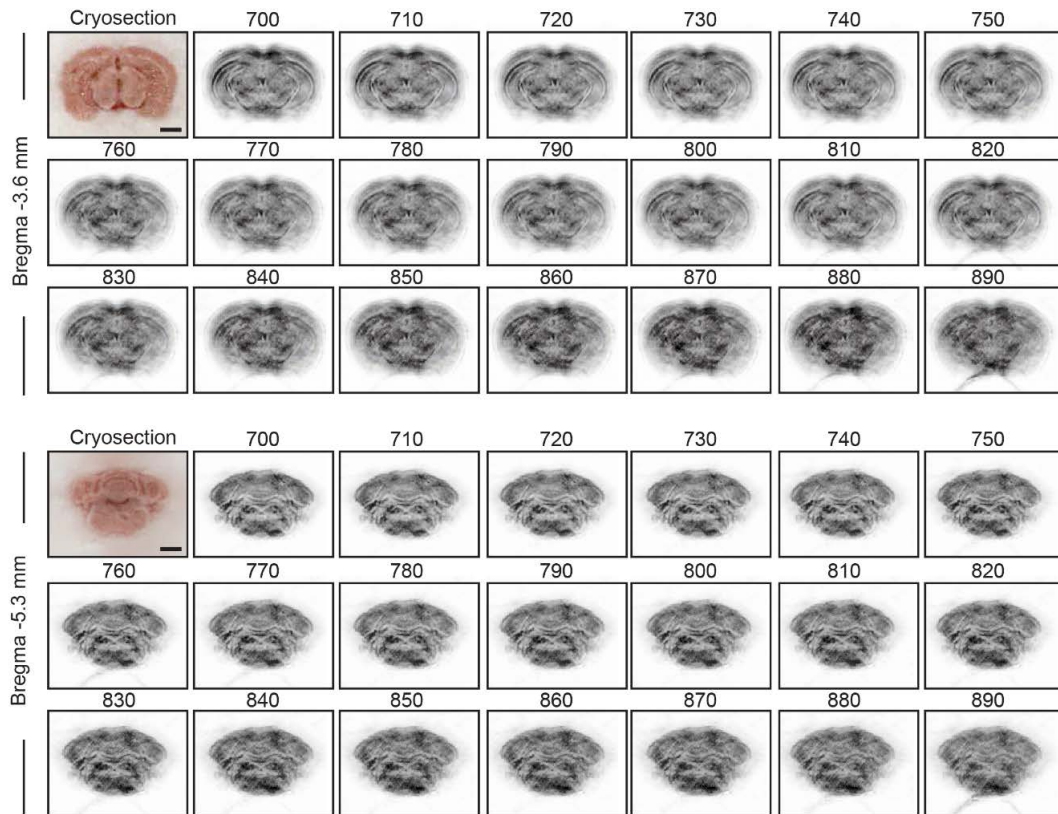
Figure S6: MSOT scans of ex vivo brain acquired at incremental wavelengths between 700 nm and 900 nm at two distinct planes corresponding to the midbrain and hindbrain levels, with corresponding cryo section image. Bregma coordinates on the left. Related to Figure 4 and 5. Note the great visibility of exquisite anatomical details throughout the brain with their wave-length dependent changes.

Mice	Functional MSOT			Structural MSOT				Optimizing Troubleshooting	Total
	No stimulation	Whisker stimulation		*Ex vivo*		*In vivo*			
Settings	Single plane	Single plane	Multiple planes	Perfused	Non-perfused	Tracer	No-tracer		
CD1	0	7	4	6	4	0	0	4	25
Nude	6	0	0	0	0	4	4	3	17

Table S1: Number of animals used for different experiments in this study. Related to STAR Methods.